

NASA Conference Publication 2050

(NASA-CP-2050) FLIGHT MECHANICS/ESTIMATION
THEORY SYMPOSIUM (NASA) 289 P HC A13/MP A01
CSCL 22A

N79-14121
THEU
N79-14135
Unclas
41041

G3/13

**Flight Mechanics/Estimation
Theory Symposium
October 1977**

Sponsored by
Systems Development and Analysis Branch
Mission Support Computing and Analysis Division
Goddard Space Flight Center
Greenbelt, Maryland



NASA

May 1978

NASA Conference Publications (CP Series) contain compilations of scientific and technical papers or transcripts arising from conferences, workshops, symposia, seminars, and other professional meetings that NASA elects to publish.

The text of these proceedings was reproduced directly from author-supplied manuscripts for distribution prior to opening of the meeting. NASA has performed no editorial review of the papers other than those contributed by its employees or contractors.

NASA Conference Publication 2050

**Flight Mechanics/Estimation
Theory Symposium
October 1977**

**Sponsored by
*Systems Development and Analysis Branch
Mission Support Computing and Analysis Division
Goddard Space Flight Center
Greenbelt, Maryland***

NASA

National Aeronautics and
Space Administration

May 1978

EDITOR'S NOTE

The papers presented herein have been derived primarily from speakers' summaries of talks presented at the Flight Mechanics/Estimation Theory Symposium held October 18 and 19, 1977 at Goddard Space Flight Center. For the sake of completeness, abstracts are included of those talks for which summaries were unavailable at press time. Papers included in this document are presented basically as received from the authors with a minimum of editing.

CONTENTS

	<i>Page</i>
Editor's Note	iii
Compression of Ephemerides by Discrete Approximations <i>H. M. Pickard, A. Deprit, and W. Poplarchek</i>	1
Application of Semianalytical Satellite Theories to Precision Orbit Determination <i>P. J. Cefola</i>	18
Critical Inclinations in Satellite Theory <i>A. Deprit</i>	28
A Singularity Free Analytical Solution of Artificial Satellite Motion with Drag <i>A. Mueller</i>	33
Effect of Atmosphere on Venus Orbiter Navigation <i>M. Ananda and B. Sanchez</i>	37
Density Models for the Upper Atmosphere <i>D. L. Dowd and B. D. Tapley</i>	38
A Demonstration of the Value of General Purpose, On-Board Satellite Computers <i>R. E. Jenkins and J. M. Whisnant</i>	79
Kalman Filter Models for Satellite On-Board Navigation Using Global Positioning System Data <i>L. Miller</i>	120
Orbit Determination Accuracies Using Satellite-to-Satellite Tracking <i>F. O. Vonbun, P. D. Argentiero, and P. E. Schmid</i>	121
On-Board Landmark Navigation and Attitude Reference Parallel Processor System <i>L. E. Gilbert and D. T. Mahajan</i>	153

THIS PAGE BLANK NOT FOR

CONTENTS (Continued)

	<i>Page</i>
Autonomous Satellite Orbital Navigation and Attitude Determination	
<i>S. P. Kau</i>	178
The Operational Feasibility of Orbit and Attitude Determination for SMS/GOES Using Only Imagery Data	
<i>B. Remondi</i>	194
Recursive Estimator for OSO-8 Attitude	
<i>R. D. Headrick and D. Y. Park</i>	207
Performance of Ground Attitude Determination Procedures for HEAO-1	
<i>L. Fallon, III and C. R. Sturch</i>	219
ISEE-C Attitude Determination Using Fine Sun Sensor Data Only	
<i>L. P. Gunshol</i>	237
Infrared Horizon Scanner Attitude Data Error Analysis for SEASAT-A	
<i>M. C. Phenneger, C. Manders, C. B. Spence, Jr., M. Levitas, and G. M. Lerner</i>	259
Attitude Acquisition Contingency Studies for the Applications Explorer Missions-A/Heat Capacity Mapping Mission (AEM-A/HCMM) Spacecraft	
<i>W. Huang, M. G. Grell, and G. M. Lerner</i>	282

COMPRESSION OF EPHEMERIDES BY DISCRETE CHEBYSHEV APPROXIMATIONS

H.M. Pickard
U.S. Naval Research Laboratory

A. Deprit and W. Poplarchek
University of Cincinnati

There has been a lot of interest lately in representing the ephemerides of satellites and planets in terms of truncated polynomial series. This paper discusses the use of Chebyshev series for this purpose and specifically a Fortran package which has been developed for fitting satellite orbits. The features desired in any approximation are 1) the ability to compress a satellite ephemeris, 2) the ability to represent a satellite ephemeris over several orbits, 3) guaranteed accuracy to within prescribed tolerance over the time interval of consideration, and 4) fast processing. These features are imposed with an eye towards adapting the approximation for use on microprocessor applications in which storage is limited and real time processing is required. GPS, for example, will require that the representation be usable not only on spacecraft but also by users on ships, aircraft, or portable land units. The use of a polynomial approximation ensures the fast processing of requirement (4) above since only multiplications, additions, and subtractions are involved in the processing. The way in which polynomial approximations can be made to satisfy the other three requirements above is the subject of this paper.

Corio [1] demonstrates the ability of a Chebyshev polynomial series to represent a satellite orbit by fitting 25 points with a 24th degree polynomial. The 25 points are equally spaced, and since the degree of the polynomial is exactly one less than the number of points, the polynomial

interpolates the 25 points. The X coordinate of a geosynchronous satellite over two periods of its orbit is shown in Fig. (1), taken from Corio's paper. The corresponding error curve, which is the difference between the true value of X and the polynomial approximation to X, is plotted in Fig. (2), also from Corio's paper. It is apparent that the error curve is not at all uniform. The approximation fits the 25 data points exactly, as it must, but the Gibbs effect is striking as we see that errors of 10 km. occur at the end points of the interval. The desired one meter accuracy can only be achieved over the middle 24 hours of the interval.

This approximation can be improved greatly by choosing at unequal intervals the reference points at which we interpolate. We can improve even further (without increasing the degree of the polynomial) by increasing the number of reference points. Naturally we must abandon polynomial interpolation to do this, and must use other methods such as least squares (L.S.) approximation or, as will be done here, linear programming (L.P.) techniques. The key to the whole procedure is to use a non-uniform distribution of reference points. This causes problems, since numerical integrators generally tabulate ephemerides at equal intervals. Therefore, the authors present a method which has been developed to remove this problem.

Best Approximations

Chevyshev conjectured that a best polynomial approximation of degree N to a function y exists.

Let $P(\underline{c}, t) = \sum_{0 \leq j \leq N} c_j T_j(\tau)$ approximate $y(t)$

\underline{c} is the vector of coefficients c_j .

T_j is the Chebyshev polynomial of degree j.

τ is linearly related to t ($a \leq t \leq b$ and $-1 \leq \tau \leq 1$).

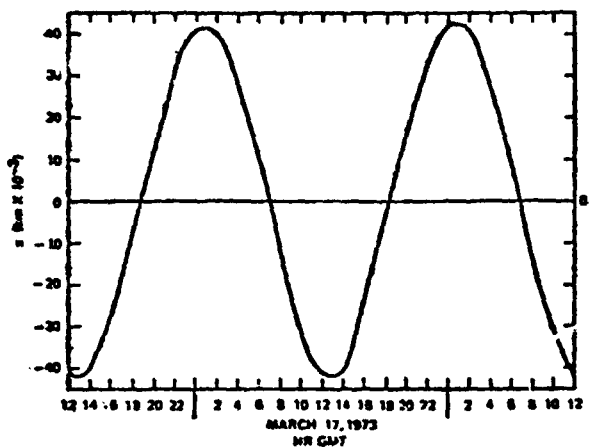


Figure 1. X-Coordinate: Geosynchronous Satellite

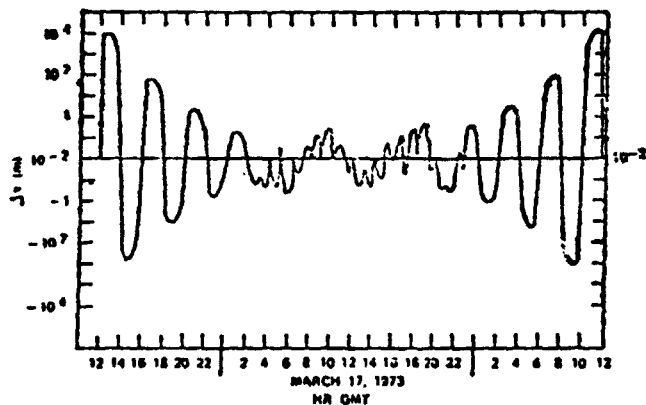


Figure 2. Corresponding Error Curve:

Degree = 24

25 Reference Points, Uniformly Spaced

N is the degree of $P(\underline{c}, t)$

Define $e(\underline{c}, t) = y(t) - P(\underline{c}, t)$ $a \leq t \leq b$.

Find the set denoted \underline{c}^* such that

$$\text{Max } |e(\underline{c}^*, t)| \leq \text{Max } |e(\underline{c}, t)|$$

for every \underline{c} and all t in $a \leq t \leq b$.

$P^*(t) = \sum_{0 \leq j \leq N} c_j^* T_j(t)$ is then the "best approximation" of degree

N to $y(t)$.

$P^*(t)$ is characterized by the following:

There exist at least $N+2$ points $(y(t_k), t_k)$ such that

$$a \leq t_0 < t_1 < \dots < t_N < t_{N+1} \leq b$$

$$e(\underline{c}^*, t_k) = (-1)^k \lambda$$

$$|e(\underline{c}^*, t)| \leq \lambda$$

$$\lambda \geq 0$$

The points t_k are called "critical points". Conversely, a polynomial exhibiting these properties is the "best approximation" of degree N to $y(t)$. The authors of [2] have developed an algorithm to move from an initial set of reference points to the critical set in a finite number of iterations. They have programmed the algorithm in PL1 and have used it in planetary applications. Unfortunately, the procedure requires an analytical or semi-analytical orbital theory, and cannot be used with the tabulated ephemerides coming from numerical integration techniques. The reason for this is that the method requires first derivatives of the function being approximated, and numerical differentiation cannot adequately evaluate these derivatives.

Discrete Approximations

The polynomial interpolation scheme of Corio (in which the

reference points are equally spaced) does not yield a uniform approximation of satellite orbit coordinates, though a polynomial interpolation can yield good results if the reference points are selected carefully. Further, a "best" polynomial of given degree to a given function does exist, but it is not possible to find the "best" approximation when all that is known are discrete values of the function. Therefore, try an approximation based on fitting a number of data points which is considerably larger than the desired degree of the approximating polynomial. This suggests that the function be approximated using a L.S. fit to the tabulated data. Another approach is to fit the data using a minmax approach with an efficient L.P. algorithm developed by Barrodale and Phillips at the University of Manitoba [3]. Both L.P. and L.S. methods will yield uniform approximations, if the reference points are properly chosen. The important advantage of using Barrodale's L.P. algorithm, is that it automatically gives the maximum error in fitting the given points, which in turn gives an estimate of the maximum error over the entire interval.

The discrete approximation problem is stated as follows:

Let $P(\underline{c}, t) = \sum_{0 \leq j < N} c_j T_j(\tau)$ approximate $y(t)$ as in the continuous case.

Define $e(\underline{c}, t)$ as before.

For M discrete points $(y(t_k), t_k)$ in the interval $a \leq t \leq b$, find a set of coefficients denoted \underline{c}^* such that

$$\text{Max } |e(\underline{c}^*, t_k)| \leq \text{Max } |e(\underline{c}, t_k)|$$

for all \underline{c} and $k = 1, 2, \dots, M$.

$P^*(t) = \sum_{0 \leq j < N} c_j^* T_j(\tau)$ is then the best approximation of degree N to the

M points $(y(t_k), t_k)$. It should be noted that Barrodale's algorithm does not

require a representation in terms of Chebyshev polynomials. In general, the T_j above can be replaced by any set of real valued functions ϕ_j . Barrodale's algorithm is a modification of the Simplex procedure for solving linear programming problems. The Fortran implementation of the algorithm is given in the ACM Transactions on Mathematical software[3]. A detailed description of Simplex method used is given [4] and can be obtained by writing directly to Barrodale or Phillips.

Before describing the package that has been developed and results that have been obtained with it, Figs. (3) and (4) are presented to emphasize the importance of carefully choosing the reference points. The dashed curves in Fig. (3) indicate the error obtained in fitting the number of points given by the abscissa with a 24th degree polynomial. The solid curves give the error evaluated at 500 points over the interval and are used as the true measure of the error over the continuum of the interval. Curves 1 correspond to a non-uniform distribution of reference points, and Curves 2 correspond to a uniform distribution. (These results are for a 12 hour satellite; the error is in meters and is logarithmically scaled.) These curves show that a uniform distribution of points gives very poor results when there are only a few reference points, while a non-uniform distribution gives reasonably good results. Even for a large number of reference points, the uniform case never does as well as the non-uniform case, even though the predicted error is always less for the uniform case. In order to get the lowest degree which will give the desired accuracy, with a minimum number of reference points, and with a reliable estimate of the true error over the interval, it is imperative that the reference points be non-uniformly spaced.

The error curves of Fig. (4) also evaluate the performance of polynomial

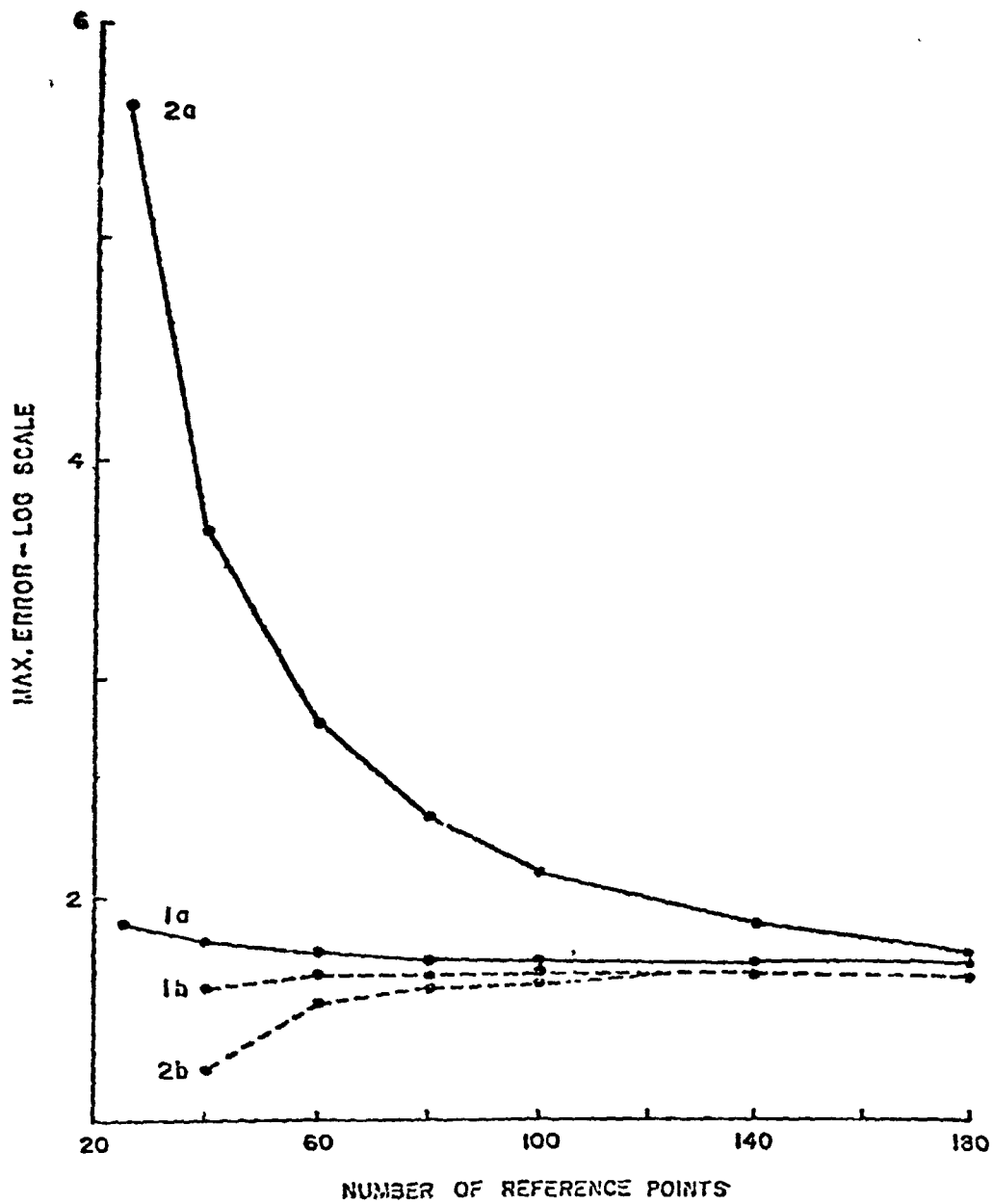


Figure 3. Comparison of Polynomial Approximations Using Uniform and Non-uniform Reference Point Distributions for Several Numbers of Reference Points

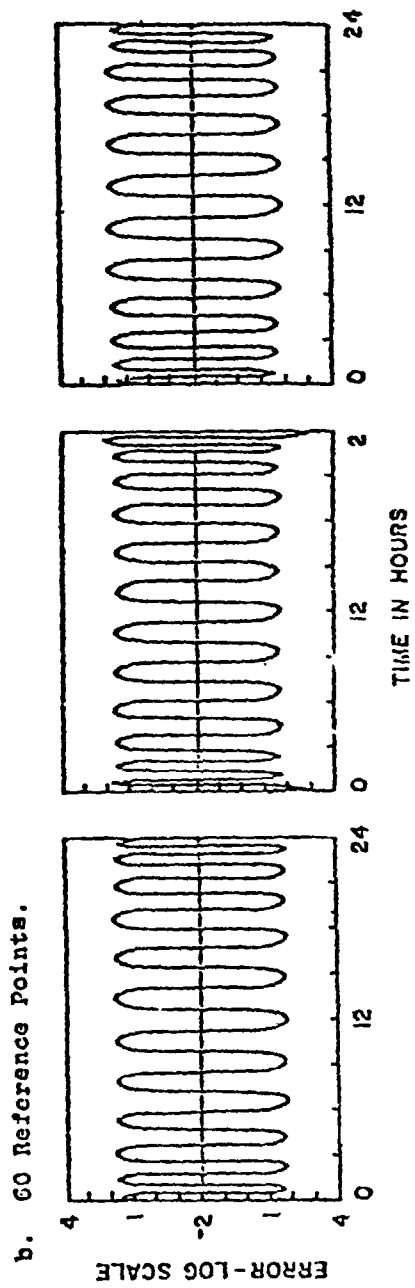
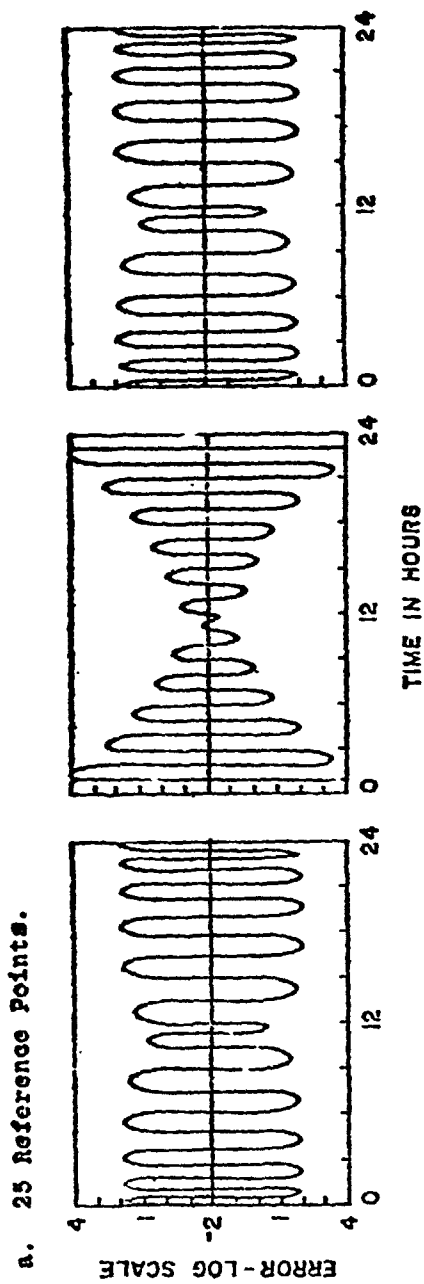


Figure 4. Error Curves for 24th Degree Fit

approximations under different situations. The fit is for two periods of a 12^h satellite; the error is in meters and is logarithmically scaled. The first curves in each set correspond to a non-uniform distribution. The approximation for 25 reference points is seen to be reasonably good. That for 60 points is close to the best approximation, since the error curve ripples uniformly over the interval. The second curves in each set correspond to a uniform distribution. For 25 points, the error is excessively large over a large portion of the interval. For 60 points, the error is much better over much of the interval, but still rises sharply near the endpoints. The third figure in each set is for a non-uniform distribution, but L.S. fitting is used rather than the L.P. method. The L.S. fit is certainly not any better than the L.P. fit, and thus, the computational superiority of the L.P. method makes it the method of choice.

The NRL Package that has been built around this algorithm is tailored to the problem of fitting satellite orbital elements. The main input to the package is an ephemeris file giving time, distance, latitude, and longitude. The time intervals in the file may, but need not be, equal. The program will automatically interpolate (using Lagrange interpolation) the data to get values of the elements at the desired times. The total time interval of consideration, the number of reference points to use, the desired accuracy of the interpolation, and the desired degree or range of degree of the approximating polynomial are entered via a separate control file. As output, the user receives the coefficients to construct the

approximating polynomial and the maximum error in fitting the reference points.

Often the user will know the accuracy he wants but will not know the degree needed to achieve this accuracy. In this case, it is possible to specify a range in the degree and the program will automatically increment the degree until the necessary degree is found. When running the program in this mode, it is often possible for the program to determine half way through the fitting procedure that the specified accuracy will not be attained, and abort the procedure. The program then increments the degree and tries again. The program also has the ability to increment the degree by more than one if it appears that the accuracy attained by the current degree will be much less than that desired. This method works well for orbits with small eccentricity, since the program converges rather quickly in this case. For higher eccentricities ($e \geq 0.5$), there is a problem. A plateau is reached, wherein it takes large increments in the degree to improve the accuracy of the fit.

It is the built-in ability to estimate the error in the approximation which makes Barrodale's algorithm much more convenient to use than L.S. fitting. When L.S. fitting is used, one obtains only the coefficients needed to construct the approximating polynomial. If the desired degree is already known, this may be sufficient, but usually some idea of the accuracy of the fit is required. With L.S., this estimate of accuracy must be obtained apart from the fitting procedure. From the standpoint of computer use, this is awkward and inefficient. Barrodale's algorithm,

on the other hand, gives not only the error in the fit, but a reliable estimate of this error half way through the fitting procedure. Then, if the reference points have been properly chosen, this error in fitting M points provides a reliable estimate of the error over the continuum of the time interval. Thus, if only the desired accuracy is known, the fitting routine can automatically increment the degree until this accuracy is achieved.

The general flow of the NRL Package is illustrated in Figure (5). The ephemeris and control files supply input to the interpolation block, which in turn prepares the reference points to be fitted. Normally, the ephemeris file will be much larger than the final reference set to be fitted. To fit all the points of the ephemeris file would be extremely costly and unnecessary. Far fewer points can usually be used if they are non-uniformly spaced. The interpolation block of the package obtains these points quickly and accurately. The Barrodale fitting routine is shown in the dashed box. It has been modified to allow early exit under certain conditions, and a looping structure has been built around it to automatically increment the degree of the approximating polynomial. `ERRMAX` is a FORTRAN variable which indicates the maximum error desired. `ERRMAX` and the desired range of degree are both supplied through the control file. `RESMAX` is a FORTRAN variable which on termination of the fitting procedure is the maximum error of the fit. At the point of the first test within the dashed box (this comes about half way through the fitting algorithm), `RESMAX` is very close to but less than this maximum

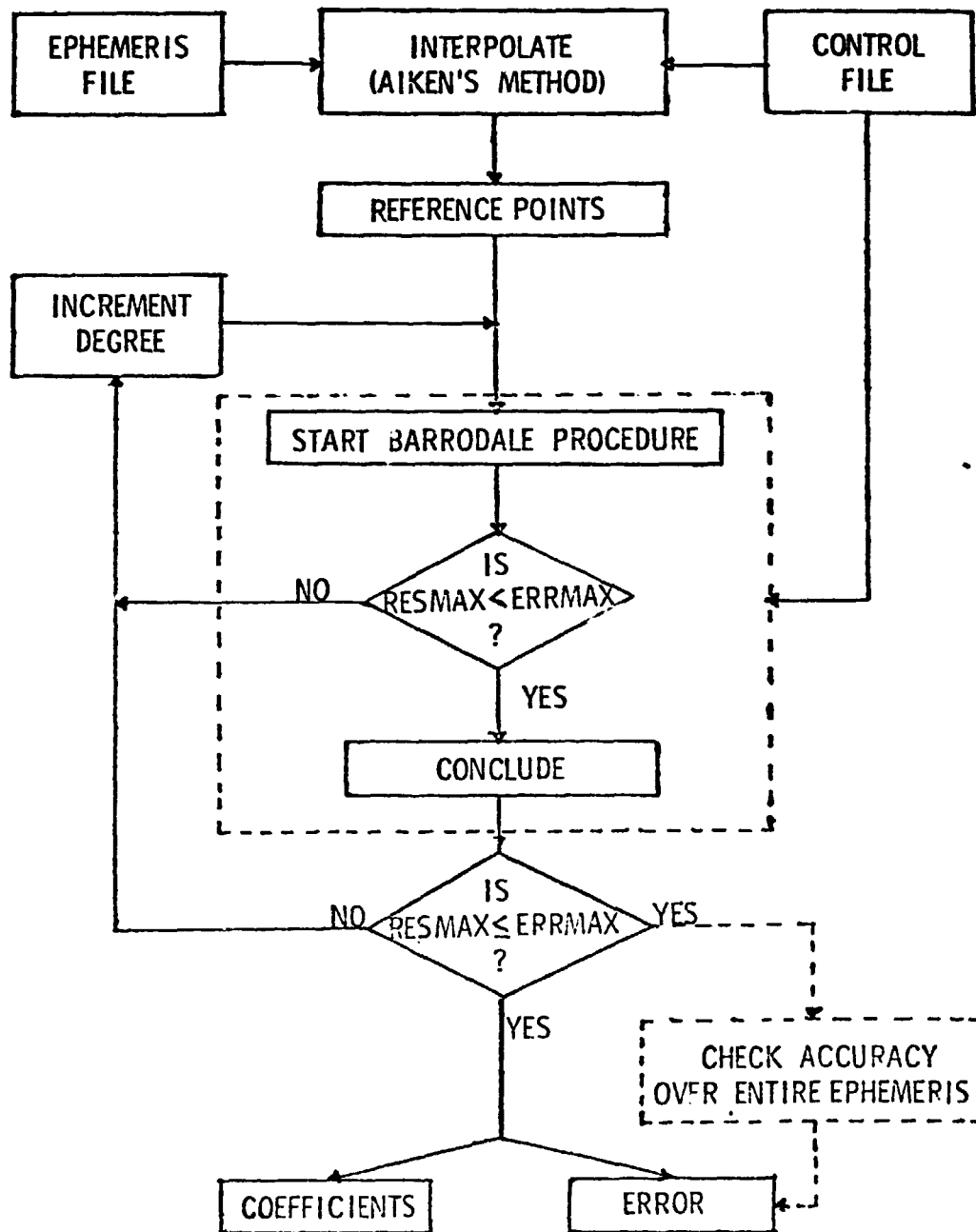


Figure 5. Flowchart of the NRL Ephemeris Compression Package

error. Thus, at this point, RESMAX is a good indicator of whether this maximum error will ultimately be achieved. The NRL package has used this feature of Barrodale's algorithm to advantage in the looping structure. Most of the looping can take place quickly, so that the second test (just outside the dashed box) is usually satisfied when it is reached. If so, the fitting procedure is finished. If not, the looping continues automatically.

The dashed box in the lower right hand corner of figure (5) is included to demonstrate the procedure if the L.P. algorithm is replaced with a L.S. algorithm. Neither of the two tests in the L.P. method can be used in a L. S. method. The entire procedure must be finished and the approximation evaluated at each of the points of the reference file to obtain the error of the fit. In the NRL package, this box has been included as an option to evaluate the performance of the polynomial approximation. The maximum error over the entire ephemeris file is calculated for comparison with RESMAX coming out of Barrodale's algorithm. Experience has shown that for satellites of small to moderate eccentricity, RESMAX is accurate to within 10% - 20%. Thus, this final check can be bypassed in most cases.

Representative examples of the use of the package are shown in Tables (1), (2), and (3). Table (1) shows the results for the compression of the 24^h satellite SMS-B. These results show that one period or less of a satellite can be easily fitted with a polynomial of low degree. Equally important is the fact that several orbits can be fitted with a polynomial

Table 1. Compression of Ephemerides for the 24h Satellite SMS-B

RANGE	DEGREE	ΔR (METERS)	ΔU (SEC OF ARC)	ΔV (SEC OF ARC)
0 ^d ,5	8	2.28	.003	.002
1 ^d .	12	0.83	.004	.002
2 ^d .	20	3.47	.02	.003
3 ^d .	28	6.17	.04	.004
4 ^d .	36	9.68	.07	.01
5 ^d .	40	33.45	.21	.02

Table 2. Compression of Lunar Ephemeris

RANGE	DEGREE	ΔR (METERS)	ΔU (SEC OF ARC)	ΔV (SEC OF ARC)	$\Delta \alpha$ (SEC OF ARC)	$\Delta \delta$ (SEC OF ARC)
7 ^d	7	3.4	.02	.01	1.00	1.17
14 ^d	10	3.70	.05	.02	.13	.12
21 ^d	18	12.70	.01	.01	.08	.03
28 ^d	40	9.3	.01	.01	.01	.01
56 ^d	50	9.87	.02	.01	.02	.01

Table 3. Difference in Degree Needed to Fit Elliptic and Real Orbits

MAX. ERROR	ECCENTRICITY			
	0.0	0.1	0.5	
1 km	0 (4)	6 (6)	18 (18)	R COMPONENT
1 m	0 (10)	12 (12)	34 (37)	1 PERIOD
1 km	11 (11)	11 (11)	25 (25)	X COMPONENT
1 m	15 (15)	15 (15)	35 (43)	1 PERIOD
1 km	0 (8)	12 (12)	*	R COMPONENT
1 m	15 (15)	22 (22)	*	2 PERIODS
1 km	18 (18)	20 (20)	*	X COMPONENT
1 m	22 (24)	30 (30)	*	2 PERIODS

of moderate degree. In this case, five periods of the satellite are approximated by a polynomial of degree 40. Table (2) gives results for the compression of the lunar ephemeris. This table again demonstrates the ability of polynomial approximation to represent more than one period of an orbit. A polynomial of degree 50 can represent 2 periods of the moon with an error of less than 10 meters, which is better than one part in 10^7 . Since the eccentricity of an orbit affects how easily it can be approximated, Table (3) shows results for a 12^h satellite of different eccentricities. Elliptic orbits were used to study the relationship between eccentricity and degree needed to fit. More complete results are given in Tables III-VII of [5], and the information in those tables may be used in estimating the degree needed to fit a particular orbit. The numbers in parentheses are the degrees needed to fit real rather than elliptic orbits. It is seen that the results for elliptic orbits carry over very well for low to moderate eccentricities. For higher eccentricities, the degrees calculated for elliptic orbits are too small, but they still give an idea of the degree needed for fitting a real orbit.

Conclusions and Recommendations

Experience has shown that polynomial approximations in terms of Chebyshev polynomials are very effective in representing satellite and planetary ephemerides. They meet all the criteria we specified for compression, accuracy, and spanning several orbits, and computationally, they are the simplest representation possible. To take full advantage

of their capabilities, it is necessary to choose reference points crowded towards the end points of the time interval. If uniformly spaced reference points are used, accuracy is sacrificed greatly, or an inordinately large number of reference points is required to find that minimum degree. The package will accept conventionally tabulated ephemerides with uniformly spaced points and interpolate to obtain the proper distinction of reference points. It is smart enough to abort the fitting procedure early when it sees the degree is too low, and then it will automatically increment the degree and start over. In this mode of operation, it is vastly superior to an L.S. formulation. Even in the case where the desired degree is known, it is superior to L.S. fitting in that the algorithms are very efficient and they automatically give the error in the fit. This package is available in card form from the Space Systems Division of NRL. Supplied with it is a set of test data with results which can be used as a benchmark. At present, it has been successfully run on Amdahl computers at the University of Cincinnati and the Draper Lab, on the NRL Advanced Scientific Computer, on the NRL DEC System 10, and on the NBS CDC computer.

REFERENCES

1. A. J. Corio, "The Use of Chebyshev Polynomials for Satellite Ephemerides," COMSAT Technical Review, Vol. 3, 1973, pp. 411-418.
2. A. Deprit, W. Poplarchek, A. Deprit-Bartholome, "Compression of Ephemerides," Celestial Mechanics, Vol. II, 1975, pp. 53-58.
3. I. Barrodale and C. Phillips, "Algorithm 495, Solution of an Overdetermined System of Linear Equations in the Chebyshev Norm," ACM Transactions on Mathematical Software, Vol. 1, 1975, pp. 264-270.
4. I. Barrodale and C. Phillips, "An Improved Algorithm for Discrete Chebyshev Linear Approximations," Proc. 4th Manitoba Conference on Numerical Mathematics, U. of Manitoba, Winnipeg, 1974, pp. 177-190.
5. A. Deprit, H. Pickard, W. Poplarchek, "Compression of Ephemerides by Discrete Chebyshev Approximation." Submitted to the Journal of the Institute of Navigation for publication.

D2
N79-14123

APPLICATION OF SEMIANALYTICAL
SATELLITE THEORIES TO PRECISION
ORBIT DETERMINATION

P. J. Cefola

C. S. Draper Laboratory

Introduction

Over the last several years, various space mission centers including NASA/GSFC, NASA/MSFC, JPL, NORAD/ADCOM, SAMSO/Aerospace and AFGL have supported the development of semi-analytical satellite theories based on the Method of Averages. The intent of all these efforts has been to produce 'fast' orbit computational algorithms for mission analysis, mission planning, orbit determination and other application programs. To date, this effort has concentrated primarily on the development of the equations of motion for the averaged orbital elements -- that is, the osculating orbital elements minus the short-periodic effects. Results include

- recursive analytical formulations for computing the averaged element rates due to gravitational perturbations (zonals, tesseral-resonance, and lunar-solar effects) (see References 1-6)*.
- the development and refinement of numerical averaging concepts for computing the rates of the averaged elements (primarily for atmospheric drag) (see References 8-12).
- the widespread application of nonsingular orbital elements in formulating the averaged equations of motion (References 2,3,5,6,8,15, et. al.).

* The pioneering work of Hunt Small (Reference 7) should be noted in any discussion of recursive satellite theories.

- investigations into the efficiency of various numerical integration processes for the solution of the averaged differential equations of motion (References 9 and 11).
- investigations into various methods for computing the averaged elements at a particular epoch, given a high precision state vector at that same epoch (the 'osculating to mean' transformation) (References 8, 9, and 11).

These results have been sufficient to make the semianalytical theory the preferred choice when very long data arcs are involved and when modelling of the short-periodic oscillations is not required. Thus semianalytical theories are used for many of the orbital computations in preflight mission analysis (for example, see Reference 13). The same situation holds when long arcs of averaged element data are being processed to construct geopotential fields or atmospheric density models (Reference 14).

In addition, preliminary consideration has been given to the computation of the short-periodic oscillations at the output points given the averaged elements, in the context of a semianalytical theory. Lutsky and Uphoff (Reference 10) provided an approach for computing first order short-periodics that could be attached to their numerical averaging program. Very promising numerical results, with respect to the accuracy, are provided in Reference 10. Vashkovjak (Reference 15) provided a detailed treatment of the short-periodics for the 24-hour synchronous equatorial orbit in the context of a semianalytical theory. Again, high accuracy was obtained. And, of course, the first transformation of canonical satellite theory provides the formulas for the recovery of the short-periodics due to J_2 (Reference 16).

Despite these efforts, the semianalytical theory has not been accepted as a replacement for the Cowell method of Special Perturbations in applications where high accuracy output is

required frequently (for example, see Reference 17). This requirement for frequent output corresponds exactly with the requirements of precision orbit determination.

The outline of the remainder of the paper is as follows. First, those factors which limit the usefulness of current implementations of the semianalytical approach are discussed. Next, numerical and analytical enhancements to the semianalytical approach are discussed. Finally, a simple mathematical model is provided to estimate the computational speed of a semianalytical theory employing the suggested enhancements. The model can factor in current experience with semianalytical theories (integration stepsizes, quadrature orders, speed of recursive formulations, etc.) and the characteristics of the particular output requirement [observation span (or orbit determination interval), observation rate, observation model, etc.]. Comparisons with numerical integration (Special Perturbations) are suggested.

Evaluation of Current Semianalytical Theories vs. the Precision Requirement

To the author's knowledge, there have been only two serious studies of a semianalytical theory in a precision orbit computation application. These are: (1) the evaluation of the MAESTRO numerical averaging theory for a detailed mission planning program (Reference 17) and (2) the evaluation of the GTDS numerical averaging theory for an orbit determination application (Reference 18).

Reference 18 concluded:

- that it was possible to successfully fit the averaged dynamics directly to raw observation data
- that observation editing criteria designed for Special Perturbations DC's might lead to the rejection of good data in an Averaged DC since short-periodics were not

modelled. Even if the editing criteria are relaxed, neglect of short-periodics might cause the data to appear biased over short observation spans (this is because the short-periodic oscillations are much larger than typical observation errors)

- that the multistep numerical integrator did not exhibit the full advantage of the semianalytical theory for 1 or 2 day orbit determination intervals.

Reference 17's prime concern was with the computation time characteristics relative to Special Perturbations. There are two points that seem important to mention with respect to this study:

- that output was required every 2 minutes over a 7200 minute span (5 days). This requirement was imposed in order to simplify (in terms of software changes) the interface between the semianalytical theory and the application program
- that the stepsizes employed in the numerical integration of the averaged equations of motion were severely constrained first, by the retention of the tesseral m-daily effects** and second, by the use of numerical averaging.

Desirable Enhancements to Current Semianalytical Theories

We first list desirable enhancements to the semianalytical satellite. The theory implemented in the R&D version of GTDS is taken as the baseline. The enhancements are:

- 1) a self-starting low-order integrator with a matching interpolator

* The 'm dailies' are due to the terms in the tesseral harmonic potential which only depend on the slowly varying satellite orbital elements and the Greenwich Hour Angle.

- 2) a recursive analytic formulation of the short-periodics including
 - zonals
 - nonresonant tesserals (including m-dailies)
 - lunar-solar

- 3) a low-order interpolation of the approximate high precision position and velocity within an observation pass

The self-starting low-order integrator is intended to take advantage of the fact that the integration stepsize for the averaged dynamics (1 to 4 days) is large relative to the observation spans typically associated with high precision batch differential corrections (for example, 1 or 2 days for Landsat). The matching interpolator provides the averaged elements at any observation time within the step without accessing the averaged force models. A low-order Hermite procedure (References 19 and 20) may be appropriate.

The need for an accurate model of short-periodics seems obvious in a production orbit determination environment. It is fortunate that first order models of the short-periodics are thought to provide accuracy down to 10m (see Kozai, Reference 21). M-dailies are included in the output time computations so as not to constrain the stepsize of the averaged integration.

Since observation rates are on the order of 6 or 10 observations per minute and since the grid interval for short-periodic interpolation is in the range of 2 to 10 minutes (Reference 20), the computation of the ephemeris at each observation time via an interpolation procedure seems to make good sense. Thus we will utilize the analytical model of short-periodics only on the interpolation grid and not on the much more 'dense' observation time grid.

Satellite Theory Simulation Model

Straightforward analysis of the semianalytical theory described in the previous paragraphs leads to the following model of the CPU time.

$$\text{CPU TIME} = (Nm_1 + 1)(t_2 + m_3t_3) + m_4m_5t_5 \quad (1)$$

m_1 = number of integration steps

N = function evaluations per step

t_2 = time for analytic contribution to single-averaged element rates

m_3 = number of density evaluations per quadrature

t_3 = time for each evaluation of the quadrature integrand

m_4 = number of observation passes

m_5 = number of output points per pass which require analytic short-periodics

t_5 = time for each computation of the analytic short-periodics

Note that Eq. (1) concentrates on the high cost mathematical functions. Eq. (1) does not attempt to model the various interpolation procedures although it does include the generation of the data required to construct the interpolation coefficients.

Table I provides sample evaluations of Eq. (1) for two typical scenarios. In both cases, it appears that significant computational advantage can be obtained via the semianalytical method. This is because we expect t_2 and t_5 to be on the order of a high precision perturbing acceleration evaluation. This has been demonstrated for t_2 in Reference 4. For t_5 , this expectation is based on mathematical analysis performed to date.

However, this advantage is dependent on the enhancements described in the previous sections. For example, suppose in Case 1 that the m -daily effects were retained in the averaged

Table I - Typical Scenarios

Case 1 - Very Low Altitude

1 day arc
16 rev/day orbit
2 minutes/obs pass
6 passes/day
10 obs/minute

$m_1 = 1$ step
 $N = 4$
 $m_3 = 24$
 $m_4 = 6$
 $m_5 = 2$

$$\text{CPU} = 5 t_2 + 120t_3 + 12t_5$$

REMARKS:

1. Cowell orbit generation would require around 1600 steps.
2. Total obs = 120/arc

Case 2 - Medium Altitude

2 day arc
14 rev/day orbit
5 minutes/obs pass
6 passes/day
10 obs/minute

$m_1 = 1$ step
 $N = 4$
 $m_3 = 9$
 $m_4 = 12$
 $m_5 = 3$

$$\text{CPU} = 5t_2 + 45t_3 + 36t_5$$

REMARKS:

1. Cowell orbit generation would require around 2800 steps.
2. Total obs = 600/arc

integration. Then m_1 might grow to 8 or 10 steps for the 1 day arc. For $m_1 = 10$, Eq. (1) gives (for Case 1)

$$\text{CPU} = 41t_2 + 984t_3 + 12t_5 \quad (2)$$

Clearly most of the advantage would be lost for all reasonable models of the atmospheric density**. Or suppose that the multi-step numerical integration procedure was retained. The starter

** This corresponds with the configuration of the semianalytical described in Reference 17.

associated with this process would reduce the advantage of the semianalytical approach. In Case 2, the advantage clearly depends on offloading the computation of short-periodics from the grid of observation times to the interpolation grid (3 points/pass).

Conclusion

While the above simulation exercise suggests that the semianalytical approach can be very desirable, what is really needed is the development of an OD test-bed employing this approach. Such a test-bed could demonstrate the advantages and disadvantages in an unequivocal manner against real observation data and scenarios.

References

1. Cook, G.E., "Basic Theory for PROD, a Program for Computing the Development of Satellite Orbits, " Celestial Mechanics, Vol. 7, 1972, pp. 301-314.
2. Cefola, P.J. and Broucke, R., "On the Formulation of the Gravitational Potential in Equinoctial Variables," Paper 75-9, presented at the AIAA 13th Aerospace Sciences Meeting, Pasadena, California, January 20-22, 1975.
3. Cefola, P.J., "A Recursive Formulation for the Tesseral Disturbing Function in Equinoctial Variables," Paper 76-839, presented at the AIAA/AAS Astrodynamics Conference, San Diego, California, August 18-20, 1976.
4. Long, A.C., and McClain, W.D., "Optimal Perturbation Methods for Averaged Orbit Generation," (AIAA preprint 76-815, presented at the AIAA/AAS Astrodynamics Conference, San Diego, California, August 1976).
5. Giacaglia, G.E.O., "The Equations of Motion of an Artificial Satellite in Nonsingular Variables," Celestial Mechanics, Vol. 15, No. 2, March 1977, pp. 191-215.
6. McClain, W.D., A Recursively Formulated First-Order Semi-Analytic Artificial Satellite Theory Based on the Generalized Method of Averaging Volume II: Explicit Development of the First-Order Averaged Equations of Motion, Computer Sciences Corporation, CSC/TR-78/6001, April 1978 (in progress).
7. Small, H.W., "Satellite Motion Around an Oblate Planet," (AIAA preprint 63-393, presented at the AIAA Astrodynamics Conference, New Haven, Connecticut, August 1963).
8. Uphoff, C., "Numerical Averaging in Orbit Prediction," AIAA J., Vol. 11, No. 11, November 1973, pp. 1512-1516.
9. Cefola, P., Long, A., and Holloway, G., "The Long-Term Prediction of Artificial Satellite Orbits," (American Institute of Aeronautics and Astronautics preprint 74-170, presented at the American Institute of Aeronautics and Astronautics Twelfth Aerospace Sciences Meeting, Washington, D.C., February 1974).
10. Lutsky, D., and Uphoff, C., "Short-Periodic Variations and Second-Order Numerical Averaging," presented at the 13th AIAA Aerospace Sciences Meeting, Pasadena, California, January 20-22, 1975.
11. Computer Sciences Corporation, CSC/TM-75/6039, Status Report on Numerical Averaging Methods, A.C. Long, September 1975.

12. Computer Sciences Corporation, CSC/TM-75/6038, Evaluation of Numerical Quadratures for Use in Numerically Averaged Orbit Generators, L.W. Early, July 1975.
13. Cook, G.E. and Palmer, M.D., "Orbital Requirements for an Astronomical Roentgen Observatory Satellite," J. British Interplanetary Society, 1975, pp. 763-778.
14. Goddard Space Flight Center, The ROAD Program, (GSFC computer software), C.A. Wagner, January 1973.
15. Vashkovjak, M.A., "On the Method of Approximate Computation of the Motion of a Synchronous Artificial Earth Satellite," Cosmic Research, Vol. 10, No. 2, March-April 1972, pp. 131-140.
16. Brouwer, D., "Solution of Problem of Artificial Satellite Theory Without Drag", Astronomical J., Vol. 64, No. 1274, November 1959, pp. 378-397.
17. Navickas, S.J., A Comparison of the Methods of Precision Integration and Numerical Averaging for Satellites in Low Altitude Orbits, Aerospace Corporation, TOR-0076 (6410-01), October 1975.
18. Computer Sciences Corp., CSC/TM-75/6022, GTDS New Techniques Evaluation: Calibration of VOP Orbit Generator, P. Desai and M. Regardie, June 1975.
19. Gordon, M.K. and Shampine, L.F., "Interpolating Numerical Solutions of Ordinary Differential Equations," Proc. ACM '74, San Diego, 1974.
20. Computer Sciences Corp., CSC/TM-76/6074, Evaluation of Ephemeris Representations for the Multimission Modular Spacecraft, P. Desai and A. Long, August 1976.
21. Kozai, Y., "Analytical Orbital Theories for Satellites," The Use of Artificial Satellites for Geodesy and Geodynamics, (Proceedings of the International Symposium on the Use of ... Athens, May 1973), ed. G. Veis, Athens, 1974, pp. 237-242.

103

N79-14124

CRITICAL INCLINATIONS IN SATELLITE THEORY

Andre Deprit*

Department of Mathematical Sciences
University of Cincinnati

The main problem of satellite theory is described in polar coordinates by the Hamiltonian function

$$\mathcal{H} = \mathcal{H}_0 + \epsilon \mathcal{H}_1,$$

$$\epsilon = C_{2,0} = -J_2,$$

$$\mathcal{H}_0 = \frac{1}{2}(R^2 + \frac{\Theta^2}{r^2}) - \frac{\mu}{r}$$

$$\mathcal{H}_1 = \frac{\mu}{r} \left(\frac{\alpha}{2}\right)^2 \left[\left(\frac{1}{2} - \frac{3}{4}s^2\right) - \frac{3}{4}s^2 \cos 2\theta\right].$$

It is proposed to find a solution of it with the following properties:

- 1°) the reference orbit is Keplerian;
- 2°) no restriction is imposed on the eccentricity; in particular, it is exempt of singularities - real or apparent - for small eccentricities;
- 3°) no restriction is imposed on the inclination; in particular, it is exempt of singularities - real or apparent - for small inclinations; also it is valid even in the neighborhood of inclinations at which the perigee is stationary.

* On leave at the Division of Applied Mathematics, National Bureau of Standards, Washington, D.C., 20234.

The construction proceeds in two steps.

In the first step, a canonical mapping, called the elimination of the (equatorial) parallax, changes the Hamiltonian into the function

$$\mathcal{H} = \frac{1}{2} \left[R^2 + \frac{\mu^2}{r^2} \psi \right] - \frac{\mu}{r},$$

$$\psi = \sum_{n \geq 0} \frac{1}{n!} \epsilon^n \left(\frac{\alpha}{p} \right)^{2n} \psi_n,$$

$$\psi_0 = 1,$$

$$\psi_n = \sum_{0 \leq i \leq [n/2]} \sum_{0 \leq j \leq i} \sum_{0 \leq k \leq n-i-j} \psi_{n,i,j,k} X^j Y^{i-j} s^{2k},$$

$$X = e \cos g,$$

$$Y = e \sin g,$$

$$s = \sin I.$$

In the second step, a canonical mapping, called the revolution in orbit, changes the Hamiltonian into that of a Keplerian system.

Both transformations are obtained in application of a perturbation algorithm based on Lie Series. The basic differential equation

$$\left(\frac{d}{dt}, \dot{h}_n \right) = \mathcal{H}_0^n - \mathcal{H}_0^n$$

may be reduced to an elementary quadrature if one makes the following observations.

- i) Assume that \dot{h}_n is of the form

$$W_n^0 = \Theta \left(\frac{\alpha}{p}\right)^{2n} W_n(\theta, X, Y, s^2).$$

Then

$$\left(\frac{W_n^0}{\Theta}\right) = -\frac{\Theta^2}{r^2} \left(\frac{\alpha}{p}\right)^{2n} \partial_1 W_n$$

where $\partial_1 W_n$ designates the partial derivative of W_n with respect to its first argument (namely θ).

(ii) Throughout the construction of the Lie triangle, the elements W_j^i may be maintained in the form

$$W_j^i = \frac{\Theta^2}{r^2} \left(\frac{\alpha}{p}\right)^{i+j} H_j^i(\theta, X, Y, s^2).$$

Therefore, at the end of any row in the Lie triangle, the partial differential equation reduces to the quadrature

$$\partial_1 W_n = H_0^n - \tilde{H}_0^n.$$

In the course of eliminating the parallax, the factor \tilde{H}_0^n emerge as finite Fourier sums in the argument θ of the latitude. It is thus natural to set the unknown factor H_0^n equal to the average of \tilde{H}_0^n . Hence W_n will be a purely periodic function of θ .

In the second transformation, the unknown factors \tilde{H}_0^n are set to zero. Hence W_n will be a finite sum of mixed terms $\theta^i \sin j\theta$ and $\theta^i \cos j\theta$.

At the first order in ϵ , the revolution in orbit transforms the argument of latitude according to the equation

$$\theta = \theta' [1 + \frac{3}{4} (\frac{\alpha}{p})^2 (1 - 5c'^2)].$$

So the rotation of the coordinate system implied by the canonical mapping becomes the identity at the inclination of stationary perigees, namely $I = \tan^{-1} 2$ for which $1 - 5c'^2 = 0$. This explains why the solution does not recognize the inclination of stationary perigees as a critical singularity: the revolution in orbit adjusts the frame of reference so that it follows the perigee. The property is typical of a non-essential resonance of type (1:1) whereby a rotation of the coordinate axes preempts the apparition of zero divisors.

The calculations have been executed by hand - with the collaboration of Mrs. Deprit-Bartholomé - to order 2 for the elimination of the parallax and to order 3 for the revolution in orbit. The results have served to check the computer programs which then carried out both transformations to order 4.

The new theory is the first one to have obtained the fourth order terms. The most accurate observations currently available require that the main problem of artificial satellite be solved to order 3. The terms of order 4 will serve to estimate the errors induced by truncating the series beyond ϵ^3 .

The generating functions for both mappings are much smaller by the number of terms than those of the conventional (Kozai) and not so conventional (Aksnes) theories.

The computer programs to execute the reduction in a literal form involve a processor for Poisson series. The latter is the latest version of MAO. From a package of subroutines written in assembler or in Fortran, MAO has evolved into a subroutine generator. At compilation, macro variables are set up to specify the type of Poisson series needed to solve a particular class of problems. The generator is coded to be preprocessed and compiled by the IBM optimizing compiler for PL/I. It will be made available to mathematicians in dynamical astronomy and non-linear mechanics as soon as the documentation has been published. The Department of Astronomy at the University of Thessaloniki is considering transferring MAO from IBM to UNIVAC.

In the course of expanding the functions generating the canonical mappings to solve the main problem of satellite theory, a "profiler" in line counted how many times the subroutines in the package were called. There have been 9452 algebraic and differential operations on Poisson series, 286773 "list" operations (to find or to create nodes in chains) and 216651 algebraic operations involving rational numbers (represented and maintained as pairs of relatively prime decimal integers). The execution time was 70".54 on an Amdahl 470-4 operating under OS/VS-2 at the University of Cincinnati.

*Strange sport! Where destination has no place
Or name, and may be anywhere we choose!
Where MAO, committed to his endless race,
Runs like a madman diving for its repose!*

24
N79-14125

A SINGULARITY FREE ANALYTICAL SOLUTION OF ARTIFICIAL
SATELLITE MOTION WITH DRAG

Alan Mueller

Analytical and Computational Mathematics, Inc.
1275 Space Park Drive, Suite 114,
Houston, Texas 77058

If an analytical satellite theory which includes the drag perturbation is to be successful, it must have three important qualities. First the theory should be based on a canonical formalism whereby one can use the powerful tools provided by hamiltonian mechanics. Secondly, the model used to describe the forces acting on the satellite must not be so simplified that the theory becomes only a mathematical exercise. Lastly, the resulting theory must be concise so that the accuracy gained outweighs the extra computer costs required to reach that accuracy.

Scheifele (reference 1) has developed an analytical satellite theory based on the regular, canonical Poincaré-Similar (PS ϕ) elements. This is a very powerful set of elements which are in an extended phase space and have an independent variable which is similar to the true anomaly instead of time (references 2, 3 and 4). A very accurate and concise satellite theory has been developed to include the first order short period and secular perturbations of an oblate central body. The drag theory has been built on top of the J_2 theory.

The assumption in this theory is that the drag force is tangential to the orbit and proportional to the square of the velocity magnitude of the spacecraft. The constant of proportionality, which is a product of the density of the atmosphere, the ballistic number, and the drag coefficient, was not specified in Scheifele's theory. Since the lifting force relative to the drag force and the inertial velocity of the atmosphere relative to the satellite velocity is small, the

model used is adequate for giving the direction of the retarding force due to the atmosphere. Thus an important contribution to the analytical solution was made. The report (reference 1) is a concentrated effort to canonically transform the forces into the PS space and also place them in a form suitable for solution. Therefore, the direction of the PS canonical forces has been determined but their magnitude was not completely specified. Also, the tools of hamiltonian mechanics were used to transform the forces correctly and reduce the size of the equations. Due to the character of the PS system, the equations which describe the motion are relatively simple and thus the first and third qualities mentioned above are satisfied.

The second task was to develop an atmospheric density model that can be used in Scheifele's theory. In developing a density model for the analytical theory one is severely restricted by the fact that the model must be in the form of a fourier series in the true longitude. As is the case in most analytical theories, the perturbations must be written in a fourier series to facilitate solution by quadrature. Several density models have been developed to predict very accurately the density at any point in space and time. Examples are the Jacchia model (reference 5) and the USSR model (reference 6). Both models are extremely complicated and too unwieldy for analytical satellite theories. In the analytical theory of Brouwer and Hori (reference 7) the density model was assumed to be an exponential function of the radius. However, the atmospheric density is strongly dependent on the sun and its position, and also the oblate figure of the earth. Thus Brouwer's assumption is not valid. A completely new model needed to be developed which is both accurate and can be written in a fourier series.

In developing the new model, the approach taken was to construct a model which is able to simulate the Jacchia density

along a particular orbit. The value of the coefficients in the new model are determined by a procedure called "calibration". A simple formulation allows the model to be inverted, i.e. given the density at different points along the orbit (as determined from Jacchia), one can compute the coefficients of the model. The coefficients are implicit functions only of long period effects and can be considered constants in the analytical theory.

The model has been fit to a particular orbit to include the variations in the observed density due to two-body changes in the height, and the two-body changes of the angle between the sun and the satellite (diurnal effect). Included in a manner similar to that of Santora (reference 8), are the density variations caused by changes in height due to the oblate figure of the earth and the short periodic oscillations in the radius due to J_2 . The density model also "accounts" for the changes in the density because of secular perturbations in the height due to drag itself.

The result is an accurate density model which can be implemented into the drag theory. Numerical experiments demonstrate the close agreement between the new model and the Jacchia model.

The last stage of the analytical theory is under development. This involves constructing a computationally efficient manner which to expand the equations of motion into a fourier series. This requires a careful balance of explicit manual computation, explicit equations by computer manipulations, and lastly but not least, the recursive relations.

Most, but not all of the theory has been implemented on the computer. Comparisons with numerically integrated solutions verify that the analytical theory is extremely accurate.

References

1. Scheifele, G., Mueller, A. and Starke, S.: "A Singularity Free Analytical Solution of Artificial Satellite Motion With Drag", ACM Technical Report TR-103, March, 1977.
2. Mueller, Alan: "The Development of the Poincaré-Similar Elements With the True Anomaly as the Independent Variable", NASA/JSC Internal Note No. 76-FM-60, August, 1976.
3. Scheifele, G. and Craff, O.: "Analytical Satellite Theories Based on a New Set of Canonical Elements", AIAA Paper No. 74-838, August, 1974.
4. Bond, V.R.: "An Analytical Singularity-Free Solution to the J_2 Perturbation Problem", NASA/JSC Internal Note. No. 77-FM-52, October, 1977.
5. Jacchia, L.: "New Static Models of the Thermosphere and Exosphere with Empirical Temperature Profiles", Smithsonian Astrophysical Observatory Special Report.
6. Elyasberg, P.; et al.: "Upper Atmosphere Density Determination from the Cosmos Satellite Deceleration Results", Space Research XII, p.727, Akademic-Verlag, Berlin, 1973.
7. Brouwer, D. and Hori, G.: Theoretical Evaluation of Atmospheric Drag Effects in the Motion of an Artificial Satellite, Astron. Journal, Vol. 66, No. 5, pp.193-225, 1961.
8. Santora, F.: "Drag Perturbations of Near-Circular Orbits in an Oblate Diurnal Atmosphere", AAS/AIAA Astrodynamics Conference, Paper No. AAS75-025, July, 1975.

MIT

Effect of Atmosphere on Venus Orbiter Navigation

Mohan Ananda and Braulio Sanchez

Jet Propulsion Laboratory
Pasadena, California

ABSTRACT

The current uncertainty for atmospheric models of Venus is significantly large. The orbital prediction requirements for Pioneer Venus Orbiter with its relatively low periapsis altitude (150 km) have brought concern on navigation capabilities. This paper investigates simplified but realistic models of the Venusian atmosphere on orbit determination accuracy. A model with polynomial representation of the atmospheric scale heights is assumed for statistical error analysis. Covariance analyses have shown the effect of model errors in the Venusian atmosphere can be minimized for trajectory prediction after processing several orbits of data. Studies include the sensitivity of periapsis data, arc length, data rate and station coverage for determining atmospheric parameters. Periapsis data are highly sensitive to the gravity field. The gravity field of Venus is essentially unknown and thus it is necessary to determine both gravity and atmospheric parameters simultaneously.

25

N79-14126

DENSITY MODELS FOR THE UPPER ATMOSPHERE[†]Douglas L. Dowd¹ and B. D. Tapley²1. Introduction

One of the more important problems associated with the task of defining the orbit of a near earth satellite is that of modeling the effects of atmospheric drag. Errors in the drag model can lead to significant errors in the determination and prediction of the satellite position. The drag acceleration is modeled by the relation

$$\vec{A}_D = -\frac{1}{2} \rho C_D \frac{A}{m} \vec{v}_r \vec{v}_r$$

where ρ is the atmospheric density, C_D is the drag coefficient, A is the cross sectional area normal to the relative velocity vector, m is the satellite mass and \vec{v}_r is the velocity vector relative to the atmosphere. Hence, the uncertainty in the drag acceleration can be separated into three components: a) errors in the atmospheric density model, b) errors in the ballistic coefficients, and c) errors in the satellite relative velocity. The first of these error sources is due to inaccuracies in a priori models and presents a limiting factor in the accuracy with which the velocity and position of an orbiting satellite can be determined.

¹Aerospace Engineer, Mission Planning and Analysis Division, L. B. Johnson Space Center, Houston, Texas.

²Professor, Department of Aerospace Engineering and Engineering Mechanics, The University of Texas at Austin, Austin, Texas.

[†]This investigation was supported by the NASA Goddard Spaceflight Center under Contract NAS5-20946 and Contract NSG 5154.

Normally, the atmospheric density is modeled by defining an a priori static model based on historical satellite tracking data. Since the atmospheric density depends on such external influences as solar and geomagnetic activity, computed values of the density will be in error due to inaccuracies in the original definition of the density model as well as time lags in updating the parameters which account for the effects of solar and geomagnetic activity.

In a number of contemporary satellite missions, the requirement for performing the orbit determination and prediction in real-time has placed an emphasis on models which, in addition to being accurate, require a minimum of computation time. In addition, if the computations are to be performed using a satellite-borne computer, the models must be efficient with regard to computer storage requirements.

In this investigation, consideration is given to three contemporary atmospheric density models which have been selected as the best candidates to meet these requirements. The models considered are the Analytic Jacchia-Roberts Model [1], the Modified Harris-Priester Model [2], and the U.S.S.R. Cosmos Satellite Derived Density Model, commonly known as either the Russian Model or the U.S.S.R. Model [3]. Each of the models and their respective variations is discussed separately, and a comparison of the computational characteristics of the models is presented. Finally, recommended modifications for improving both the computation speed and accuracy are presented.

2. The Analytic Jacchia-Roberts Model

The Analytic Jacchia-Roberts Model calculates atmospheric densities for altitudes at 90 km and above. The model, an analytic representation of

Jacchia's 1970 tabular density model [4] developed by Roberts [1] incorporates the revisions to the tabular model which were published in 1971 by Jacchia [5]. The method divides the upper atmosphere into three altitude bands for the calculation of atmospheric density. Specifically, these bands are 90-100 km, 100-125 km, and higher than 125 km. The terminal conditions in each lower band are the initial conditions for the next higher band. Therefore, the determination of the density within any given altitude band requires the calculation of the terminal conditions in each of the lower bands. The method is predicated on the assumption of a temperature profile and assumed values for the molecular mass of the major atmospheric constituents. The atmospheric density is determined then by integrating either the barometric equation for altitudes from 90 km to 100 km or the diffusion equation for altitudes above 100 km. The major constituents considered by Jacchia are nitrogen (N_2), argon (Ar), helium (He), molecular oxygen (O_2), atomic oxygen (O), and hydrogen (H).

For altitudes in excess of 125 km, the temperature profile is defined mathematically by an asymptotic function. Jacchia originally chose to use the inverse tangent function which did not produce an exact differential in the diffusion equation and his tabular model is a result of numerical integration of the diffusion equation. Roberts [1] assumed an exponential temperature profile which allows for the analytic integration of the diffusion operation. In either of the assumed temperature profiles, there is no mathematical upper altitude limit. As altitude increases without bound, the temperature asymptotically approaches the exospheric temperature. At some unspecified altitude, the density of the atmosphere has decreased to the point where the gas atoms move in ballistic trajectories and no longer

interact with one another in support of the laws of fluid dynamics. Therefore, the temperature profile approaches its bound, the validity of the diffusion becomes suspect. The altitudes at which this occurs in the model is highly dependent upon the value of the exospheric temperature [5] and ranges from 880 km for an exospheric temperature of 500°K to 2000 km at 1900°K.

In the original Jacchia model, and in the analytic model as well, the exospheric temperature (T_{∞}) calculation accounts for the observed variations in the density. The variations in T_{∞} are correlated with variations in the 90-day mean flux of the solar 10.7 cm radiation, where

$$\bar{F}_{10.7} = \left[\frac{1}{T} \int_0^T F_{10.7} dt \right] \times 10^{-22} \text{ m}^{-2} \text{ Hz}^{-1},$$

and with the daily variations of $F_{10.7}$ from the mean. The value of the $\bar{F}_{10.7}$ solar flux varies with an 11-year period while the $F_{10.7}$ flux has a 27-day period with an apparently random amplitude due to the effects of the solar rotation. The temperature calculation also accounts for the variation in density as a function of the local solar time of the point in question (diurnal effect) and changes in the geomagnetic activity. The atmospheric density determined from this exospheric temperature is corrected for the seasonal-latitude variations of helium, and the variations in hydrogen concentrations above 500 km. A simple logic flow chart of the Analytic Jacchia-Roberts Model is shown in Figure 1 while the specific algorithm for the atmospheric density model is described in detail in Reference [6].

An efficient modification to the basic Jacchia-Roberts Model has been adopted for use in the Goddard Trajectory Determination Subsystem

(GTDS) [2]. The essential modifications are that the atmospheric density at 100 km. and the density numbers of the major atmospheric constituents at 125 km. are all approximated by sixth degree polynomials in T_0 instead of being calculated as the terminal conditions of the two lowest altitude bands. Further discussion regarding the computational aspects of these modifications is given in Section 6.

3. The Modified Harris-Priester Model

The Modified Harris-Priester Model [2] is based on an extensive tabular static model of the upper atmosphere in the altitude band from 120 km. to 800 km. [7]. The first modification of the Harris-Priester Model, accomplished at the NASA Goddard Space Flight Center, was to exponentially extrapolate the tables to include altitudes down to 100 km and up to 1,000 km. The model, as incorporated into GTDS [2], retains its tabular form in a modified format. In the original formulation, there are 10 separate tables, each being associated with a particular value of the smoothed (5-month average) flux of the solar 10.7 cm radiation ranging from $\bar{F}_{10.7} = 65$ to $\bar{F}_{10.7} = 275$. This range of $\bar{F}_{10.7}$ encompasses the total variation of $F_{10.7}$ over the 11-year solar cycle. Each table consists of 12 subtables which list the atmospheric densities for the local solar time at 2-hour intervals. The tables for the Modified Harris-Priester Model are formed by extracting the maximum and minimum densities for each altitude from the subtables for each solar flux level. The absolute maximum and minimum are chosen without regard for the local solar time. This was done because the diurnal maximum and minimum densities do not appear in the tables at 1400 hours and 0400 hours at altitudes below 320 km, as is the case for the observed extrema. The Modified Harris-Priester Model

then derives the atmospheric density from a set of 10 tables associated with the smoothed flux of the 10.7 cm solar radiation, where each table relates a diurnal maximum and minimum density for each of the tabulated altitudes from 100 to 1,000 km.

The atmospheric density for a given altitude is determined then by entering the table associated with the value of $\bar{F}_{10.7}$ most nearly equal to the measured solar flux, exponentially interpolating the maximum and minimum densities with respect to altitude, and then applying a cosine interpolation for the diurnal variation. This procedure yields a density distribution which is symmetric with respect to the apex of the diurnal bulge. The apex of the diurnal bulge is assumed to follow the subsolar point by 30° in the same latitude. It is known [8] that the observed diurnal variation is not symmetric and the Analytic Jacchia-Roberts [1] and the U.S.S.R. Cosmos Satellite Derived Models [3] account for the asymmetry. The Jacchia-Roberts Model accomplishes this by computing an asymmetric temperature distribution from which density is determined. In this investigation, a similar procedure has been applied directly to the density computation to provide an asymmetric density distribution in the Modified Harris-Priester Model. The model with this procedure is referred to as the Asymmetric Modified Harris-Priester Model. The detailed computational algorithms are given in Reference [6].

The pertinent equations for describing the diurnal variation in the Modified and Asymmetric Modified Harris-Priester Models are as follows:

Modified Harris-Priester Model

$$\rho(h) = \rho_{\min}(h) + [\rho_{\max}(h) - \rho_{\min}(h)] \cos^n(\psi/2) \quad (2)$$

where h is the altitude, $\rho_{\min}(h)$ and $\rho_{\max}(h)$ are the interpolated daily minimum and maximum densities from the modified tables [2], and ψ is the angle between the geocentric position vectors of the point where the modeled density is desired and the apex of the diurnal bulge.

Asymmetric Modified Harris-Priester Model

$$\rho(h) = \rho_N(h) + [\rho_D(h) - \rho_N(h)] \cos^n (\tau/2) \quad (3)$$

where

$$\begin{aligned} \rho_N(h) &= \rho_{\min}(h) + [\rho_{\max}(h) - \rho_{\min}(h)] \sin^m \theta \\ \rho_D(h) &= \rho_{\min}(h) + [\rho_{\max}(h) - \rho_{\min}(h)] \cos^m \eta \\ \theta &= \frac{1}{2} |\phi + \delta| \\ \eta &= \frac{1}{2} |\phi - \delta| \\ \tau &= H + \beta + \lambda \sin(H + \gamma) \quad (-\pi \leq \tau \leq \pi) \end{aligned} \quad (4)$$

In the above equations, H is the local solar time, ϕ is the geographic latitude of the subsatellite point, and δ is the solar declination. The values for the parameters appearing in Equations (4), taken from Jacchia's temperature equation [5], are:

The shape of the diurnal bulge, as modeled by the Asymmetric Modified Harris-Priester Model, is illustrated in the polar plots in Figures 2 and 3. In Figure 2, the angle measure is latitude, and the magnitude in the radial deviation represents the normalized modeled density variation at some assumed constant altitude h where $\rho_{\min}(h) = 1.2$ and $\rho_{\max}(h) = 2.0$ are the assumed density values at h . The specified solar hour angles H are for the right halves of the plots with the hour angle for the left halves being $H + 180^\circ$. In both Figures 2 and 3, the assumed solar declination is 15° . The unit circles in each figure are included to emphasize the changes in the density magnitude. In Figure 3, the angle measure is longitude (or solar hour angle) measured from noon, and the radius magnitude represents the modeled variation at constant altitude and latitude. The Figures 2 and 3 show the global maximum density occurring at the subsolar latitude ϕ_δ and 31.226° after noon and the global minimum occurring at latitude $-\phi_\delta$ and 137.01° before noon.

4. The U.S.S.R. Cosmos Satellite Derived Density Model

The U.S.S.R. Cosmos Satellite Derived Density Model is based on the observations of 145 Cosmos satellites over the time period from 1964 through 1970 [4]. The model determines the atmospheric density directly by substituting the input parameters into a set of equations containing twenty coefficients derived by fitting density observations over the range of altitudes and temperatures encountered by the Cosmos satellites. The use of the current model is restricted because the coefficients were empirically determined over a limited altitude region and during only a portion of the 11-year solar cycle. The data were extended by using Jacchia's 1970 Model, but the altitudes for which the model is valid is still only between 140 and 500 km.

The coefficients are given in four sets for four reference values F_0 of the 10.7 cm. solar radiation flux; specifically, 75, 100, 125, and 150×10^{-22} WATTS m^{-2} Hz $^{-1}$. Since the model uses the reference value F_0 which is nearest the 6-month average of the daily $F_{10.7}$, the model is valid for 6-month averages of $F_{10.7}$ between 65 and 165×10^{-22} WATTS m^{-2} Hz $^{-1}$.

The details of the U.S.S.R. Model are given in Reference [6]. The essence of the model is that the nighttime density profile ρ_h is corrected by four multiplicative factors K_i , $i = 1, 2, 3, 4$. The K_i -factors include corrections for the diurnal density variation, K_1 , the daily variation of $F_{10.7}$, K_2 , the observed semi-annual variation in density, K_3 , and fluctuations in geomagnetic activity, K_4 .

The total density is then represented by the equation

$$\rho = \rho_h K_1 K_2 K_3 K_4 \quad (5)$$

5. Explanation of Atmospheric Density Profiles

A study of atmospheric density and its effect on the motion of a near earth satellite would not be complete without an explanation of the correlation between the orbit of the satellite and the density profile which is encountered by the satellite. Normally, the atmosphere is discussed as a separate system with density presented as a function of altitude for various values of the other parameters which have been correlated to variations in the observed densities. In this discussion, the intersection and interaction of two dynamical systems, the atmosphere and the orbiting satellite, will be considered. The density profiles which will be discussed are referred to the Modified Analytic Jacchia-Roberts Model since this model contains all of the essential variations while retaining computational efficiency.

It is not difficult to understand the relationship between atmospheric density and altitude--as altitude above the earth's surface increases, density decreases, provided everything else is constant. Therefore, if the variation of the satellite altitude is known as it moves in its orbit, one would expect to see an inverse variation in atmospheric density. Obviously, orbital eccentricity has a large effect on the altitude variation. Considering that the earth is not spherical, orbital inclination also has an influence on the altitude variation as does the orbital perturbations due to the nonsphericity of the geopotential. To illustrate these points, refer to Figure 4 which shows time histories of altitude above the reference ellipsoid, geocentric radius and atmospheric density for one orbital period. The orbit used to generate these results is approximately circular with initial osculating Keplerian elements as follows

a = 6682473 m
e = .000646254
i = 67.99°
ω = 0.0°
Ω = 0.0°
E = 0.0°

epoch 16^d 2^h 47^m 55.537^s Dec. 1973

It should be noticed that the amplitudes of the variations in radius and altitude are not of the same magnitude which indicates the dual effect of the earth's nonsphericity on the altitude variation and, in turn, on the density profile. The density curve indicates that there are other major

effects involved in shaping the density profile. To aid in the identification of the most obvious of these effects, consider the histograms in Figure 5 which were generated exactly as those in Figure 4, except that the nodal line has been rotated ninety degrees, i.e. $\Omega = 90^\circ$. The altitude variation and latitudinal displacement from the diurnal bulge are the same in both cases, whereas the longitudinal displacement from the diurnal bulge is offset by ninety degrees. There is a marked difference between the density profile which appears as a phase shift in an apparent once-per-revolution variation. This difference illustrates the diurnal variation and its relative importance in modeling atmospheric density.

Up to this point the discussion has related to the shape of the density profile. The magnitude of the atmospheric density exhibits other variations which are still present when altitude and diurnal variations are eliminated. Most significant are the variations in density due to variations in solar radiation and the interaction of the solar wind with the earth's magnetic field. Density profiles are presented in Figures 6 through 8 which illustrate the changes in density that are correlated with both long and short term variations in solar extreme ultraviolet (EUV) radiation as evidenced by the flux of the 10.7 cm. solar radiation. The effects of geomagnetic heating on the magnitude of density are shown in Figure 9 in which density profiles are presented for four values of the planetary geomagnetic index K_p . The initial conditions used to generate the orbits for Figures 6 through 9 are the same as those used for Figure 4.

6. Comparison of the Density Models

Each of the density models discussed in the preceding sections will yield a density profile along any given trajectory which is different than

the density computed by any other model. Comparisons of the density profiles are shown pictorially in curves of density versus time in this section. The trajectories were generated from the initial osculating elements:

$$\begin{aligned} a &= 6678155 \text{ m.} & \omega &= 3.02^\circ \\ e &= 0.0 & \Omega &= 254.26^\circ \\ i &= 67.99^\circ & E &= 356.98^\circ \\ \text{epoch} &= 16^{\text{d}} 2^{\text{h}} 47^{\text{m}} 55.537^{\text{s}} \text{ Dec. 1973} \end{aligned}$$

The Newtonian equations of motion were numerically integrated by a fixed step size third order Runge-Kutta method with a ten second step size. A single trajectory was generated and the various atmospheric density models were evaluated on this common trajectory. The force model for drag used densities from the Modified Analytic Jacchia-Roberts Model in the generation of the comparison orbit. The remaining modeled forces used to generate the comparison orbit were:

$$\text{Two body} - \mu = 3.986013 \times 10^{14} \text{ m}^3/\text{sec}^2$$

Nonspherical Earth - 1969 Smithsonian Standard Earth II to 4th Order and 4th Degree

n body - Solar and lunar gravitational perturbations based on Jet Propulsion Laboratory Development Ephemeris Number 19

The density profiles shown in Figure 10 are those which would be modeled by various forms of the Modified Harris-Priester Model. The reference profile is the generating density profile modeled by the Modified

Jacchia-Roberts Model where

$$F_{10.7} = 75$$

$$\bar{F}_{10.7} = 75$$

and

$$K_p = 1$$

The other four profiles shown in Figure 10 are those density profiles which were computed by either the Modified Harris-Priester or Asymmetric Modified Harris-Priester Models associated with $\bar{F}_{10.7} = 75$ where the shapes of the profiles shown were determined by setting the value of n in Equations 2 and 3 to either 3 or 6. The key to the symbols used to identify the curves in Figures 10 and 11 is given in Table 1.

Table 1. Key to Symbols in Figures 10 and 11

SYMBOL	DEFINITION
MJR Δ	Modified Jacchia-Roberts Analytical Model (Reference Model)
MHP \circ	Modified Harris-Priester Model $n = 3$
MHP \square	Modified Harris-Priester Model $n = 6$
AMHP \blacktriangle	Asymmetric Modified Harris-Priester Model $n = 3$
AMHP \blacklozenge	Asymmetric Modified Harris-Priester Model $n = 6$

The density profiles shown in Figures 11 are similar to those in Figure 10 except that the values of $F_{10.7}$ and $\bar{F}_{10.7}$ used in the models is 275, a value representing the maximum extreme in the 11-year solar cycle. Close inspection reveals that the density profiles determined by the Asymmetric Modified Harris-Priester Model with $n = 3$ most closely approximates the Jacchia-Roberts profile in shape. It appears that by judiciously scaling ρ_{MIN} and ρ_{MAX} in Equation 4 and by applying a small correction to n near the value $n = 3$, the Asymmetric Modified Harris-Priester profile could be made to very nearly coincide with the Modified Jacchia-Roberts profile.

There is a systematic difference in the density profiles generated by the Jacchia-Roberts and Asymmetric Modified Harris-Priester Models which is not apparent in Figure 10. This difference is a result of the assumption by Jacchia [4] of a static temperature profile, whereas Harris and Priester used a dynamic temperature profile to generate their atmospheric density tables [7]. These differing approaches are manifested in the models through the temperature equations

$$T_D = T_C (1 + R \cos^m \eta) \quad (2.1)$$

$$T_N = T_C (1 + R \sin^m \theta)$$

in the Analytic Jacchia-Roberts Model and the density equations

$$\rho_D = \rho_{\text{MIN}} (1 + Q \cos^m \eta)$$

$$\rho_N = \rho_{\text{MIN}} (1 + Q \sin^m \theta)$$

in the Asymmetric Modified Harris-Priester Model. The quantity R appears as a constant in the former model whereas Q is given by

$$Q = (\rho_{\text{MAX}} - \rho_{\text{MIN}}) / \rho_{\text{MIN}}$$

which is not a constant valued quantity, in the latter model. The effect of this systematic difference in the two models is illustrated in Figure 12 which shows the density profiles generated by the Modified Analytic Jacchia-Roberts and Asymmetric Modified Harris-Priester Models during one orbital period along a trajectory with initial osculating Keplerian elements

$$a = 6682473.58 \text{ meters}$$

$$e = .00064625$$

$$i = 68.0 \text{ degrees}$$

The difference is most apparent between 3000 and 4000 seconds after the beginning of the orbit propagation. In this regard, the Asymmetric Modified Harris-Priester Model more accurately reflects the real world diurnal density variation than the Jacchia-Roberts model.

Density profiles calculated by the U.S.S.R. Cosmos Satellite Derived Density Model are compared with the Modified Analytic Jacchia-Roberts profiles in Figures 13 and 14. The initial conditions for the generation of the comparison orbit are the same as those used for Figure 10. The pertinent parameters supplied to the models to generate the profiles in Figure 13 were $F_{10.7} = 79.1$, $\bar{F}_{10.7} = 84.2$, and $K_p = 1$ for the Jacchia-Roberts Model and $F_{10.7} = 79.1$, $F_0 = 75$, and $a_p = 4$ for the U.S.S.R. model. It should be noted that $K_p = 1$ and $a_p = 4$ are equivalent measures of geomagnetic activity. For the profiles shown in Figure 14, the defining parameters are $F_{10.7} = \bar{F}_{10.7} = 150$ and $K_p = 1$ for the Jacchia-Roberts profile and $F_0 = F_{10.7} = 150$ and $a_p = 4$ for the U.S.S.R. profile. The density profiles in these cases are similar in some sense, but not as much so as the Asymmetric Modified Harris-Priester profiles.

Comparison of the time required to compute the model densities is shown in Table 2. In terms of computational speed, the U.S.S.R. is the most efficient model, with the Modified Harris-Priester Model following closely. It should be noted that there is practically no difference in the computation time between the Modified and Asymmetric Modified Harris-Priester Models. The Analytic Jacchia-Roberts Model requires much more time than either the Harris-Priester or U.S.S.R. models. Even though the modification of the Jacchia-Roberts Model proposed in Reference 7 reduces the time requirements by over 20%, the other models are still more than twice as fast.

In an independent study, Botbyl [9] investigated the sensitivity of the density calculation to the evaluation of a fifth order polynomial occurring in the Analytic Jacchia-Roberts algorithm. Botbyl showed that perturbing the coefficient of the fifth order term by 1 in the 14th digit resulted in density calculations accurate to no more than two or three digits. However, the reference density used for comparison did not consider the errors due to inaccurate determination of the roots discussed above. To resolve the question of the computational accuracy of the model, three density-vs-altitude profiles were determined with (1) all single precision arithmetic, (2) double precision computation of the polynomial and single precision arithmetic otherwise, and (3) all double precision arithmetic. The density digits for the three profiles are shown in Table 4. In general, it can be seen that the single precision computation is accurate to three or four digits and that computing only the polynomial with double precision arithmetic does not

significantly increase the accuracy of the computation. The importance of the increase in accuracy achieved by performing the density calculations in double precision must be weighed against the increase in computation time and core storage requirements.

It has been mentioned previously that the Modified Analytic Jacchia-Roberts Model is approximately 20% faster than the unmodified version. A comparison of the densities calculated by the unmodified model using double precision arithmetic with densities calculated by the modified model using single precision arithmetic is shown in Table 5. The densities were computed for T_{∞} from 800°K to 2000°K. The largest error encountered was .08% which occurred at an altitude of 125 km. when $T_{\infty} = 2000^{\circ}\text{K}$. Between the altitude of 90 and 100 km., the unmodified and modified algorithms are identical. The Modified Analytic Jacchia-Roberts Model then is at least as accurate, and most of the time is more accurate than the basic algorithm when using single precision arithmetic.

The Modified Harris-Priester Model is a very simple, straightforward method which displays no computational idiosyncracies. However, potential users of the model should consider the physical interpretation of Equation 3 which shapes the density profile with respect to the diurnal density variation. The value of the exponent n could be any real number. Common sense, however, tells us that certain values of n would produce profiles that almost certainly are not physically realizable. It is not improbable that the density variation due to diurnal heating is a smooth process, that is to say at least continuously differentiable. The diurnal variation given by the Modified Harris-Priester Model would then be smooth when $n > 1$ so that $n = 1$ is an absolute lower bound. However, for values $1 < n \leq 2$,

the modeled diurnal variation would be such that the profile is broader around the maximum than the minimum and this characteristic opposes the observed character of the diurnal variation [8]. Conversely, when n is large (greater than 8), the density profile becomes too sharp near the diurnal maximum. The curves shown in Figure 15 of $\cos^n(\psi/2)$ for various values of n show that the changes in the shape of the curve are large for small changes in n when $2 \leq n \leq 8$ and the shape changes very little with n when $n > 8$. The point to be made here is that when a powered cosine function is to be used to describe the diurnal density variation, the exponent should be limited to values between 2 and 8. Indeed, Jacchia has consistently arrived at exponents in this range [5, 8, 10, 11, 12].

The U.S.S.R. Model is also a relatively simple, straightforward algorithm. It is very fast and relatively sophisticated; however, its use is limited to the altitude band from 140 km to 500 km and to solar flux levels from 65 to 165×10^{-22} Watts m^{-2} Hz $^{-1}$. Furthermore, certain conditions can cause the model to yield negative densities. These conditions, which are physically realizable, occur when the 6-month average of the daily $F_{10.7}$ is near enough to 150×10^{-22} W m^{-2} Hz $^{-1}$ that $F_0 = 150$ is chosen as the reference flux. The scale factor K_1 which corrects the density for short term fluctuations in solar activity becomes negative for values of the daily $F_{10.7}$ and altitudes below the curve shown in Figure 16. It is true that the conditions for which K_1 becomes non-positive are not likely to occur often, but variations in $F_{10.7}$ of the magnitude of 75×10^{-22} W m^{-2} Hz $^{-1}$ have occurred and the potential user should be aware of this limitation in the model. The other factors are always positive in the altitude region between 140 and 500 km.

The Jacchia-Roberts models are the most sophisticated of the models considered and provide upper atmosphere density values over the greatest range of altitudes. The Jacchia-Roberts models and the U.S.S.R. Model provide corrections for the diurnal variation, variations in solar activity over both the 11-year and 27-day cycles, semiannual variation, and for variations in geomagnetic activity. In addition, the Jacchia-Roberts models account for seasonal-latitudinal variations in the assumed constant boundary condition at 90 km. and seasonal latitudinal variations in helium concentrations. The Modified and Asymmetric Modified Harris-Priester Model accounts for only the diurnal variation and the variation in density due to the variation of solar activity over the 11-year solar cycle. It should be remembered that the original model given by Harris and Priester [7] does include procedures for accounting for all of the variations discussed herein. However, one of the fundamental motives in this investigation was the determination of an efficient model which can be adapted to model "real-time" atmospheric density variations and the Asymmetric Modified Harris-Priester Model has the desired characteristics of computational efficiency and adequate fidelity in representing the diurnal variation to form the base for such an adaptive model. The details of the formulation of such an adaptive model are given in Reference [6].

7. Conclusions

Three widely used atmospheric density models have been discussed. The computational aspects of each model have been shown and comparisons of the computational speeds and computer storage requirements have been made. In general, all of these models can be said to be quasi-dynamic representations of the atmospheric density; that is, they are neither completely static nor completely dynamic. The time dependent variations in the model density profiles are determined by both the evaluation of explicit continuous functions of time and by the input of time varying parameters to the algorithms. These input parameters, specifically measured values of solar and/or geomagnetic activity, are available for use by the algorithms in discrete form only. Solar activity is reported as 1-day averages and geomagnetic activity is available every 3 hours. Since the time delay between the measurement of a change in geomagnetic activity and the corresponding response in the atmospheric density is approximately 6.7 hours [5], a direct data link with the geomagnetic activity index reporting agency would be required for real time or near real time applications. Usually, though, some predicted average values are used with the ensuing errors being accepted as unavoidable. However, even if the input parameters are available within the lag time interval, the density models are still static with respect to the time interval between successive re-evaluations of the parameters and this lack of fidelity constitutes an error source in the evaluation of the drag forces.

A method to overcome this shortcoming in the current density models is to provide a continuous input of measured solar and geomagnetic activity indices. However, such a solution would be difficult to implement in a near real

time mode. Another method to possibly accomplish accurate drag determinations, especially in real time or near real time, is to estimate the drag by processing satellite observations with a sequential linear filter.

This latter concept is attractive for a number of reasons. Besides allowing for real time determinations, the technique could allow for improved time and spatial resolution in the drag model, improve the performance of the filter by minimizing errors in the drag model, and significantly reduce the requirement for external data input.

Table 2. Comparison of Central Processor (CP) Time Required for Drag Acceleration Computation

Model	CP Time for Drag Computations (Sec)	Total CP Time for Run* (Sec)
Analytic Jacchia-Rober's Model	20.34	58.77
Modified Analytic Jacchia-Roberts Model	15.97	54.61
Modified Harris-Priester Model	7.67	46.05
Russian Model	5.53	44.36

* Each run consisted of an integration of the equations of motion for approximately five periods in the circular orbit. The integrator was the fixed step third order Runge-Kutta with Ralston's coefficients. The step size was 25 seconds.

**Table 3. Sample Density Profile Determined by the
Analytic Jacchia-Roberts Model Using
Single Precision Arithmetic**

ALTITUDE (METERS)	DENSITY KG/M³ x 10¹¹
300000.01	2.16516
300001.53	2.16338
300006.65	2.16673
300015.38	2.16670
300027.70	2.16165
300043.60	2.15915
300063.09	2.15988
300086.14	2.16069

Table 4. Comparison of Density Calculations with the Analytic Jacchia-Roberts Model

ALTITUDE (KM)	SINGLE PRECISION	DENSITY DIGITS DOUBLE PRECISION EQUATION (A.12h) SINGLE PRECISION ALL OTHER CALCULATIONS	DOUBLE PRECISION
90	3.46	3.46	3.46
100	5.4952	5.4956	5.4977
150	2.5798	2.5800	2.5809
200	3.9305	3.9308	3.9322
400	8.0247	8.0253	8.0283
600	4.2362	4.2365	4.2381
800	3.8025	3.8028	3.8042
1000	8.8327	8.8333	8.8366
1500	1.5922	1.5923	1.5929
CENTRAL PROCESSOR TIME (SEC)	.289	.292	.376
CENTRAL MEMORY CORE STORAGE (WORDS)	12000 ₈	12700 ₈	15300 ₈

Table 5. Comparison of Densities Calculated by the Analytic Jacchia-Roberts Model and the Modified Analytic Jacchia-Roberts for $T_{\infty} = 1100^{\circ}\text{K}$

ALTITUDE (KM)	ATMOSPHERIC DENSITY DIGITS		PERCENT ERRCR
	UNMODIFIED MODFL	MODIFIED MODEL	
100	5.4977423	5.4977547	.0002
110	9.9303006	9.9303229	.0002
120	2.4596339	2.4596394	.0002
125	1.4018303	1.4018202	.0007
200	2.9381290	2.9379562	.0058
300	2.7866646	2.7863754	.0104
400	4.8761861	4.8755852	.0123
500	1.0416292	1.0414961	.0128
750	3.6213252	3.6210061	.0088
1000	4.4213508	4.4214982	.0033
1500	7.6597326	7.6603699	.0083

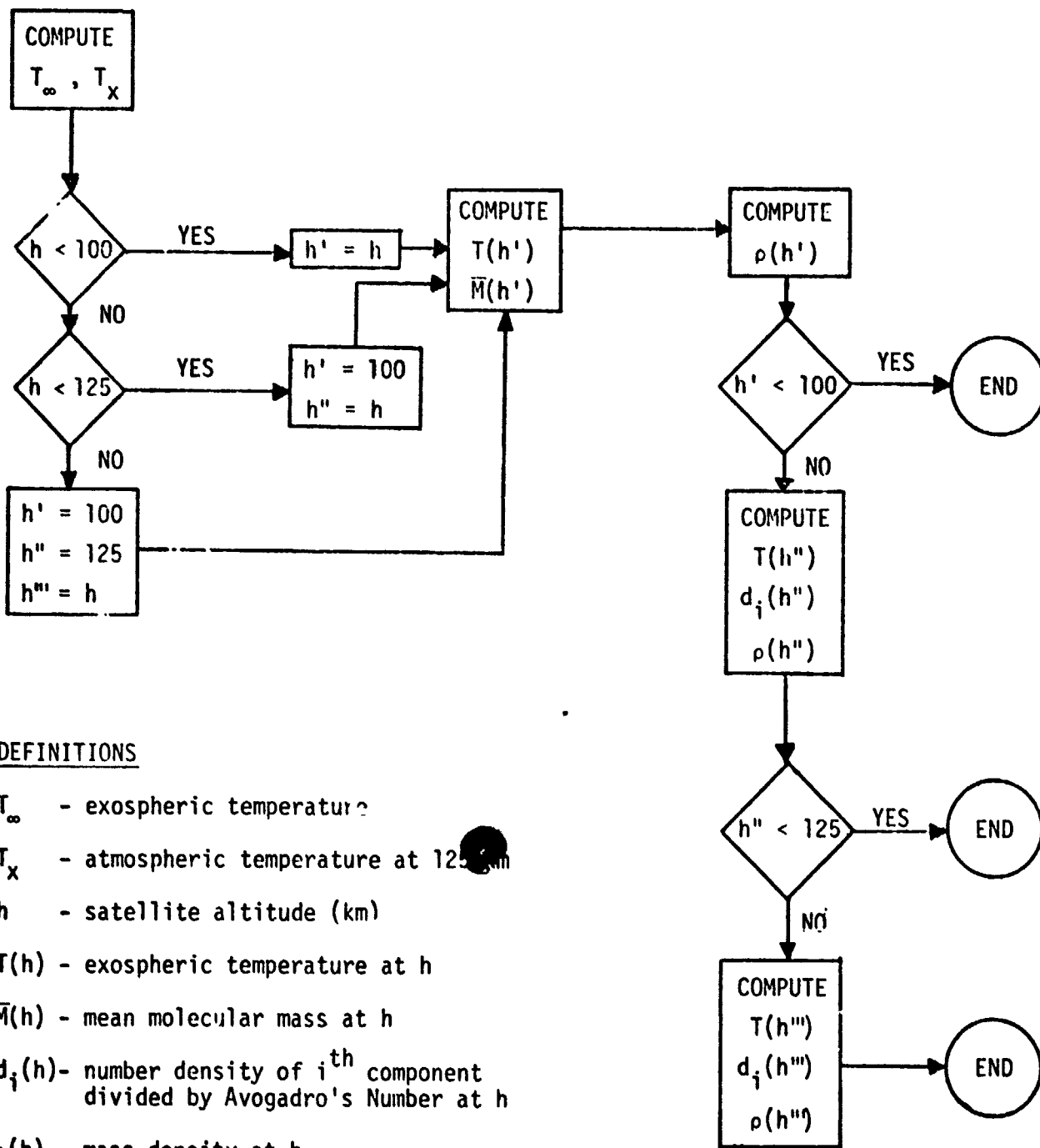


Figure 2. Logic Flow Chart for Analytic Jacchia-Roberts Model

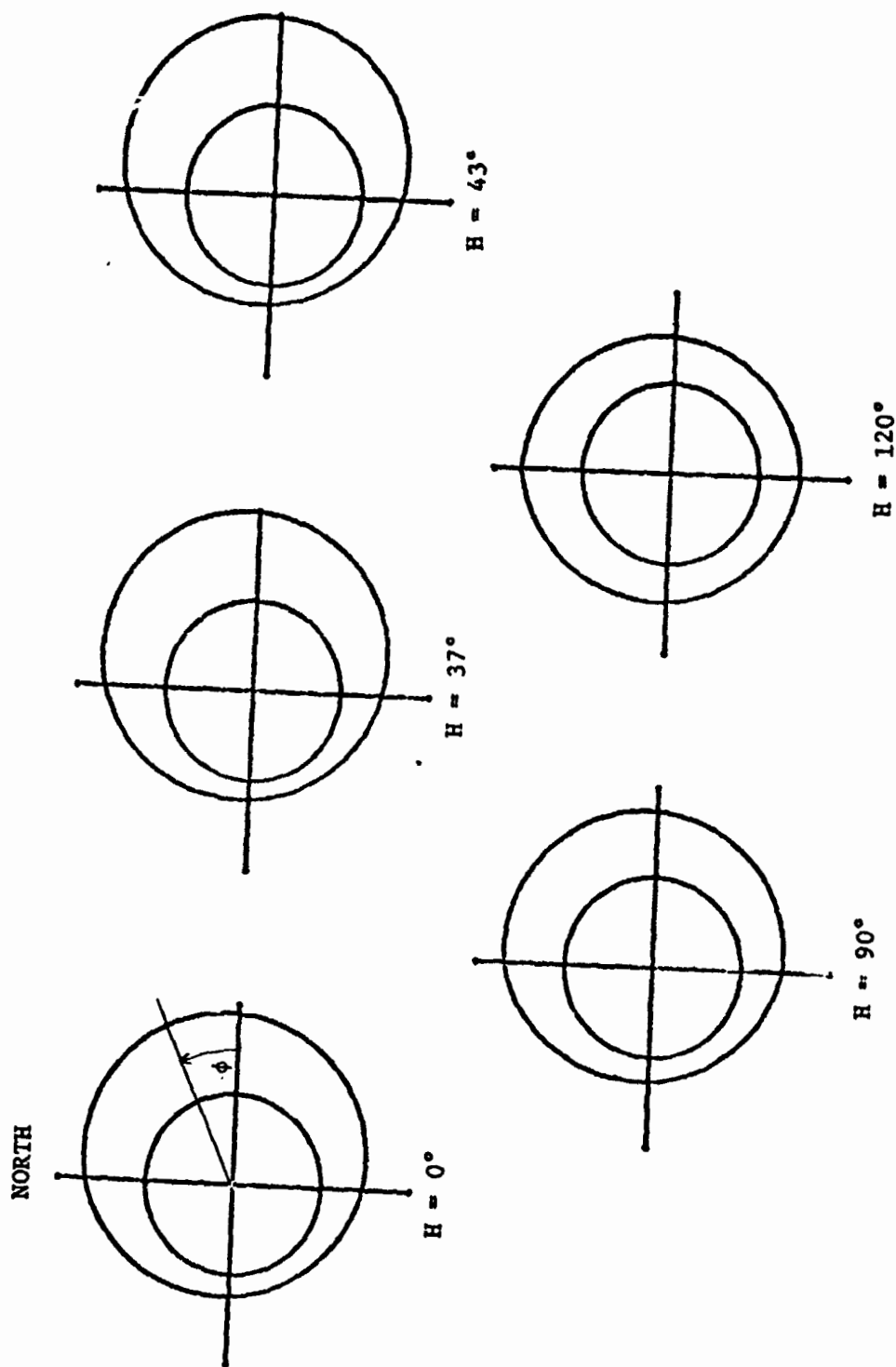


Figure 2. Latitudinal Density Profile at Solar Hour Angles H

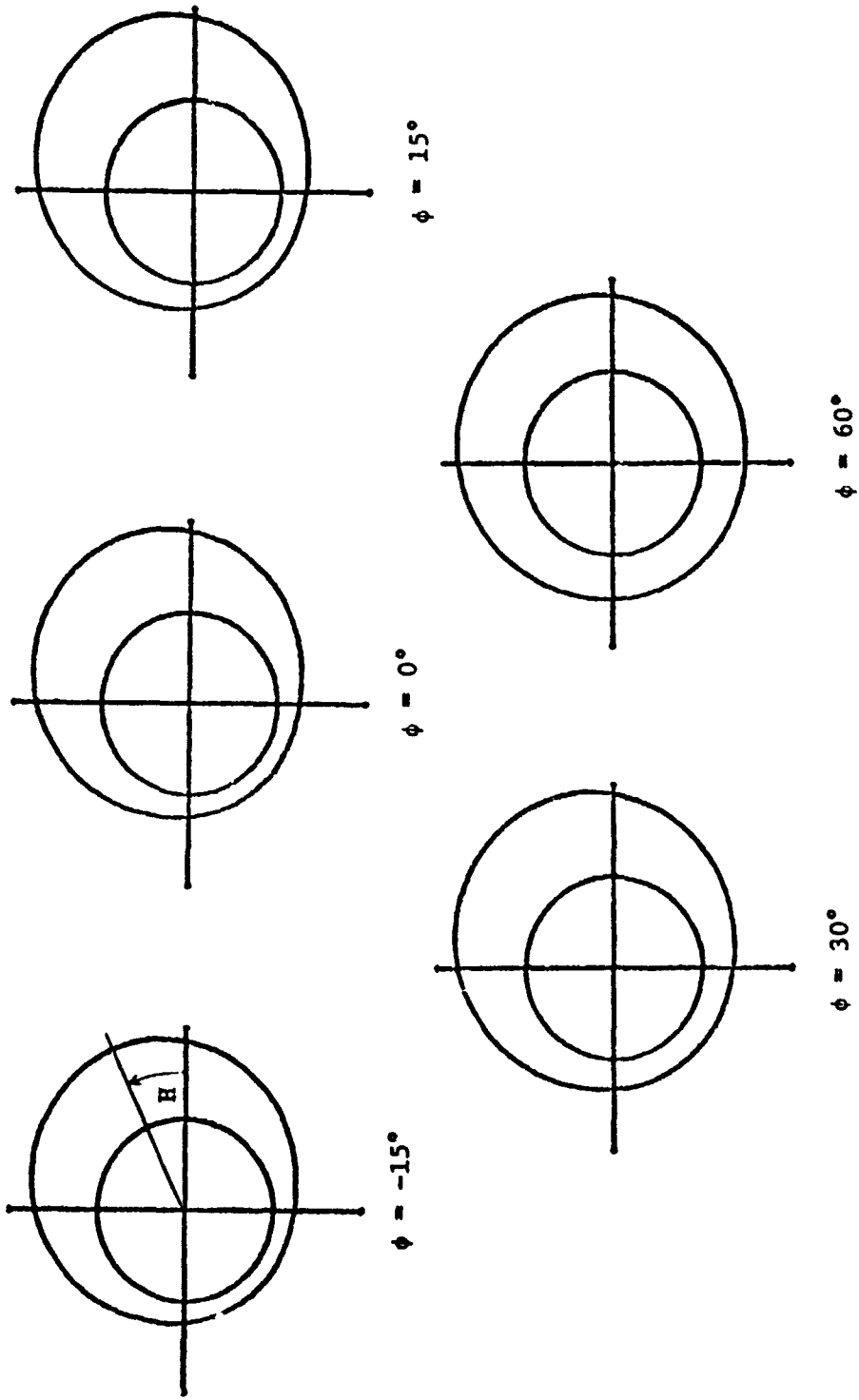


Figure 3. Longitudinal Density Profile at Latitudes ϕ

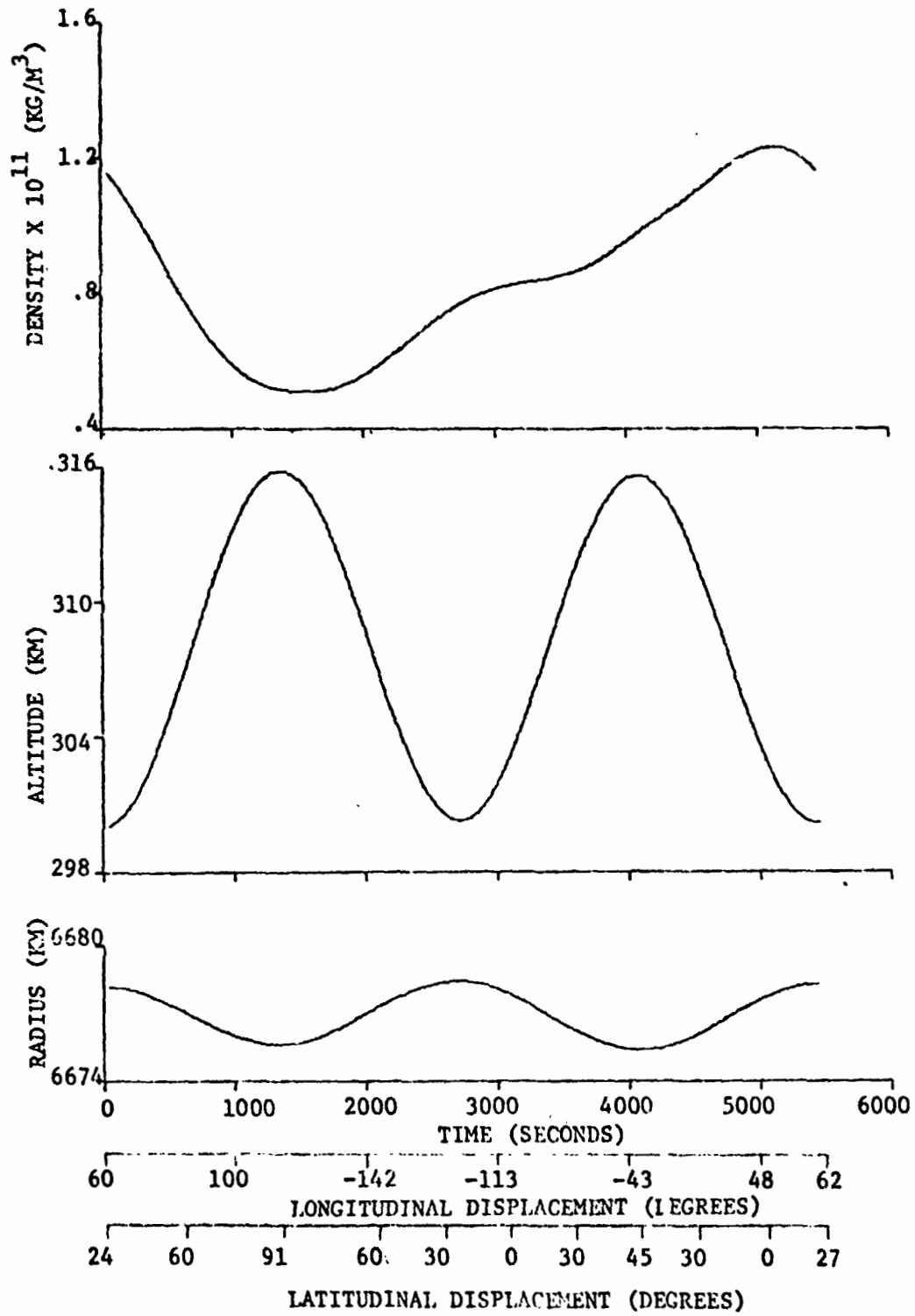


Figure 4. Density Profile ($\Omega = 0^\circ$)

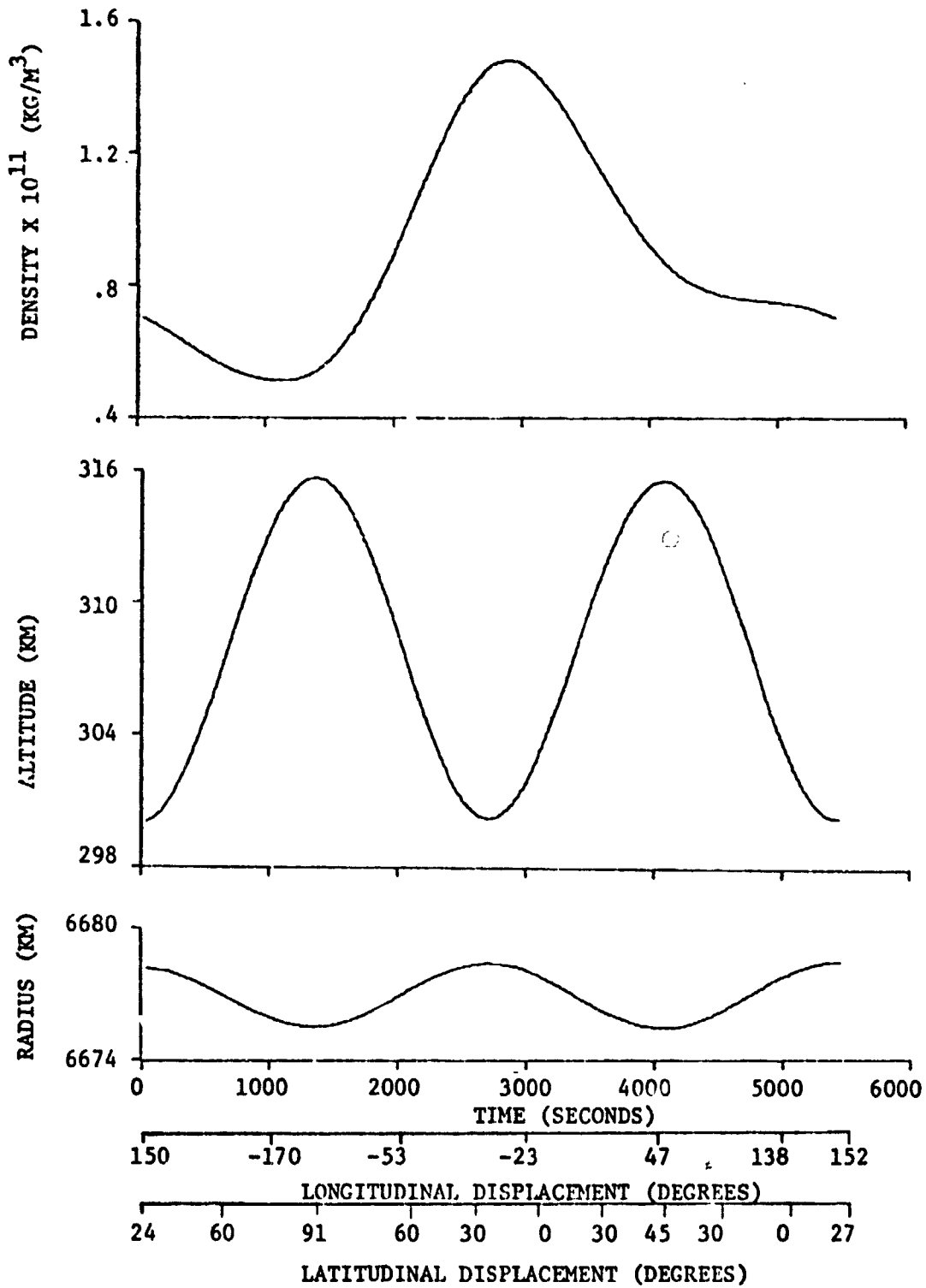


Figure 5. Density Profile ($\Omega = 90^\circ$)

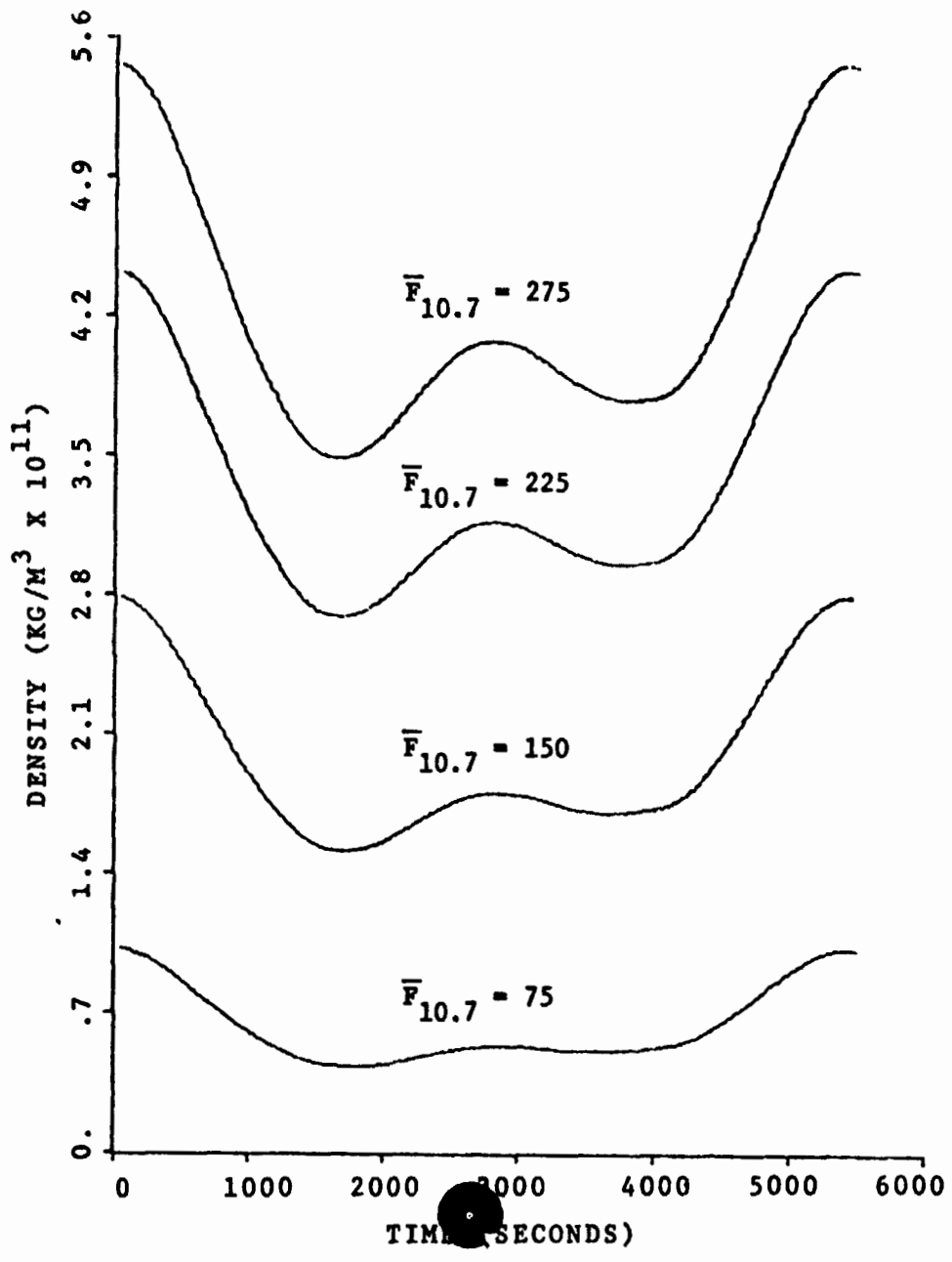


Figure 6. Density Profile Variations due to Changes in $\bar{F}_{10.7}$

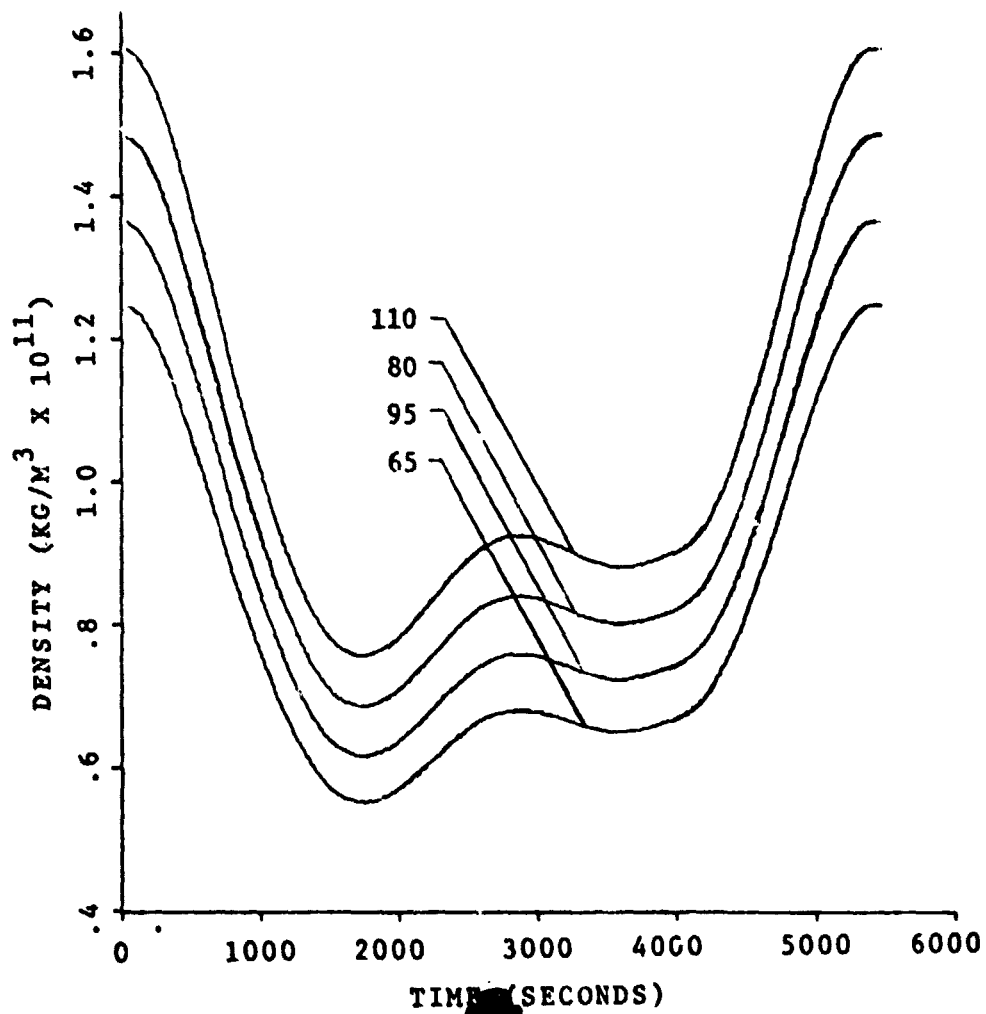


Figure 7. Density Profiles for Values of Daily $F_{10.7}$ about $F_{10.7} = 85$

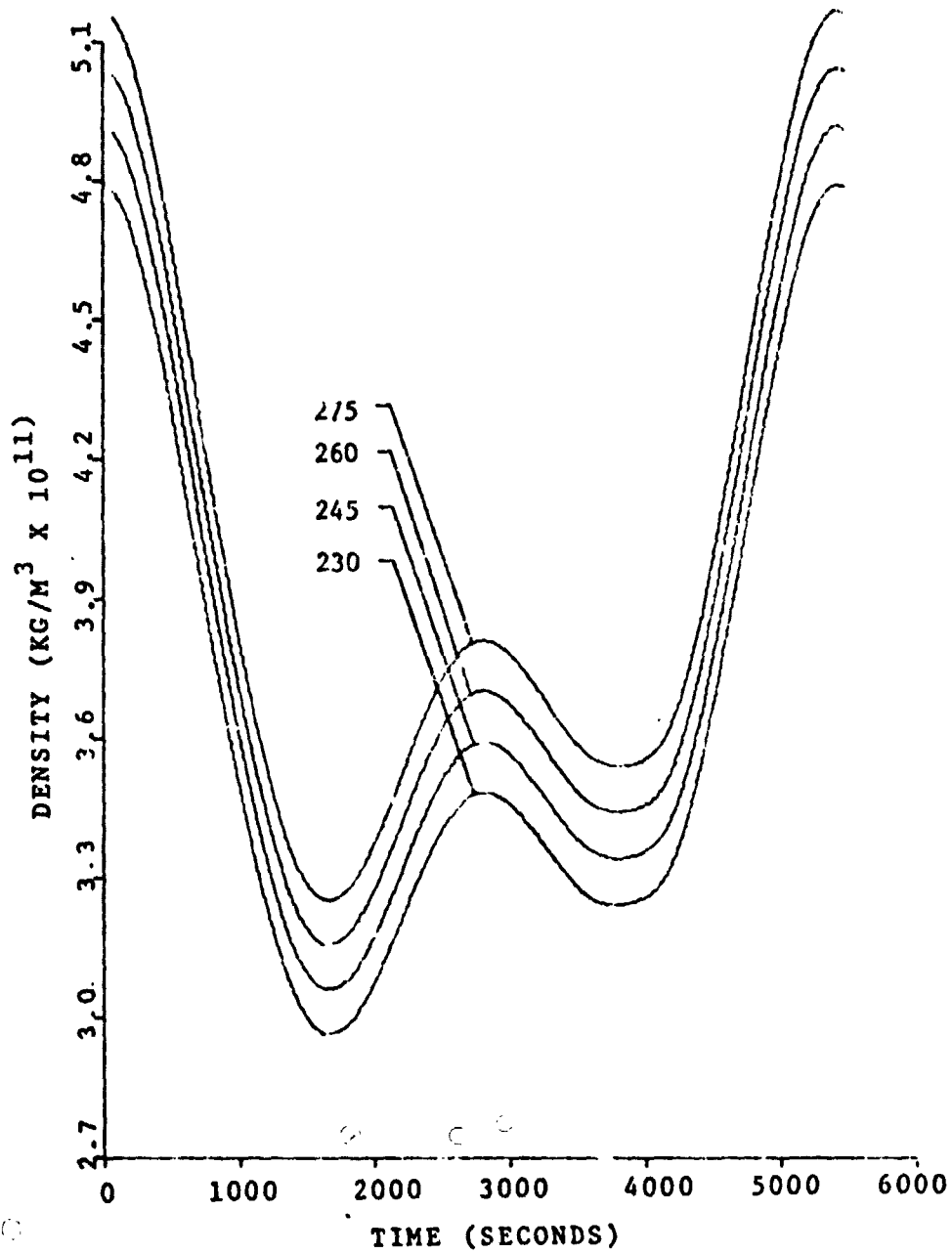


Figure 8. Density Profiles for Values of Daily $F_{10.7}$ about $\bar{F}_{10.7} = 250$

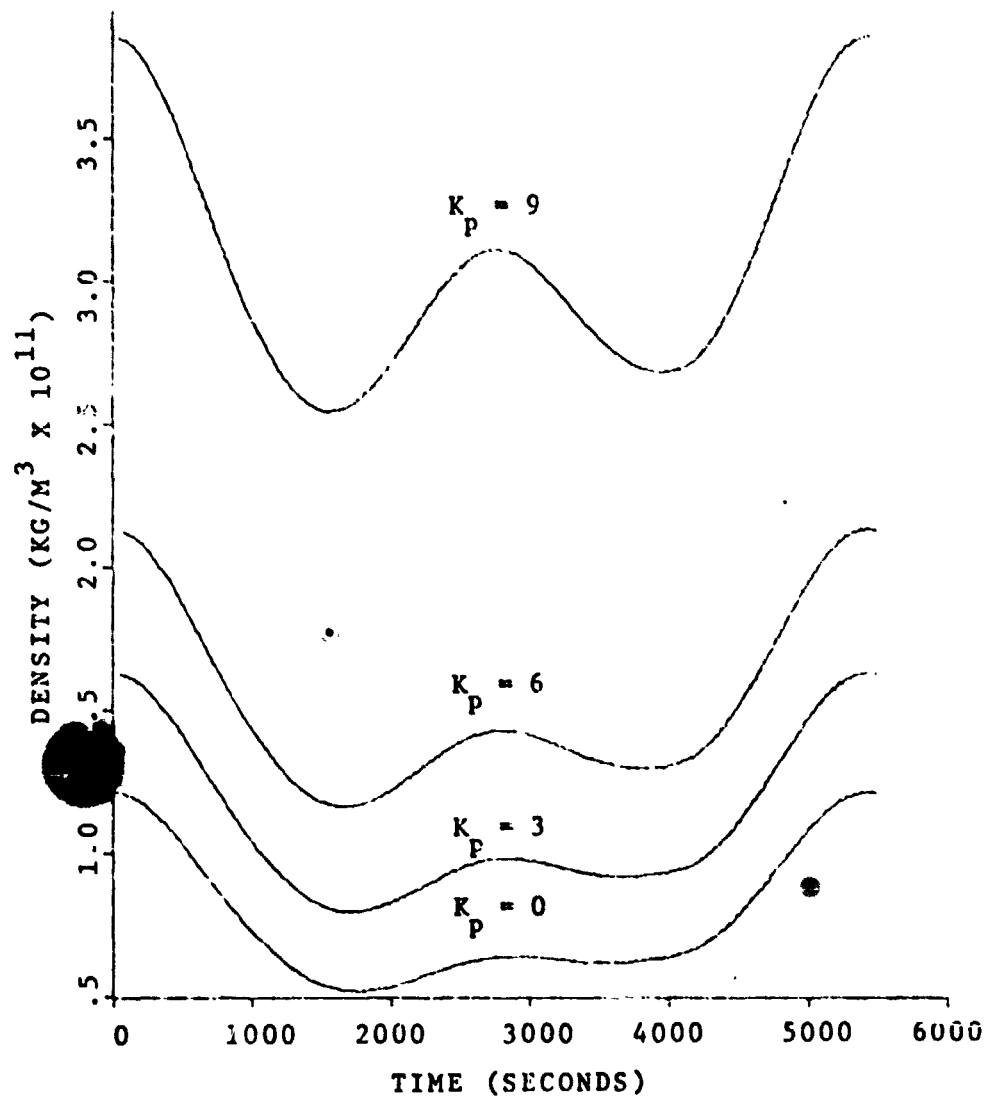


Figure 9. Density Profile Variations due to Changes in Geomagnetic Activity Index

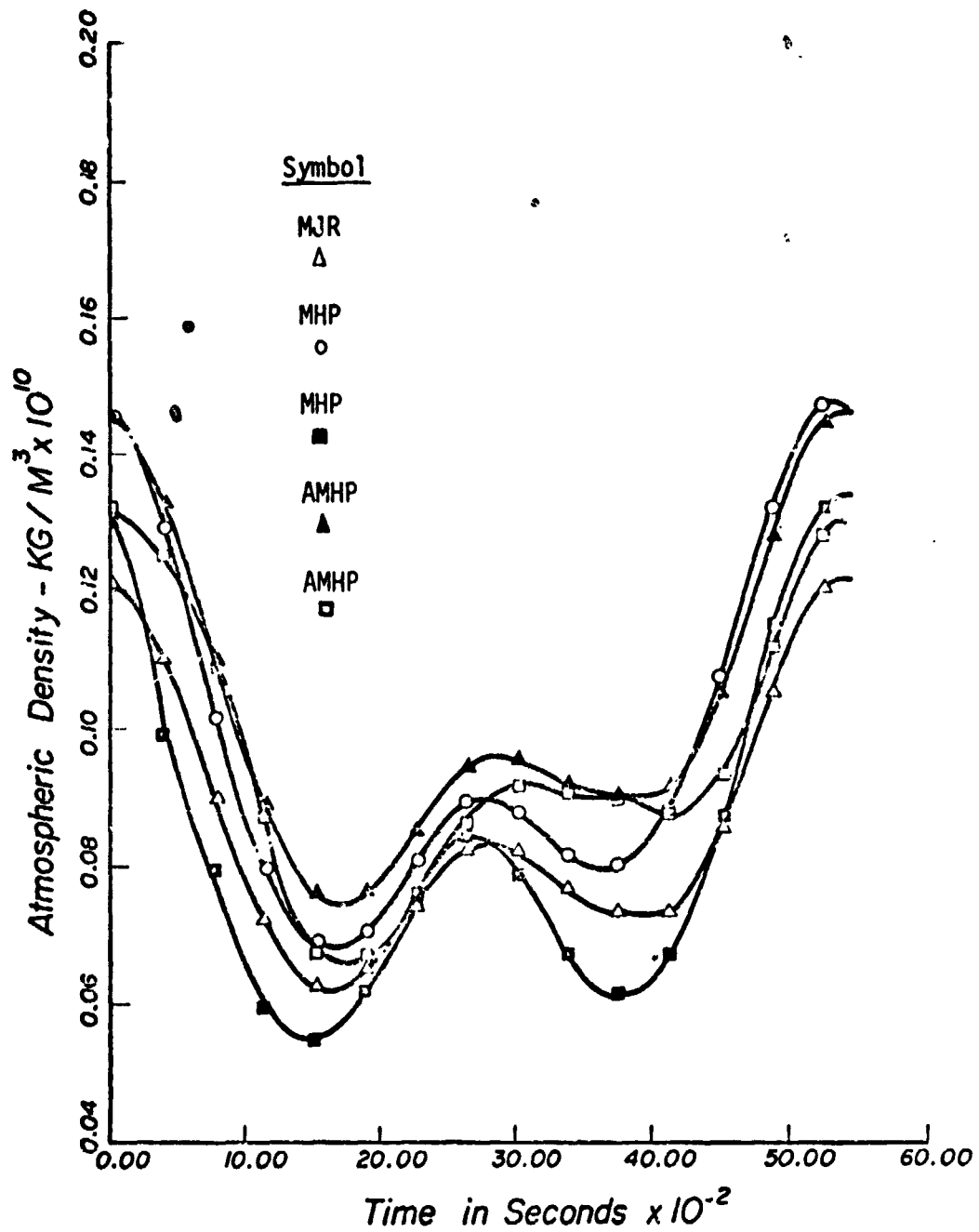


Figure 10. Comparison of Jacchia-Roberts and Harris-Priester Density Profiles at Low Solar Activity Level

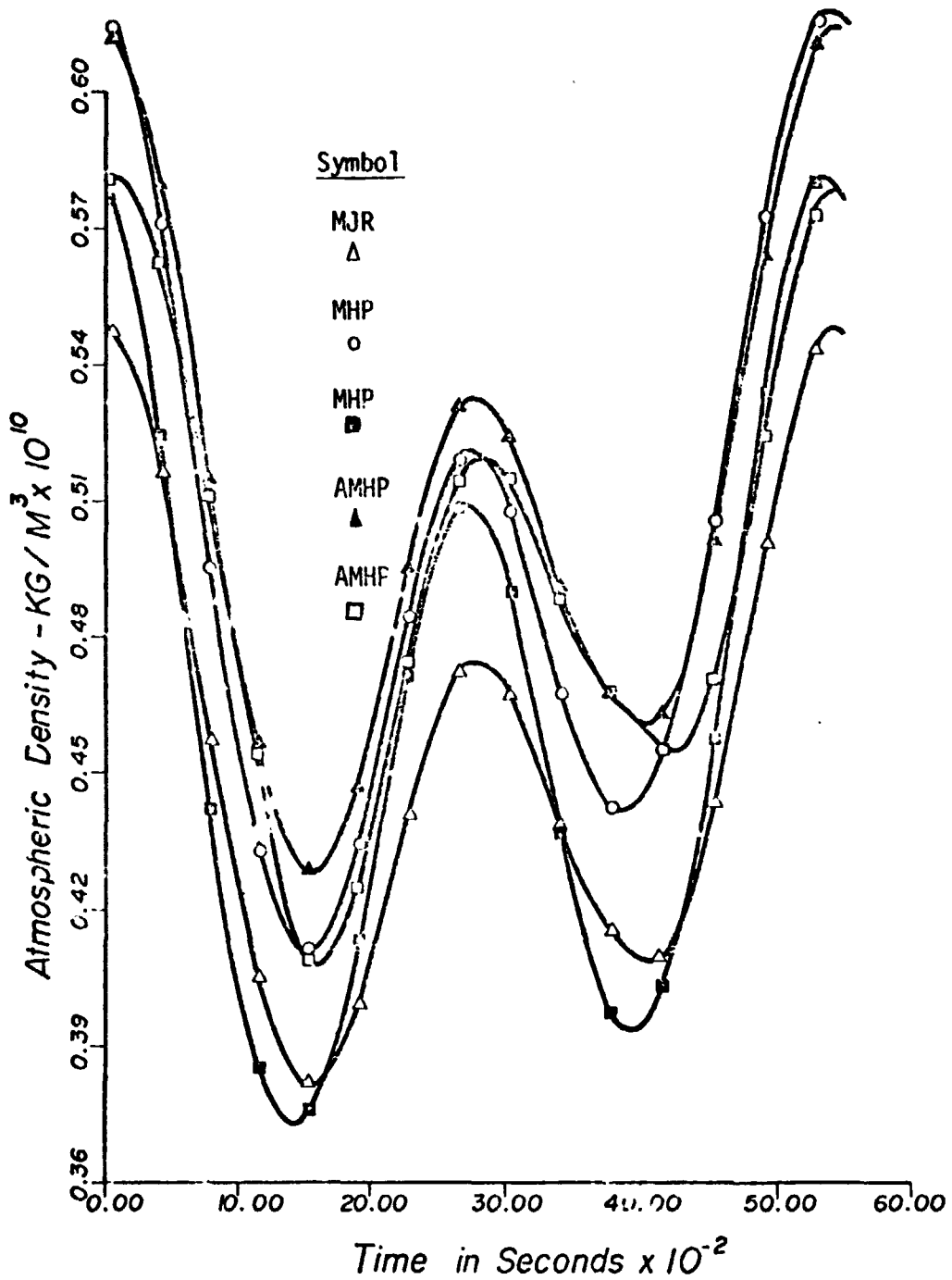


Figure 11. Comparison of Jacchia-Roberts and Harris-Priester Density Profiles at High Solar Activity Level

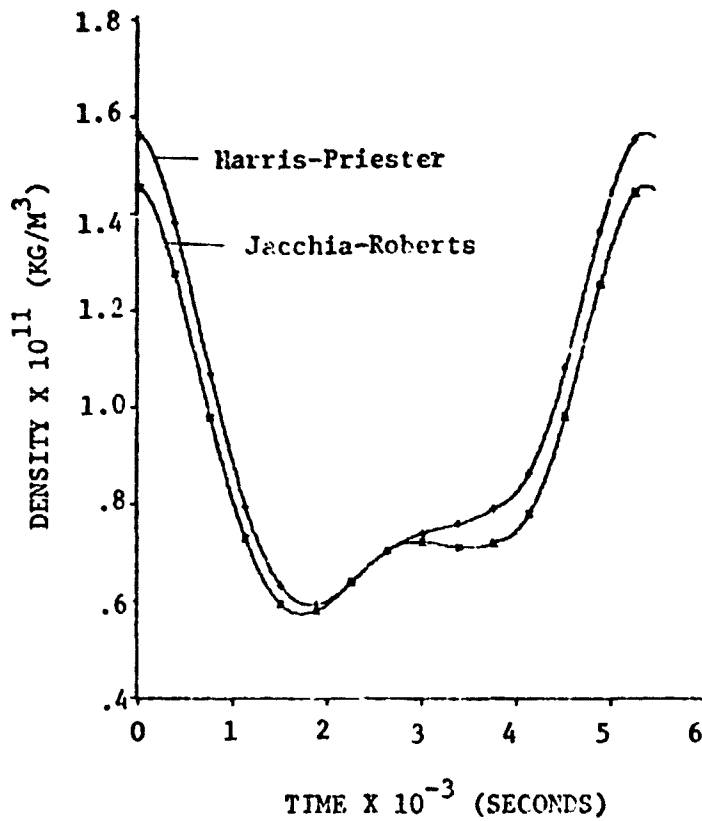


Figure 12. Comparison of Modified Analytic Jacchia-Roberts Density Profile with Asymmetric Modified Harris-Priester Density Profile in a Nearly Circular Orbit

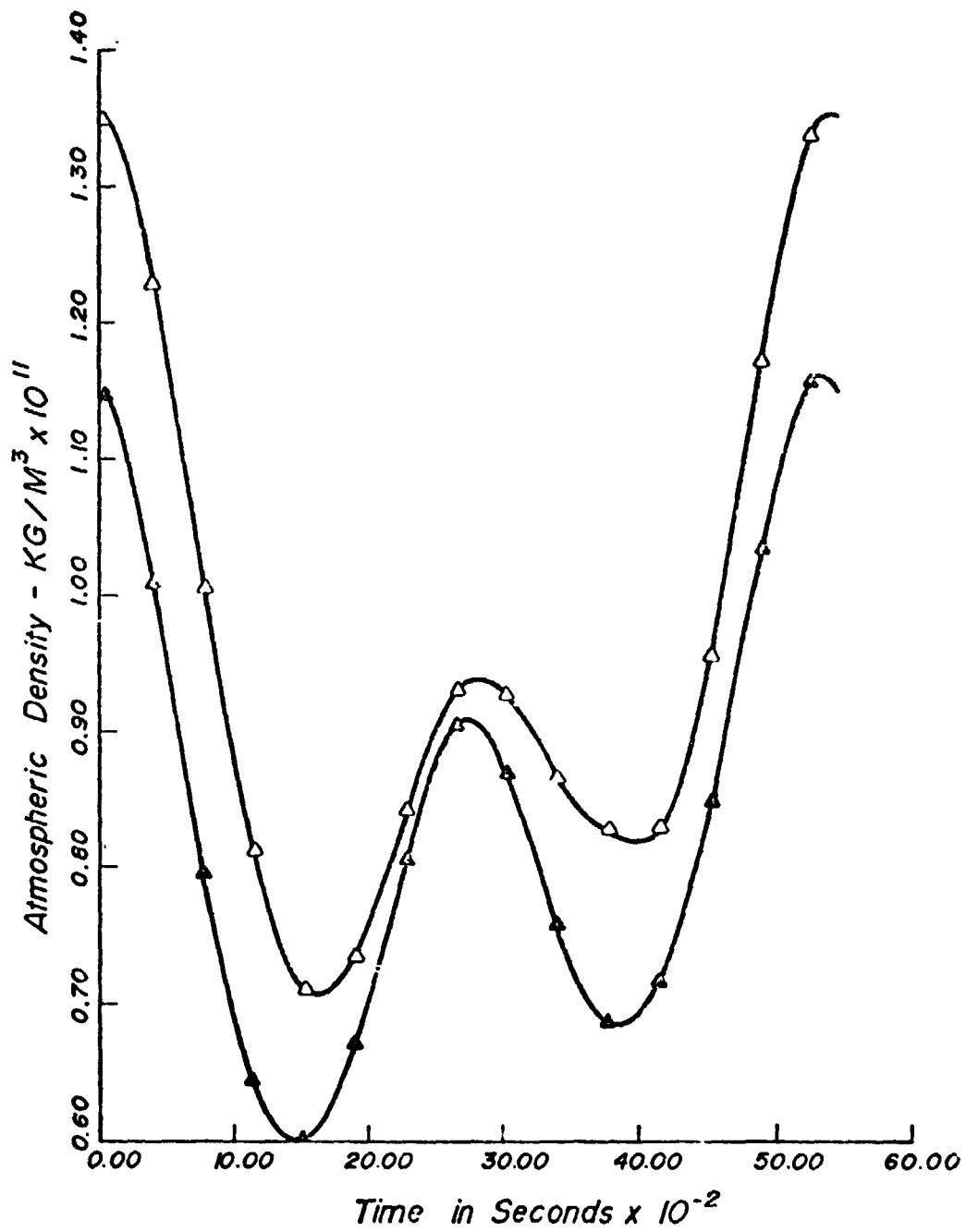


Figure 13. Comparison of Jacchia-Roberts (Δ) and Russian (\blacktriangle) Density Profiles at Low Solar Activity Level

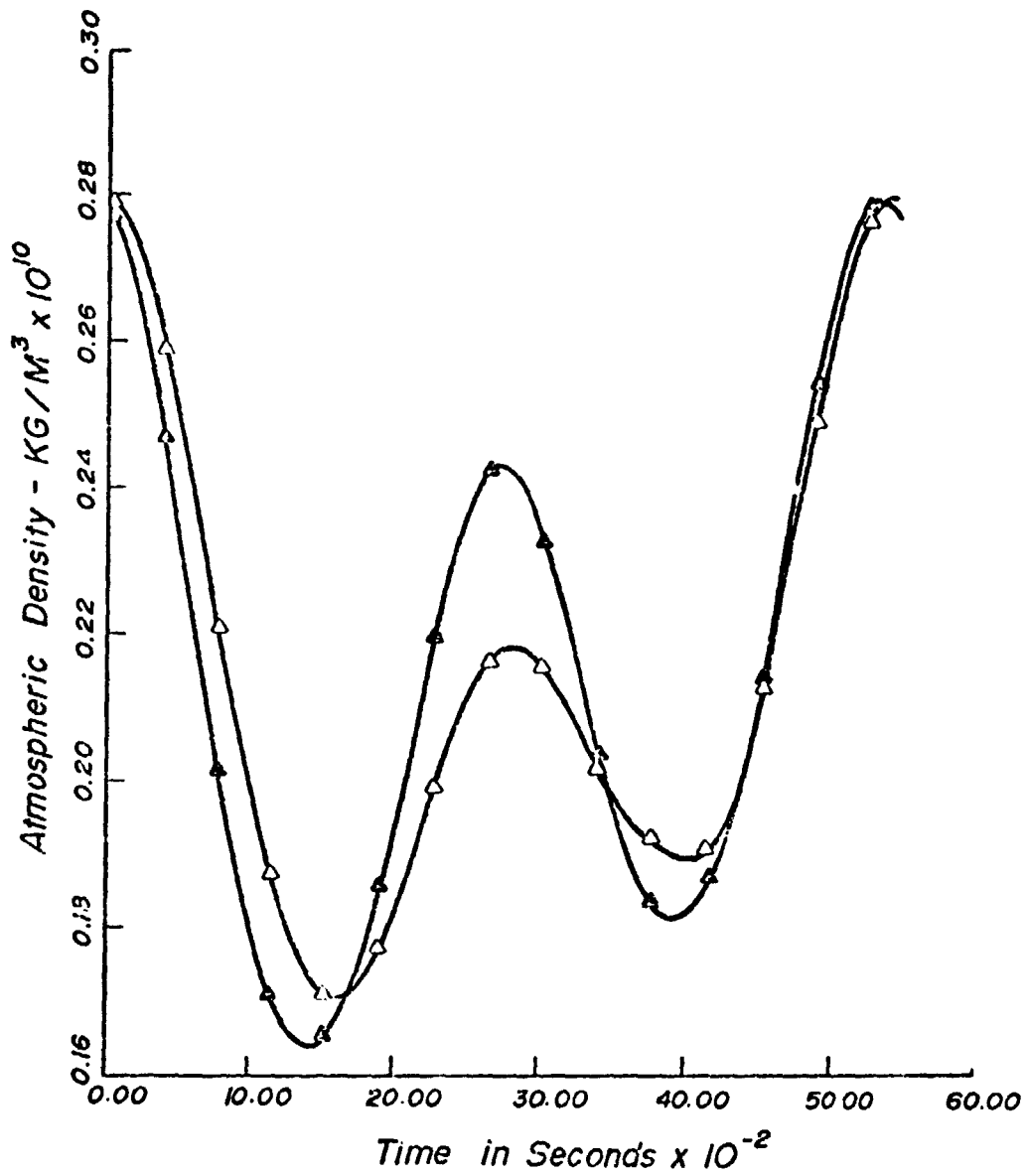


Figure 14. Comparison of Jacchia-Roberts (Δ) and Russian (\blacktriangle) Density Profiles at Medium Solar Activity Level

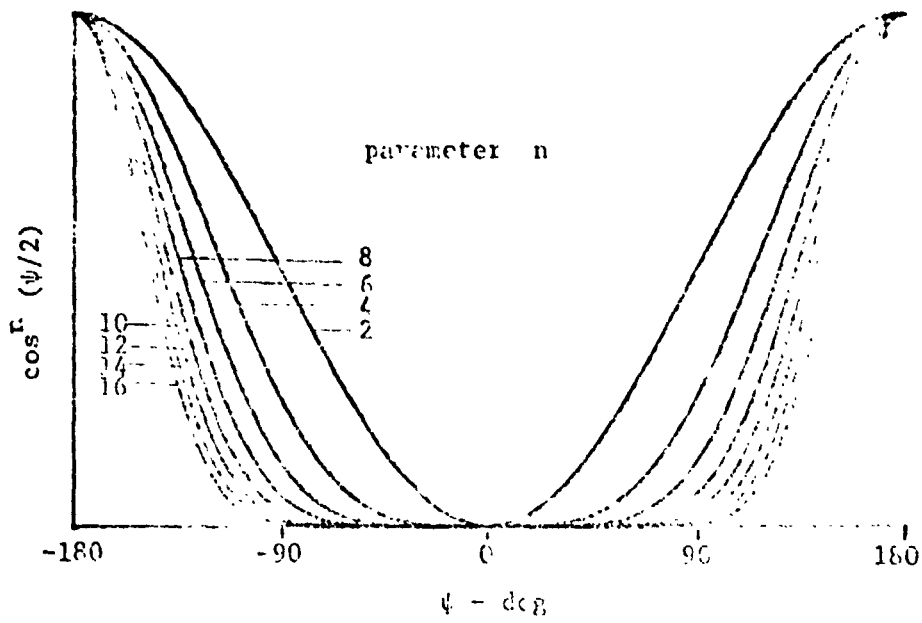


Figure 15. Effect of n on $\cos^n(\psi/2)$

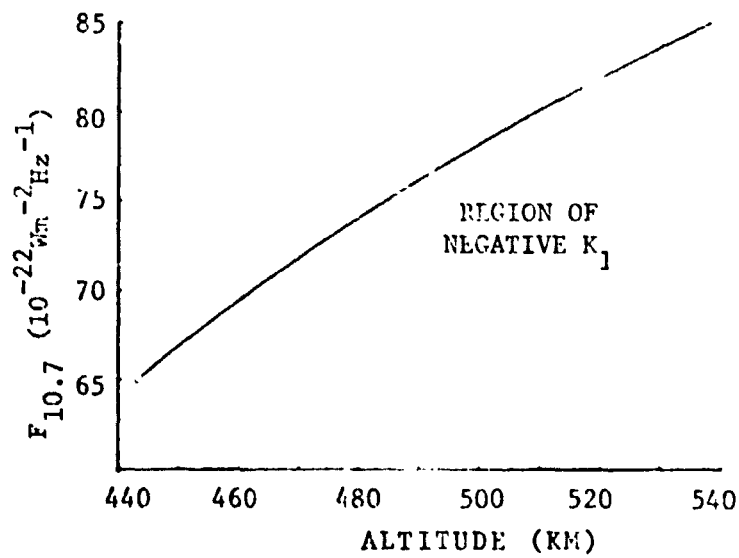


Figure 16. Curve of $K_1 = 0$ for
 $F_0 = 150$

References

1. Roberts, C. E., Jr., "An Analytical Model for Upper Atmosphere Densities based upon Jacchia's 1970 Models," *Celestial Mechanics* 4, 1971.
2. Wagner, W. E., and C. E. Velez, "Goddard Trajectory Determination Subsystem Mathematical Specifications," NASA Goddard Spaceflight Center, March 1972.
3. Elyasberg, P.E., B.V. Kugaenko, V.M. Synitsyn and M.I. Vaikovsky, "Upper Atmosphere Density Determination from the Cosmos Satellite Deceleration Results," *Space Research XII*, 1972.
4. Jacchia, L. G., "New Static Models of the Thermosphere and Exosphere with Empirical Temperature Profiles," Smithsonian Astrophysical Observatory, Special Report 313, May 6, 1970.
5. Jacchia, L. G., "Revised Static Models of the Thermosphere and Exosphere with Empirical Temperature Profiles," Smithsonian Institution, Astrophysical Observatory, Special Report No. 332, May 1971.
6. Dowd, D. L., "Adaptive Estimation of Atmospheric Drag on Near Earth Satellites," Center for Advanced Study in Orbital Mechanics Technical Report 77-4, The University of Texas at Austin; Austin, Texas, December 1977.
7. Harris, I. and W. Priestler, "Atmospheric Structure and Its Variations in the Region from 120 to 800 km," COSPAR International Reference Atmosphere (CIRA), 1965.
8. Jacchia, L. G., and J. Slowey, "The Shape and Location of the Diurnal Bulge in the Upper Atmosphere," *Space Research VII*, 1967.
9. Botbyl, G.W., "Technical Note on Expected Significance Using Subroutine ATDENS," Department of Aerospace Engineering and Engineering Mechanics, The University of Texas at Austin, unpublished, 1973.
10. Jacchia, L.G., "A Variable Atmospheric Density Model from Satellite Accelerations," Smithsonian Institution Astrophysical Observatory Research in Space, Special Report #39, 1960.
11. Jacchia, L.G.; T.G. Campbell; and J. W. Slowey, "A Study of the Diurnal Variation in the Thermosphere as Derived by Satellite Drag," *Planetary and Space Science*, Vol. 21, pp. 1825-1834, Pergamon Press 1973.
12. Jacchia, L. G., "Static Diffusion Models of the Upper Atmosphere with Empirical Temperature Profiles," *Smithsonian Contributions to Astrophysics*, Vol. 8, No. 9, 1965.

A DEMONSTRATION OF THE VALUE OF
GENERAL PURPOSE, ON-BOARD
SATELLITE COMPUTERS

Robert E. Jenkins
J. Miller Whisnant

Space Analysis and Computations Group
The Johns Hopkins University Applied Physics Laboratory

I. INTRODUCTION

The TRANSIT Improvement Program (TIP) satellites were designed and built by the Johns Hopkins University Applied Physics Laboratory for the U. S. Navy. These are navigation satellites which have onboard a general purpose mini-computer with 32 K words of memory. Also, each TIP satellite has a hydrazine-fueled Orbit Adjustment System (OATS), and an attitude control system which operates in both a gravity gradient and spin stabilized mode. The spacecraft is spin stabilized during the orbit adjust phase, and, later, operates in the gravity-gradient mode as a drag-free satellite. A similar drag compensation system (DISCOS) was flown on the first satellite of the series, TRIAD.

A picture of the fully deployed spacecraft is shown in Fig. 1. During the initial orbit adjust phase, the scissors boom is folded, and the hydrazine rocket and tank are attached to the spacecraft. The four solar panels provide a configuration for stable spin about the longitudinal axis, labeled z in the figure. Later, after the hydrazine is used up, the boom is extended with the empty rocket system acting as an end mass for gravity-gradient stabilization.

The solar panels are designed to unfold immediately after the spacecraft achieves orbit. When the panels failed to erect, the TIP-II spacecraft was left in a low power condition and with unfavorable moment-of-inertia ratios for spin stabilization. One year later, TIP-III experienced an identical failure. In addition, a boom deployment problem

later caused the scissors boom links to break on TIP-II under normal motor driven deployment.

Under ordinary circumstances, with hard-wire spacecraft logic, these problems would have precluded any parts of the mission being achieved, and would have even prevented important engineering checkout of many of the on-board subsystems. However, the ability to change the flight computer software after launch allowed us to implement various complicated work-arounds and achieve a partial mission success.

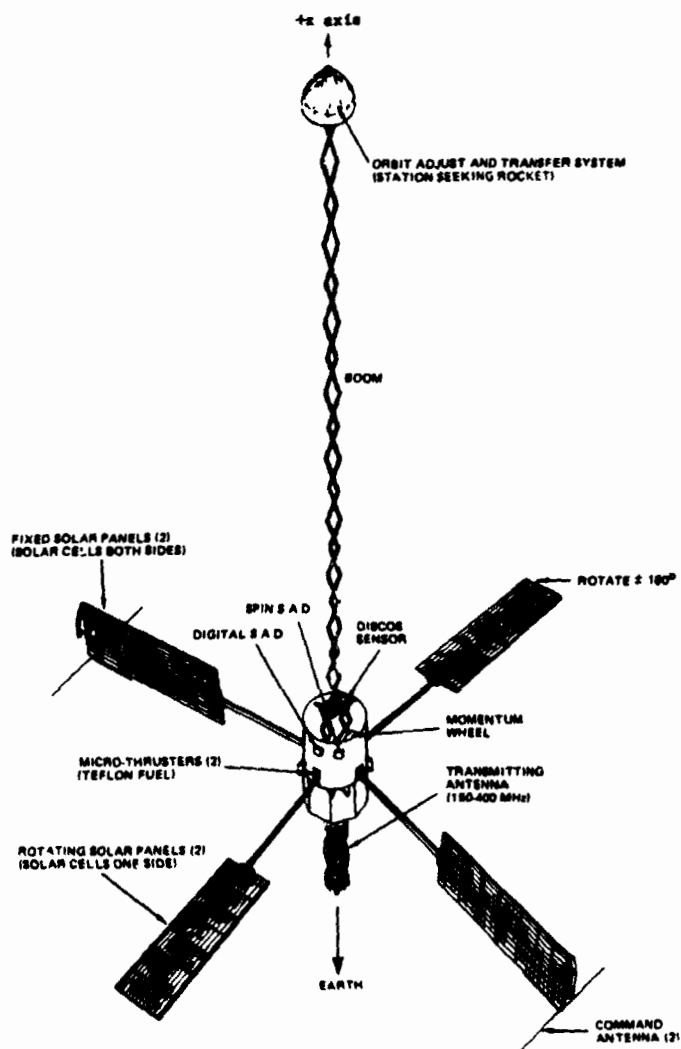


Figure 1. TIP-II Orbital Configuration

This paper describes how the flight computer was quickly reprogrammed to perform various control functions which:

- 1) performed power management to avoid troublesome spacecraft blackouts;
- 2) achieved enough spin stability to fire the OATS thruster;
- 3) raised the parking orbit to a workable altitude;
- 4) removed a high (45 rpm) tumble rate which was the indirect result of one of the failures; and
- 5) deployed the gravity-gradient boom successfully on TIP-III.

II. THE FLIGHT COMPUTER AND ITS SOFTWARE

The TIP flight computer shown in Fig. 2 is a general purpose mini-computer with specialized Input/Output (I/O) logic to service various spacecraft functions in real-time. The computer consists of two redundant CPU's complete with I/O logic and two magnetic core memories. Either memory or both may be used with either of the redundant CPU's. Each memory provides programmable storage of 16,384 words of 16 bits each. There is also a 64-word hard wired, Read-Only Memory (ROM) containing a special loader program for restarting the software (Ref. 1-2).

The TIP computer was designed for assembly language programming. The memory cycle time for the computer is 4.8 μ sec, with the time for an ADD operation being 9.6 μ sec. The TIP interrupt system is a hard-wired priority system containing 32 inputs. The 24 highest priority interrupts are labeled external and the last eight are internal. As implied by their name, external interrupts are driven by systems external to and independent of the computer. The eight internal interrupts are controlled by the software and are used for high-speed linkage to various subroutines. These interrupts can also be masked and enabled via software.

All computer input data are transmitted via RF link. The satellite can receive digital data at a rate of 10 bps or 1000 bps. The slow rate can feed the computer or the command system, while the 1000 bps data can only be used by the flight computer. There are a number of ways, direct and indirect, in which computer outputs can be realized. Direct outputs occur when data from memory are transmitted by the RF downlink channel to the ground. Indirect outputs are inferred when another satellite sub-system changes in response to a directive from the flight computer. The most useful direct output occurs in the computer dump mode. Upon command, the telemetry system transmits continuous flight computer data (via TM modulation). This mode requires a dump program in the computer to relay the contents of memory to the TM system at the proper rate.

ORIGINAL PAGE IS
OF POOR QUALITY

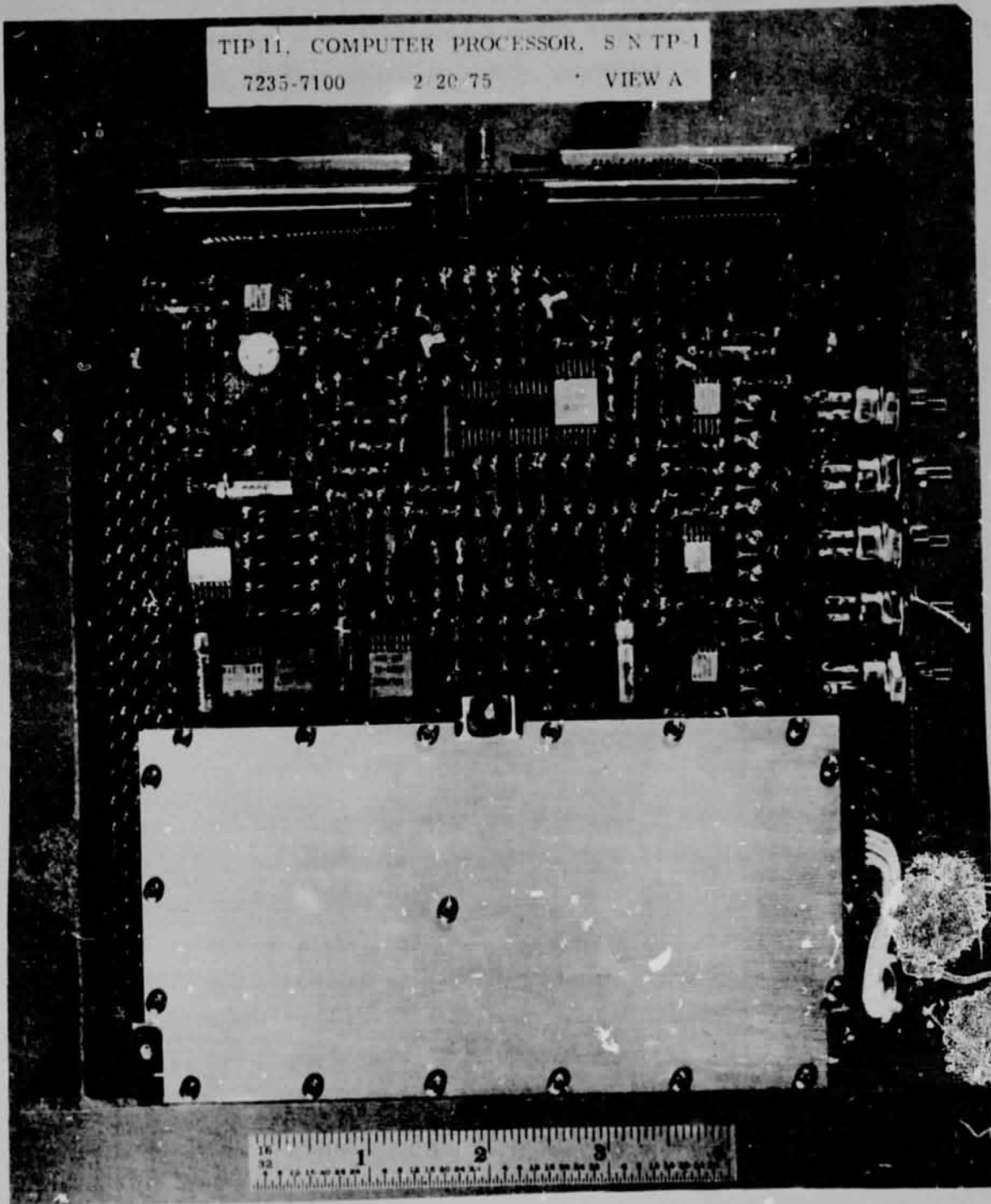


Figure 2. TIP-II, Computer Processor, S/N TP-1

The flight computer software consists of a system of interrupt driven, real-time programs. These programs perform on-board data management and interact through special hardware interfaces with other subsystems to give the computer far-reaching powers in controlling and monitoring the satellite.

The flight computer derives most of its power to perform control functions by virtue of its direct interface to the spacecraft telemetry and command systems. The TIP hardware includes a telemetry (TM) system whose function is to gather, process and format spacecraft data for transmission to the ground in a serial bit stream. The TM system is digital, with 8 bits per channel, 172 channels per frame, and a 4.227 sec frame rate. The TM interface allows the computer to exchange data with the TM system under direct software control.

To receive TM data, the software requests via the interface one of the 172 TM addresses. When this address occurs within the normal cycling of a TM frame (every 4.3 sec), the computer is interrupted and receives the data for storage or processing. Generally, data stored in the flight computer memory is later returned to the TM system in the form of a memory dump transmission.

The TIP command subsystem contains digital (10 bps) logic to perform the remote execution of relay commands, pulse commands, digital data commands and slow (10 bps) loading of the computer memories. Through the command interface, the flight computer has direct access to the front end of the command system. Any command can be issued by the flight software by serially transmitting the command bits through the interface at the required 10 bps rate. The length of a relay command bit string requires 2.3 secs for complete transmission. Any command can be executed with a programmed time delay by allowing the computer to issue the command. This "delayed command" capability results from loading the information for the delayed commands into the computer memory to be processed at a programmed time.

The main implications of the I/O interface described above are that the computer is limited to a data sampling rate of 4.3 sec for any given TM channel, and the maximum command rate is one every 2.4 sec. These constraints became quite important in some of the control functions implemented.

The TIP ground support system is illustrated in Fig. 3. The software for this system includes at least five major programs and uses four different computers. An overview of the ground system is contained in Ref. 3. The backbone of the system is the ground station PDP-11-40, operating through a front end PDP-8. This system is used to control all real-time satellite operations, and is also used for data formatting, real-time conversions and display, and miscellaneous utilities.

A program to be injected into the TIP flight computer begins as a card deck which contains the program code written in the flight computer assembly language. The card deck is input to the IBM 360/91 computer and processed by an assembler program called ARTIC. The output of ARTIC is the machine code on a magnetic tape along with a printed listing of both the input assembly language instructions and the corresponding machine code. The program tape is then stored on a disk file in the PDP-11 by the TIPLIB program. This disk file library contains the latest versions of all the flight computer software, including operational and diagnostic programs.

The PDP-11 program that selects flight computer programs from the library and formats them for transmission to the satellite is called TIPLOAD. The input to TIPLOAD is a card deck which defines the programs to be selected from the disk file library. This data from the library is then merged with other flight operation inputs and formatted for transmission to the spacecraft. The output of TIPLOAD is a disc file (LDM file) in the PDP-11. The data on this file is arranged into segments called "modules" which can later be individually transmitted to the spacecraft.

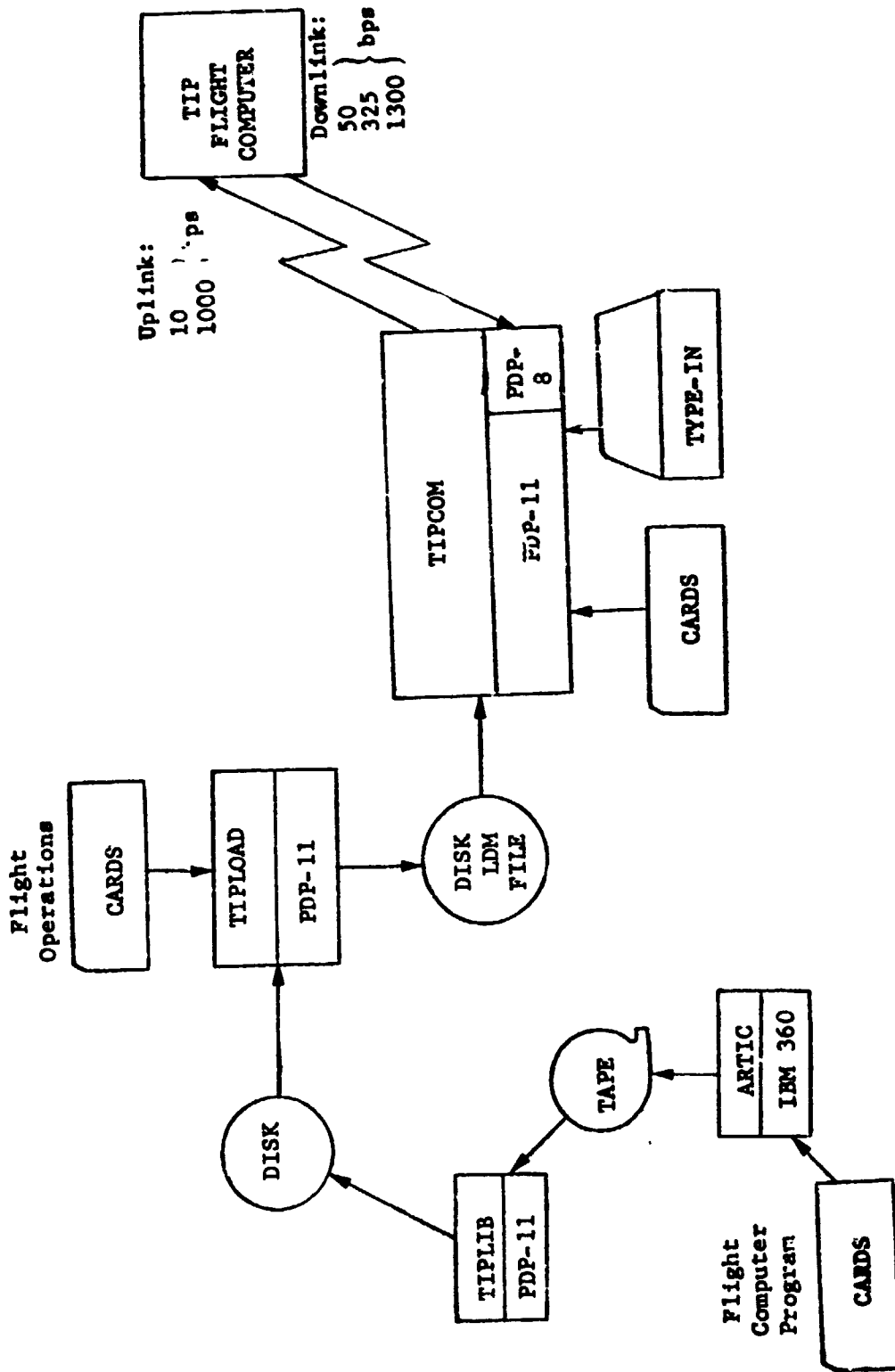


Figure 3. TIP Ground Support System

86 C-2

During a satellite pass the LDM file data is transmitted to the TIP spacecraft under control of the TIPCOM program, which also resides in the PDP-11. In addition to transmitting data up to the flight computer, TIPCOM also receives and records downlink loading feedback flags from the flight computer. All real-time communications are handled through TIPCOM. In addition, TIPCOM converts and displays on CRT much of the normal TM data in real time.

The overall ground system is complicated, but very flexible. It gave us the ability to completely reprogram the flight software after launch, as well as to manage the system in orbit in ways we had never dreamed of when the software was developed.

The main flight computer software is a set of basic programs called SYS which are resident in memory at all times. SYS contains

1. loading programs which can handle data at 10 bps or 1000 bps;
2. a memory dump program which can read out areas of memory on either a 325 bps or 1300 bps downlink;
3. a status routine which sends 80 bits of computer information to the TM system each TM frame;
4. a timekeeping routine that keeps a high precision universal time (UT) clock. The basic unit of time is referred to as a "tock" and is precisely 120/6103 seconds;
5. a Time-Queue program which controls the chronological sequencing of computer events such as delayed commands.

For details on the complete flight software system, see Ref. 4-5

In addition to SYS, there are other special programs which are loaded by SYS when needed. Two of those programs are

1. Delayed Command Program (DCPRO)

"Delayed command" refers to a relay or data command which is sent by the flight computer directly to the satellite command system at

some pre-specified time. The delayed commands are prepared by special card inputs to the TIPLOAD Processing Program. The TIPLOAD Processor automatically formats the command bit strings and the appropriate Time Queue entries as needed by the flight computer. Note that the command system hardware requires that there be at least .1 seconds between commands. DCPRO may also be used to send commands upon the occurrence of certain events. This is done in conjunction with the next program to be described, TMON. TMON initiates delayed commands whenever the data in certain telemetry words matches prespecified criteria. Since it takes 2.3 seconds to send a relay command, the flight computer software must make sure that the externally triggered delayed commands do not interfere with each other or with the time ordered ones being controlled by the Time Queue.

2. Telemetry Storage Program (TMON)

TMON is used to sample and store real-time telemetry data in the flight computer. The program expects as inputs:

- i) A start time (Time Queue Entry);
- ii) A list of TM channels to be stored and the rate at which each is to be stored.

TMON allows each TM channel to be sampled at its own rate, hence all channels need not be sampled during the same frame.

The program remains operating in the flight computer until the specified storage area fills up. The program automatically stops storing data at this point. Once the program has completely executed, a memory dump procedure is needed to transfer the stored data from the flight computer to the ground station.

The use of the Time-Queue for delayed commands, and the ability to send commands while monitoring TM functions proved to be extremely valuable after the TIP failures. In our wildest imagination we could not have foreseen the use we would make of these programs, nor the salvation they would provide for the crippled mission.

III. THE EFFECT OF THE FAILURES

The TIP spacecraft are launched by Scout Vehicles into a nominal polar, 180 x 400 n. mi. altitude parking orbit. The orbit adjust system is then used to change the orbit to circular at 600 nm altitude. At the same time the inclination is precisely trimmed to a selected value near 90° to control the nodal precession. An important part of this operation is to select optimum directions for thrusting to correct the altitude and inclination together and minimize the fuel requirements.

The spacecraft is designed to be spin stabilized about its longitudinal symmetry axis (z axis) to provide stable directional control during firing and to compensate for thruster misalignments. To achieve spin, an analogue magnetic dipole spin-up system provides continuous torque about the z axis using the earth's magnetic field. Passive nutation dampers on the end of the solar panels negate the effect of random transverse torques introduced by the spin-up system during this operation. To slew the z axis to a desired firing direction, once spin is achieved, a reversible z-dipole coil is aboard to provide precessional torques using the earth's magnetic field.

After the orbit is adjusted, the remaining hydrazine is vented, and the empty OATS system becomes the end mass on a scissors type boom for gravity-gradient stabilization (see Fig. 1).

When the solar panels failed to deploy on TIP-II we were left in the following situation:

- a) the spacecraft was generating less than half normal power;
- b) the spacecraft was not stable in spin about z;
- c) the nutation dampers were not in the correct position to be effective in damping out torques transverse to z; and

d) the 60 lbs of liquid hydrazine at the top of the spacecraft was an effective mechanism to quickly transfer any spin about z into tumble about the stable transverse axis.

For various reasons, the spacecraft needed to be at an average altitude of at least 400 n. mi. to be able to operate effectively as a navigation satellite. Also it was necessary to reduce the eccentricity to achieve the gravity-gradient stability required to do a good DISCOS experiment.

As will be described, we managed to achieve this, leaving about half the hydrazine to be vented before putting out the boom. Unfortunately, the hydrazine venting system was designed for stable z-axis spin; and with our configuration a tumble torque was inevitable. We had no way of knowing how bad this would be, and were forced to take our chances and vent. The next time we saw the spacecraft, the tumble* rate was 45 rpm and the solar panels had been ripped free by the centrifugal force. This improved the power situation, but before the boom could be deployed, the tumble motion had to be dissipated. This was done by implementing an interesting digital phase-locked-loop and using the spacecraft z-coil to work against the earth's magnetic field.

When we finally attempted to run out the boom on TIP-II, the links broke because of an unforeseen problem with scissors booms. Unfortunately, this happened after TIP-III was launched so the problem had not been corrected. It was possible, however, to work around the problem on TIP-III by using centrifugal force generated by a tumble motion. We were able to solve this problem by reversing the de-tumble program mentioned above.

* Throughout, we will refer to motion about the spacecraft longitudinal (z) axis as "spin," and motion about a transverse axis as "tumble."

IV. POST LAUNCH OPERATIONS

1. Power Management

The immediate problem after the solar panels failed to deploy on TIP-II was the severely restricted power capability of the spacecraft. This problem was particularly bad when we tried to use the magnetic system for spin-up and precession, and the problem was exacerbated by the fact that we launched into a minimum sun orbit.

To protect the battery, the power system is equipped with a low-voltage sensing switch, (LVSS) which shuts down the main power bus automatically when the battery voltage reaches 13.8 volts. Although this is not a disaster, it was extremely inconvenient when it occurred because the spacecraft had to be restored to its previous state through a complicated series of commands. The spacecraft oscillator shifted frequency dramatically during the first few minutes of warm-up making it very hard to keep the receivers locked up. Also, the flight computer system had to be re-loaded, restarted, and the U. T. clock reset each time the LVSS tripped. With passes only about 8 minutes long, this led to a hectic operation with the spacecraft frequently rising silent and not responding immediately to the recovery commands.

To solve the problem, we modified the TM storage program to monitor the battery voltage channel once per minute. When the voltage fell to a threshold level, the program used delayed commands to throw off the magnetic system power. The threshold was inputtable and usually set to 14.5 volts. The magnetic system draws about 60 - 70 watts, and relieving this load when the battery got to 14.5 volts was generally sufficient to prevent the LVSS from tripping.

Even with the battery voltage monitored, the spacecraft systems had to be duty cycled to prevent power drain. The Time-Queue feature of the flight software, discussed previously, was used to turn systems off and on at scheduled times to effect the duty-cycling. However,

this proved to be a great deal of work--punching cards, preparing updated Time-Queue files with the TIPLOAD program, and injecting the data into the spacecraft memory. When the Time-Queue software was developed, its primary purpose was to fire the OATS rocket out of view of a ground station, and it was not designed to easily handle a large number of delayed commands (like 100/day). The operations team quickly found most of their time taken up trying to keep the flight computer fed with duty cycle data. We were really spinning our wheels.

It proved rather easy to reduce this workload dramatically. We quickly recognized that nearly all of the chronological delayed commands for duty-cycling were periodic in time. They were generally tied to the orbit geometry, such as: systems turned off and on over the equator or the poles, systems turned off in the earth's shadow, etc. The answer was to make the Time-Queue automatically cycle itself.

A program called CYCLE was written to cause the Time-Queue actions to repeat with an inputtable period. This is done by calling CYCLE via the last Time-Queue entry in the list. The CYCLE program sets appropriate pointers to the starting conditions and then restores the original Time-Queue list, adding the input period to the time for each entry. This causes the Time-Queue actions to be periodically repeated indefinitely, until the process is stopped by ground command.

Some people were nervous at first about relinquishing control to the computer and allowing the spacecraft to operate autonomously. However, this simple fix worked beautifully and they soon became believers. Even the simplest operation would have been difficult to carry out without CYCLE; and, as will be seen, it would have been next to impossible to carry out the more complicated operations we eventually undertook.

2. Spin-Up Operations

The early operations with TIP-II were involved with attempts to spin the spacecraft about the z-axis. There were two reasons for these attempts: (1) early in the game we had hopes that sufficient spin could generate enough centrifugal force to break the solar panels loose; and (2) stable spin was required to fire the OATS rocket.

The spin-up system is a feedback control system that uses the earth's magnetic field to torque the spacecraft. Two orthogonal coils (x and y) provide a dipole moment in the spacecraft to supply the torque. The earth's field is continuously sensed, and the x and y coil currents are automatically phased to keep the resultant dipole orthogonal to the component of the earth's field that lies in the x-y plane. (The geometry is shown in Fig. 4.) This results in a torque about z that is always in the same sense, along with random torques transverse to the z axis. With a stable configuration the spin about z will gradually build up to the desired level, while passive dampers remove the nutation induced by the transverse torques.

With our unstable configuration, it was a different story. When the spin system was turned on, the liquid hydrazine was sloshed by the transverse torques and acted as an effective mechanism to quickly transfer any spin into tumble motion. Initial attempts to achieve any spin above a 1/4 rpm were unsuccessful. To help the problem, we modified the flight software to control the times that the spin system was on, so as to minimize the transverse torques.

The spacecraft are equipped with 3 orthogonal magnetometers measuring the body-fixed x, y, and z components of the earth's field. We modified the TM storage program to sample the channel for the z component every frame, and use it as criterion for turning on the spin system. Each TM frame the program made the following test:

$$|M_z| < c$$

where M_z is the z magnetometer reading, and
c is an inputtable threshold.

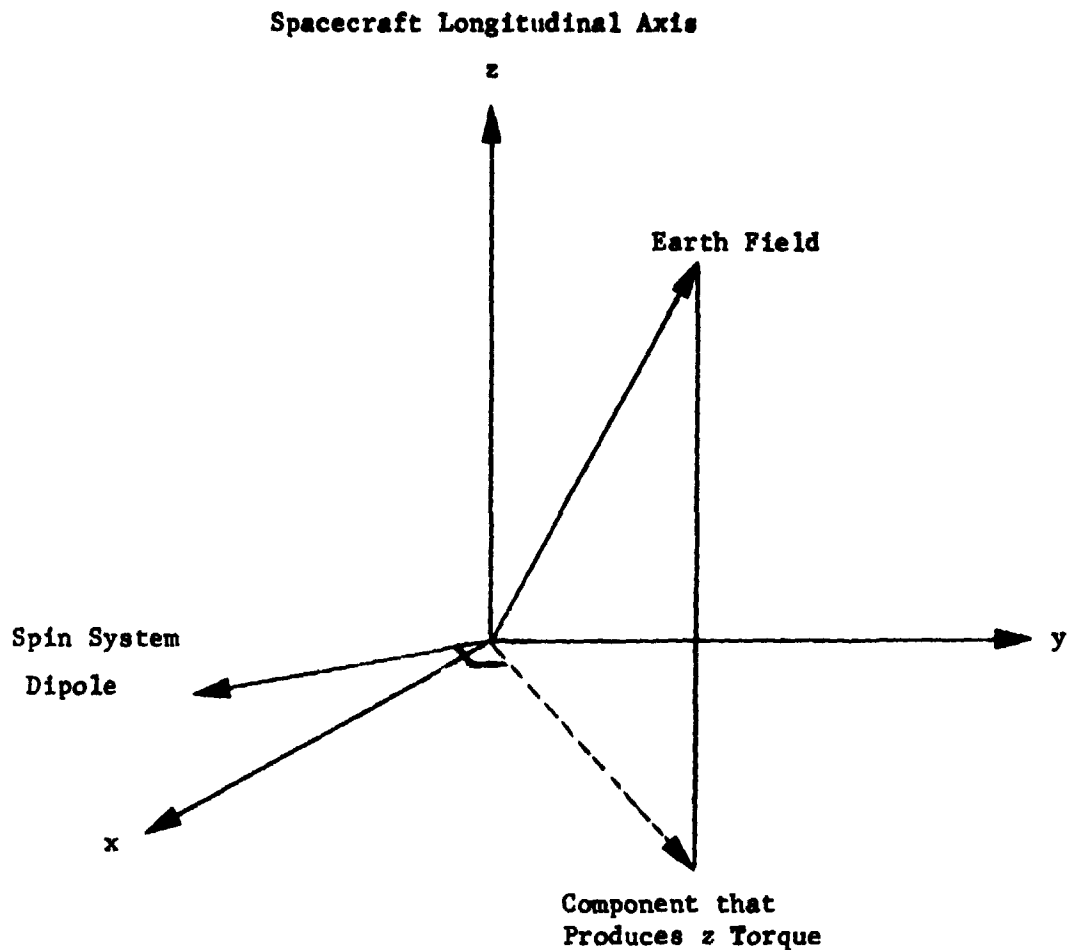


Figure 4. Magnetic Spin-Up Geometry

When the threshold was satisfied, the program used a delayed command to turn on the spin system, and conversely turned the system off when the z component was out of range. We had to include additional logic to prevent the program from continuously sending commands once the system was in the correct state. By allowing the system to be on only when the z component was near zero, the transverse torques were nearly eliminated.

It happens that there are two relays in series to control the magnetic system power. This turned out to be quite useful since we could let one relay (normally on) be controlled by the battery voltage and the other be controlled by the z magnetometer reading. Thus we

could allow both monitoring functions to operate in parallel, keeping our protection against the LVSS tripping during spin-up. This turned out to be about the only piece of good luck that we had in the operation.

It took about two days to generate the spin-up program, and after some trial and error we settled on a value for c of about 10 per cent of the full-scale field reading. The program helped quite a bit. We were able to achieve spin rates up to 1 rpm, but then the spacecraft would gradually build up nutations and transfer to tumble with a time constant of about 1 orbit (90 minutes). This was still not enough spin rate or stability to fire the OATS rocket.

At this point the idea arose of using the spacecraft z-coil as a device for actively damping the nutational motion to maintain more stable spin. This is the coil that is normally used to provide precessional torques for pointing the rocket nozzle. The coil can be switched by relay command to either the plus (dipole along +z) or the minus (dipole along -z) state.

For clean spin without nutation, the spacecraft magnetometers record a very distinctive pattern from the earth's field vector. Since the earth field is varying rather slowly due to the orbital motion, the attitude dynamics dominates the magnetometer's variations. The x and y coils record a sinusoidal variation 90° out of phase with period equal to the spin period, and the z magnetometer records a nearly constant value. As nutation (coning) builds up, the z reading begins to show an oscillation with period equal to the nutation or coning period.

The idea behind the damping program (DAMP) was to let the computer sense the derivative of the z magnetometer reading, and then set the polarity of the z-coil to produce a transverse torque (using the earth's field) that opposed the derivative. Again we could modify the TM storage program, this time to control the z-coil polarity based on the z magnetometer reading. The logic was simple.

1. Each frame, compute the difference between the current z magnetometer reading and the previous frame's reading, as an estimate of the derivative.
2. When the difference changed sign from plus to minus, send a delayed command to set the z-coil polarity to a minus dipole.
3. When the difference changed sign from minus to plus, send the command to change the z-coil to a plus dipole.

We also had to include additional logic to correct the TM reading for the z-coil effects. The z-coil strength is of the same order as the earth's field at 800 km altitude so it has a large effect on the z magnetometer reading.

Note also that the DAMP program can be used to de-tumble the spacecraft when it is in stable tumble about a transverse axis. In this case the z magnetometer records a sinusoidal variation. The effect of the program is to continuously adjust the z-coil polarity to produce a torque opposite the motion. This proved to be quite handy in reducing the time required to dissipate tumble motion.

The magnetic system is designed so that the spin system or the z-coil can be in use, but not both modes at the same time. As soon as we had the DAMP program written, we quickly found that it worked well, but we needed to continuously alternate between the spin-up mode and the damping mode to be effective. This meant we needed a way of dynamically switching between the SPINUP logic and the DAMP logic in the TM monitoring program.

The idea of changing the program logic dynamically while the flight software was actively running was a completely new feature for our software system. It was not hard to implement, and it turns out to be a very powerful capability.

We compiled both sets of logic (SPINUP and DAMP) into the TM monitoring program, with a simple program switch to select which path would be used to evaluate the z magnetometer reading. We then wrote a

program (ALTPRO) which was called by a Time-Queue entry to change the switch at a scheduled time. ALTPRO was written to be rather general, driven by an input list of memory addresses and their corresponding new contents. Each time the program is called at a scheduled time, it works on the next entry in the list, putting the new contents into the specified addresses.

To accomplish a spinup, then, the scenario ended up something like the following. At a pre-scheduled time, with the spacecraft essentially motionless, the computer would select the magnetic system for spinup, turn on the TM system, and activate the SPINUP logic. Near each equator, the computer would select the z-coil by delayed command and switch to the DAMP logic using the ALTPRO program. After several minutes of damping, the spin system would be re-selected and the logic switched back to the SPINUP program. This entire set of Time-Queue entries were then cycled with the orbital period by the CYCLE program for continuous operation. Of course, during the complete scenario, the battery voltage was monitored to prevent the LVSS tripping. If the battery monitoring program did shut down the magnetic system, the Time-Queue cycle would turn it back on at the beginning of the next cycle.

By starting with a fully charged battery, the above scenario achieved spin rates up to 4 rpm, which was enough to be able to fire the OATS rocket. However, we still did not have directional control over the spin axis. If we left the spacecraft alone after achieving 3-4 rpm, it would maintain its spin stability reasonable well for about one orbit (90 minutes). After that it would begin coning, and once it started, it would go quickly into tumble. As soon as we tried to precess the spin axis with the z coil, the induced nutations would make the motion become unstable.

We tried alternately precessing and damping, but we rapidly ran out of power*. There was no way to get directional control, and

* and also spin. The damping program continuously robs the spin of energy.

without it the orbit adjustment looked very bleak. The solution to this problem required ingenuity, hard work, and nerves of steel.

3. Firing the OATS Rocket

The basis for the time and inertial direction of the OATS firings is a solution to an optimization problem to minimize fuel for the required orbit change. Our normal procedure is to solve for the true anomaly and the direction of thrust from the current orbit and desired orbit parameters. This gives us three degrees of freedom to solve for each firing, and thereby optimally correct the semi-major axis, the eccentricity, and the inclination. Without directional control we could not hope to use this scheme.

After some thought, however, we came up with a "far-out" idea that we suspected might work. Each time we ran the spin-up scenario we came up with a distinctly different inertial attitude, and although we could not change it, the spin axis direction remained gyroscopically stabilized for about one orbit. We could make use of this fact in the following way.

Instead of solving for a time and direction of thrust from the orbit parameters, we could accept the direction we had, and solve for the optimum time to fire, given that attitude and the orbit. We could then obtain a measure of how effective the thrust would be by comparing the resulting orbit changes to those we would have achieved if we could have chosen the direction. If this measure was reasonably high, we would fire the rocket. Otherwise we would de-tumble the spacecraft and try again. With the spacecraft coming up in a random attitude each time we spun it up, a certain percentage of the time we would get lucky and obtain a favorable attitude.

Several problems needed to be solved before the above scheme could be implemented. First of all, the calculations for the optimum firing point had to be done in real time during a single pass because the spacecraft would not spin stably longer than about one orbit.

Thus, we needed to begin an automatic spinup scenario four or five hours before our pass, such that the spacecraft rose spin-stabilized at 3 - 4 rpm. Then in real time during the pass we would:

1. Determine the inertial attitude of the spin axis.
2. Calculate from this and the current orbit the optimum time to fire in the next 90 minutes.
3. Make the decision whether the thrust would be effective enough.
4. Inject the appropriate Time-Queue and Delayed Command data into the spacecraft to control the firing at the specified time.

We had about 8 - 10 minutes during the pass to accomplish the above operation.

Luckily the first requirement was already satisfied by an existing capability. The TIP attitude determination software had been designed so that it could be run in real time during the satellite passes. We begin by describing this system.

The attitude calculation (and the orbit calculation as well) is too complex to be handled by the PDP-11 ground station computer. This computer has its hands full during the pass handling the satellite data link. The attitude calculation is done on the large IBM-370 computer which is connected by telephone data link to the PDP-11. The TM data for the attitude is fed in real time to the IBM-370, where the calculation is done interactively in a "time-shared" operation (TSO) session. The system is shown schematically in Figure 5, and you will note that we had the capability to operate through a station in Hawaii as well as the APL ground station. In this set up, the PDP-11 acts as a TSO terminal for the 370 computer, controlling a second TSO session which receives the raw TM data and passes it through a shared disc file to the attitude/orbit TSO session.

To use the system for our scheme, we had to add to the 370 attitude software the extra program to handle the orbit calculation described as item 2 above. The required equations are developed and discussed in Appendix A. This turned out to be a non-trivial program.

The software was run interactively and the information about the firing was displayed on a CRT graphics terminal in real time. A sample of the output display is shown in Figure 6.

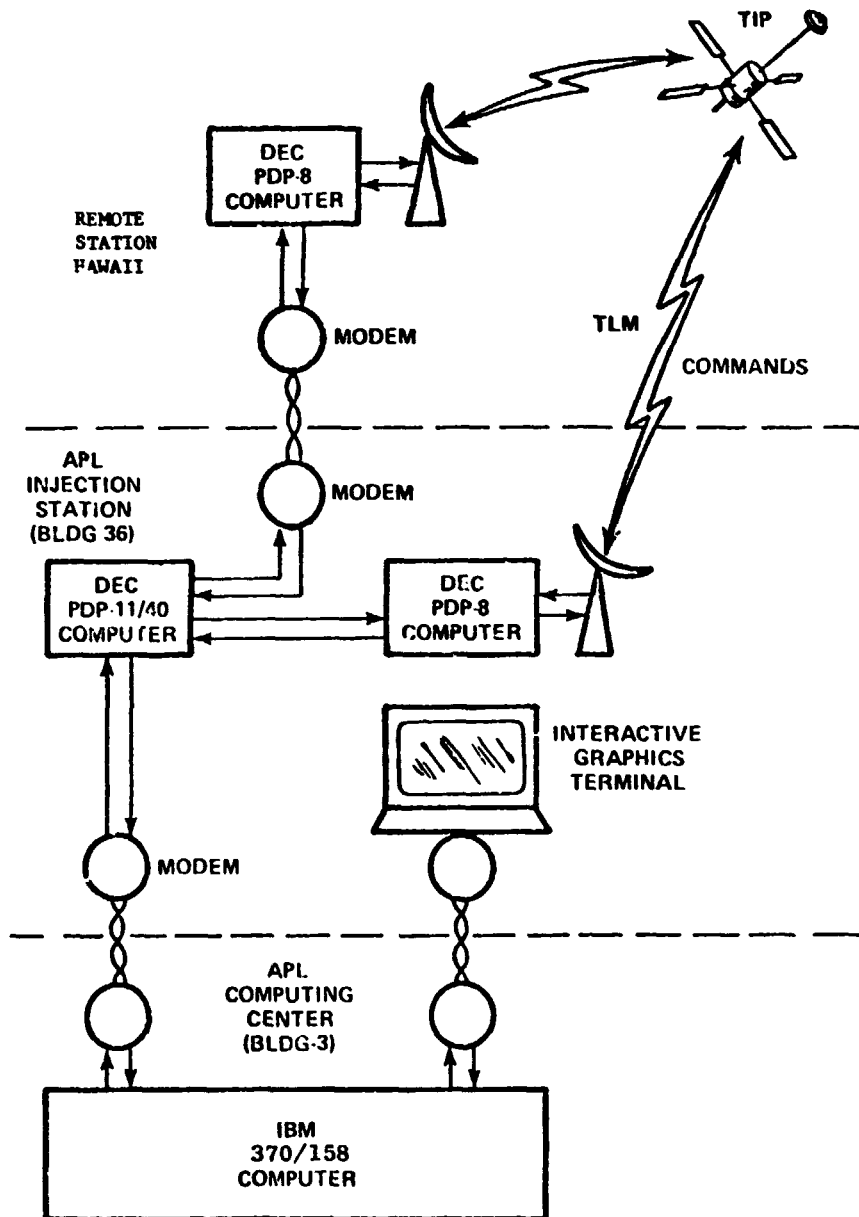


Figure 5. Real-Time Computing System Used for OATS Firings

OATS FIRING INFORMATION

THE BURN FIGURE OF MERIT • 1.853244E+00
S-T-U DIRECTION AT FIRE • 0.8039 0.5790 -0.1360

CHANGE TO SEMI-MAJOR AXIS • 13.50 (NM)
CHANGE TO ECCENTRICITY • 3.845E-03
CHANGE TO INCLINATION • -0.023 (DEG)
ARG. OF LATITUDE AT FIRE • 342.8 (DEG)

UT TIME OF FIRING • 50940 (SEC)
TIME OF FIRING • 76.00 (MINUTES AFTER SET)

CLOCK SETTING IN HEX TOCS - 236A,5F9B

HIT CARRIAGE RETURN TO RETURN

:

Figure 6. Real-Time CRT Display for OATS Firing

From the program display, the decision was made whether to fire or not. We generally had 3 - 4 minutes to run the program and make this decision. The decision was based on many factors, not the least of which was whether we believed the answers we were getting from the software.

At times the decision was difficult. For example, in the case where the optimum firing time was nearly one full orbit after set, this meant we had just passed the optimum point. The question then became: should we wait for nearly 1-1/2 hours to get to the optimum point and risk the inevitable nutation build-up? Or, should we fire immediately during the pass while we had good stability and accept somewhat less than optimum geometry? This type decision had to be based on a multitude of factors such as the current spin rate and nutation angle, how far past the optimum point we were, and how good the thrust would be if we waited.

There was one final problem to be solved before the entire scheme could be made to work. This involved item 4 above - transmitting the firing data back to the satellite computer in real time. As mentioned in Section 2, the Time-Queue and Delayed Command data are prepared and formatted for transmission by the PDP-11 program called TIPLOAD. The problem was that TIPLOAD was not designed to be run in real time during a pass. It was a pre-pass utility. And even if it could be run in real-time, the PDP-11 was completely taken up during the pass by the TIPCOM program handling the real-time data links. The TIPLOAD function is a formidable task and there seemed to be no way to get in the Time-Queue data to control the firing.

The answer turned out to be beautifully simple. We made all of the times in the calculation and in the Time-Queue be relative to the satellite set time for the pass. Then we simply controlled the firing time by setting the satellite clock to a dummy value to make the rocket fire at the correct amount of time after set. The clock was already designed to be easily set in real time by simple keyboard type-in. The Time-Queue and Delayed Command data for firing could be formatted as a fixed set of times, and prepared for injection once and for all in a single TIPLOAD run.

The actual OATS firing passes were quite complicated. A successful operation required that all of the computers involved as well as the telephone data links be operable for the pass. We had many operations scrubbed because of computers going down, or because of simple human error caused by the time pressures. A synopsis of the entire operation is as follows:

1. On the day prior to the pass, transmit a spin-up scenario into the flight computer, scheduled to begin five hours before the pass.
2. Just before the pass, bring up all computers, establish the telephone data links in full duplex, and initialize the TSO sessions on the IBM-370.

3. As soon as the satellite rose, send commands to begin transmitting TM attitude data. At this point we had less than 10 minutes to complete the operation.
4. Record attitude data on the IBM-370 for about three minutes and then begin the attitude and orbit computations.
5. While the orbit computation is being carried out, inject the "relative-time" delayed command and Time-Queue data into the flight computer.
6. Make the decisions about the firing.
7. Either fire immediately, set the satellite clock to the correct dummy value, or abort.
8. On the next pass, set up the computer to begin a two-day de-tumble operation using the DAMP program.

The scheme worked well, although it was a trying experience. (On one harrowing pass we actually fired the rocket backwards, but all other firings were successful.) We were able to average about two four-minute firings a week for a month or so, using up nearly half the fuel. But then, things began to go badly. We had always felt that a half-empty fuel tank would cause worse stability problems than a full one simply because there would be more sloshing around of the hydrazine. Sure enough, this began to happen, and worse yet the spacecraft began to come up spinning, consistently oriented normal to the orbit plane. We attributed this to spin-orbit coupling which got worse with the increased damping of a half empty tank. Since we were most interested in raising the altitude, this geometry was totally unfavorable. After trying without success for several weeks, we realized that a new idea was needed. The idea was not long in coming, and once again the on-board computer saved the day.

4. The Tumble-Thrust Program

The new idea for firing the OATS rocket was a radical departure from our previous method - we completely abandoned the idea of trying to maintain any attitude control during the firing. Instead we decided to let the spacecraft tumble, since that is what it wanted to do, and fire the rocket in short bursts when it happened to be pointing in the best direction.

Thus, we could let the flight computer continuously determine the spacecraft attitude and then quickly fire the rocket by delayed command at the correct times. Attitude determination programs are non-trivial, and this would have been an extremely difficult program to write had it not been for some simplifying circumstances in our case.

At that point in time we were getting close to the orbit we wanted; we needed only to raise the perigee altitude some more. Thus we were willing to do all our firings in the along-track direction in the vicinity of apogee (within 30° or so in true anomaly). This would raise the orbit without increasing the eccentricity and without affecting the inclination. It turns out for a near polar orbit that there is a simple relationship between the magnetic field in the equatorial regions and the along-track direction. This geometry is illustrated in Fig. 7.

It can be seen from Fig. 7 that the field lines are roughly parallel to the flight path in the regions near the equator, so that when the spacecraft is aligned with the field it is aligned with the velocity vector. Hence the approximate determination of along-track orientation in these regions becomes trivial using the sampled magnetometers.

We had observed during our prior operations that, when tumbling, the spacecraft angular momentum vector tended to align itself normal to the orbit plane. Apparently there was a strong spin-orbit coupling caused by the perturbing torques. In this case the tumble motion is in the orbit plane, and it continuously carries the longitudinal axis through the spacecraft velocity vector giving ample along-track firing opportunities.

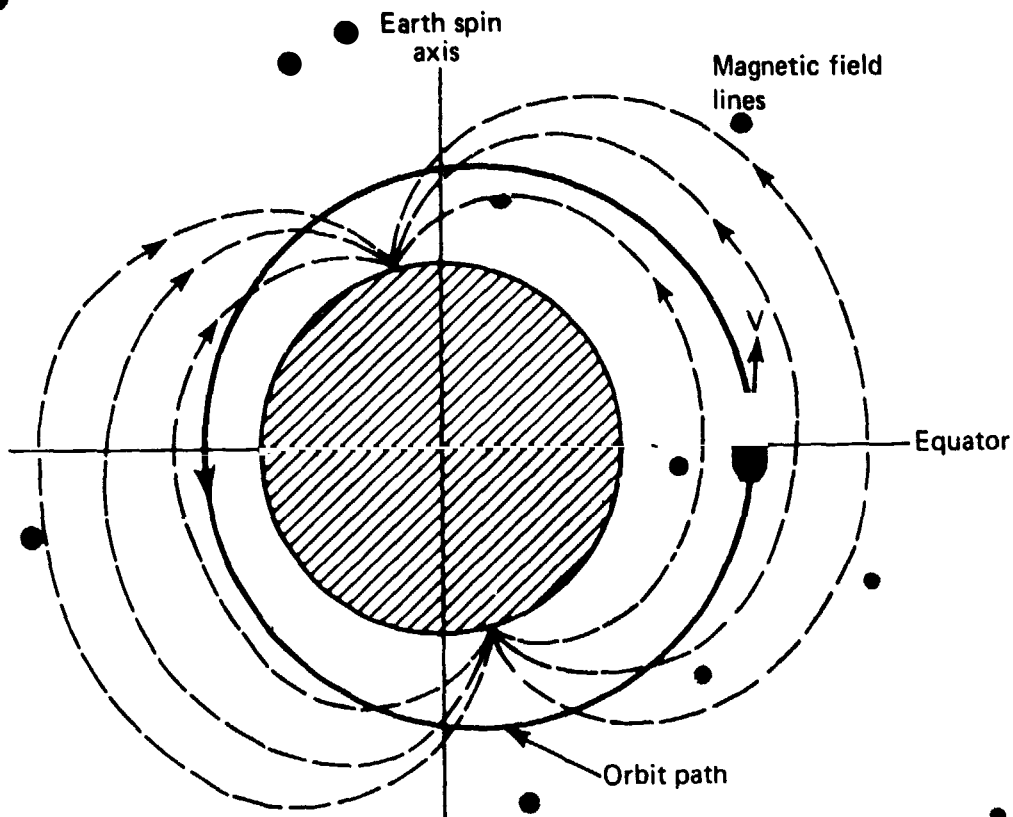


Figure 7. TIP Orbit Geometry for Tumble-Thrust Program

To control the firings, we developed a program called THRUST which was another special version of the TM monitoring program. This program continuously monitored all three magnetometer channels, and determined when the spacecraft was aligned with along-track by the following test:

$$|M_x| < C_1 \text{ and } |M_y| < C_2 \text{ and } KM_z < 0,$$

where M_x , M_y , and M_z are the orthogonal body-fixed magnetic field readings, C_1 and C_2 are inputtable thresholds, and $K = +1$ for a north-going geometry or -1 for a south-going geometry. The test on M_z is to establish that the thrust direction will be parallel to the velocity vector, rather than anti-parallel. When the tests were satisfied the program would immediately issue delayed commands to fire the rocket for two

seconds and then rearm for another firing. The CYCLE program was used to activate the THRUST logic periodically for about 10 minutes near each equator crossing closest to apogee.

The program worked best at a low tumble rate because of the TM sampling rate and the 2.3 second time required to issue the firing command. For example, if the tumble rate were 1 rpm, the thrust axis would move about 14° in the time needed to issue the command and another 12° during the 2 second burn. This would amount to an effective 20° pointing error for the thrust. Also, at 1 rpm the spacecraft would move about 26° between TM samples at the 4.3 second frame rate. Thus we had to open the thresholds C_1 and C_2 to a reasonably high value (about 20% of full scale) to insure an angular window large enough to avoid missing opportunities due to the TM sampling rate.

We needed only approximate along-track orientation ($\pm 45^\circ$) on each firing to do the job, relying on the off-track components to cancel from firing to firing. The TM sampling times tended to fall randomly in the angular window established by C_1 and C_2 , and this helped average the off-track components. However the command time lag caused biases. These were not too serious since the off-track components tended to be radial thrusts which only affected the eccentricity a bit.

Because of the above considerations, about one rpm was the practical limit in tumble rate for the program to work effectively. We started the spacecraft tumbling very slowly, and found that the firings themselves caused the tumble rate to continuously increase, due to the small displacement of the thruster axis with the spacecraft center of mass. The rate increased about 1 rpm for each minute of firing. This meant that the scenario had to periodically switch to the DAMP program to de-tumble and prevent the tumble rate from building up.

Once the scenario was worked out, the process worked well. We simply sat back while the flight computer continuously pushed the altitude up for a week or so (The people determining the orbit were quite startled when the period began creeping up orbit by orbit. Their

software could not handle that case. From an initial parking orbit of about 180 n.mi. perigee altitude by 380 n.mi. apogee altitude, we finally achieved an orbit of about 320 n.mi. by 450 n.mi.

At that point, it was important to vent the remaining hydrazine so that the spacecraft could be put into the gravity gradient mode. The next spacecraft, TIP-III, was scheduled for launch, and we wanted to continue the engineering checkout so that other potential problems would be uncovered before it was launched. The venting system was designed to release the hydrazine to the side with the spacecraft spinning about the z axis. Since the spacecraft was unstable in spin, a large tumble motion resulted from the venting operation.

The tumble motion was much faster than we had hoped for. The solar panels were wrrenched free by the centrifugal force and the spacecraft ended up tumbling at 45 rpm. This was being dissipated at the rate of about .2 rpm per day because of the spacecraft magnetic hysteresis. The gravity gradient boom could not be erected until the spacecraft was stationary, and we needed to do this in less than three months to properly lead the TIP-III launch. We were in an obvious time bind, and needed to use the z coil to help dissipate the tumble motion. The program developed for this turned out to be the most complicated of all the special post-launch programs.

5. A Digital Phase-Locked Loop for De-Tumble

The DAMP program, which switches the z-coil to produce a de-tumble torque, begins to lose effectiveness over about 1.5 rpm. At 2 rpm it does not work very well, and at 45 rpm it is useless. Some simple arithmetic shows the problem. It takes two TM frames to sense the derivative in the z magnetometer, and then another 2.3 seconds to send the command to switch polarity. The resulting average time delay

is 6.6 seconds and at 2 rpm this amounts to 79° in the phase of the tumble motion. At 45 rpm, the period of the motion is 0.7 seconds so that even continuous commanding cannot switch the z-coil polarity once per cycle.

A program was needed that could determine the phase of the tumble motion well enough to anticipate the peaks and troughs in the z magnetometer reading. Then the command strings could be started with precisely the lead time needed to have the commands take at the right instant. For motions faster than 25 rpm where the period is less than the 3.4 second command time, the polarity could be switched in phase with the motion every-other cycle. Switching every other cycle makes the damping only 50% as effective, but it was still a big improvement over the magnetic hysteresis.

We decided to implement a digital phase-locked loop in the flight computer to lock on to the phase of the tumble motion and control the z-coil switching. There were some non-trivial problems to overcome in this implementation. First of all, we were performing the computations on a computer that had no floating point arithmetic capability (either hardware or software) and also had no hardware divide capability. As a consequence we had no programs for generating the trigonometric functions needed to construct (digitally) the local oscillator signal inside the computer. To work around this difficulty we struck upon the idea of locking a "saw-tooth" function onto the magnetometer signal, rather than a sine wave. The unit amplitude saw-tooth shown below can be generated from simple fixed point operations.

* The average delay is based on one frame since the first frame is equally likely to occur just before or just after the derivative changes sign.

** The VIF computer, in keeping with its primary functions, was oriented toward logic and bit string manipulations rather than arithmetic operations.

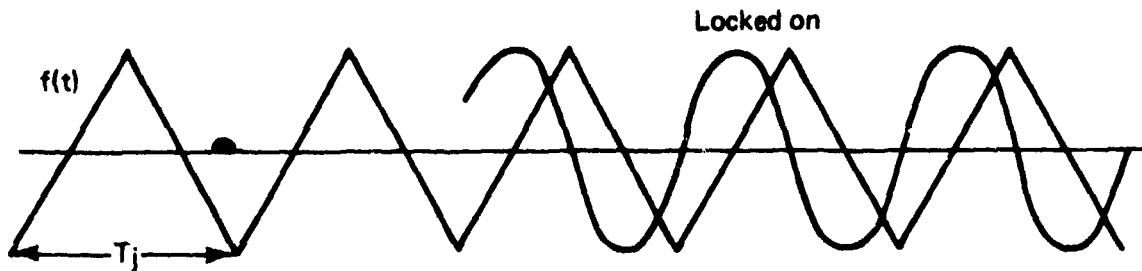


Figure 8. Saw Tooth Function for Phase-Locked Loop

At any time t the saw-tooth value, $f(t)$ is given by

$$f(t) = 4\omega_j(t - T_t) \quad \text{when } \omega_j(t - T_t) < .5$$

$$f(t) = 3 - 4\omega_j(t - T_t), \quad \text{when } \omega_j(t - T_t) \geq .5$$

where

$$\omega_j = \text{current saw-tooth frequency} = 1/T_j$$

$$T_t = \text{time of last saw-tooth trough.}$$

After estimating the amount of work involved in developing a software floating point package, we decided that the phase-locked loop could be written in fixed point arithmetic using the saw-tooth function. The calculations had to be properly scaled, and double and triple word precision was used in some places where needed.

The calculations were designed to avoid division wherever possible. In two places it was unavoidable, so we wrote a software division algorithm using an iteration method for the inverse. This consists of iterating the following equation:

$$Y_{j+1} = Y_j (2 - XY_j) \quad , \quad \text{from } Y_0 = 1$$

where X is the number we wish to obtain the inverse of, and Y is the estimated inverse. The method converges for all positive $X < 2$, and we ensured convergence by proper scaling.

The error signal for the phase-locked loop was the product of the sampled signal (the z magnetometer reading) and the sampled VCO output (the internally generated saw-tooth function). The filtered error signal then drove the saw tooth in phase, frequency, and frequency drift.

The main problem to be overcome was the aliasing problem caused by the low sampling rate of the TM system. Our sampling frequency was .236 hz and we were trying to stay locked to a signal (the z magnetometer reading) whose frequency was in the range 0 to .75 hz. As the tumble rate decreased, the signal frequency passed through the multiples of the sampling frequency causing singularities where the error signal was driven to a constant value. We avoided this problem by making the loop of second order with variable gain, and using the frequency drift to "flywheel" through the singular points. As the frequency approached a multiple or half multiple of .236 hz, the gains were reduced to zero so that the saw tooth was running open loop. As the frequency passed through the singular point, the gains were gradually reestablished to their closed loop values.

We were aided in the implementation by knowing rather accurately the frequency drift when the z magnet was both off and on. These were determined experimentally early in the game using the DAMP program at low tumble rates. It can be shown from simple mechanics that the effect of the z -coil on the tumble frequency is independent of the frequency. We had determined the effect to be .09 rpm per 10 minutes of z -coil operation near the earth's equator. Thus we could switch to the appropriate drift value as the z -coil was activated or turned off, and thereby avoid introducing large transients into the loop. This meant we could duty-cycle the z -coil as necessary and still maintain phase lock.

We could also determine to within about .1 rpm the frequency of the tumble motion by independent analogue means. Since the tumble

motion rotated the spacecraft antenna, the ground receiver AGC voltages could be monitored to determine the tumble rate. This method was used to give the program starting values for the frequency when needed.

We provided an AGC feature to compensate for the varying amplitude of the z magnetometer signal caused by the change in the earth field strength with orbital motion. The field amplitude changes by a factor of 3 within one orbital revolution. This control was accomplished by filtering the absolute value of the signal and using it to normalize the magnetometer readings to unit amplitude before generating the error signal. The readings also had to be corrected for the effects of the z-coil dipole.

The details of the loop are shown in Appendix B. We determined the appropriate gains and filter time constants by making a computer simulation of the complete process and experimentally adjusting things until we could make it work through the range of frequencies from 15 rpm to 2 rpm. We found that the phase error would build up to 20° or so as the frequency passed through the aliasing points, but this was more than enough accuracy to provide effective de-tumble. The simulation showed that the loop could achieve phase lock from a 180° initial phase error with an initial frequency error of .2 rpm. The time required to lock on was about 20 minutes.

The system was implemented in the flight computer as two separate programs: (1) a special version of the TM monitoring program which processed the magnetometer readings and locked onto the phase of the motion, and (2) a program operating off the clock interrupt which used the latest phase information from the first program to control the z-coil commands. The two programs ran independently, but worked in concert, passing information back and forth through shared memory locations. The phase lock program ran continuously, and the switching program was cycled on for about 15 minutes each orbit period.

6. Generating a Tumble Motion for Centrifugal Force

After the de-tumble was complete, the gravity-gradient boom was erected on TIP-II. Because of an unforeseen problem with scissors booms, the links broke during the deployment. It was too late to change the boom on the next spacecraft; but the problem was understood, and the boom could be successfully deployed if it was kept in tension using centrifugal force. This centrifugal force could be generated by tumbling the spacecraft at the correct rate.

On TIP-III the boom was successfully deployed in this manner. The spacecraft was tumbled by using the phase-locked loop program and simply reversing the z-coil polarity commands. It was important during the tumble-up operation that the rate not get too high at any stage or the boom links could have been broken in tension. It proved easy using the existing special programs to let the flight computer automatically increase the tumble momentum bit by bit as the boom was gradually deployed over a three-week period.

V. FINAL REMARKS

As a result of the flight computer control capability, the TIP-II and TIP-III spacecraft achieved a substantial partial success. The TIP-III spacecraft was able to achieve 3-axis stability with the drag-compensation system in full operation. This allowed valuable in-orbit testing of this important sub-system. The TIP-II spacecraft was able to go operational as a navigation satellite for limited periods (when the percent sunlight was high enough). As the first spacecraft in a new series it also provided valuable training and debug capability to the operators of the Navigation Satellite System.

The experience proved to be a dramatic illustration of the power of having a programmable computer on board a spacecraft. By having enough flexibility built into the system, we had a powerful capability to modify the onboard logic after launch. We seemed to be limited only by our own ingenuity in finding ways to use the system.

APPENDIX A
FINDING AN OATS FIRING POINT GIVEN AN ATTITUDE

We define the S, T, and W directions in inertial space as follows:

S in the direction of the radius vector to the spacecraft
T normal to S in the orbit plane in the direction of motion
W normal to orbit plane along angular momentum vector.

The attitude of the spacecraft when spinning about its longitudinal axis is given in terms of the right ascension, α , and the declination, δ , of the spin vector in the direction of thrust. α is measured from the equinox and δ is measured northward from the equator. Hence, the unit vector in the thrust direction is

$$\hat{F} = \begin{pmatrix} \cos \delta \cos \alpha \\ \cos \delta \sin \alpha \\ \sin \delta \end{pmatrix} \quad (\text{A.1})$$

The STW components of \hat{F} are related to \hat{F} by

$$\begin{pmatrix} S \\ T \\ W \end{pmatrix} = R_z(\beta) R_x(i) R_z(\Omega) \hat{F} \quad (\text{A.2})$$

where $R_a(\theta)$ is a rotation of angle θ about the "a" axis

β is the argument of latitude

i is orbit inclination

Ω is orbit ascending node

We can define components A, B, and C as

$$\begin{pmatrix} A \\ B \\ C \end{pmatrix} = R_x(i) R_z(\Omega) \hat{F}, \quad (\text{A.3})$$

so that

$$\begin{pmatrix} S \\ T \\ W \end{pmatrix} = \begin{pmatrix} \cos \beta & \sin \beta & 0 \\ -\sin \beta & \cos \beta & 0 \\ 0 & 0 & 1 \end{pmatrix} \begin{pmatrix} A \\ B \\ C \end{pmatrix} \quad (\text{A.4})$$

Multiplying out the matrix equations A.1 and A.3 we get

$$A = \cos \delta \cos \alpha \cos \Omega + \cos \delta \sin \alpha \sin \Omega$$

$$B = -\cos \delta \cos \alpha \sin \Omega \cos i + \cos \delta \sin \alpha \cos \Omega \cos i + \sin \delta \sin i$$

$$C = \cos \delta \cos \alpha \sin \Omega \sin i - \cos \delta \sin \alpha \cos \Omega \sin i + \sin \delta \cos i$$

The planetary equations to zeroth order in eccentricity can be integrated assuming an impulsive thrust with direction components S, T, and W. Using Eq. A.4 the integrated equations can be written in terms of A, B, and C

$$\Delta a = \frac{2}{n} \left[-A \sin \beta + B \cos \beta \right] F \Delta t \quad (\text{A.5})$$

$$\Delta e = \frac{F \Delta t}{na} \left[A \cos \beta \sin f + B \sin \beta \sin f + 2\beta \cos \beta \cos f - 2A \sin \beta \cos f \right]$$

$$\Delta i = \frac{F \Delta t}{na} \cos \beta \cdot C$$

where F = the magnitude of the thrust,

f = the true anomaly

These give the changes in the orbital elements, a , e , and i for a firing of duration, Δt . The thrust magnitude is known a priori from the fuel tank pressure, and the thrust duration is selected to be of significant length but not too long that the impulsive nature of the thrust is destroyed. Generally this is 4-8 minutes.

The optimum changes in the orbit elements (Δa_T , Δe_T , Δi_T) can be calculated as if the same duration thrust were to be made, but with freedom to choose the direction (α, δ) as well as the true anomaly. The equations for the Δa_T , Δe_T and Δi_T are not given here, but the results are such that the ratios

$$\frac{\Delta a_T}{\Delta e_T} \quad \text{and} \quad \frac{\Delta a_T}{\Delta i_T}$$

are maintained constant from firing to firing.

The program to determine the time to fire loops through the true anomaly in 1° increments completely around the orbit. At each position the changes Δa , Δe , and Δi are computed and a figure of merit constructed:

$$\text{F.M.} = \sqrt{W_1 \left(\frac{\Delta a}{\Delta a_T} - 1 \right)^2 + W_2 \left(\frac{\Delta e}{\Delta e_T} - 1 \right)^2 + W_3 \left(\frac{\Delta i}{\Delta i_T} - 1 \right)^2}$$

where the weights W_1 , W_2 , and W_3 are inputtable. If the orbit changes were all equal to the optimum changes, the F.M. would be 0. The program determines the true anomaly which minimizes the F.M., and repeats the process for a new set of input weights on operator command. Thus the results could be obtained for various cases and compared before a choice was made.

An example of the cases examined was to set $W_3 = 0$ and $W_1 = W_2 = 1$, so as to remove any constraint on changing the inclination, and just do the best we could at raising the orbit and circularizing. The idea here was that if we could get a really favorable along-track thrust today at the expense of a small inclination change in the wrong direction, we could probably make up the inclination change on the next thrust.

Once the optimum true anomaly was selected, the program then calculated from the orbit geometry the length of time after set which would center the firing on that position. This was then converted to a "dummy" setting for the satellite clock, and displayed for the spacecraft controller to use if the decision was made to fire.

APPENDIX B

DIGITAL PHASE-LOCKED LOOP FOR Z-COIL CONTROL

Each TM frame, the program receives a sample of the raw z-magnetometer, M_i , which we refer to as the i th measurement. This measurement is then processed to give an updated phase and period for the saw-tooth function to control the z-coil commands. The loop is shown schematically in Fig. B.1. The computations are given in the following steps.

1. Each measurement, correct for effect of z-coil -

$$m_i = M_i - K\Delta$$

where m_i = corrected measurement

M_i = raw measurement

Δ = z-coil dipole moment

$K = \pm 1$, depending on z-coil state

2. Normalize measurements -

$$AM_i = (1 - A) AM_{i-1} + A |m_i|$$

$$FM_i = \frac{m_i}{1.5 AM_i} = \text{normalized measurement}$$

$$A = 1/256$$

3. Compute saw-tooth value based on last known trough time and frequency -

$$r_i = \left[(t_i - T_t)\omega \right]_{\text{modulo } 1} \quad (\text{fractional part})$$

$$\begin{cases} f_i = 4r_i - 1, & \text{if } r_i < .5 \\ f_i = 3 - 4r_i, & \text{if } r_i \geq .5 \end{cases}$$

where r_i = fractional part of a cycle since last trough

t_i = time of present measurement

T_t = time of last trough

ω = current saw-tooth frequency

f_i = value of saw-tooth function

4. Compute and filter error signal recursively -

$$P_i = FM_i \times f_i \quad (\text{current product})$$

$$R_i = BP_i - CP_{i-1} + DR_{i-1} \quad (\text{Error signal})$$

$$B = 3/256$$

$$C = 1/128$$

$$D = 31/32$$

5. Check for aliasing points and reduce error signal if necessary -

$$\text{If } |\omega - \omega_a| < \delta, \quad R_i = R_i \left(\frac{\omega - \omega_a}{\delta} \right)^2$$

$$\delta = .1 \text{ rpm}$$

6. Apply controls to saw-tooth -

$$\dot{\omega} = \dot{\omega} - K_2 R_i \quad (\text{drift})$$

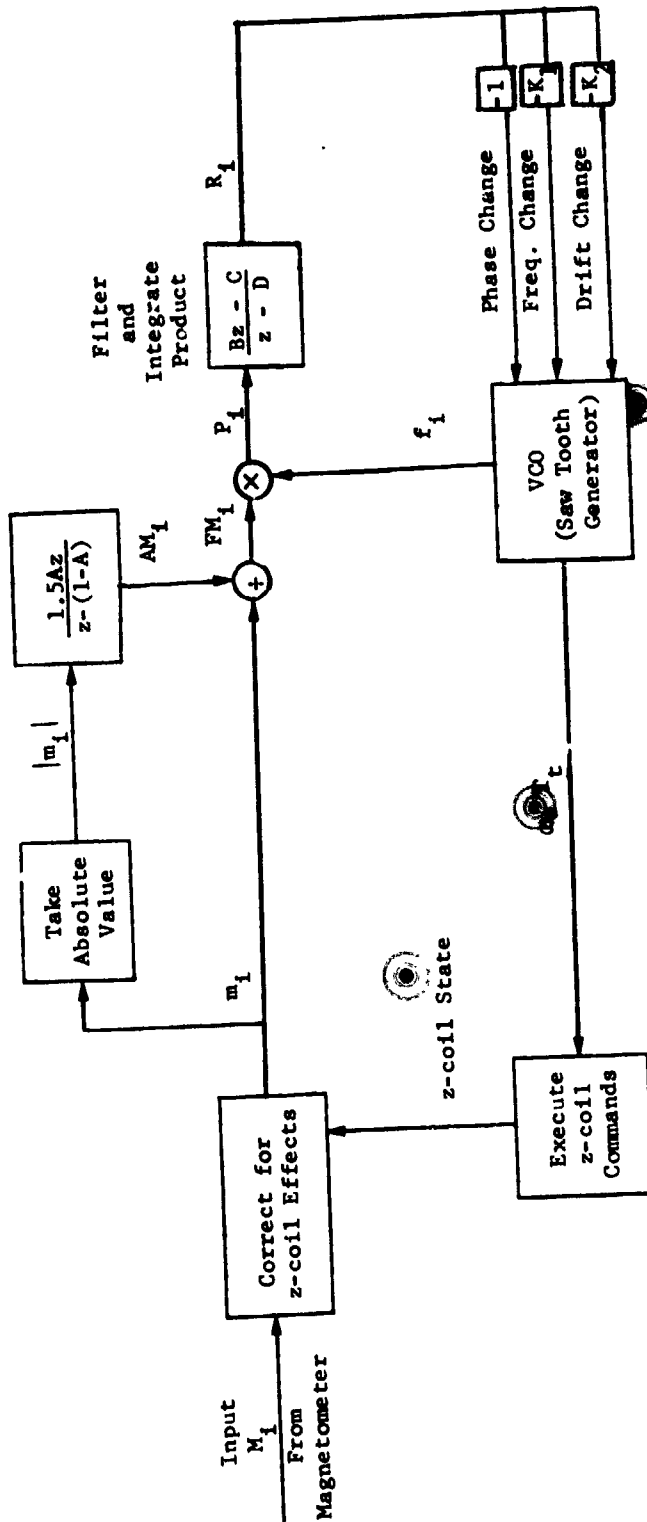
$$\omega = \omega + \dot{\omega} \Delta t - K_1 R_i \quad (\text{frequency})$$

$$T_t = t_i - \frac{(r_i - R_i)}{\omega} \quad (\text{time of last trough})$$

where r_i is the fractional part of a cycle calculated in Step 3.

Commands to control the z-coil are then issued based on T_t and $1/\omega$. The value of $\dot{\omega}$ is changed to the appropriate theoretical value if the z-coil is turned off or on. This results in a small ramp type transient.

Gain Control to Correct
for Amplitude Variations



Loop Parameters:

- A = 1/256
- B = 3/256
- C = 1/128
- D = 31/32
- $K_1 = 2^{-10}$ hz
- $K_2 = 2^{-20}$ hz/sec

Figure B.1 Digital Phase-Locked Loop for z-coil Switching

References

1. Perschy, J. and Elder, B. M., "TRIAD Computer," JHU/APL Report TG-1212, August 1973.
2. Utterback, H. K., "A Guide to the TIP Computer," JHU/APL Report TG-1263, September 1974.
3. Marvin, C., "NNSS Software System: An Introduction to TIP II Digital Operations," JHU/APL Report SDO 4318, January 1976.
4. Whisnant, J. M. and Jenkins, R. E., "NNSS Software System: Post-Launch and Operational Flight Computer Programs," JHU/APL Report SDO 4268, Volumes I and II, 1977.
5. Utterback, H. K., Whisnant, J. M. and Jenkins, R. E., "A System of Software for the TIP Spacecraft Computer," to be presented at the British Interplanetary Society Symposium on Computer Techniques for Satellite Control and Data Processing, Slough, England, October 11-12, 1977.

ACKNOWLEDGEMENT

The writers thank Mr. Cloyd Marvin of APL for his help in developing the phase-locked loop and in its simulation.

0117

**KALMAN FILTER MODELS FOR SATELLITE
ON-BOARD NAVIGATION USING GLOBAL
POSITIONING SYSTEM DATA**

L. Miller

Naval Surface Weapons Center

ABSTRACT

A Kalman filter is presented which processes pseudo-range and delta-pseudo-range data from the NAVSTAR Global Positioning System for the onboard navigation of a host satellite. The formulation and structure of program components is described, and sample results are given.

D7
N79-14128

ORBIT DETERMINATION ACCURACIES
USING SATELLITE-TO-SATELLITE TRACKING

F. O. Vonbun, P. D. Argentiero, P. E. Schmid

Goddard Space Flight Center

1.0 INTRODUCTION

The possibility of using geostationary satellites for communications was discussed in the popular literature as early as 1956 (1). The first detailed proposal for a synchronous tracking satellite system for the purposes of orbit determination was provided by Vonbun in 1967 (2, 3). Since then a number of papers (4, 5, 6, 7, 8, 9,) have considered the use of satellite-to-satellite tracking for orbit determination and for gravity field model refinement. These papers mention that with regard to coverage, a satellite-to-satellite tracking system has a significant advantage over ground based tracking systems. For instance, with a single synchronous relay satellite, a satellite-to-satellite tracking system is capable of observing an earth orbiting satellite during almost half of every orbit. Equivalent coverage of a satellite in a high inclination orbit would be difficult to obtain with a ground based system.

In 1968 during the early planning phases of the geostationary ATS-6 and near-Earth NIMBUS-5 experiments it became clear that this satellite configuration would be ideally suited to evaluate the concept of satellite-to-satellite tracking and to provide valuable experience in processing this new data type. The experiment as defined in October 1968 (10) incorporated both radio time delay (range) and Doppler frequency shift (range rate) measurements. This experiment, entitled the "Tracking and Data Relay Experiment" (T&DRE) was conducted as planned except that NIMBUS-6, which was launched June 12, 1975, rather than NIMBUS-5 carried the T&DRE equipment. In early 1972 plans were completed for a very similar ATS-6/GEOS-3 satellite-to-satellite tracking experiment. The GEOS-3 satellite was launched on April 9, 1975. Another satellite-to-satellite tracking effort involving the ATS-6 was the Goddard Apollo-Soyuz Geodynamics Experiment (11) performed

during 1975. However the accent of this experiment was gravity anomaly detection rather than orbit determination. The ATS-6, which was the relay satellite for these experiments, was launched on May 30, 1974 and is still in operation.

The results of these experiments are relevant because NASA intends to use the Tracking and Data Relay Satellite system (TDRSS) (12) for operational orbit determination of NASA satellites. The system will consist of two synchronous relay satellites (one at 41 degrees west and one at 171 degrees west) and a common ground station under construction at White Sands, New Mexico. Operations will begin in November 1980. Hence by the early nineteen eighties satellite-to-satellite tracking data will be routinely processed to obtain orbits.

This paper is a report on the results of the ATS-6/GEOS-3 and the ATS-6/NIMBUS-6 satellite-to-satellite tracking orbit determination experiments. The tracking systems used in these experiments differ from the TDRSS, primarily in the use of one rather than two synchronous relay satellites. However the authors believe and simulations mentioned in this paper indicate that the insights gained from the experiments with regard to proper data reduction techniques and expected results are applicable to the TDRSS.

1.1 EXPERIMENT SPACECRAFT

The key to all satellite-to-satellite experiments to date has been the geostationary ATS-6 spacecraft (13, 14). During the past three years the equatorial ATS-6 has been stationed over both the Pacific in proximity of continental U.S.A. and Africa. Accordingly, ATS-6 ground stations have at various times been operated at Rosman, North Carolina; Mojave, California and Madrid, Spain. The near-Earth satellites tracked via ATS-6 have been GEOS-3 (15), Apollo-Soyuz (16), and NIMBUS-6 (17).

The nominal GEOS-3 orbital parameters are a mean altitude of 843 km, an inclination of 115° , an eccentricity of 0.004, and a period of 101.6 min. The orbital parameters

were chosen to minimize resonance of the subsatellite trace with any given Earth feature and to provide orbit traces which cover the Earth in a gridwork pattern.

The Apollo-Soyuz mission included the Geodynamics experiment where Apollo was tracked via ATS-6 for the mission duration (19 July to 24 July 1975). The nominal Apollo orbit at insertion was 150 km by 170 km at an inclination of 51.8° .

Finally, the NIMBUS-6 weather satellite is in a Sun synchronous polar orbit with a mean altitude of 1110 km, an inclination of 100° , and a period of 107.4 min.

2.0 SATELLITE-TO-SATELLITE TRACKING

Satellite radio or laser tracking system makes measurements of such parameters as range, range rate, angles and direction cosines to a spacecraft relative to a given tracking station. In two-way tracking a signal is transmitted from a well surveyed ground station to a spacecraft transponder which frequency translates the signal for re-transmission directly back to the ground station or, as in the case of satellite-to-satellite tracking, to another spacecraft. The two-way tracking system developed for the experiments discussed in this paper measures "range" in terms of the round-trip time delay on a 100 kHz tone and range rate in terms of the Doppler shift on a 2 GHz carrier signal (14, 18).

2.1 GEOMETRY

The tracking geometry is shown in figure 1. The ground station transmits a signal to the near Earth satellite via the synchronous spacecraft. This same signal is "turned around" and transmitted (at a slightly offset frequency) back to the ground site again via the high altitude satellite. For purposes of stability NASA geostationary orbits have been maintained at inclinations which extend from 1.5° to 6° . As a consequence the path indicated as R_1 (figure 1) varies as a function of time as does R_2 (13). Because of the radio propagation times involved and the fact that both spacecraft are in motion relative to the ground site, four distinct paths must be considered when interpreting the Doppler (range-rate) and time delay range/measurements (13, 19).

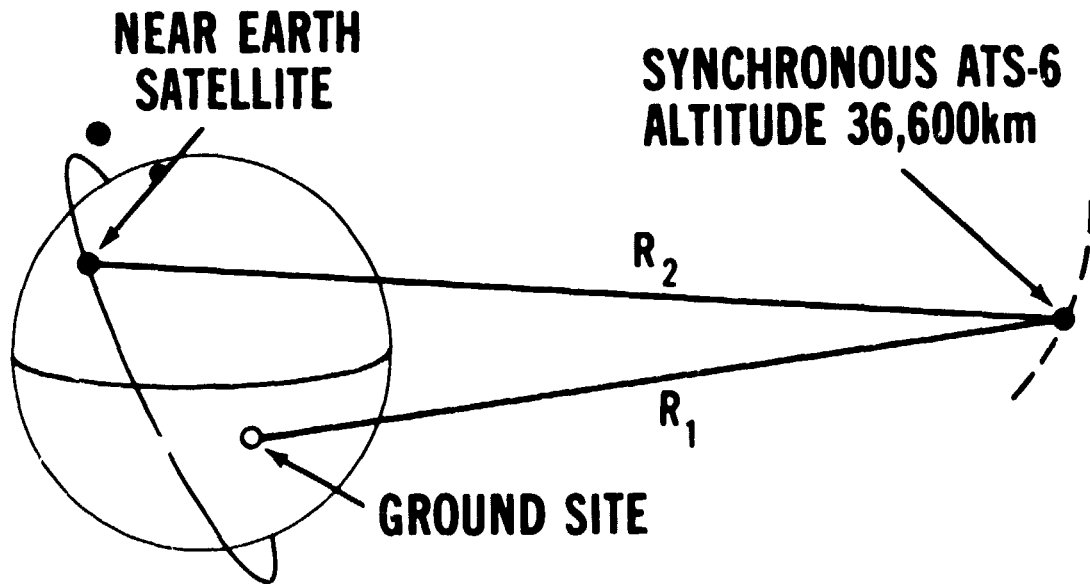


Figure 1. Basic Tracking Geometry

2.2 SYSTEM DESCRIPTION

The "range" measurement is performed by comparing transmitted and received tone zero crossings, the highest resolution tone frequency in this case being 100 KHz. Lower frequency tones are sequentially used during acquisition for ambiguity resolution. The lower tones are at 20 KHz, 40 Hz, 80 Hz, 160 Hz, 32 Hz, and 8 Hz.

The tone ranging measurement is quite straightforward and ranging accuracy depends chiefly on the quality of preflight calibration of both the ATS and NIMBUS transponder group delay. Such preflight calibration data have been taken over a range of frequencies and temperatures. Indications are that with careful calibration the total systematic delay error in the ranging measurement can be held to a few meters of equivalent one-way range.

The "range rate" measurement is performed by counting cycles of Doppler over a measured time interval. In the case of TIROS-3 and Apollo the measurement consisted of the number of Doppler cycles accumulated in the regular sampling interval (1 or 10 seconds

depending on mode of operation). For NIMBUS-6 the measurement consisted of the time interval required to accumulate a fixed number of Doppler cycles (18). The electronics for ATS-6 satellite-to-satellite tracking have been so configured that the Doppler output is approximated by:

$$f_d \doteq \frac{-2f_t k}{c} [a_1 \bar{r}_1 + a_2(\bar{r}_1 + \bar{r}_2)]$$

where

f_d = measured average Doppler frequency

f_t = uplink frequency

c = speed of light

k , a_1 and a_2 are scalar constants determined by equipment frequency multiplications

\bar{r}_1 = average range-rate ATS to ground site

\bar{r}_2 = average range-rate ATS to NIMBUS, Apollo, or GEOS-3

A detailed discussion of Doppler factors in satellite-to-satellite tracking is given in (19).

The uplink to ATS-6 (f_t) is at a nominal 6 GHz. The link to and from the low satellite is nominally 2 GHz and ATS-6 back to ground at 4 GHz. The range and Doppler measurements will also be biased by the Earth's troposphere and ionosphere. Measurement biases up to meters in range and tens of cm/sec in range rate can be expected at 2 GHz. Atmosphere refraction effects can to a large extent be modeled out. Some of the work done in this area at NASA-GSFC is indicated in (20, 21, 22). The atmospheric range bias is frequency independent through the troposphere and inversely proportional to frequency squared through the ionosphere. The range rate bias, in addition to the foregoing, is proportional to the rate of scan through the atmosphere as well as to the magnitude of horizontal gradients.

2.3 ORBIT DETERMINATION TECHNIQUES

Problems of Orbit Determination with Satellite-to-Satellite Tracking

The unfamiliar feature of determining user satellite orbits by means of a satellite-to-satellite tracking system is the presence of the relay satellite state as an error source. The simplest procedure for estimating user satellite state in the presence of this error source is to estimate a satellite epoch state from the satellite-to-satellite tracking data with the relay satellite state constrained to a previously determined orbit and left unadjusted in the reduction process. With this approach the uncertainty in relay satellite state is manifested as an unmodeled and time varying error source which alters the estimate of user satellite state. Some subtleties are encountered in determining the effect of this error source. The time history of relay satellite state error is a function of the way in which the epoch state was computed. For example, suppose the relay satellite is independently and continuously tracked over a given period and a least squares algorithm used to estimate epoch state at the beginning of the period. If this epoch state is then propagated to the end of the period using the same dynamic model that was used to process the data, the resultant errors will be constrained by the data fitting criterion implicit in the least squares reduction algorithm. The errors so obtained will be smaller than the errors obtained if either one did not match dynamic models or if one propagated the epoch state beyond the data collection period. The same phenomenon can be understood from a statistical vantage point by observing that when the dynamic models are matched the epoch state errors become correlated with dynamic parameter errors, and that over the data arc these correlations tend to minimize the errors in the epoch state propagation.

Relay satellite state uncertainty appears to be a significant error source even when the relay satellite or satellites are continuously and independently tracked. Argentiero and Loveless (23) simulated the orbit recovery of a satellite in a 300 km, polar, circular orbit

with the Tracking Data Relay Satellite System (TDRSS) (24). The TDRSS satellites can relay range and Doppler information from a low altitude user satellite to a ground station. The simulations assumed that each synchronous satellite was continuously tracked from two ground stations and that 24 hour data spans were processed to estimate user satellite state. The same dynamic models which were employed to estimate relay satellite epoch states were also used to estimate user satellite state from the satellite-to-satellite tracking data. The effect of Geopotential and atmospheric drag errors were included in the simulation. The results showed that user satellite position could be recovered with an average total position error of 260 m. The major part of this error is caused by the error in estimates of relay satellite epoch states. When these simulations are repeated without the assumption of continuous tracking the results are considerably worse.

A standard approach to dealing with troublesome error sources in an orbit determination is to augment the list of estimated parameters in the data reduction by including these error sources. This approach can certainly be implemented with regard to relay satellite state errors by simultaneously estimating user and relay satellite epoch states from information supplied by the satellite-to-satellite tracking data. From one vantage point this is an undesirable solution in that the user is uninterested in the state of the relay satellite and would rather not burden the numerical procedures with the need for simultaneously estimating relay satellite state with the user satellite state. However, the results of independent covariance analyses performed by Fang and Gibbs (25), and Argentiero and Garza-Robles (26) indicate that an unconstrained simultaneous estimate of user and relay satellite states using satellite-to-satellite tracking data can yield an estimate of user satellite state which is consistently better than 100 m.

Numerous simultaneous unconstrained solutions have been attempted using range sum and range sum rate measurements obtained from the ATS-6/GEOS-3 combination and the ATS-6/NIMBUS-6 combination and in all cases the solutions have been inaccurate and numerically unstable. Clearly our experience with real reductions of satellite-to-satellite tracking data is not compatible with the results of previous error studies. In order to understand the discrepancy we have performed a numerical simulation of the ATS-6/GEOS-3 satellite-to-satellite tracking experiment. The difference between a numerical simulation and a covariance analysis can be described as follows: in a simulation, data are generated and a least squares adjustment process is actually performed. The estimated state is then compared to the reference or unperturbed state at various points along the orbit and conclusions can be drawn concerning the accuracy of the process. In a covariance analysis mode, the least squares adjustment process is postulated rather than actually performed, and under the assumption that over the range of expected errors, perturbations of orbital estimates are approximately linear functions of perturbations of the error sources, the associated covariance matrix of the epoch state recovery is computed. With the aid of state transition matrices the covariance matrix at epoch can be propagated to obtain the covariance matrix of the satellite state recovery at any point in the orbit.

For the numerical simulation a computer program was used to generate 12 hours of range and Doppler satellite-to-satellite tracking data from the ATS-6/GEOS-3 satellite combination. In this data generation the Naval Weapons Laboratory (NWL) geopotential field was used. A random number generator added white noise of standard deviation 1 mm/sec to the Doppler data and white noise of 2 m to the ranging data, values consistent with tracking system performance. The SAO 69 geopotential field and an orbit determination program were used to reduce the data to simultaneously estimate the ATS-6 and GEOS-3 epoch states. The estimated GEOS-3 epoch state was propagated along the entire 12 hour data

collection period using the SAO 69 geopotential field. This orbit was compared at selected time points to the true GEOS-3 orbit which was obtained by propagating the GEOS-3 reference epoch state with the NWL geopotential field. The average difference between the two orbits was over 900 m. Also the nominal covariance matrix of the data reduction revealed that several correlations between estimated parameters were of absolute value near unity. This implies that the normal matrix which is inverted in the least squares estimation process is poorly conditioned. Hence small perturbations of the elements of this matrix such as those caused by computer roundoff and other effects cause major perturbations of the elements in the inverted matrix. This amplification effect in the inversion of a poorly conditioned matrix can lead to an inaccurate estimate of a satellite epoch state or in some cases a divergence of the least squares iteration procedure. This is the probable cause of poor results using a simultaneous estimation approach in both the simulated and real data reductions. In a covariance analysis of the simultaneous estimation approach the least squares algorithm is not actually executed and consequently these numerical problems are never manifested. For this reason the techniques of covariance analysis provide a somewhat optimistic assessment of orbital accuracies obtainable from simultaneous estimation with satellite-to-satellite tracking data.

Thus the two conclusions of our analyses are: 1) The uncertainty in relay satellite state is a significant error source which cannot be ignored in the reduction of satellite-to-satellite tracking data and 2) that based on both simulations and real data reductions it is numerically impractical to use simultaneous unconstrained solutions to determine both relay satellite and user satellite epoch states. The estimation technique used to generate the results shown in subsequent sections may be described as a Bayesian or least squares with a-priori procedure. This approach permits the adjustment of relay satellite epoch state in the reduction of satellite-to-satellite tracking data but without the numerical difficulties

introduced by an ill-conditioned normal matrix. Theoretically this technique obtains the best possible estimate of user satellite state based on all available information. A mathematical description follows.

Mathematical Description

In this mathematical development we assume the existence of two separate data sets:

y_1 – Ranging observations between ATS-6 and ground based tracking stations

y_2 – Satellite-to-satellite tracking of user satellite (range sum and range rate sum) with ATS-6 as relay satellite.

The parameter set to be estimated consists of two satellite epoch states.

x_1 Six dimensional ATS-6 state at epoch time T_1

x_2 Six dimensional user satellite state at epoch time T_2

The data set y_1 is corrupted by errors in the measuring process. Hence represent y_1 as:

$$y_1 = \tilde{y}_1 + v_1, \quad e(v_1) = \bar{0}, \quad e(v_1 v_1^T) = Q_1 \quad (1)$$

where \tilde{y}_1 is the correct or noiseless representation of the data set, v_1 is a vector of random errors of zero expectation and covariance matrix Q_1 . Describe the functional relationship between \tilde{y}_1 and x_1 as

$$\tilde{y}_1 = f(x_1) \quad (2)$$

The right side of eq. 2 represents a computational algorithm obtained by integrating satellite motion to each observation time and computing the ideal observations. The standard least squares estimator \hat{x}_1 of x_1 is that vector which minimizes the loss function.

$$L(\hat{x}_1) = (y_1 - f(\hat{x}_1))^T Q_1^{-1} (y_1 - f(\hat{x}_1)) \quad (3)$$

Assuming the linearity of eq. 2, the vector which minimizes the right side of eq. 3 is also known to be a minimum variance estimator. A first approximation to the desired minimum can be obtained by expanding equation 2 in a first order Taylor series about nominal value

$x_{1,0}$

$$\delta \tilde{y}_1 = A_1 \delta x_1, A_1 = \left. \frac{\partial f(x_1)}{\partial x_1} \right|_{x_1 = x_{1,n}} \quad (4)$$

where $\delta \tilde{y}_1$ and δx_1 are deviations of \tilde{y}_1 and x_1 from nominal values and A_1 is the so-called sensitivity matrix. The estimate of δx_1 is

$$\delta \hat{x}_1 = (A_1^T Q_1^{-1} A_1)^{-1} A_1^T Q_1^{-1} \delta y_1 \quad (5)$$

where

$$\delta y_1 = y_1 - f(x_{1,n})$$

The vector $\delta \hat{x}_1$ is added to $x_{1,n}$ to form an estimate of \hat{x}_1 . This estimate can be used as a new nominal and the process can be repeated until a convergence criterion is satisfied.

The covariance matrix of the least squares estimate \hat{x}_1 of x_1 is

$$c = e([\hat{x}_1 - x_1] [\hat{x}_1 - x_1]^T) = (A^T Q_1^{-1} A)^{-1} \quad (6)$$

The next step is to obtain an optimal processing of the data set y_2 . Define a 12 dimensional vector z as

$$z = \begin{bmatrix} x_2 \\ x_1 \end{bmatrix} \quad (7)$$

Represent the data set y_2 as

$$y_2 = \tilde{y}_2 + v_2, e(v_2) = \bar{0}, e(v_2 v_2^T) = Q_2 \quad (8)$$

where \tilde{y}_2 is the correct or noiseless representation of the data set, v_2 is a vector of random errors of zero expectation and covariance matrix Q_2 . The functional representation between \tilde{y}_2 and z is presented as

$$\tilde{y}_2 = g(z) \quad (9)$$

As was the case with equation 2, the right side of eq. 9 represents a computational algorithm involving the integration of satellite equations of motion.

The least squares estimate of z would not be optimal unless all available information were included in the loss function. Hence it is appropriate to treat the least squares or minimum variance estimate \hat{x}_1 of x_1 as an a-priori estimate weighted by the inverse of the covariance matrix provided by equation 6. The resulting loss function to be minimized is

$$L(z) = (y_2 - g(z))^T Q_2^{-1} (y_2 - g(z)) + \left(z - \begin{bmatrix} \bar{z} \\ \hat{x}_1 \end{bmatrix} \right)^T \begin{pmatrix} \bar{z} & \bar{z} \\ 0 & c^{-1} \end{pmatrix} \left(z - \begin{bmatrix} \bar{z} \\ \hat{x}_1 \end{bmatrix} \right) \quad (10)$$

Again, the required minimum can be obtained iteratively by expanding equation eq. 9 in a first order Taylor series about a nominal estimate z_n of Z

$$\delta \tilde{y}_2 = A_2 \delta z, \quad A_2 = \left. \frac{\partial g(z)}{\partial z} \right|_{z=z_n} \quad (11)$$

where $\delta \tilde{y}_2$ and δz are deviations of \tilde{y}_2 and z from nominal values and A_2 is the sensitivity matrix. The estimate of δz is

$$\delta \hat{z} = \left(A_2^T Q_2^{-1} A_2 + c^{-1} \right)^{-1} \left(A_2^T Q_2^{-1} \delta y_2 + \begin{bmatrix} \bar{z} & \bar{z} \\ 0 & c^{-1} \end{bmatrix} \begin{bmatrix} \bar{z} \\ \delta \hat{x}_1 \end{bmatrix} \right) \quad (12)$$

where

$$\delta \hat{x}_1 = \hat{x}_1 - x_{1,n}, \quad \delta y_2 = y_2 - g(z_n)$$

The vector $\delta \hat{z}$ is added to z_n to estimate \hat{z} . This estimate is used as a new nominal and the process is repeated until a convergence criterion is satisfied. The final covariance matrix for the estimate of satellite state x_1 and satellite state x_2 is

$$E \left[\left(\hat{z} - \begin{bmatrix} x_1 \\ x_2 \end{bmatrix} \right) \left(\hat{z} - \begin{bmatrix} x_1 \\ x_2 \end{bmatrix} \right)^T \right] = \left(A_2^T Q_2^{-1} A_2 + c^{-1} \right)^{-1} \quad (13)$$

It can be shown that the two step process defined above in which data set y_1 is processed and then data set y_2 is processed is equivalent to a single step unconstrained least squares estimation of x_1 and x_2 using both data sets y_1 and y_2 . Hence this procedure leads to the most accurate estimate of both user and relay satellite state based on available information.

3.0 EXPERIMENTAL RESULTS

The experimental results can be considered in three categories — namely,

- tracking system performance
- geostationary satellite orbit evaluation
- near Earth satellite orbit evaluation

3.1 TRACKING SYSTEM PERFORMANCE

The expected error for the NASA range and range rate satellite-to-satellite tracking system is a function of many controlled parameters such as range tone frequency, sample rate, bandwidth settings, signal-to-noise spectral density ratios, spacecraft dynamics, etc. (13). However, the system is generally used with what might be termed a standard set of options such as: 100 kHz maximum range tone frequency, signal levels such that system is not thermal noise limited, 1 per second or 6 per minute data rate, and a 25 Hz range tracking loop two-sided noise bandwidth. Table I lists the theoretical system performance for the foregoing selected options. Doppler averaging time is approximately one half the sample time interval for NIMBUS tracking and equal to the sample interval for Apollo and GEOS tracking.

For averaging times, T , up to about 10 seconds the noise decreases as $1/T$. The principal Doppler noise contribution comes from receiver voltage controlled crystal oscillators and the analog to digital conversion. For longer integration times the Doppler noise is also influenced by noise falling off as $1/T$, an effect attributed to the phase jitter in the

TABLE I
Tracking System Measurement Resolution

Range (Meters)		Range Rate (Cm/Sec)	
Systematic	Random	Systematic	Random
1.2	1.2	Negligible	0.03

NOTE: 10 Sec. Averaging

transmitter reference signal used at the Doppler extractor. For satellite-to-satellite tracking involving ATS-6 the range-rate resolution for T seconds of averaging (27) is given by:

$$\sigma_{\dot{R}} = \sqrt{\left(\frac{0.3}{T}\right)^2 + \left(\frac{0.07}{\sqrt{T}}\right)^2} \text{ cm/sec}$$

This range-rate resolution versus Doppler measurement averaging time is plotted in Figure 2.

It should be mentioned that the least significant range bit recorded is 1.5 meters which is consistent with the best expected one way performance of 1.7 meters resolution. Measured results indicate close agreement with expected system performance. System random errors or "noise" are generally observed by the least squares fitting of short data spans (i.e., 1 to 10 minutes) with polynomials of at least 5th degree to account for spacecraft dynamics. Care must be taken such that the polynomial itself does not introduce apparent error. If the data is from a static or collimation tower test a least squares straight line fit is appropriate.

Assuming reasonable tracking geometry the accuracy of spacecraft position and velocity determination will be primarily limited by tracking system performance for any computation spanning the data collection interval. That is, if continuous tracking is provided from a set of well surveyed stations the computation is essentially one of geometry. On the other hand the accuracy of orbit prediction based on an initial spacecraft vector

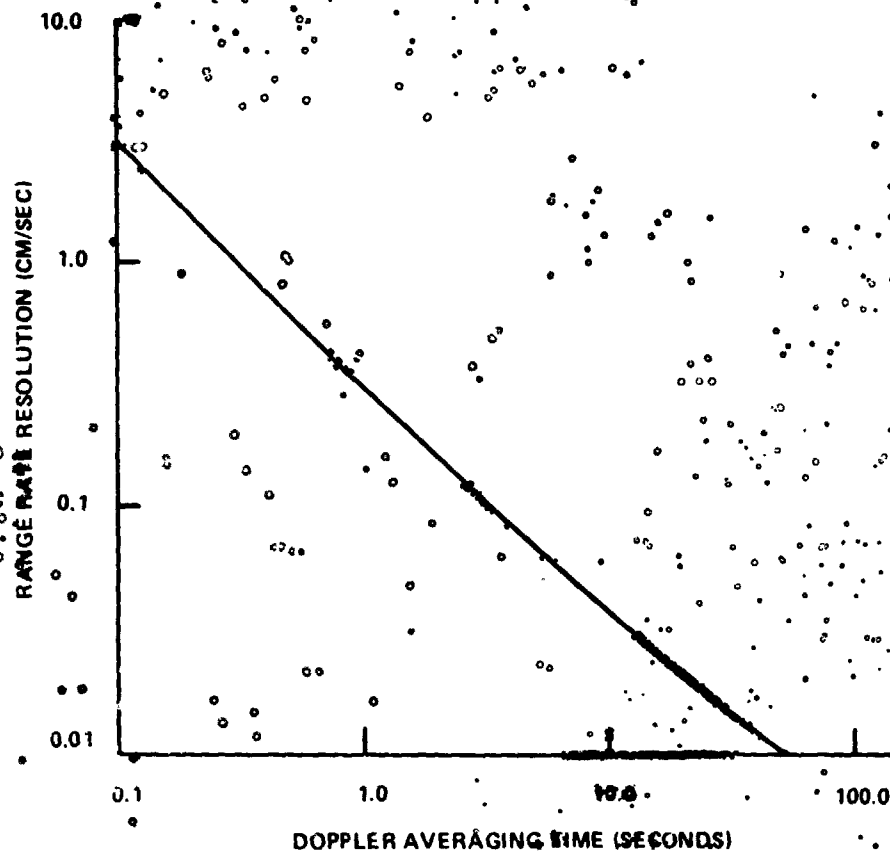


Figure 2. Range Rate Resolution

determination will be degraded as a function of time in direct relation to the accuracy to which physical parameters are modeled. This modeling includes gravitational fields, atmospheric drag and refraction effects, solar pressure, station location determination and so on. The most critical of these modeling parameters in terms of orbit determination accuracy is the gravity field model which at present is generally expressed in terms of a spherical harmonic expansion.

3.2 ATSC ORBIT DETERMINATION RESULTS

The optimal reduction of satellite-to-satellite tracking data to determine a user satellite orbit requires an accurate a priori estimate of relay satellite state. Hence, it is important

to determine the expected errors in the estimate of ATS-6 state from ground based tracking.

More precisely, we require answers to these questions:

- 1) How accurately can the ATS-6 orbit be determined over an orbital period (24 hr) from data which spans the orbital period?
- 2) Once an ATS-6 epoch state is determined, how accurately can that state be propagated beyond the data arc which was used in its estimation?

GEOSTATIONARY SATELLITE SHORT TERM ACCURACY

The first question was investigated by examining reductions of ATS-6 trilateration tracking obtained on November 3, 1974. Trilateration data is obtained by sending a signal from a single tracking station to several strategically deployed unmanned low cost transponders via the satellite whose state is to be determined. The time required for the radio signals to complete the round trip to and from each transponder is measured at the transmitter site. The interrogating sites were located at Rosman, North Carolina and Mojave, California. The transponders were located at Rosman, Mojave, Greenbelt, Maryland, and Santiago, Chile.

The method of "orbit overlaps" was used to evaluate the orbit determination accuracy of the system. This procedure can be outlined as follows:

- 1) Determine a satellite epoch state using each of two independent data sets
- 2) Propagate estimated epoch states over a common or overlapping interval
- 3) Difference the two orbits over the common interval (differences are usually displayed in along track, cross track, and radial components).

In some cases the orbit overlap method can lead to an under-estimation of orbit errors since biases in orbit estimates may cancel in orbit differences. Hence, the method should be viewed as a test of the internal consistency of an orbit determination process rather than an

absolute **measure of accuracy**. Data set 1 used in the **orbit overlap test** was obtained with **Rosman** as a transmitting site and with transponders at Rosman, Mojave, Greenbelt, and **San** **trigo**. Data set 2 was obtained with the same transponder sites but with the transmitter located at Mojave. The tracking schedule is shown in figure 3. The two interrogating sites are identified in figure 3 under TRANSMITTER as Rosman, North Carolina and the Mojave, California "Hybrid Transportable" station. Each data stretch was approximately 5 minutes long and the data rate was one sample per 10 seconds. Separate orbit arcs were computed from data set 1 and data set 2. The total position differences between the two orbits over the 24 hours of Nov 3, 1974 were computed and are displayed in figure 4. The mean position error is about 100 m. A typical set of range residuals is shown in figure 5. The **range** residuals over this arc are on the order of 20 m.

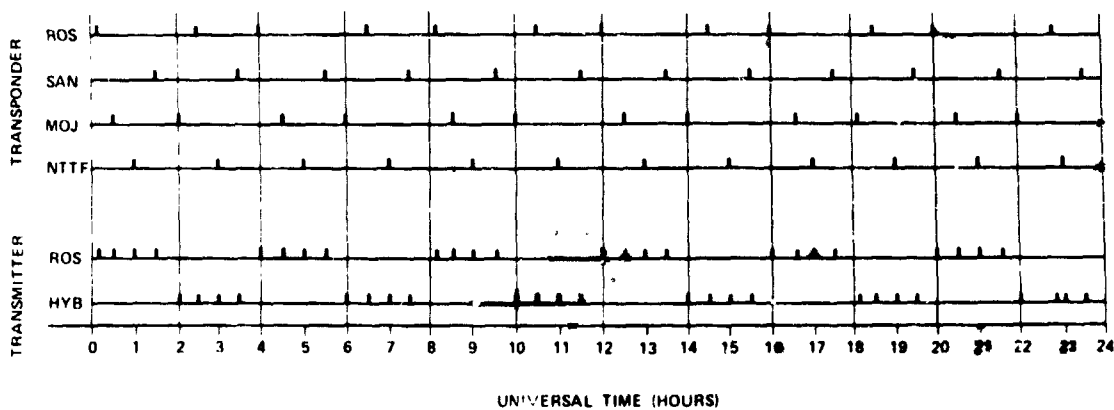


Figure 3. Tracking Schedule 3 November 1974

Assuming that there are no significant biases in the **trilateration orbit determination** whose effects cancel in the orbit overlap test, the results of figure 4 suggest that **continuous** tracking of ATS-6 over a 24 hour period leads to **an orbit estimate over** the period which is accurate to about 100 m.

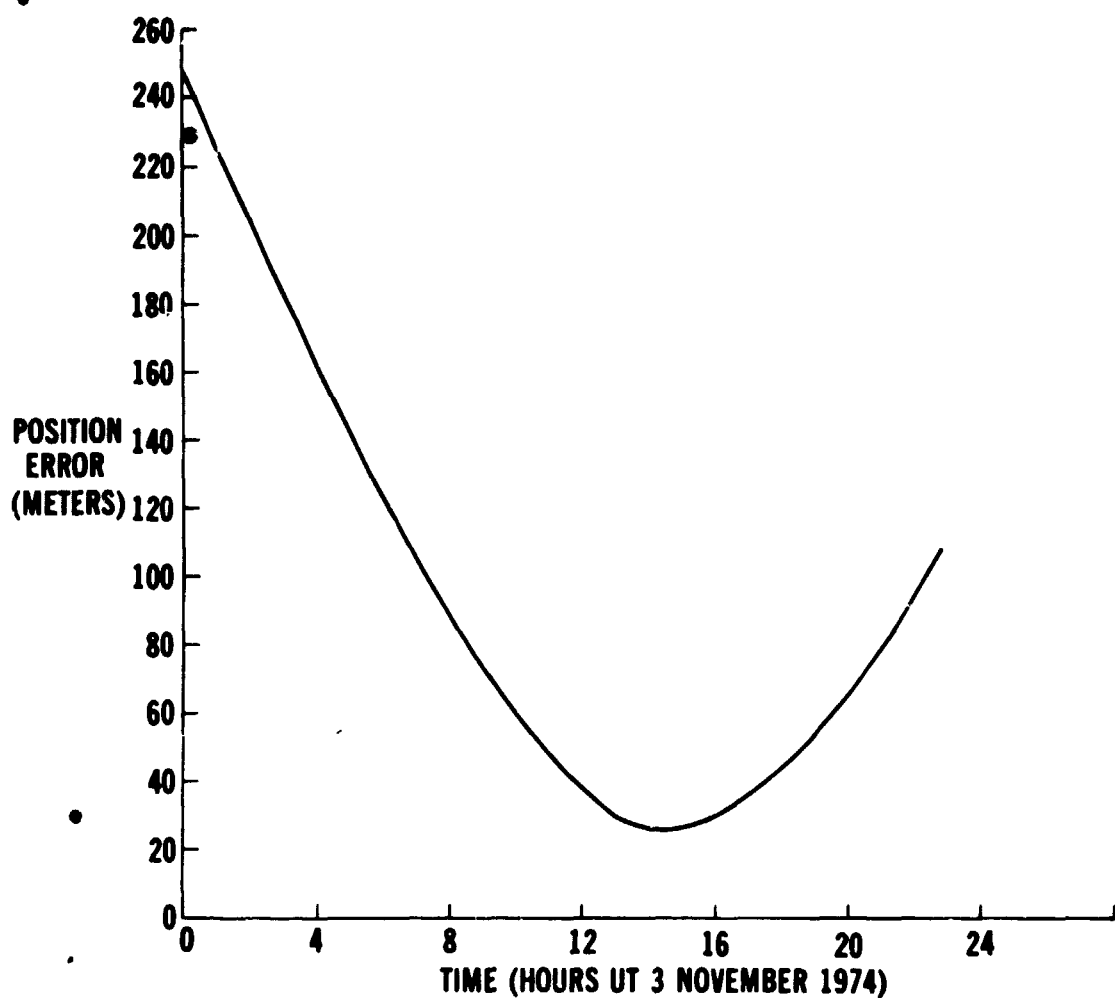


Figure 4. ATS-6 Total Position Error

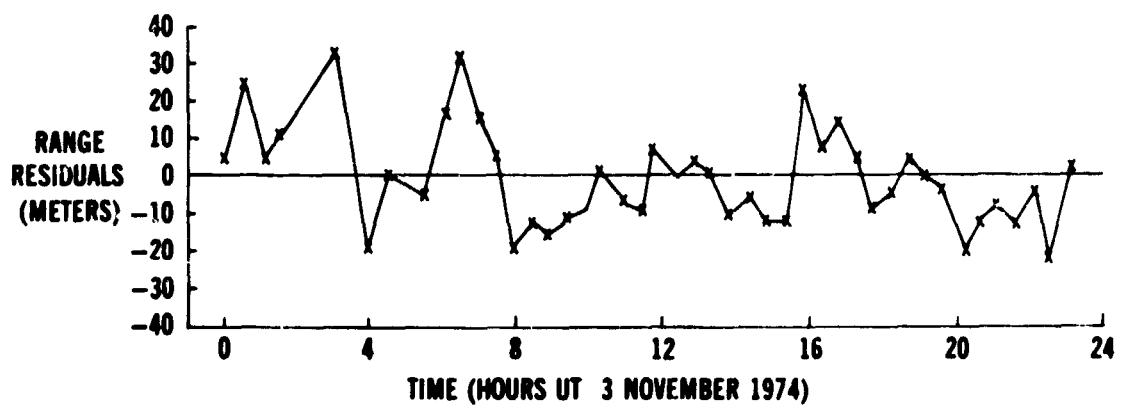


Figure 5. ATS-6 Orbit Residuals

GEOSTATIONARY SATELLITE LONG-TERM ACCURACY

In general one cannot assume that relay satellites are continuously tracked. Hence, in the reduction of satellite-to-satellite tracking data, it may be necessary to use an estimate of user satellite state obtained through a propagation that was unconstrained by the data fitting criterion of a least squares algorithm. When this occurs the accuracy of the orbit estimate is entirely dependent on the correctness of the force models used in the propagation.

The orbit overlap technique (30), utilizing data obtained during July 1975 was used to estimate the accuracy of a free or unconstrained propagation of an ATS-6 epoch state. The data sets used in the overlap tests were:

Data Set 1 – 24 hours of data over July 13, 14, 1975. Tracking stations located at Madrid, Ascension Island, and Johannesburg.

Data Set 2 – 24 hours of ranging data over July 25, 1975. Tracking stations located at Madrid, Ascension Island, and Johannesburg.

Each data set was processed to estimate an ATS-6 state vector for epoch time July 16, 1975 at 7 hr., 25 min. The epoch states were propagated forward for 10 days and along track, cross track, and radial differences were computed at 15 minute intervals. The root mean square along track difference was over 2 km. Figure 6 is a plot of these along track differences.

The large errors which occur during the free propagation of an ATS-6 epoch vector must be caused by a misrepresentation of force models. The obvious candidates are:

- 1) Unmodeled venting and thrusting of ATS-6 to accomplish satellite attitude corrections. Motions due to antenna maneuvering may also introduce errors.

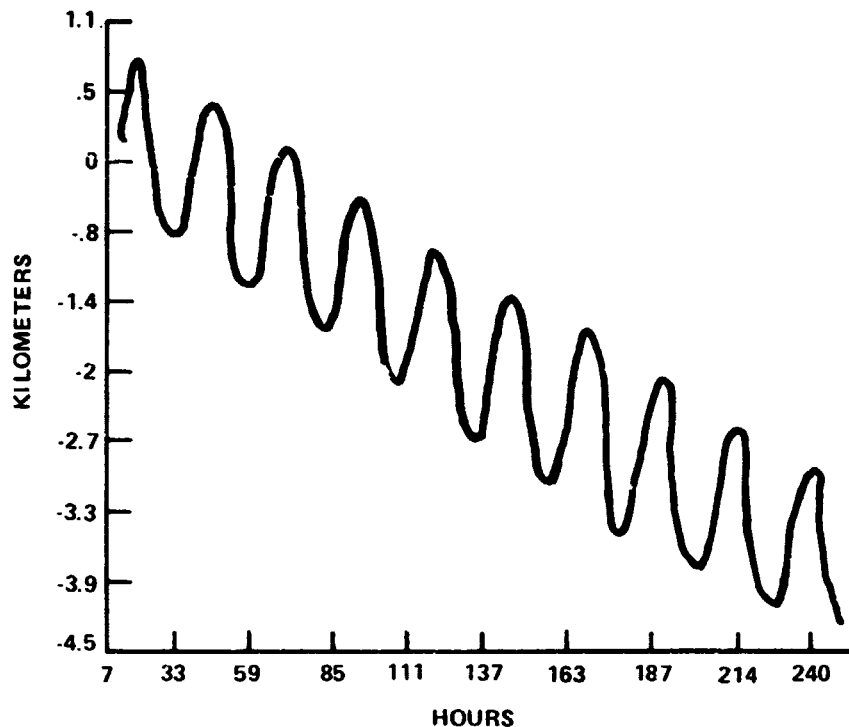


Figure 6. Along Track Orbit Differences for ATS-6 Overlap Test, July, 1975

- 2) Mismodeling of solar radiation pressure. In all data reductions, ATS-6 was assumed to present a constant cross section to the sun. In fact, this is not the case.
- 3) An error in representation of the central force term of the Earth's gravity field. An estimate of the uncertainty in estimates of this parameter is one part in 10^6 .

Error source number 3 appeared to us as the most likely cause for the major part of the errors exhibited in figure 6. In order to measure the effect of uncertainty in the gravity field parameter on the free propagation of ATS-6, the following simulation was performed; ranging observations to the ATS-6 from sites at Rosman, Santiago, and Mojave were generated for a three day span. The observations were corrupted with white noise with a standard

deviation of 10 m. The value of the gravity field parameter used to generate the data was perturbed by one part in 10^6 and this value was used along with a least squares estimator to estimate an epoch state at the beginning of the three day data span. The perturbed value of the gravity field parameter was used to propagate this epoch state for six days. Over the three days covered by data the propagated orbit differed from the assumed true orbit by about 100 m. But at the end of the six day propagation period the errors were approximately 2 km. The results of this simulation suggest that the error in the central force term of the Earth's gravity field is sufficient to account for the errors in the ATS-6 free propagation as manifested in figure 6.

SUMMARY OF RESULTS

Overlap tests performed with real data together with simulation results suggest that by processing data over one ATS-6 orbital period, the ATS-6 state over the orbital period can be determined with an average accuracy of about 100 m. But other results show that when longer data arcs are used or when an estimated ATS-6 epoch state is propagated well beyond the data arc used in its estimation, errors in the kilometer region are encountered. These facts indicate that there are significant errors in the models of the forces acting on the ATS-6. The most likely candidate is the error in representation of the central force term of the gravity field.

3.3 GEOS-3 ORBIT DETERMINATION RESULTS

The GEOS-3 orbit determination results were derived from data obtained over the weekend of May 3, 1975. The tracking schedules and the tracking systems used in the evaluation are shown in figure 7. The figure shows that five passes of range sum and range sum rate data were available. A Bayesian estimation technique described in a previous section was used to obtain two separate and overlapping GEOS-3 orbits. A GEOS-3 epoch state at May 2, 22 hr was estimated using all the ATS-6 ranging data and the first three passes of

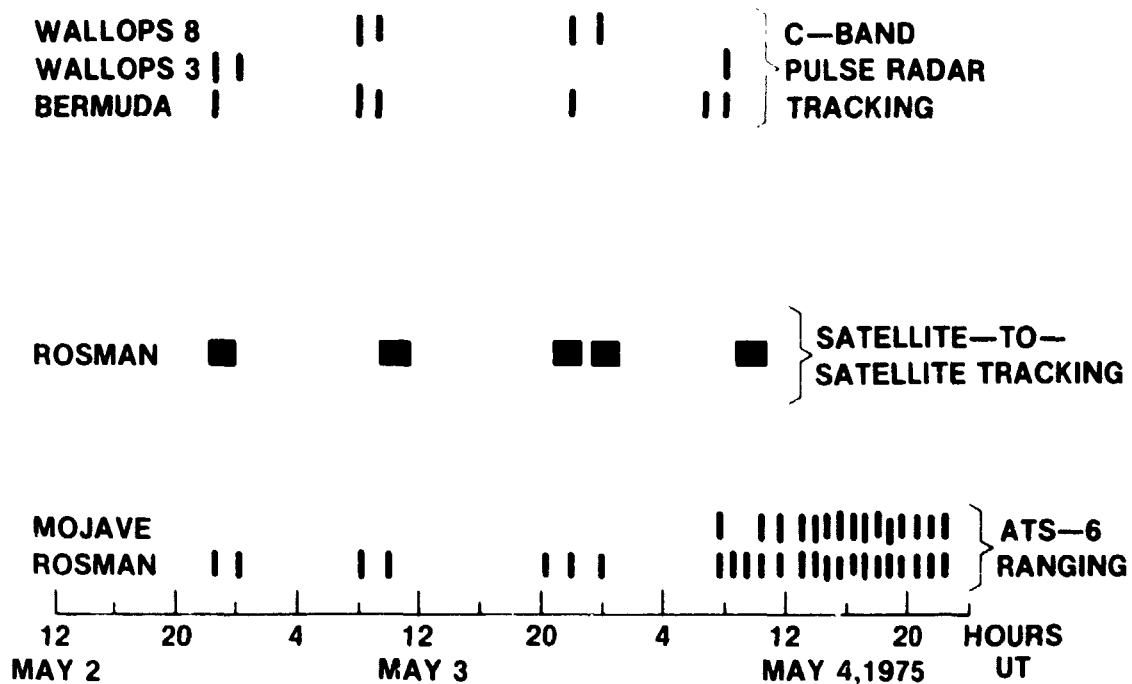


Figure 7. Data Summary

range sum and range sum rate data. The ATS-6 ranging data was weighted according to a standard deviation of 2 m. The range sum and range sum rate data were weighted according to standard deviations respectively of 2 m and 1 mm/sec. The complete GEM-7 geopotential field was used in this and all other data reductions. The estimated epoch state was propagated to the end of the data span of May 3, 22 hr. The process was repeated with the last four passes of range sum and range sum rate data to estimate a GEOS-3 epoch state at May 3, 10 hr. This epoch state was propagated to the end of its data span at May 4, 10 hr. The total position difference between the two orbits during the 12 hr overlap period as shown in figure 8 varies periodically between 10 and 25 meters.

As mentioned in a previous section, orbit overlap procedures can provide an overly optimistic assessment of orbit determination accuracy. A more objective measure of accuracy is obtained by comparison with an orbit derived from an independent and well

calibrated data set. Figure 7 displays the C-band tracking available from Wallops Island and Bermuda during the weekend of May 3, 1975. A three-day GEOS-3 arc was derived from the C-band data and compared to a similar arc derived from the five passes of satellite-to-satellite tracking data and ATS-6 ranging data. The root mean square differences in the two arcs were:

radial	5 m
cross track	200 m
along track	39 m

Various orbit results indicate that total position error for C-band derived GEOS-C orbits is on the order of 50 m (31). Hence, it is only in the cross track direction that the orbit determination derived from satellite-to-satellite tracking data differs significantly from the C-band orbit. The large cross track errors can be explained in terms of the tracking geometry. For each of the five satellite-to-satellite tracking passes shown on figure 7, the GEOS-3 satellite passed almost directly under the ATS-6 satellite. Consequently there was little cross track information in the range sum and range sum rate data. It is a reasonable assumption that with a better geometric distribution of passes the cross track errors would be substantially reduced.

3.4 NIMBUS-6 ORBIT DETERMINATION RESULTS

The NIMBUS-6 overlap results were derived from data obtained over the weekend of Feb 8, 1976. For this experiment a highly accurate reference orbit suitable for the purpose of comparison was unavailable. This implied that the primary measure of the quality of the orbits derived from satellite-to-satellite tracking would be obtained from orbit overlap test. Hence the orbit overlap test for the ATS-6/NIMBUS-6 experiment was performed in a way which was more rigorous and less optimistic than the overlap test performed for the ATS-6/GEOS-3 experiment. Notice that for the ATS-6/GEOS-3 experiment the overlap test was

performed with data sets which intersected through the entire overlap interval. Hence both orbits used in the comparison were constrained by data at each end of the interval. With such a procedure it is possible for the effects of errors in the measuring system to cancel in the test results. It will be seen that for the ATS-6/NIMBUS-6 overlap test the two data sets in question are abutting rather than overlapping and effect of measurement system errors are less likely to cancel in the test results.

The tracking schedules and the tracking systems used in the evaluation are shown in figure 9. The first two rows of this figure show the tracking schedules for the ranging data from Madrid, Spain to ATS-6, and from Ahmedabad, India to ATS-6. The third row

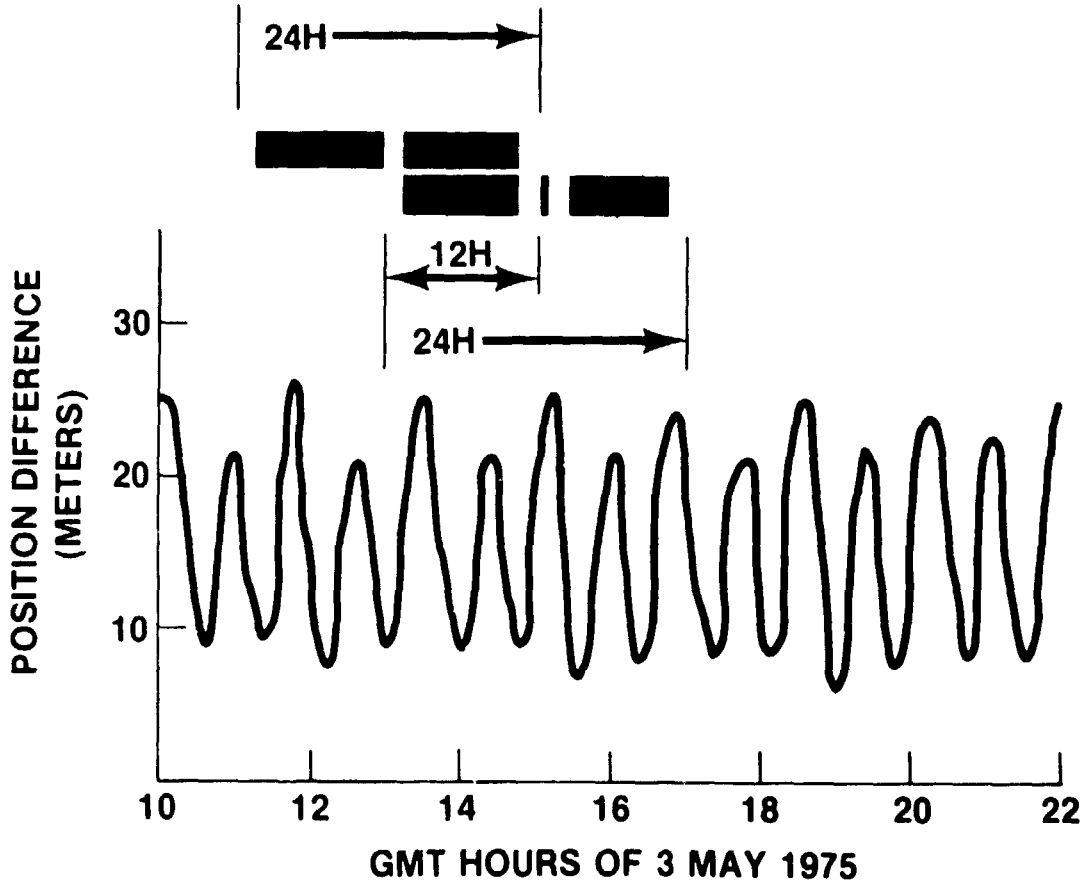
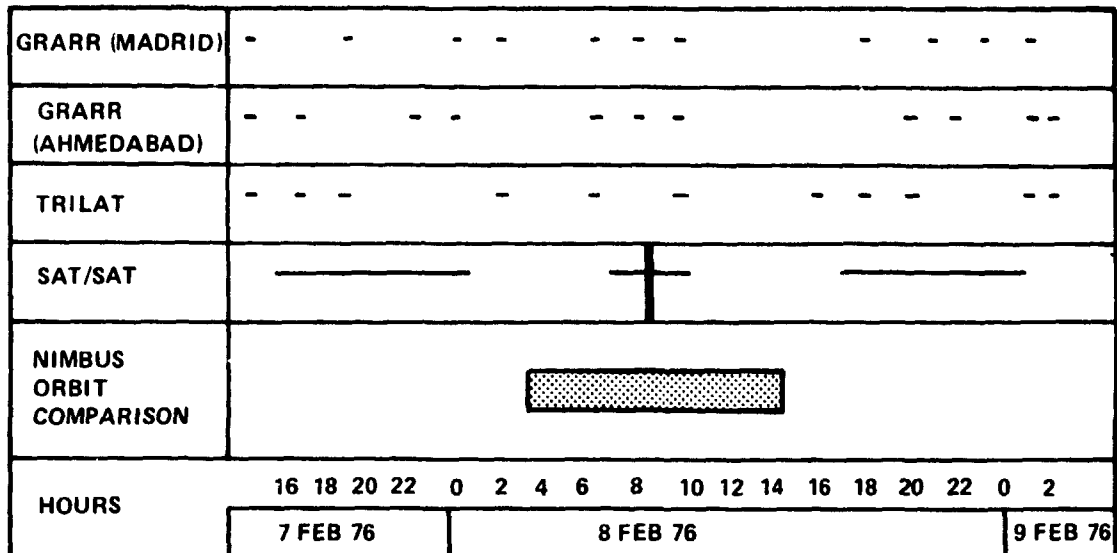


Figure 8. GEOS-3 Overlap Position Differences



NOTE: DATA ON LEFT HAND SIDE OF VERTICAL BAR IN SAT/SAT ROW USED FOR RECOVERY OF FIRST NIMBUS EPOCH VECTOR, DATA ON RIGHT HAND SIDE USED FOR RECOVERY OF SECOND NIMBUS EPOCH VECTOR.

Figure 9. Measurement Periods and Period for Nimbus Orbit Comparison

indicates the tracking schedule for trilateration data (Madrid-ATS-6-Ascension Island). The fourth row shows the tracking schedule for the range sum and range sum rate data with Madrid as the ground station. The vertical bar located at 9HR/UT Feb. 8 indicates the epoch time for two estimated NIMBUS-6 epoch states. Epoch state 1 was obtained by executing a Bayesian least squares estimator with all the ATS-6 ranging and trilateration data and all the satellite-to-satellite tracking data to the left of the epoch time. Epoch state 2 was obtained by repeating the procedure with the satellite-to-satellite tracking data to the right of the epoch time replacing the data to the left of the epoch time. The horizontal bar in row 5 of the figure displays the common interval over which the two NIMBUS-6 epoch states were propagated. The complete GEM-7 gravity field model was used in all data reductions and propagations. The relative weights for the data types were obtained by first using nominal weights and processing all the data to estimate ATS-6 and NIMBUS-6 epoch states.

The residuals of the estimation were used to determine the standard deviations of the noise on the various data types. These standard deviations were used to obtain weights for the final data reductions. The computed standard deviations are shown on table 2.

TABLE 2

Standard Deviation Used for Weighting Measurements in Nimbus-6
Satellite-to-Satellite Tracking Orbit Determination

RANGE (INDIA) TO ATS	168 m
RANGE (MADRID) TO ATS	50 m
TRILATERATION (MADRID, ATS, ASCENSION)	15 m
SATELLITE-TO-SATELLITE RANGE	11 m
SATELLITE-TO-SATELLITE RANGE RATE	.3 cm/sec

The data reductions were complicated by the fact that an experiment onboard the NIMBUS-6 was responsible for some outgasing. This effect was modeled as a constant along track thrust whose magnitude was estimated in the data reductions. The recovered magnitude was approximately 10^{-7} m/sec².

Figures 10, 11, and 12 display the along track, cross track, and radial differences in the two epoch state propagations during the overlapping period. The R.M.S. differences are 40 m along track, 30 m cross track, and 12 m radial. The secular growth of residuals in the along track direction is explainable in terms of gravity field error and an imperfect modeling of the outgasing effect whose direction was probably not exactly along track and whose magnitude was probably not constant.

Finally it should be mentioned that a NIMBUS-6 orbit derived from satellite-to-satellite tracking data was compared to a NIMBUS-6 orbit derived from minitrack data. The orbit differences were well within the stated accuracy for minitrack orbits of 500 m.

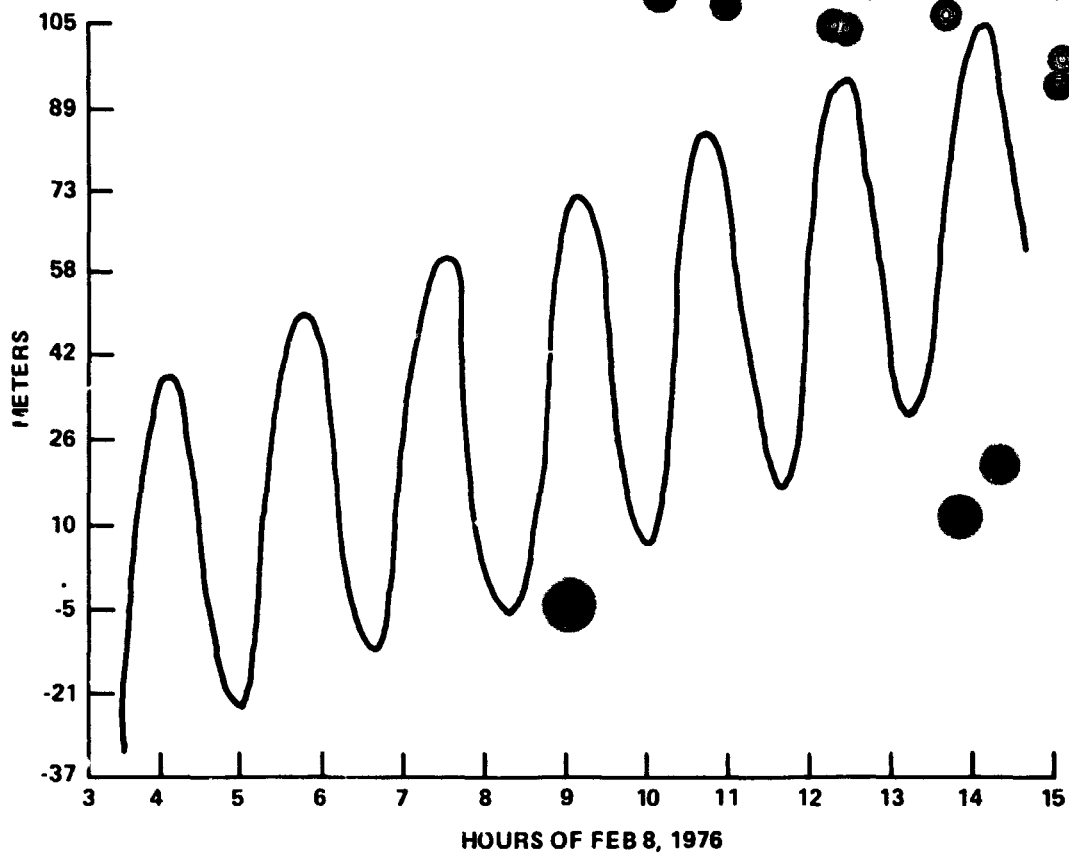


Figure 10. Along Track Differences for Nimbus-6 Satellite-to-Satellite Tracking Orbit Determination

4.0 CONCLUSIONS

The ATS-6/NIMBUS-6 and ATS-6/GEOS-3 satellite-to-satellite radio tracking system performs as specified with a resolution of 1 meter in range and .03 cm/sec in range-rate for a 10 second averaging.

A Bayesian least squares estimation technique utilizing a good a priori estimate of relay satellite state was used during these experiments to obtain user satellite orbits with accuracies comparable to what is obtainable from ground tracking systems. The limiting

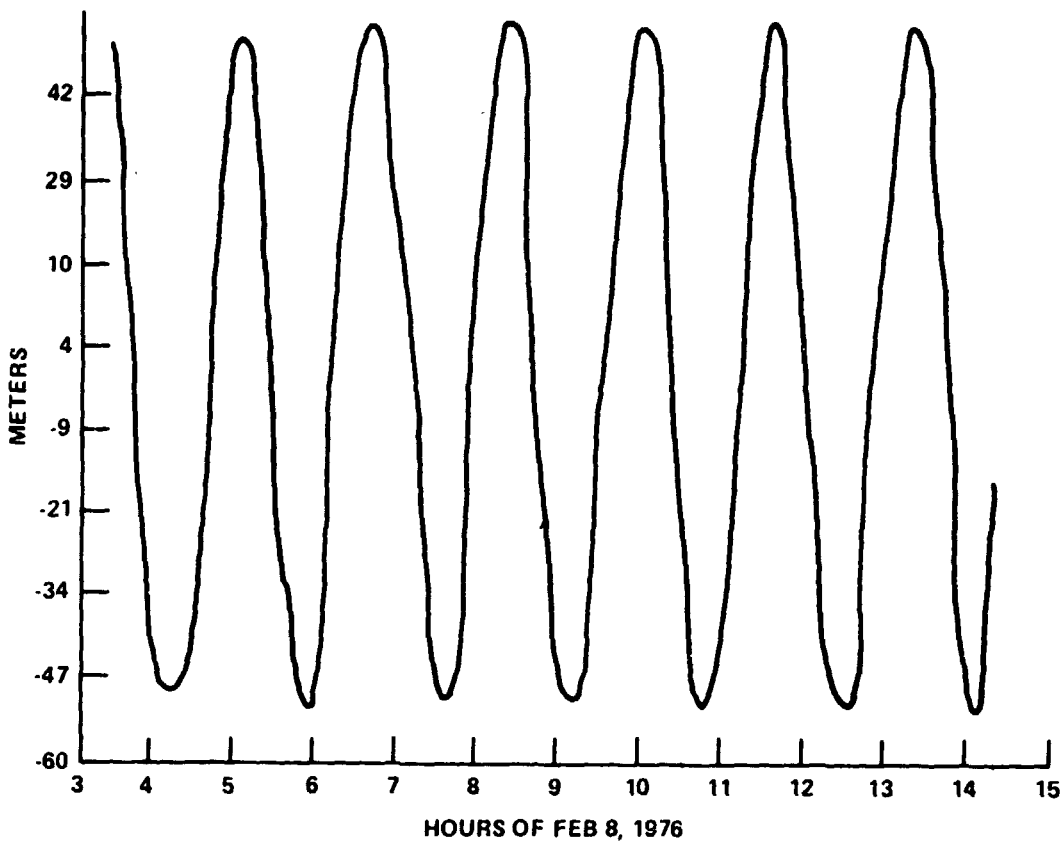


Figure 11. Cross Track Differences for Nimbus-6 Satellite-to-Satellite Tracking Orbit Determination

factor in an orbit determination with satellite-to-satellite radio tracking appears to be the accuracy of the force models rather than tracking system precision.

The results of these experiments imply that with the proper data reduction procedures, the tracking data relay satellite system should provide orbit determination capability comparable to what is now obtainable from ground based systems.

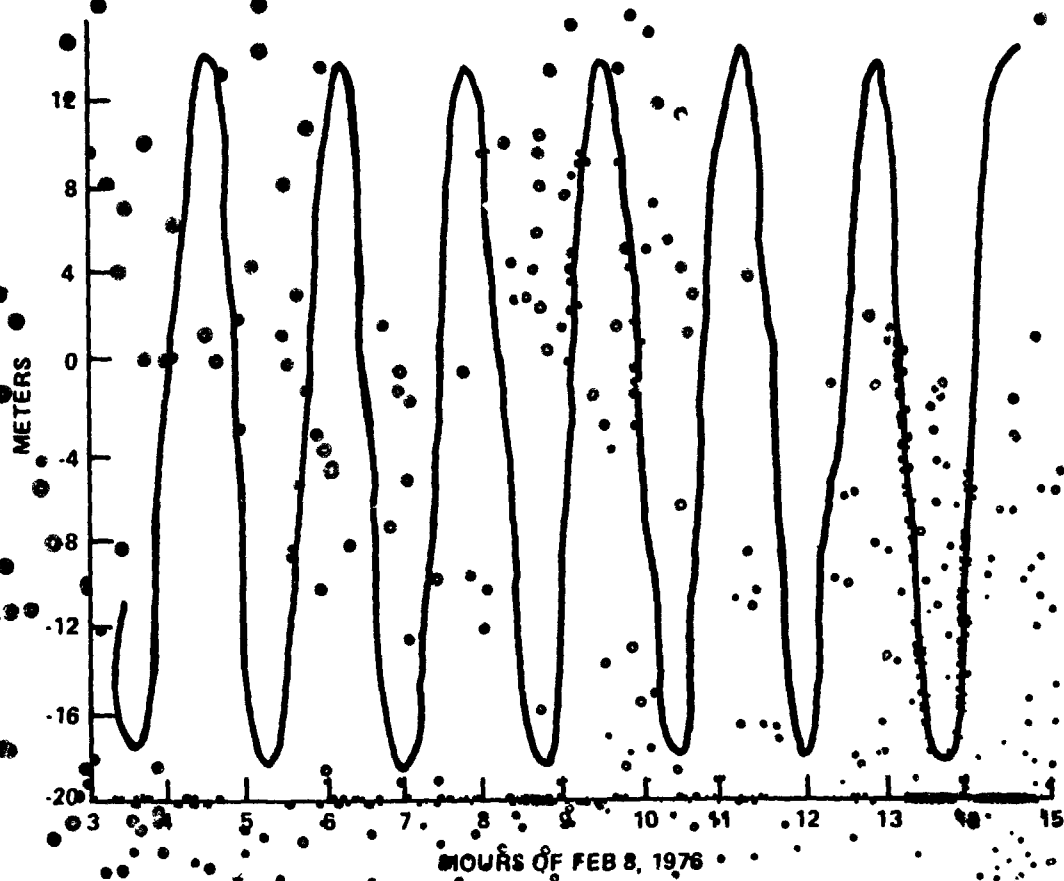


Figure 12. Radial Differences for Nimbus-6 Satellite-to-Satellite Tracking Orbit Determination

ACKNOWLEDGMENTS

The authors thank Dr. Georg Morduch and Mr. John Bryan for their aid during the course of this research.

REFERENCES

1. Bergstein, E. and W. Beller, "Satellite", p. 135, Hanover House, Garden City, New York, 1956.
2. Vonbun, F.O., "Tracking and Communications" presented at AIAA 4th Annual meeting, paper 67-976, Anaheim, California, October 23-27, 1967.
3. Vonbun, F.O. and J. T. Mengel, "Tracking and Communications for Planetary Manned Missions", Journal of Spacecraft and Rockets, Vol. 5, No. 7, pp 863-865, July 1968.
4. Martin, C.F., "Accuracy of Orbits Obtainable by Synchronous Satellites Tracking," in Dynamics of Satellites (1969), 120-129, edited by B. Morando (Berlin, Springer Verlag, 1970).
5. Martin, C.F., "Evaluation of Satellites Tracking Satellites for Orbit Determination and Geopotential Recovery," Final Technical Report on Contract NAS 5-11736-Mod 3, June 1970.
6. Cooley, J.L., and A. Marlow, "Orbital Error Studies - Tracking from a Synchronous Spacecraft," GSFC X-551-6-7, January 1969.
7. Martin, C.F., T.V. Martin and D.E. Smith, "Satellite-to-Satellite Tracking for Estimating Geopotential Coefficients," The Use of Artificial Satellites for Geodesy, AGU Mono. 15, 139-144, 1972.
8. Schwarz, C.R., "Refinement of the Gravity Field by Satellite-to-Satellite Doppler Tracking," The Use of Artificial Satellites for Geodesy, AGU Mono. 15, 133-138, 1972.
9. Kaula, W.M., "Error Analysis of Earth Physics Satellite Systems," Final Report, Part I, on NASA Grant No. NGR 05-007-280, October 1972.
10. Heffernan, P.J., "ATS-F/NIMBUS-F Tracking and Data Relay Experiment Technical Summary", NASA-GSFC, 1 October 1968.

11. Vonbun, F.O., et al., "Gravity Anomaly Detection - Apollo/Soyuz", NASA-GSFC X-920-75-308, December, 1975.
12. Teles, J., Ayres, C., "Advanced Spacecraft Tracking Techniques Using the Tracking and Data Relay Satellite System", presented at the AAS/AIM Astrodynamics Conference, Sept. 7-9, 1977, Grand Teton National Park, Wyoming.
13. Schmid, P.E. and F.O. Vonbun, "The ATS-F/NIMBUS-F Tracking and Orbit Determination Experiment", 1974 IEEE INTERCON, New York City.
14. Schmid, P.E., F.O. Vonbun, and B.J. Trudell, "ATS-6 Satellite-to-Satellite Tracking and Data Relay Experiments", pp. 1048-1058, IEEE Transactions on Aerospace and Electronic Systems, Vol. AES-11, No. 6, November 1975.
15. Vonbun, F.O., "Geodetic Satellite Missions and GEOS-C Spacecraft", Space Research XI-Akademie-Verlag, Berlin 1971.
16. Vonbun, F.O. et al., Geodynamics Experiment MA-128, Apollo-Soyuz test Project, Preliminary Science Report, NASA TMX-58173, February 1976.
17. Vonbun, F.O., "The ATS-F/NIMBUS-E Tracking Experiment", pp. 112-120, "Rotation of the Earth", P. Mechior & S. Yumi (eds), D. Reidel Publishing Co., Dordrecht, Holland, 1972.
18. Schmid, P.E., "The Tracking and Data Relay Experiment (T&DRE)", pp. 207-218, The NIMBUS-6 User's Guide NASA-GSFC, February 1975.
19. Marini, J.W., "Doppler Factors in Satellite-to-Satellite Tracking", NASA-GSFC X-932-74-93, April 1974.
20. Schmid, P.E., R.B. Bent, S.K. Llewellyn, G. Nesterczuk, and S. Rangaswamy, NASA-GSFC Ionospheric Corrections to Satellite Tracking Data", NASA-GSFC X-591-73-281, December 1973.

21. Marini, J.W., "Correction of Satellite Tracking Data for an Arbitrary Tropospheric Profile", Radio-Science Volume 7, No. 2, pages 223-231, February 1972.
22. Marini, J.W., "Tropospheric Range-Rate Tracking Data Correction", NASA-GSFC X-551-72-277, August 1972.
23. Argentiero, P., and Loveless, F., "Orbit Determination with the Tracking Data Relay Satellite System", NASA-GSFC X-932-76-185, February 1977
24. Clark, George Q., "Tracking and Data Relay Satellite Systems (TDRSS) User's Guide", STDN. No. 101.2, NASA-GSFC Greenbelt, Maryland, May 1975.
25. Fang, B., and Gibbs, B., "TDRSS Era Orbit Determination System Review Study", Planetary Sciences Department Report No. MT010-75, Wolf Research and Development Group, December 1975.
26. Argentiero, P., and Garza-Robles, R., "GEOS-C Orbit Determination With Satellite-to-Satellite Tracking", Journal of the Astronautical Sciences, Vol. XXIII, No. 3, pp 241-256, July - September 1975.
27. Schmid, P.E., Argentiero, P., and Vonbun, F.O., "Satellite-to-Satellite System and Orbital Error Estimates", presented at the Precision Time and Time Interval Conference, NASA-GSFC, December 2-4, 1975.
28. Schmid, P.E. and J.J. Lynn, "Results of the 3 November 1974 Applications Technology Satellite-6 (ATS-6) Trilateration Test", NASA/GSFC X-932-75-104, April 1975.
29. Lynn, J.J., P.E. Schmid and R.F. Anderson, "A New Method for Satellite Orbit Determination Using an Operational Worldwide Transponder Network", NASA-GSFC X-591-74-2, January 1974.
30. Vonbun, F.O., "Satellite Trajectory Determination and Their Expected Errors OGO-IV, GEOS-1" Dynamics of Satellites (1969), p. 89-103, Springer-Verlog, Berlin, Heidelberg, New York, 1970.
31. Marsh, J., Goddard Space Flight Center, Private Communications.

**ON-BOARD LANDMARK NAVIGATION AND ATTITUDE REFERENCE
PARALLEL PROCESSOR SYSTEM**

Lloyd E. Gilbert and Dhema T. Mahajan
Martin Marietta Aerospace
Denver, Colorado

ABSTRACT

An approach to Autonomous Navigation and Attitude Reference for Earth observing spacecraft is being developed. The technique is to incorporate Landmark identification into the spacecraft on-board navigation and attitude control system. A fast landmark detection and registration system based upon a Sequential Similarity Detection Algorithm (SSDA) is being examined and laboratory experiments undertaken to determine if better than one pixel accuracy in registration can be achieved consistent with on-board processor timing and capacity constraints. The SSDA is to be implemented using a multi-microprocessor system including synchronization logic and chip library. The data is processed in parallel stages, effectively reducing the time to match the small known image within a larger image as seen by the on-board image system. Shared memory is incorporated in the system to help communicate intermediate results among microprocessors. The functions include finding mean values and summation of absolute differences over the image search area. The hardware is planned to be a low power, compact unit suitable to on-board application with the flexibility to provide for different parameters depending upon the environment.

INTRODUCTION TO LANDMARK TECHNIQUE

The concept of using Landmarks to register images is common in the field of image processing.¹ Landmarks, also known as Ground Control Points (GCP), Registration Control Points (RCP) or anchor points are small images with known geophysical coordinates. The known Landmark is found in a larger scene and thus the larger scene (at least the local area in the scene) is registered. The technique involves finding the best fit of a "chip" in a "window." A chip is a small image (size varies from 3x8 pixels to 32x32 pixels) of known latitude and longitude. The window is the large area to be searched, its size appropriate to the amount of uncertainty in where the chip will match. Figure 1 shows an example of a chip/window pair. By finding the location of the chip in the window, the whole image can be registered. Many examples are found in the literature, for example Cloud Tracking from ATS pictures.²

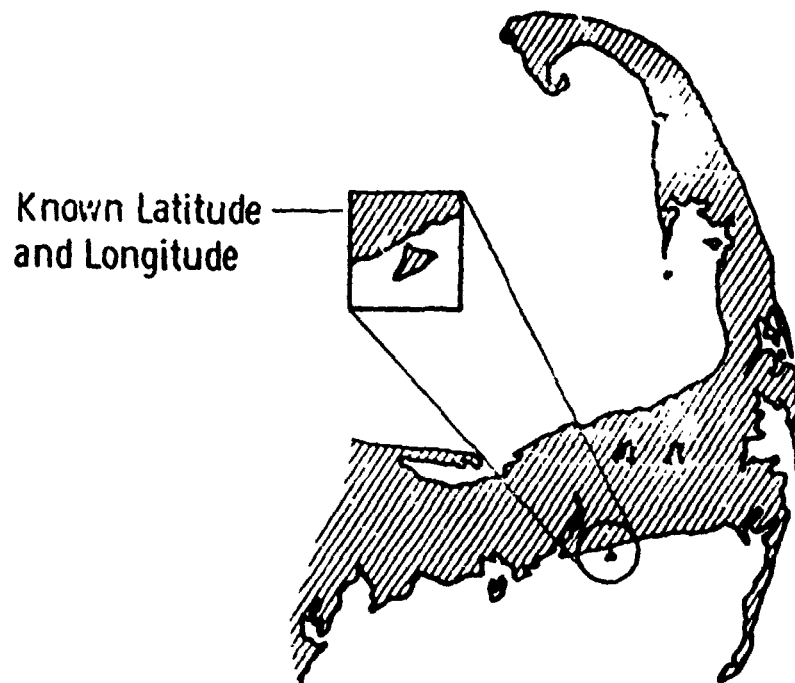


Figure 1. Illustration of a Chip/window Pair

The chip contains the known Landmark. The window is the area to be searched.

The chip is compared to a possible location on the window by doing a one pixel at a time comparison over a placement of the chip on the window. The chip is then moved and the comparison repeated. A best fit is chosen. This gives a best whole-pixel match. There are two predominant styles of comparing chips to windows. The classical correlation coefficient involving square roots of sums and products requires that the calculations be carried out over every pixel of a chip/window placement before a numerical answer is derived. Sequential Similarity Detection Algorithms³ involve sums of absolute differences between chip and window pixels and may be terminated before comparing every pixel of a chip/window placement.⁴ Using an SSDA approach with a decreasing threshold to allow only partial processing of most chip/window placements, a match can be quickly found.

After the best whole pixel match is found there are several techniques to obtain best subpixel registration. These involve image enhancement⁵ or image resampling⁶; in any case interpolation between whole pixel placements is required. (It should be noted that there are several techniques to prepare the images for subpixel evaluation. Although the raw data can be compared, some techniques involve edge detection or contour following.)

Implications on Spacecraft Navigation and Attitude Reference

The idea of using Landmark data to determine spacecraft attitude and ephemeris information and incidentally register the images taken by the spacecraft is workable. Currently Goddard Space Flight Center uses the Landmark technique exclusively in their NAVPAK system. This system completely registers images from Synchronous Meteorological Satellite (SMS). The NAVPAK output provides for the updating of orbit/attitude state parameters exclusive of ranging or any other data.⁷ The Landmark technique has been shown to be better than traditional satellite tracking methods.

Various studies have been made which show not only the feasibility of doing spacecraft attitude and orbit determination but have shown that the knowledge gained can be of higher accuracy than that derived from control system sensors. A 1971 work for SAMSO⁸ studied the mathematical techniques necessary to determine the attitude of a spinning geosynchronous satellite. Using as few as four Landmarks and a Kalman filter, the state vector of the spacecraft could be adequately described. The error analysis showed that high accuracy could be achieved in a few scans containing between two and four carefully selected Landmarks.

A study of potential attitude and orbit determination and image registration techniques for the Earth Observatory Satellite⁹ examined various mixes of traditional and Landmark methods. Their study concluded that the attitude control system design must be considered as a part of the image positioning problem. The opposite is also true, the imaging system can be considered as part of the guidance and navigation system. The combination of onboard sensors (such as gyros) and Landmark identification can be illustrated to be a good control mechanism as well as enhancing the image processing procedure. There are various papers given at this symposium which address the problem of autonomous, on-board spacecraft calculations of attitude and orbit information.

It is proposed at this time that the Landmark technique could be applied to a processor on-board a satellite to provide autonomous attitude and ephemeris update.

**THE TECHNIQUE TO USE A SSDA TO
ACHIEVE MEASUREMENTS FOR A GUIDANCE
AND NAVIGATION SYSTEM**

Figure 2 illustrates the general sequence of events. The Spacecraft (S/C) is orbiting the earth with an imaging system which has a ground track such as shown in Figure 3. The image processing system contains numerous known Landmarks in its memory such as the chip shown in Figure 1. The estimated location of the chip in the field of view of the S/C can be calculated from the current S/C attitude and orbital knowledge. The location where the chip is actually found in the input data vs the estimated location generates error values which can be used to update attitude and ephemeris via techniques such as Kalman filters.

The generation of this measurement on-board the spacecraft is the topic of this paper. The two algorithms of interest are the SSDA and the resampling approach.

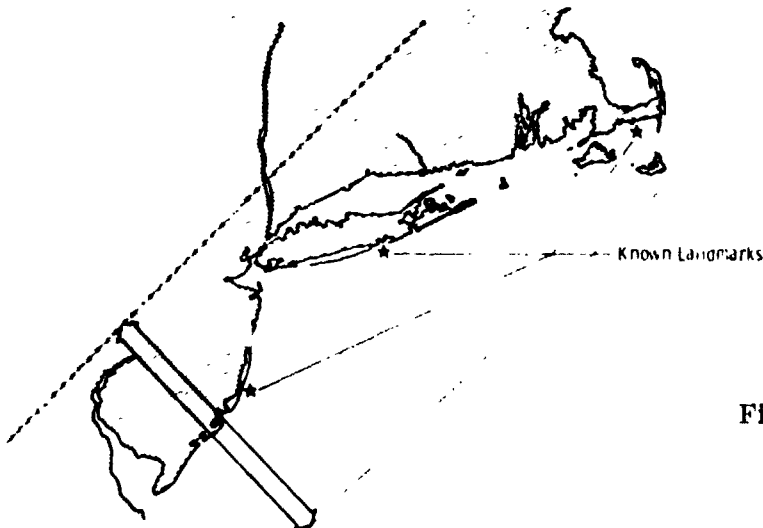


Figure 3. Image Sensor Ground Track

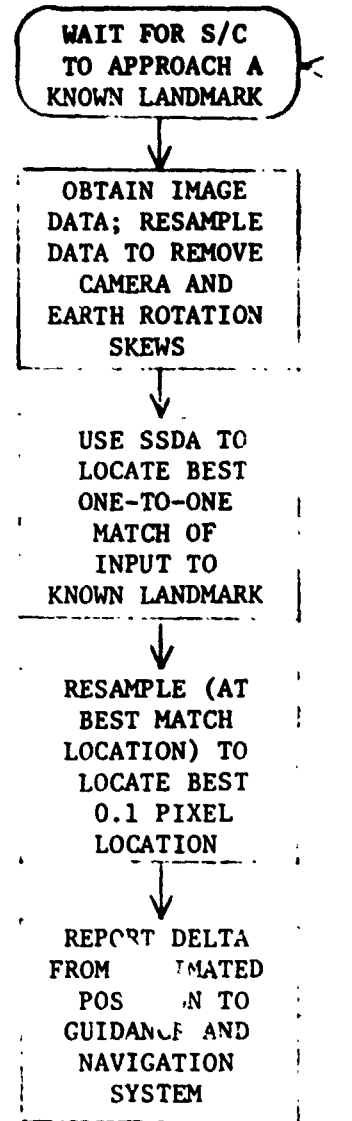


Figure 2. General Sequence of Events to Obtain a Landmark Data Point

The SSDA is traditional with the addition of a pseudo normalization to account for shifts in the mean value of the area of interest due to camera gain changes or lighting conditions on the Earth's surface. The SSDA equation is:

$$\text{SSDA Value} = \sum_{i=1}^n \sum_{j=1}^n \text{Abs. Value } ((\text{CP}_{ij} - \text{Chip Mean}) - (\text{WP}_{ij} - \text{Window Mean}))$$

where Σ implies sum over every pixel of the $n \times n$ Chip and the $n \times n$ area it is covering in the $m \times m$ Window

CP_{ij} is a pixel from the known chip

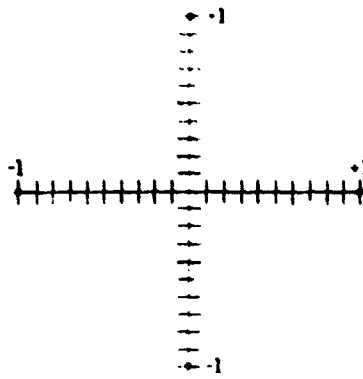
WP_{ij} is the corresponding pixel in the unknown window at this placement

$$\text{Chip Mean} = \frac{\sum_{i=1}^n \sum_{j=1}^n \text{Chip Pixels}}{n^2}$$

$$\text{Window Mean} = \frac{\sum_{i=1}^n \sum_{j=1}^n \text{Window Pixels}}{n^2} \quad \text{for the current placement of the chip}$$

The chip is placed at a trial position of the window, the mean of the window under that position is taken, and the SSDA value for the sum of the absolute differences between chip and window on a pixel-by-pixel basis is determined. The chip is then moved to the next trial position and the process repeated. The best fit is the location where the SSDA value is a minimum. (A perfect match would result in an SSDA value of zero.) Note that the SSDA summation can be terminated when the summation exceeds any previous summation.

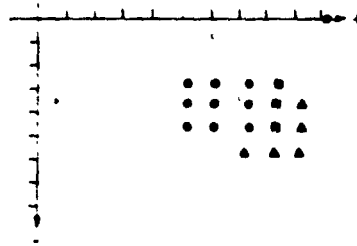
After the best one-to-one match location is determined, the chip is resampled at 0.1 pixel intervals along-line and along-element axes. (Figure 4a.) The minimum SSDA value along each axis is the starting point for off-axis calculations. The nine locations surrounding the intersection of the on-axis minimums are calculated as shown in Figure 4b. After this, values are generated to determine the minimum subpixel SSDA location. Figure 4b shows an example of two additional sets of measurements being required to surround the minimum value (*).



Resample and obtain SSDA along elements and along rows independently.

Figure 4a

ADDITIONAL PAGE IS
OF POOR QUALITY



Resample and obtain SSDA at 9 surrounding intersections of on-axis minimums.

"Chase" minimum until smallest SSDA is located.

Figure 4b

Several resample techniques are well known, among these are nearest neighbor (NN), bilinear and cubic convolution (CC). The nearest neighbor is useless in this application in that it simply duplicates the nearest pixel value and would not produce any change when attempting to generate a new sub-image. Bilinear is a straight line interpolation between adjacent values and has been found to be the best interpolator for discontinuous data where higher order techniques tend to produce unjustifiably "undulating" values. For continuous data, that is, image data where adjacent pixels overlap or nearly overlap, higher order interpolation techniques such as the CC have been found to be highly successful interpolation schemes. The general form of a CC is:

$$P_{n_{\text{new}}} = K_1 P_{n-1_{\text{old}}} + K_2 P_{n_{\text{old}}} + K_3 P_{n+1_{\text{old}}} + K_4 P_{n+2_{\text{old}}}$$

where:

$$K_1 = C_1 - C_2 (1 + dP) + C_3 (1 + dP)^2 - C_4 (1 + dP)^3$$

$$K_2 = C_5 - C_6 (dP)^2 + C_7 (dP)^3$$

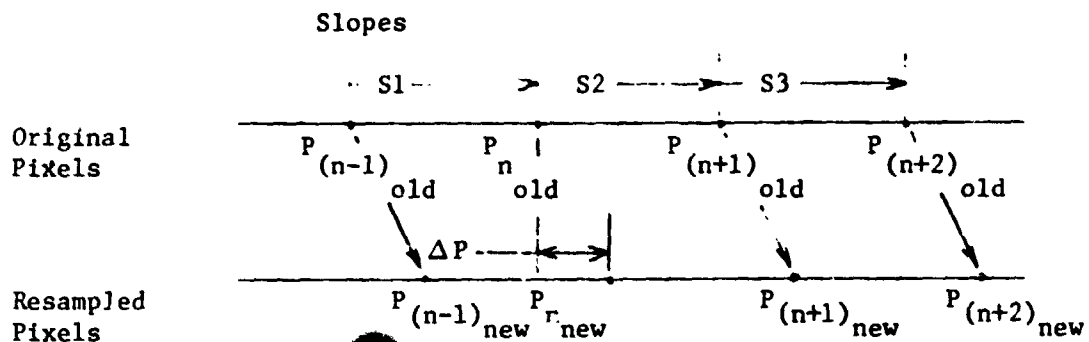
$$K_3 = C_5 - C_6 (1 - dP)^2 + C_7 (1 - dP)^3$$

$$K_4 = C_1 - C_2 (2 - dP) + C_3 (2 - dP)^2 - C_4 (2 - dP)^3.$$

where dP = Subpixel displacement.

Another technique has been found to be highly successful in chip placement. This technique will be called the "bilinear exaggerator" (BiEx). Before a new pixel can be generated, the slopes surrounding the area where the new pixel is to be generated are examined. If a trend is apparent which indicates the new value is not on the slope between the current pixel and its nearest neighbor then the modified slope of the preceding segment is extrapolated to generate the new pixel. (See Figure 5) An example of this case is: if the preceding pixel and the current pixel indicate a slope toward zero value and the next two subsequent pixels indicate a slope away from zero, then a local valley is indicated and the new pixel is generated based upon the slope from the preceding pixel. On the other hand, if there is a trend defined which indicates a continuous change, then a standard bilinear approach is used, i.e., the new pixel is generated on the slope between the current pixel and its neighbor. It should be noted that a new pixel will never be generated that is more than half a pixel distance

away. If the resample is required for greater than 0.5, the resample technique is run in the opposite direction. (Thus a move right of 0.7 is accomplished by calculating a move left of 0.3.) This assures that the exaggerator will not produce unrealistic values. For a two dimensional resample the same technique is used with one exception. To generate a new pixel there exists a term which contains DL times DE, where DL is the move along a line and DE is the move along elements. This term is always treated as a bilinear case. (To continue to use the slopes in either the along-line or along-element direction would introduce a bias which has no physical justification.)



	S1	S2	S3	New Pixel Value
Case 1	+	NA	-	$P_{n_{new}} = P_{n_{old}} + \frac{(S1+S2)}{2} (\Delta P)$
Case 2	-	NA	+	" "
Case 3	∅	-	+	" "
Case 4	∅	+	-	" "
Case 5	+	-	+ or 0	" "
Case 6	-	+	- or 0	" "
All Others	NA	NA	NA	$P_{n_{new}} = P_{n_{old}} + (S2) (\Delta P)$

Figure 5. Resample Technique

As chips are chosen which intentionally contain marked discontinuities (coast lines, cross-roads, etc.) the BiEx proves highly successful as it tends to exaggerate the very discontinuities the chip was chosen for and thus generates a "similarity field" with very sharp edges. Additionally, due to the relative speeds in digital processors, the selection of the proper slope for resampling takes less time than the additional multiplications in the CC technique.

EXPERIMENTAL RESULTS

The use of the SSDA to achieve subpixel accuracies has been examined in a laboratory environment. A PDP 11/45 computer with a video display is utilized. Programs have been written in Fortran with no attempt at optimization with respect to size or speed of execution with one exception. The exception is that a moderate attempt has been made to stay with fixed point arithmetic where ever possible. (The PDP 11/45 does fixed point arithmetic in 2 to 4 μ s. For floating point an add takes approximately 7 μ s and a multiply approximately 10 μ s.) These programs accept magnetic tapes which contain image data from either Landsat or SMS spacecraft. The programs require extensive memory because of the statistic keeping and reporting done in the laboratory environment. The actual Landmark registration programs have been kept isolated however, and require approximately 3000 words (bits) of memory. The whole pixel search requires approximately 750 words and the subpixel search requires an additional 2300 words. The ability to use various resample techniques as well as a classical correlation or SSDA whole pixel search technique is available.

The program allows an operator to select the size of a chip and the size of the window. The following tables give some not untypical timing requirements.

Table I. Whole Pixel Search Timing Requirements

Window Size	Chip Size	Time Required (Seconds)
40 x 40 Pixels	30 x 30 Pixels	8.8
40 x 40 Pixels	26 x 26 Pixels	12.3
40 x 40 Pixels	22 x 22 Pixels	14.3
40 x 40 Pixels	18 x 18 Pixels	14.3
40 x 40 Pixels	14 x 14 Pixels	12.3

Table I. Whole Pixel Search Timing Requirements (Cont.)

<u>Window Size</u>	<u>Chip Size</u>	<u>Time Required (Seconds)</u>
40 x 40 Pixels	10 x 10 Pixels	8.8
32 x 32 Pixels	16 x 16 Pixels	3.6
76 x 76 Pixels	16 x 16 Pixels	69.5

Table II. Subpixel Resample and Search Timing Requirements

<u>Chip Size</u>	<u>Time Required (Seconds)</u>
30 x 30 Pixels	19.0 to 27.0
26 x 26 Pixels	17.0 to 18.0
22 x 22 Pixels	10.0 to 13.0
18 x 18 Pixels	8.5 to 10.0
14 x 14 Pixels	4.5 to 6.0
10 x 10 Pixels	2.5 to 3.0

The times shown in Tables I and II reflect the experimental mode of operation where each SSDA is summed to completion so that analysis may be done on the approach to the minimums. The programs may also be run with the SSDA terminated whenever a previous minimum is exceeded. Experiments show that a 6 to 1 improvement in execution time is achieved in this mode. (In this mode a seed value is calculated based upon the mean value of the chip.) Additionally, analysis of the execution of the programs indicates that a 3 to 1 improvement in run time can be achieved if the resample algorithm is linked to the SSDA such that only enough pixels are resampled to provide input to a terminating SSDA.

The results of numerous runs shows that the SSDA will whenever possible find a correct match when the subpixel algorithm is included. That is to say, the whole pixel SSDA results occasionally point to an adjacent whole pixel location; however, the subpixel algorithm will then work its way to the proper location. Thus a subpixel offset of 0.7 pixel indicates a better match closer to the adjacent pixel than to the minimum valued one.

Experiments with unrecognizable chips (heavy cloud cover on the window tape where the chip was chosen from a cloud-free tape) show that the SSDA exhibits a characteristic wandering when no match is available. Calculations in the program cause a "No-Match" indicator to be set under these conditions. Experiments with chips which were purposely chosen to be of questionable quality (partial cloud cover, one dimensional characteristics) indicate that the SSDA is sensitive to slight misregistrations and has characteristics which allow a "quality" value to be placed upon any given match.

Figure 6 shows typical SSDA responses to an excellent chip (clear, two dimensional characteristics) a poor chip (partial cloud cover on chip or window or one dimensional characteristics) and an inadequate chip (heavy cloud cover or a nondescript chip selection).

Experimental Conclusions

While we are still in the process of developing such experimental knowledge as the correct size of the chip and the optimum resampling techniques, some tentative conclusions can be reached. The three most important are:

The SSDA will generate a minimum value at the correct location to ± 0.1 pixel with continuous input data. (However, note that the effect of all possible noise sources has not yet been included in the laboratory experiments.)

The SSDA will generate a unique profile that indicates the quality of the match.

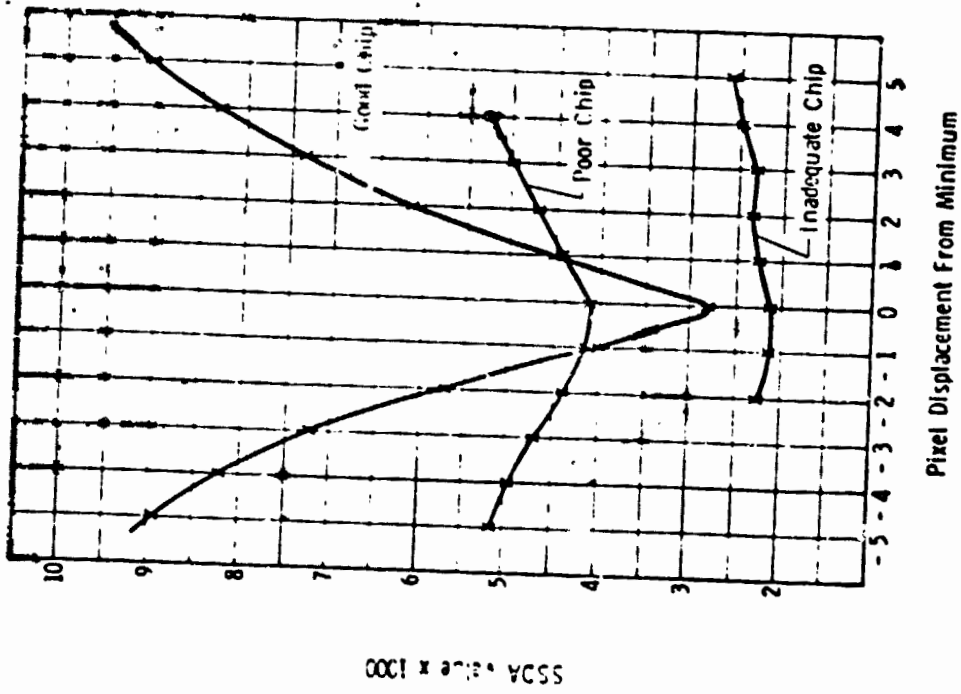
The search pattern for the best subpixel location works in all cases; there is no need to generate every possible subpixel value.

IMPLEMENTATION

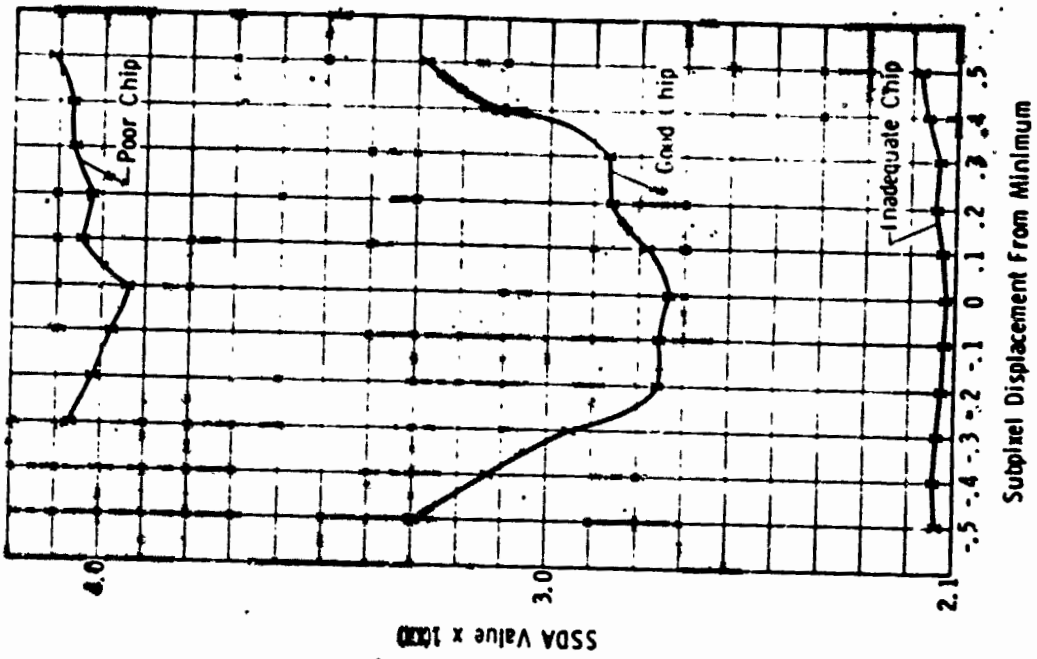
Overview

The Sequential Similarity Detection Algorithm (SSDA) described in the previous section lends itself for parallel processing. A mult-microprocessor system (MMS) is proposed to implement the SSDA. Simple processing elements with only moderate processing power are proposed because of the elementary nature of the computations involved. The MMS is well suited for space-borne applications:

Using a serial conventional computer to implement the SSDA poses three main problems; weight, power and space. Although most conventional computers have a large processing power, they are not suitable for space-borne applications due to their high volume, weight and power consumption. It is not practical, from the point of view of real time



• SSDA VALUES VS DIE PIXEL DISPLACEMENT OF THE CHIP



• SSDA VALUES VS SUBPIXEL DISPLACEMENT OF THE CHIP

Figure 6. Typical SSDA Values for Three "Qualities" of Chip

response, to use single processor, either. Therefore the authors have proposed a light weight, low power multi-microprocessor system. It is estimated that the MMS will be able to process the data received from the Image System and provide response to Guidance and Control System almost in real time.

The main point of this section is to show that with currently available microprocessors and RAM memory devices a system can be economically developed for Autonomous Landmark Navigation and Attitude Reference task on-board rather than using ground support computer. An estimate is made of the time and cost required to solve this problem on the proposed system and compared with the simulation values obtained for a DEC PDP 11/45.

The following sections describe the MMS salient hardware and software features. It is a system tailored to a specific application, i.e. implementation of SSDA, and no generality is intended. The overall system diagram is shown below, in Figure 7.

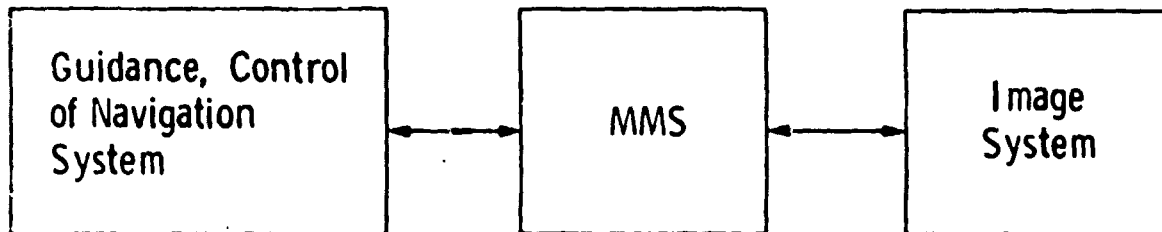


Figure 7. Overall System Diagram

The scope of this section is limited to describing the processing function of the MMS. Other necessary features for a space-borne application such as fault-tolerance, ruggedized design and downloading communications interface are reserved for future study.

Architecture

The following set-up is proposed for on-board implementation of the SSDA, using the MMS, Guidance and Control System and Image System.

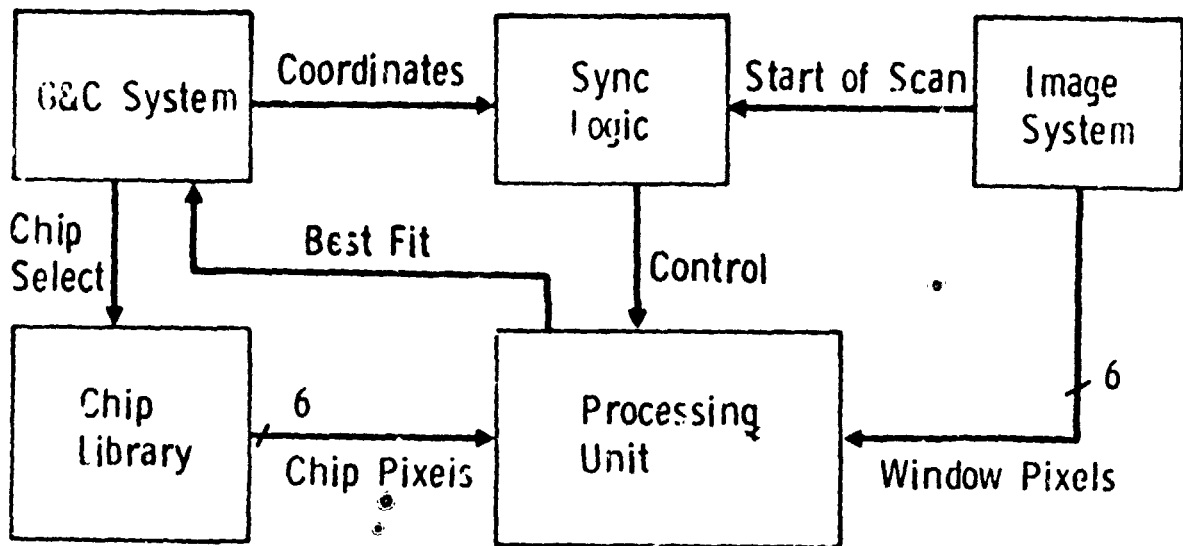


Figure 8. System Block Diagram

The MMS comprises of Processing Unit (PU), Synchronization Logic (SL) and Chip Library (CL). Figure 8 shows System Block Diagram with interconnections of the MMS elements to the Image System and Guidance & Control System. This paper assumes that the following inputs are available to the MMS.

Image System : The image system views a strip of 240 Km width on the earth surface. The picture is quantized into gray scale values. The scanning mechanism scans along the width of the strip and outputs 6 pixel values in parallel. One scan contains (6 x 3000) pixels and takes about 70 milli-seconds. The pixel values are eight bit quantities and vary from X'00' through X'FF'. Here X denotes hexadecimal values. The image system also sends a signal to indicate start of a scan, and a signal to indicate transmission of a pixel.

G & C System : The Guidance, Control of Navigation System outputs coordinates indicating when in a scan the MMS should start collecting Window pixel data received from the Image System. The G & C System also outputs Chip Select information so that the MMS can pull the chip data from library and store it in memory modules M1 through M6. Input to the G & C System is a set of coordinates

(x, y) indicating where in window the best fit occurred for a given chip. These coordinates are with respect to the window position output by the G & C System. The G & C System, then, may take any necessary navigation and attitude reference corrective action.

Synchronization

A synchronization logic is a unit of the MMS that interfaces to the G & C System and the Image System. Its function is fully implemented in hardware, mainly because of the simplicity and invariance of the function.

It is assumed that the G & C System will send the following data to locate a window

- (1) Number of scans to elapse from now
- (2) Pixel number in the scan of interest where the window starts.

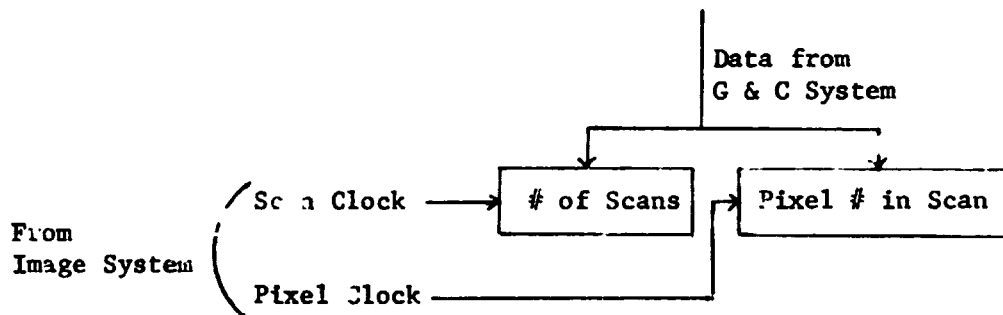


Figure 9. G and C System

The G & C System will set up two registers in the synchronization logic as shown in Figure 9. These registers are simple count down registers using appropriate clocks from the Image System as shown in the above figure. When the "Number of Scans" register reduces to zero, the "Pixel number in scan" register starts counting down. When the later reduces to zero a "start" control signal is sent to the PU.

Chip Library

The Chip Library unit of the MMS holds pixel data for chips. The number of chips should be sufficient for Landmark Navigation and Attitude Reference task all over the surface of the earth. The authors

propose to implement the Chip Library using bubble memory technology, because it is a more reliable and compact auxiliary memory unit as compared to the error prone magnetic tape unit. Table III below shows performance of a TI magnetic-bubble memory system.¹⁰

Table III

Capacity	92	Kilobytes	
Weight	0.69	lb	
Volume	38	in ³	
Transfer rate	44	kb/s	
Power dissipation	11.5	Watts	
Hard error rate	10 ^{-9nd}	per bit	n = years residence time d = operating duty cycle

One 92 Kilobyte memory system is sufficient for 92 30 x 30 chip or for 276 18 x 18 chips. Further study is required to determine size and number of chips necessary for the Navigation and Attitude Reference problem.

Processing Unit

The Processing Unit is the most important unit of the MMS. Figure 10 shows Organization of the Processing Unit. There are two types of main components: Processing Elements (PE) and Memory Modules (M). The PEs are arranged to process parallel data received from the Image System and from the Chip Library. They are also arranged to form a pipeline to process received data. The Memory Modules are used to hold and transfer data from one processor to another.

Processing Element: A Processing Element consists of a 8-bit, fixed-instruction-set microprocessor. We have chosen 8-bit wide microprocessor because the pixels are 8-bit wide. However, the microprocessor must have instructions to manipulate 16-bit data because the SSDA values are 16-bit wide. The third requirement is to have at least 2 index registers to effectively manipulate window and chip data, each stored in a matrix form. There are number of microprocessors currently available and the authors think that Zilog Z-80 microprocessor¹¹ suits well for the Processing Element. We have chosen a fixed-instruction-set microprocessor as against a microprogrammable processor because the MMS is to perform a well defined dedicated function rather than to be used for general purpose processing tasks. The choice also reduces space requirement. Each of the Processing

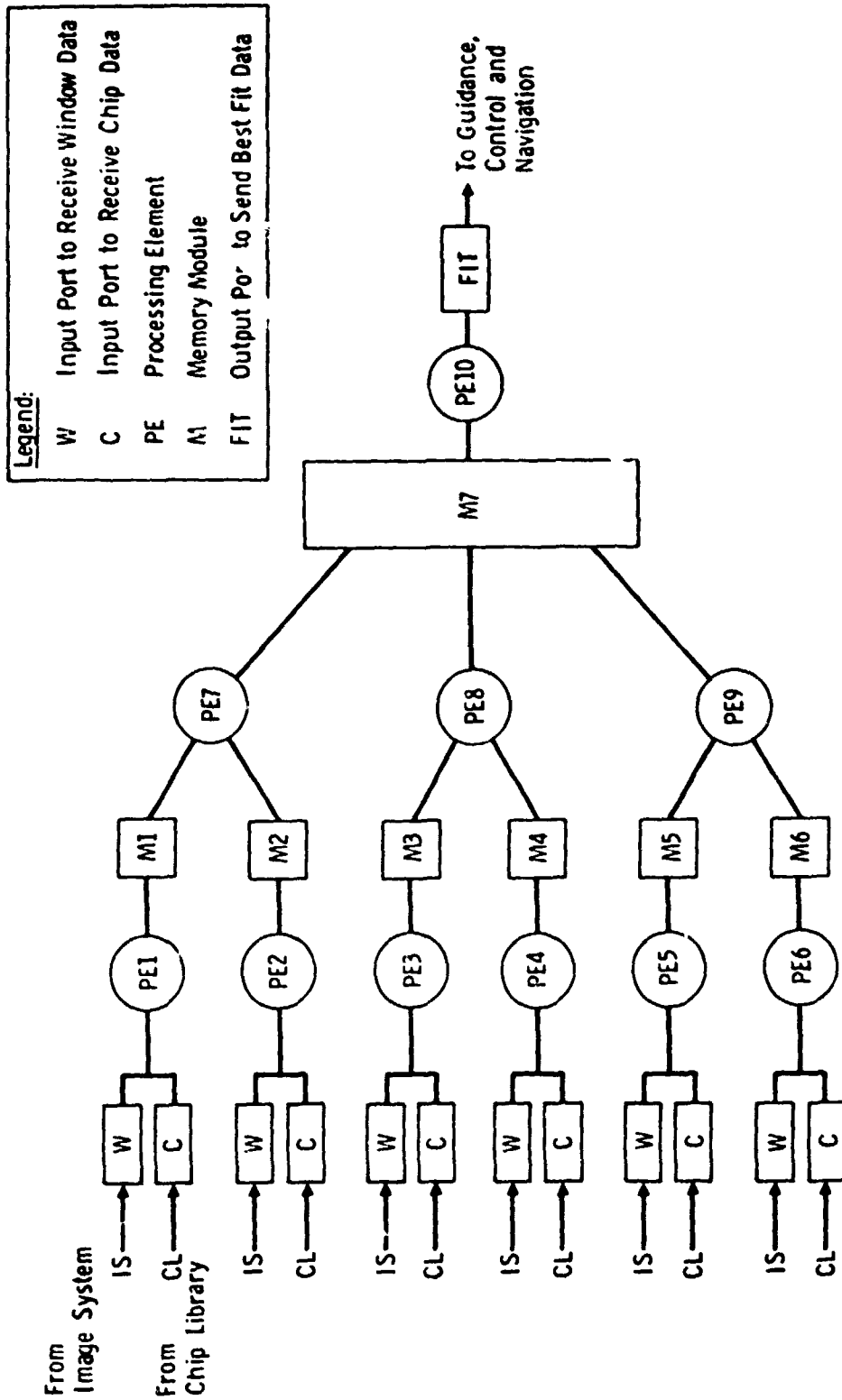


Figure 10. Processing Unit

Elements PE1 : PE6 has two input ports. One input port is to get chip pixel data from the Chip Library unit. Other input port is to get window pixel data from Image System. The Processing Elements PE7 : PE9 do not have any I/O port. The Processing Element E10 has one output port to send best fit coordinates to the G & C System. Each of the microprocessors has an address space of 64 K bytes. This space is divided into three categories: Read only Memory (ROM), local memory and shared memory. The ROM holds program to handle power up, down loading etc. The local memory holds part of a program peculiar to the microprocessor to implement the SSDA algorithm. The local memory also holds local data.

Shared Memory

The shared memory holds data that is to be transferred from one processor to another. The shared memory modules are labeled M1 through M7 in Figure 10. The details are shown in Figure 11.

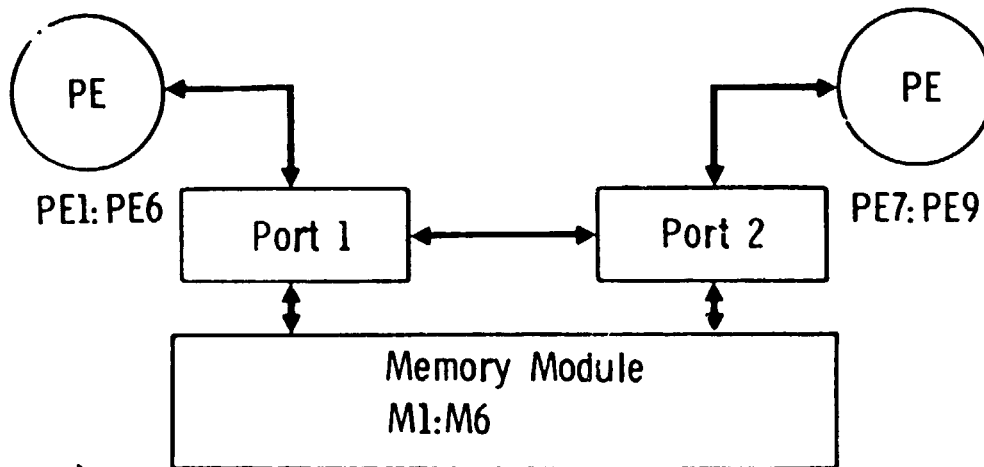
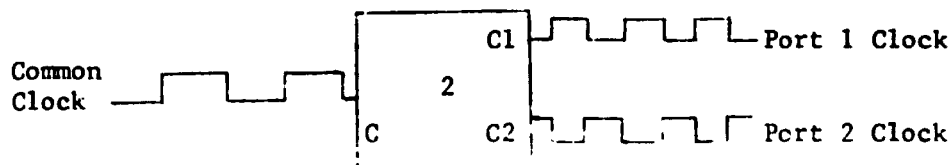


Figure 11. Dual Port Shared Memory Module

A shared memory module has two (for M1 : M6) or four (M7) ports connected to the microprocessors. We describe operation of a 2-port memory which is similar to 4-port memory module. Two ports are controlled by clocks derived from a single clock as shown below.



Memory access requests from microprocessors are sampled at the, say, rising edge of the clock. Once a request is detected from one microprocessor, requests from other microprocessor are blocked by sending WAIT signal to that microprocessor. Once the request from the first microprocessor is completed, second microprocessor is allowed to access the memory. This technique assures mutual exclusiveness of memory accesses in shared memory module from two microprocessors.

An example is shown below to illustrate the point.

Let ADRF = address of flag in shared memory
 ADRD = address of data in shared memory

Assume that the flag is reset. Data is to be passed from PE1 to PE7. Assuming Zilog Z-80 microprocessor instruction set, the following codes accomplish the task.

<u>PE1</u>		<u>PE7</u>	
LOOP1	LD (ADRF)	LOOP7	LD (ADRF)
	ADD A		ADD A
	JP NZ, LOOP1		JP Z, LOOP
	LD (ADRD), HL		LD HL, (ADRD)
	LD A, 1		LD A, 0
	LD (ADRF), A		LD (ADRF), A

In the example, the loop at LOOP1 assures PE1 that previous data is processed by PE7. Then PE1 stores data to be transferred at (ADRD) and sets a flag at (ADRF). The loop at LOOP7 assures PE7 that the data to be transferred is available. Then PE7 gets that data and resets a flag to indicate to PE1 that next data can be transferred.

Parallel Processing

We consider some programming aspects in this section. We describe a few steps of the SSDA algorithm to show the parallel nature of the processing involved. Two processing steps, Input and SSDA computation, are shown in Figures 12 and Figure 13 respectively. Horizontal lines indicate process, whereas blanks indicate idle time. Figure 12 shows that the process PE1 : PE 6 starts after receiving a signal from the Synchronization Logic. All 6 microprocessors accept data from the Image System in parallel and store it in their local memories. Each microprocessor is programmed to accept the number of pixels equal to the length of the window along the scan direction. Then each processor computes partial sums from the data just received. If we have a $m \times m$ window and $n \times n$ chip, then $(m-n+1)$ partial sums have to be computed per scan. Then the microprocessors wait till a "continue" signal

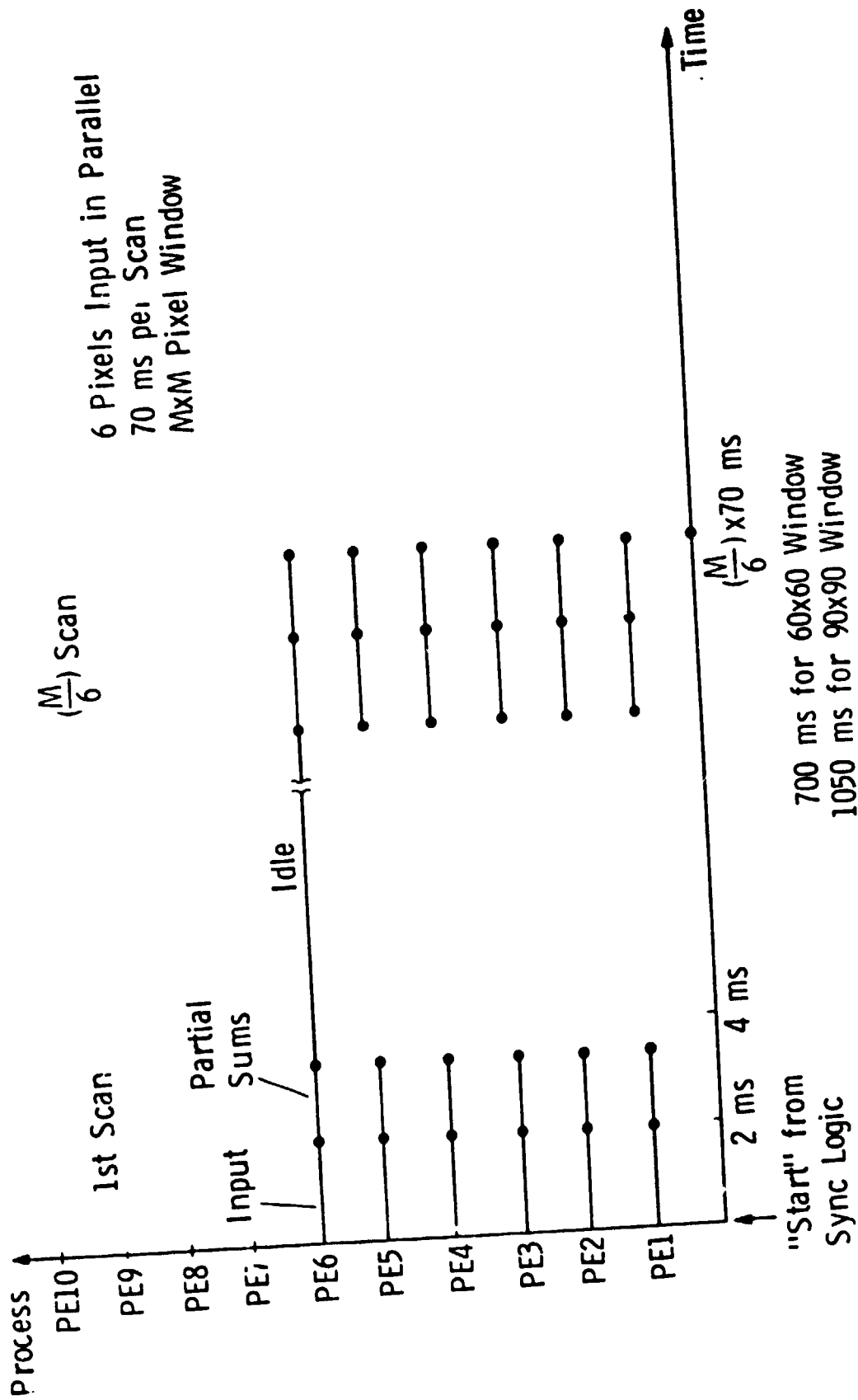


Figure 12. Parallel Processing : Input Window Pixels

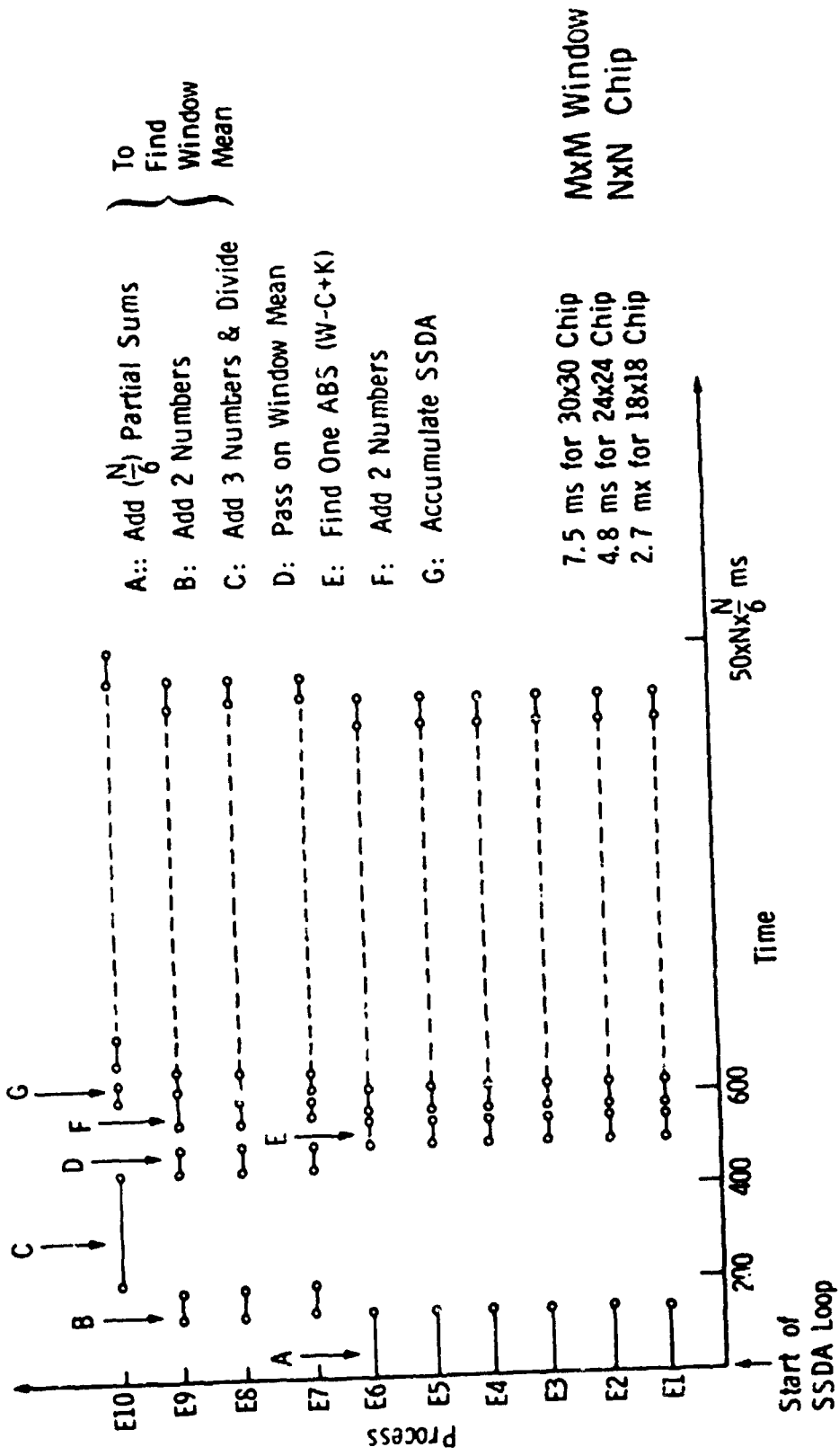


Figure 13. Parallel Processing : SSSA Computation

is received from the Synchronization Logic. The microprocessors repeat same operation until $\left(\frac{m}{6}\right)^{th}$ scan is completed.

During the Input step, microprocessors P7 : P10 are idle. However, they are active during the SSDA computation and subsequent steps. Figure 13 shows SSDA computation step split into 7 separate processes, A through G. We assume that the top of window corresponds to top of the first scan. To compute a SSDA value, the first step is to find a Window Mean, i.e. to add $(n \times n)$ window pixels at current coordinates and divide by n^2 . Add operation reduces to adding n partial sums that were computed during the previous step. For each microprocessor the operation further reduces to adding $\left(\frac{n}{6}\right)$ partial sums. In the next process, B, microprocessors E7 : E9 add numbers supplied by E1 : E6 and pass on 3 numbers into M7. In the third process, C, microprocessor E10 adds 3 numbers as they become available and divides the sum by n^2 . Since it is an unsigned division and overflow, underflow conditions are ruled out, the division algorithm is simple, and takes less than $200\mu s$ for 4 MHz Z-80 microprocessor. The Window Mean obtained in E10 is passed on to E1 : E6 by E7 : E9 in process D.

Once the current Window Mean value is available in E1 : E6, a pipeline-like process is started. The microprocessors E1 : E6 compute the ABS $(W-C+K)$ value, E7 : E9 add 2 numbers and pass on sum to E10 which accumulates sums to form a SSDA value for the current coordinates.

PERFORMANCE PREDICTIONS

Although it is almost impossible to analyse complete performance of the MMS here, we give below results of some timing calculations pertaining to two SSDA algorithm steps described in the Parallel Processing section. For our calculations, we have assumed a 4 MHz, Zilog Z-80 microprocessor to be used in a Processing Element. We have also assumed window and chip sizes to get some figures from the formula.

	= m x m =	= n x n =
Window	Size 90 x 90 pixels	Chip size 30 x 30 pixels

Input

Image System: Sends 6 pixels (bytes) in parallel
Total bytes sent = (6×3000) in 70 ms.

$$\# \text{ of scans of interest} = \frac{m}{6} = \frac{90}{6} = 15$$

$$\text{Input time} = \frac{m}{6} \times 70 = 15 \times 70 = 1050 \text{ ms.}$$

MMS:
(E1 : E6) 6 microprocessors accept data in parallel at the Image System rate of about $20 \mu\text{s}$ per pixel, although they can accept at a faster rate of $10 \mu\text{s}$ per pixel. Input time per scan = $m \times 20 = 90 \times 20 \mu\text{s} = 1.8 \text{ ms}$
Partial sums per scan = $m-n+1 = 61$
Time to find partial sums = $(m-n+1) \times 25 \mu\text{s} = 1.5 \text{ ms}$
Idle time per scan = $70 - 1.8 - 1.5 = 66.7 \text{ ms}$

Window Mean

E1 : E6 Each processor adds $(\frac{n}{6}) = 5$ partial sums
Time required = $150 \mu\text{s}$.
E7 : E9 Add 2 numbers & pass on sum = $25 \mu\text{s}$
E10 Add 3 numbers & divide = $250 \mu\text{s}$
E7 : E9 Pass on window mean to M1 : M6 = $15 \mu\text{s}$

SSDA Computation

E1 : E6 To find one ABS (W-C+K) value = $50 \mu\text{s}$
Total time = $n \times \frac{n}{6} \times 50 = 30 \times \frac{30}{6} \times 50 \mu\text{s} = 7.5 \text{ ms}$
E7 : E9 Add 2 ABS values and store it in M7
No extra time due to pipeline effect.
E10 Accumulate sums of ABS values, to form SSDA value, for current coordinates. No extra time due to pipeline effect.

Total time to find coarse location of best fit is equal to $7.5 \times (m-n+1)^2 = 7.5 \times 3600 = 27.0$ seconds which compares favorably with 70 seconds obtained on PDP 11/45 for a Fortran program written for 76×76 window and 16×16 chip.

We list below the main components needed to build hardware for proposed multi-microprocessor system. The cost given is approximate and does not include hardware/software development efforts.

For a 90×90 pixel window and 30×30 pixel chip, the MMS needs following memory capacity.

Local Memory : PE1 through PE6 = 4 Kbytes each
PE7 through PE9 = 1 kbytes each
PE10 = 8 kbytes each

Shared Memory : M1 through M6 = 1 Kbytes each
M7 = 4 Kbytes each

Total Memory size = 45 Kbytes

Using a 1 x 1 k military temperature range RAM chips at about \$8 each (including addressing logic) gives us an estimate of \$3600.

Cost of 10 microprocessors and support chips at \$300 each gives us an estimate of \$3000.

Early price of one bubble memory device (TI 92 k bits)¹² was quoted at \$200 and is expected to drop in 1978.

The power consumption is expected to be of the order of 70 -75 watts. The approximate break up is 15 - 20 watts for microprocessors, 20 watts for RAM, 15 watts for bubble memory, and 20 watts for other logic chips.

The weight of the MMS is estimated to be of the order of 20 -25 lbs. including bubble memory and chassis.

99 N79-14130

AUTONOMOUS SATELLITE ORBITAL
NAVIGATION AND ATTITUDE DETERMINATION

Shing Peter Kau

Avionics Division
Honeywell Inc.

ABSTRACT

A known linear landmark navigation system is described in this paper. It involves the use of an electro-optical sensor to provide sightings to linear earth features such as highways and coast lines. The sensor concept and the navigation system mechanization are described. Performance analysis results show that landmark sightings provide accurate navigation update and that this accuracy can be preserved using radar altimeter measurements.

Description on a stellar inertial attitude determination system is also presented. Attitude reference performance consistent with the requirement of the navigation system is shown to be achievable by this method.

1.0 INTRODUCTION

This paper describes methods of autonomous satellite navigation and attitude determination using on-board sensing and processing capabilities. Sensor concepts, system mechanization approaches, and projections of navigation and attitude reference performances are presented. The paper is divided into two parts for separated discussions on the navigation and attitude determination problems.

2.0 AUTONOMOUS NAVIGATION VIA LANDMARK SIGHTINGS

Satellite navigation using known or unknown earth landmarks have been intensively explored in the past, References 1, 2 and 3. Navigation information is derived from tracking known or unknown landmarks. This implies that the landmark sensor will be required with large or movable Field of View (FOV) and that the landmark will be a point target or small area with distinct signature having well defined centroid. For low altitude orbital applications, known landmark navigation approaches typically are less sensitive to pointing errors than the unknown landmark approaches. Requirements on attitude reference and landmark sensor accuracy are therefore less stringent. The unknown landmark approaches, on the other hand, are attractive in that the task of landmark identification can be eliminated, thus relieving the requirements on storage of landmark signatures.

The autonomous navigation method considered here uses such known linear earth features including highways and coast lines as candidate landmarks. Due to their long physical dimension, strap-down sensor with relatively small FOV can be mechanized for detection of landmark crossings. Being a known landmark approach in nature, the proposed method has the advantage of low sensitivity to pointing errors. Thus, the design requirements for the landmark sensor are quite relaxed. Also, the simple signature of linear features does not require extensive storage for known landmark catalog.

2.1 SENSOR CONCEPT

The landmark sensing down sensor is an electro-optical device. It consists of a telescope that images earth surface features onto two linear silicon detector arrays which are separated by 3 degrees and oriented 45 degrees with respect to the direction of nominal image motion as depicted in Figure 1. Due to the cross array component of image motion, the FOV of detectors over terrain scenery sidesteps from scan to scan. Hence, two dimensional discrete images of terrain scenery can be created from successive samplings of detector cell readouts. These digital images are processed to derive landmark sighting information for system navigation update.

The measurement provided by the down sensor is the LOS-vector to the centroid of the segment of a linear earth feature that falls into the sensor FOV. This is obtained from processing the discrete image for detection of the presence of a linear feature and for extraction of the feature orientation and the segment centroid location. Due to the deterministic signature of linear landmarks, deterministic image processing techniques such as thresholding and edge enhancement are used. The data processing techniques and potential sensor accuracy will be demonstrated through the discussion of simulation data for a test case.

The test case involves viewing a road of 50 ft width from 100 n.m. altitude under a 45 degree sun angle lighting condition. The linear feature is characterized by pavement with uniform reflectivity of 0.5. The background is represented by an exponentially correlated spatial process with correlation distance of 500 ft, mean reflectivity of 0.25, and standard deviation of variation of reflectivity of 0.08. A portion of the simulated original scene is shown in Figure 2a. with each letter representing the reflectivity, in steps of 0.1, of the elementary area ($\approx 20 \times 20 \text{ ft}^2$). The down sensor detector cell width, scaled to 37 arc seconds, has a ground projection of approximately 110 ft. With an array scan rate of 1000 Hz, the FOV of a detector in consecutive scans has an overlap of 5/6 of a cell width. This overlap of FOV, together with the multilevel cell readout, allows a limited degree of improvement of image resolution. A super-positioned image created from consecutive scans of the array cell readouts is shown in Figure 2b. The terrain radiometry, detector and electronics noises, and the 3-bit quantization of cell readouts have been fully simulated. The result obtained from a simple thresholding operation

is shown in Figure 2c. Finally, a directional gradient operation is performed on the resulting image shown in 2c to yield Figure 2d with the linear feature significantly enhanced. The directional gradient is defined as the dot product between a prespecified unit vector \underline{S} and the gradient vector ∇W of the image function $W(X,Y)$. With $W(X,Y)$ treated as mass densities, the center of mass, the moment of inertias and the principal axes are computed. To facilitate the detection of the presence of linear feature, a shape factor is computed as the ratio of moment of inertias about the principal axes. The center of mass provides the information of the location of the centroid of the linear feature segment. The orientation of the linear feature is provided by the principal axes. A summary of the results obtained from the feature detection and extraction processing on the three images generated from the intermediate steps of enhancement is presented in Table 1.

2.2 AUTONOMOUS NAVIGATION SYSTEM MECHANIZATION APPROACH

The autonomous navigation system concept described in this paper consists of a down sensor for landmark sighting, an on-board computer and resident software, a long term stable clock, a radar altimeter, and an attitude reference subsystem. A functional block diagram description of the system concept is shown in Figure 3. The nominal navigation solution is computed through the integration of vehicle equation of motion using modeled accelerations (drag, gravity). Due to errors in the initial conditions and uncertainties in the acceleration models, the error buildup of the nominal navigation solution requires periodic updates using sensor measurements. These include the down sensor known landmark crossing detection and the altimeter altitude measurements. The optimal implementation of these measurements calls, naturally, for the application of Kalman filtering techniques. An important operation involved in any approach of known landmark navigation is that of landmark identification. The system mechanization approach will be outlined in the following in terms of the interpretation of down sensor measurement geometry required in the Kalman filter formulation for implementing these measurements and the data processing flow of the landmark identification procedure.

2.2.1 Kalman Filter Formulation

The measurement provided by down sensor is the LOS-vector, denoted as \underline{L} , to the center of the segment of the linear feature that falls into the sensor FOV. Since the sensor FOV is small compared with the length of a linear landmark, the exact point where the sensor LOS intercepts the linear feature is ambiguous. To circumvent this ambiguity, a miss distance is computed from the LOS-vector measurement prior to Kalman filter navigation update processing.

Let the vehicle position vector be \underline{R}_v and the intercept of \underline{L} with the linear landmark be \underline{I} (the target) as depicted in Figure 4. The target position can be computed as:

$$(\bar{T}^I) = S_R(\bar{L}^I) + (\bar{R}_V^I) \quad (1)$$

where the notation convention is such that (\bar{X}^I) denotes the inertial-frame coordinates of a given vector \underline{X} . The slant range can be computed as:

$$S_R = -(\bar{R}_V^I)^T(\bar{L}^I) - \left\{ r_e^2 - (\bar{R}_V^I)^T(\bar{R}_V^I) + [(\bar{R}_V^I)^T(\bar{L}^I)]^2 \right\}^{1/2} \quad (2)$$

where r_e is earth radius, superscript T denotes matrix transpose and

$$(\bar{R}_V^I)^T(\bar{L}^I) \triangleq \underline{R}_V \cdot \underline{L}$$

Let \underline{N} be the unit vector normal to the plane containing the linear landmark. The miss distance between the projected down sensor target point and the linear landmark is computed as the dot product,

$$d \triangleq (\bar{T}^I)^T(\bar{N}^I) \quad (3)$$

In the case where perfect knowledge of vehicle position and LOS-vector were involved in the evaluation of equations (1), (2) and (3), the resulting miss distance would be identically zero. The actual value of dot product reflects errors existed in the a priori knowledge of vehicle position, attitude, and down sensor LOS-vector measurements. A formal expression that relates miss distance to errors in navigation $(\Delta \bar{R}^I)$ attitude $(\Delta \bar{\alpha}^B)$ and sensor errors (\bar{n}) is given as follows:

$$d = H_1(\Delta \bar{R}_V^I) + H_2(\Delta \bar{\alpha}^B) + H_3(\bar{n}) \quad (4)$$

Actual expressions for H_1 , H_2 and H_3 can be obtained by differentiations of equations (1), (2) and (3).

2.2.2 Landmark Identification

The linear landmark involved in a down sensor measurement must be correctly identified to enable the extraction of useful navigation information from landmark sightings. A landmark catalog will be carried on-board to facilitate the identification procedure. Each linear landmark is defined within the catalog in terms of the location of a reference point and the orientation of the feature with respect to local north.

Upon a down sensor linear feature detection, candidate landmarks in the vicinity of the projected sensor FOV will be tested in two steps for identification. First, the orientation of candidate landmarks will be compared against the measured feature orientation using a threshold established from expected attitude reference and feature orientation measurement errors. Miss distances to the candidate linear landmarks that survive the orientation screening are then computed. The miss distance, in

general, consists of two components. First, the actual miss from sensor target point to the candidate landmark. Second, the equivalent miss contributed by errors in the a priori navigation and attitude information and the sensor measurements. For the correct candidate, the first component is identically zero.

The level of the second component can be predicted from the navigation and attitude covariance matrix evaluated as part of the Kalman filter computations. By careful selection of candidate landmarks to avoid sightings from congested areas, the first component of the miss distance to incorrect candidate can be made considerably larger than the second component. This permits the discrimination between the correct and the incorrect candidates. A reasonableness test on the miss distance can be devised using a threshold computed from the statistics of a priori errors.

The down sensor landmark measurement will be implemented for navigation if, and only if, a unique candidate is identified.

A flow diagram summary of the landmark identification procedure is contained in Figure 5.

2.3 NAVIGATION PERFORMANCE ANALYSIS

The known linear landmark navigation performance results presented in this section were obtained assuming a system that employed only one down sensor looking along the yaw axis of a local vertically stabilized vehicle. The down sensor errors are characterized by 0.15 mrad white noise and 0.15 mrad bias. The assumed attitude reference errors consisted of 0.15 mrad random noise and 0.15 mrad bias. A 9 state Kalman filter was assumed for navigation update using down sensor landmark sightings and radar altimeter measurement of vehicle vertical position. State variables considered in the filter formulation included 3 position, 3 velocity and 3 residue errors for acceleration modelings. The ground track of the reference orbit used for performance analysis is plotted in Figure 6 indicating the down sensor landmark sighting schedule and the times altimeter is activated. The altimeter is activated only over ocean where the mean geoid height can be accurately modeled. Figure 7 contains the plots of the 3 axes RSS position errors from two covariance analysis runs. The curve labeled (a) is obtained implementing the landmark sightings scheduled for all two orbits. The curve labeled (b) is obtained implementing only the landmarks encountered in the first orbit. These results show that accurate navigation information can be derived from down sensor landmark measurements. Also, the navigation accuracy can be preserved over an extended period of orbital flights without additional landmark sightings. An implication of this is that the frequency of landmark sightings required for high accuracy autonomous navigation can be rather small. System errors assumed in generating these performance results are summarized in Table 2.

3.0 AUTONOMOUS ATTITUDE DETERMINATION VIA STAR SIGHTINGS

Satellite attitude determination can be accomplished by the integration of the vehicle rates measured by a set of body fixed gyros. However, this attitude solution will diverge with time due to gyro drift errors. Periodic stellar updates can remove this attitude error build up and result in a high accuracy system suitable for applications with extended mission duration.

The stellar-inertial system considered here consists of a body mount star sensor, a set of three nominally orthogonal gyros, and an on-board computer. The star sensor consists of a telescope with a set of six detector slits placed on its image plane as depicted in Figure 8. A transit pulse is produced when the image of a star moves across a detecting slit. The basic star sensor measurement is the precise time when the star transit occurs. Kalman filtering technique is employed for optimal implementation of stellar attitude update. The descriptions of the update mechanization and the performance analysis results are presented in the following paragraphs. These results are included to support the attitude reference system error budgeted in preceding analysis of autonomous navigation performance.

3.1 STELLAR UPDATE MECHANIZATION

The autonomous attitude determination approach considered here involves the solution of vehicle nominal attitude and the update of this nominal attitude with star sensor transit time measurements.

From the geometry shown in Figure 8, the condition for the star transit is described by the equation:

$$d = \underline{N} \cdot \underline{S} = 0$$

Where \underline{S} is the LOS-vector to the transit producing star, \underline{N} is a unit vector normal to the plane containing the detecting slit.

To implement the transit measurement for attitude update, the dot products for all candidate stars and slits are evaluated using the nominal attitude T_{BI}

$$d_{ij} = (\underline{N}_i^B)^T T_{BI} \left(\underline{S}_j^I \right) \Big|_{T_r} \quad (5)$$

where

\underline{N}_i = normal vector for i^{th} detector slit,

\underline{S}_j = LOS to j^{th} candidate star

T_r = measured transit time.

The star and slit identification is accomplished by comparing all the dot products for a reasonableness test. Similar to previous discussions on landmark identification, the dot product here consists of two components. The first component is the angular miss distance between the candidate star and slit. This is identically zero for true transit producing star and the true detecting slit. The second component is due to errors in the nominal attitude solution and in the detected time of star transit.

The candidate dot products are compared with a threshold computed based upon the covariance matrix evaluated in the attitude Kalman filtering computations. The success of this identification procedure lies in the fact that attitude errors are small when compared with angular spacing between detectable stars.

Here, again, the on-board star catalog can be tailored to avoid congested regions in the celestial sphere. The star transit will be implemented for attitude update if, and only if, the star and the slit are uniquely identified.

The dot product evaluated for the true transiting star and detecting slit provides a scalar measurement of the error in the nominal attitude solution. Through first order perturbation of equation (5), the value of dot (perturbed from the true value of zero) is related to attitude errors as:

$$d = (\underline{N}^B)^T \Delta T_{BI} (\underline{\xi}^I) = -(\underline{N}^B)^T S[(\underline{\xi}^B)] (\Delta \underline{\alpha}^B) \quad (6)$$

where

$$(\underline{\xi}^B) = T_{BI} (\underline{\xi}^I)$$

$$\Delta T_{BI} \triangleq S[(\Delta \underline{\alpha}^B)] T_{BI}$$

$$(\Delta \underline{\alpha}^B) = (\Delta \alpha_x, \Delta \alpha_y, \Delta \alpha_z)^T$$

= roll, pitch, yaw attitude errors,

$$S[(\Delta \underline{\alpha}^B)] = \begin{bmatrix} 0 & \Delta \alpha_z & -\Delta \alpha_y \\ -\Delta \alpha_z & 0 & \Delta \alpha_x \\ \Delta \alpha_y & -\Delta \alpha_x & 0 \end{bmatrix}$$

Equation (6) defines the attitude error observation provided by star sensor transit measurements. A Kalman filter can be formulated on the basis of this equation to implement the sensor for attitude update. A block diagram showing the stellar attitude update processing is shown in Figure 9. Details on the development of the filtering equations can be found in Reference 4.

3.2 ATTITUDE REFERENCE PERFORMANCE ANALYSIS

The stellar inertial attitude reference performance results presented in this section were obtained assuming a system that employed only one star sensor with its LOS pointed outward 30° off the vehicle pitch plane. The star sensor errors are characterized by 0.05 mrad white noise and 0.05 mrad bias error. A 6 state (3 attitude and 3 gyro bias) Kalman filter was assumed for attitude update using the star sensor transit measurements. Figure 10 contains the plots of the 3 axes RSS attitude errors from two covariance analysis runs. The curve labeled (a) is obtained assuming a local vertically stabilized vehicle. The curve labeled (b) is obtained assuming an attitude maneuver for star transit acquisition. The convergence characteristics is significantly improved. This maneuver, depicted in Figure 11, is designed to acquire complete observability on the six attitude and gyro bias states. The observability analysis leading to the selection of this maneuver can be found from Reference 4. Numerical values assumed in these analyses for various attitude reference system error sources are summarized in Table 3. Notice that the attitude reference performances presented in Figure 10 are consistent with that allocated in the navigation analysis.

4.0 SUMMARY AND CONCLUSIONS

Methods for autonomous satellite navigation using known linear landmark sightings and attitude determination using stellar-inertial sensor measurements have been presented in the above discussions. Performance analysis results obtained for the proposed autonomous navigation approach show that sightings to linear landmarks provide highly accurate navigation updates. Also, it is shown that the navigation accuracy can be preserved over extended periods of landmark free orbital flights using radar altimeter measurements. Frequency of landmark sightings necessary to satisfy given navigation performance goals can thus be relieved. Performance analysis results obtained for the stellar-inertial attitude reference system show that accuracy consistent with that required by the autonomous navigation.

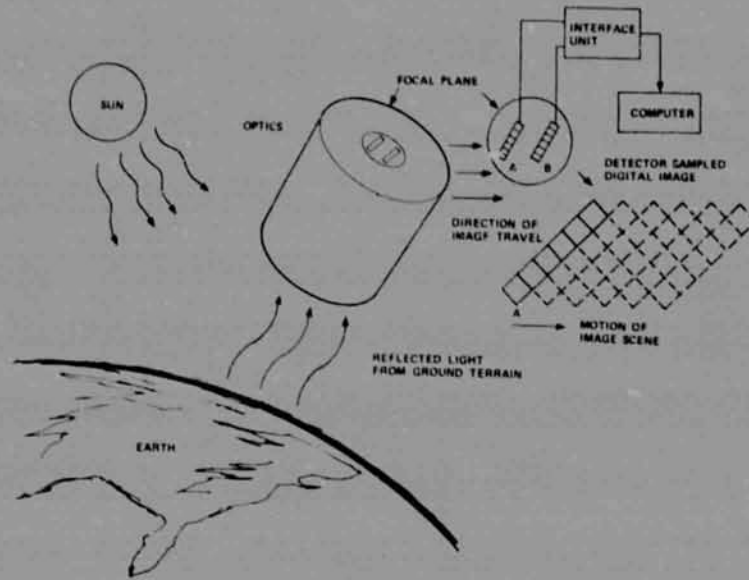


Figure 1. Down Sensor and Discrete Image of Terrain Scene Created from Detector Cell Readout Samples



Figure 2. Down Sensor Linear Landmark Processing

Table 1. Linear Landmark Measurement Performance for the Example Case

	CENTROID ERROR		ORIENTATION ERROR	LLM SHAPE RATIO (LENGTH/WIDTH)
	$\Delta\alpha$	$\Delta\beta$		
NO THRESHOLD NO GRADIENT FIGURE 2 (B)	57 ARC-SEC	64 ARC-SEC	2.0 DEG	1.1
THRESHOLDING ONLY FIGURE 2 (C)	61 ARC-SEC	70 ARC-SEC	1.3 DEG	1.1
THRESHOLDING AND GRADIENT FIGURE 2 (D)	26 ARC-SEC	4 ARC-SEC	1.1 DEG	51

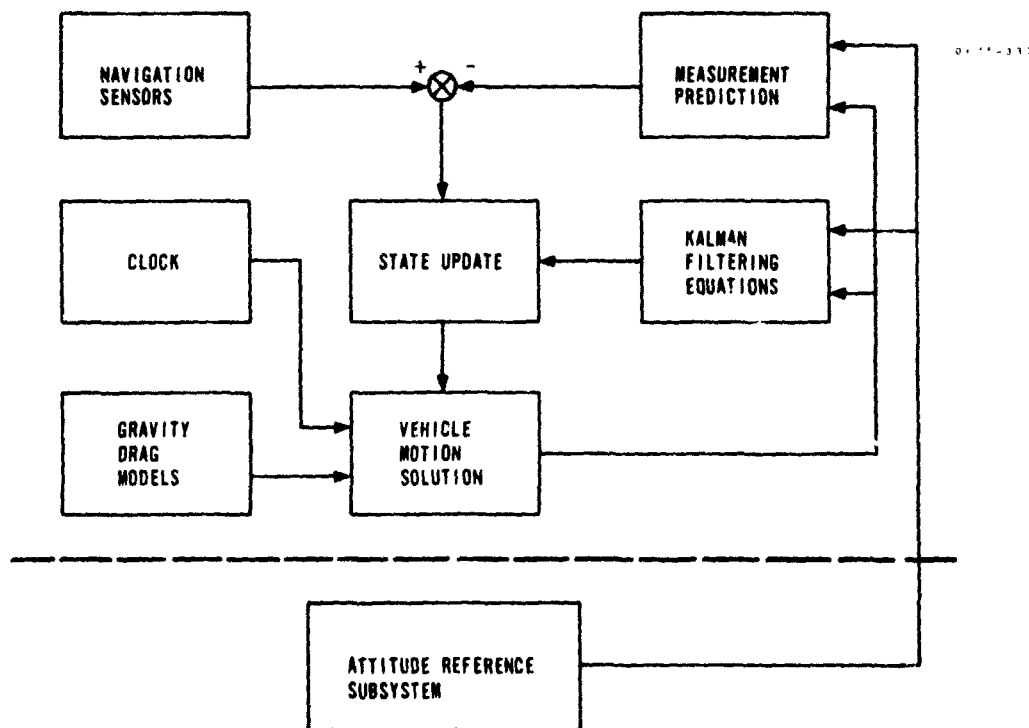
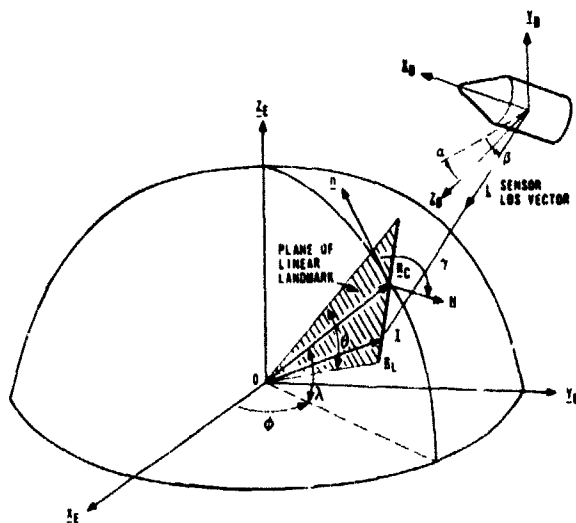
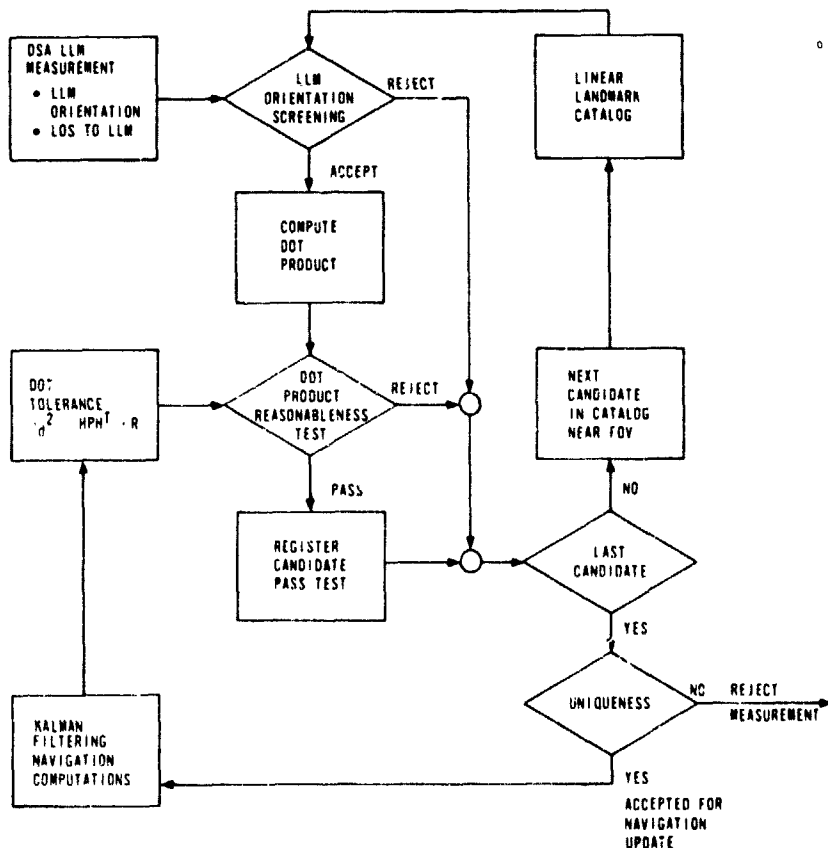


Figure 3. Functional Block Diagram of Autonomous Navigation System



0174-78

Figure 4. Geometry of Linear Landmark Sighting



0675-309

Figure 5. Linear Landmark Identification Procedure

ORIGINAL PAGE IS
OF POOR QUALITY

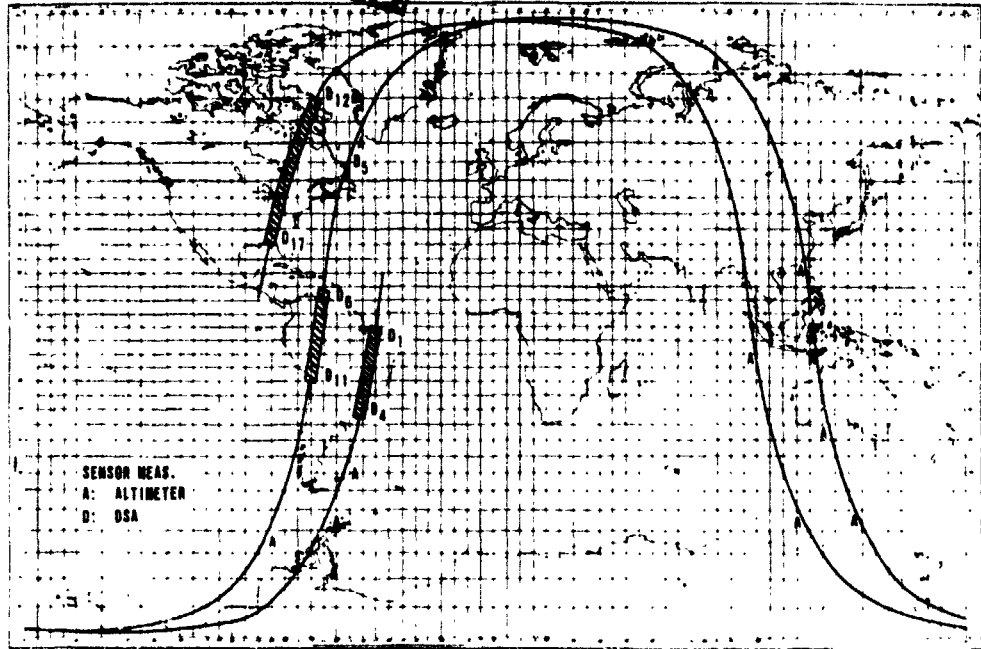


Figure 6. Ground Track of Reference Orbit
(100 x 120 nm, 83 Deg Inclination)

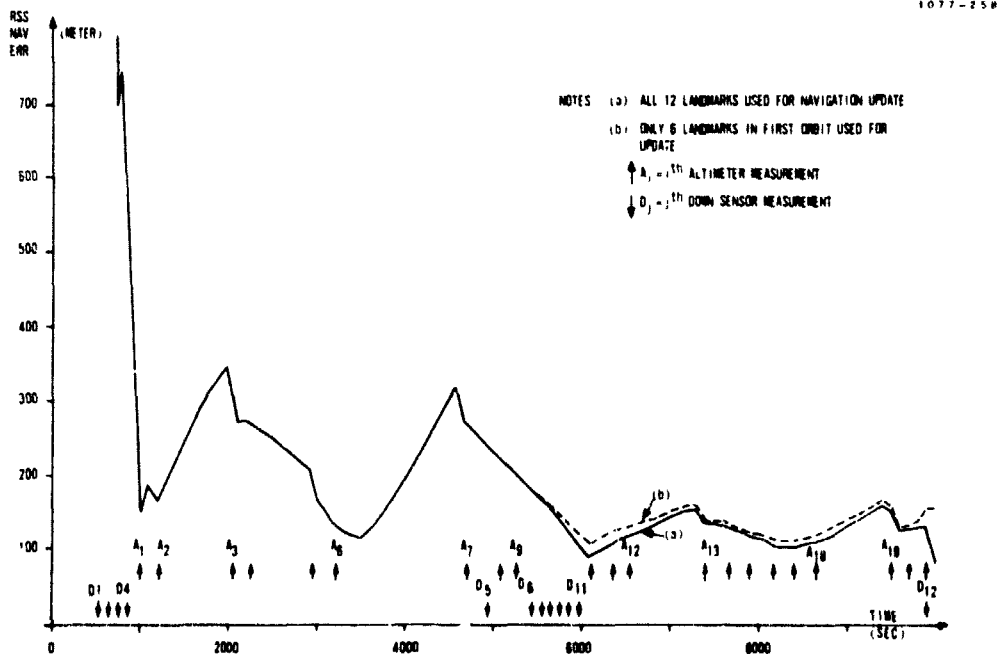
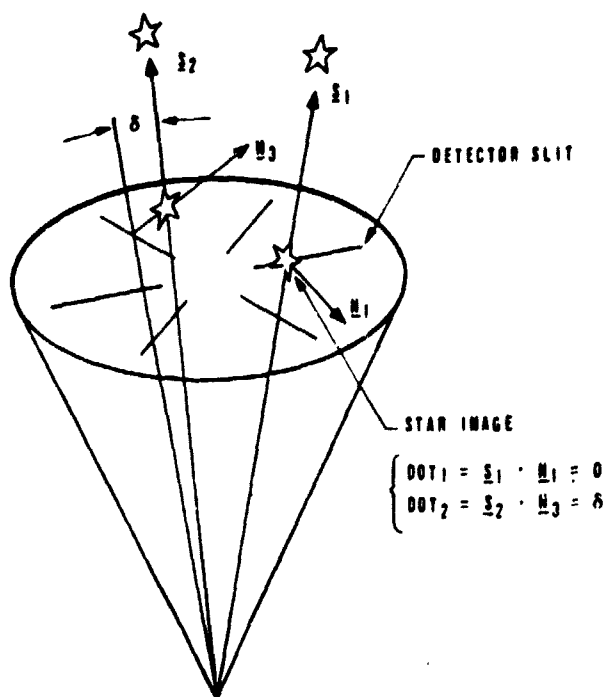


Figure 7. Navigation Error History Obtained
from Covariance Analysis

Table 2. Nominal Values of Navigation Error Sources

<u>ERROR SOURCES</u>	<u>STANDARD DEVIATION</u>	<u>CORRELATION</u>
I. SENSORS		
DOWN SENSOR: RANDOM	0.15 M RAD	WHITE
BIAS	0.15 M RAD	BIAS
ATTITUDE REFERENCE:		
RANDOM	0.15 M RAD	50 MIN
BIAS	0.15 M RAD	BIAS
ALTIMETER:	8 METER	WHITE
II. ENVIRONMENT		
GEOID HEIGHT:	15 METER	WHITE
GRAVITY ERROR:	10 MICRO-G	2.5 MIN
DRAG COEFFICIENT:	10 PERCENT	BIAS
EXOSPHERIC TEMP.:	200 DEGREE K	50 MIN



0976-2010

Figure 8. Star Transit Geometry

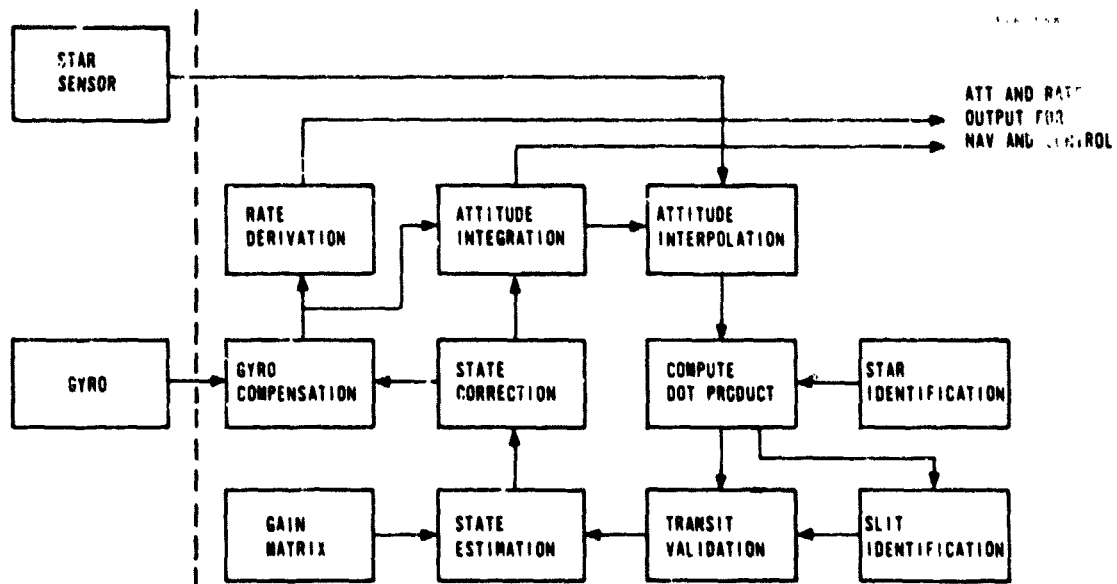


Figure 9. Stellar Update Processing Block Diagram

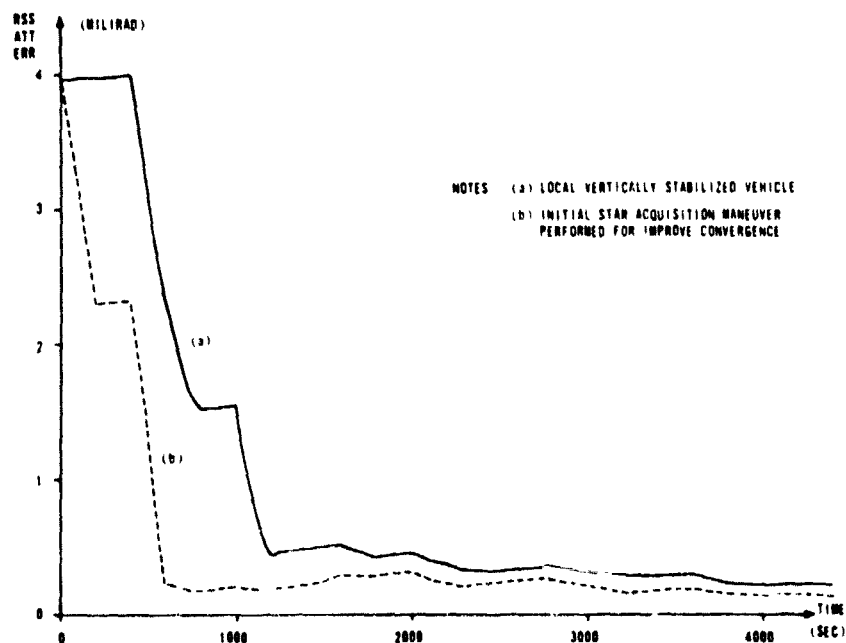
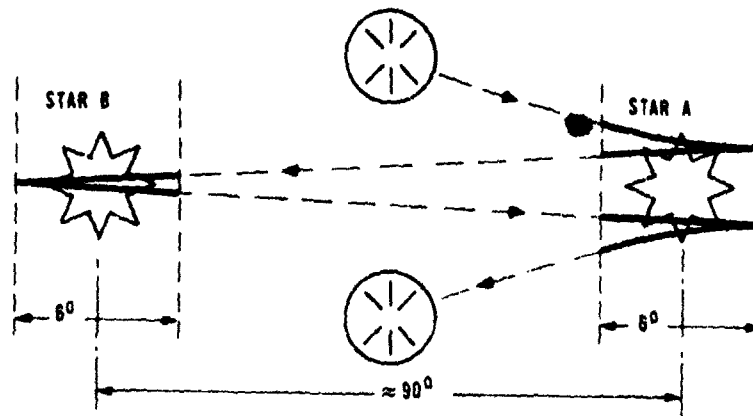


Figure 10. Attitude Reference Errors Obtained from Covariance Analysis



NOTES

- A AND B ARE BRIGHT AND ISOLATED STARS
- 1 DEG SEC RATE (---) LARGE ANGLE MANEUVER
- 360 SEC SEC RATE (—) TRANSIT ACQUISITION
- TOTAL MANEUVER TIME = $6 \times \frac{6 \times 3600}{360} + 2 \times \frac{90}{1} = 720 \text{ SEC} = 12 \text{ MIN}$

Figure 11. Star Acquisition Attitude Maneuver Profile

Table 3. Nominal Values of Attitude Reference Error Sources

<u>ERROR SOURCE</u>	<u>STANDARD DEVIATION</u>	<u>CORRELATION</u>
GYRO:		
BIAS	0.1 DEG/HR	BIAS
SCALE FACTOR	50 PPM	BIAS
MISALIGNMENT	0.05 M RAD	BIAS
RANDOM	0.2 DEG/HR	WHITE
STAR SENSOR:		
BIAS	0.05 M RAD	BIAS
RANDOM	0.05 M RAD	WHITE

5.0 REFERENCES

1. "Autonomous Satellite Navigation - A Historical Summary and Current Summary", W.L.Brogan and J.L.Lemay, Proc. 1973 JACC.
2. "A Method of Orbital Navigation Using Optical Sightings to Unknown Landmarks", G.M.Levine, AIAA/ION Guidance and Control Conference, August 1965.
3. "Autonomous Satellite Orbital Navigation Using Known and Unknown Earth Landmarks", S.P.Kau, AIAA Guidance and Control Conference, August 1975.
4. "Update Strategy for a Strapdown Stellar-Inertial Navigation System", S.P.Kau and S.S.Steadman, Proc. IEEE Conference on Decision and Control, December 1976.

910
N79-14131

THE OPERATIONAL FEASIBILITY OF ORBIT AND ATTITUDE
DETERMINATION FOR THE GEOSTATIONARY OPERATIONAL
ENVIRONMENTAL SATELLITE (SMS/GOES)
USING ONLY IMAGERY DATA

E. Mack and M. Jurotich
Presented by B. Remondi

U.S. Department of Commerce, NOAA
National Environmental Satellite Service

ABSTRACT

The National Oceanic and Atmospheric Administration (NOAA) uses Trilateration Range and Range Rate (TRRR) data, infrared (IR) earth-edge data and landmarks for the determination of orbit and attitude in the SMS/GOES operations. For many reasons, NOAA would like to remove its dependence on TRRR data and determine the orbit and attitude using only imagery data. Consequently, NOAA has undertaken an investigation to determine the operational feasibility of determining orbit and attitude for the SMS/GOES spacecraft using imagery alone (either with landmarks only or with the combination of landmarks and IR earth-edge data). There are three aspects to this investigation: (1) determining the orbit/attitude state under normal (no maneuvers) situation, (2) determining the orbit/attitude state after the maneuver, and (3) determining the criticality of both quality and distribution of the landmark data.

I. INTRODUCTION

NOAA currently uses TRRR data, IR earth-edge data, and landmark data extracted from visible earth images generated by the on-board Visible and Infrared Spin-Scan Radiometer (VISSR) for the determination of orbit and attitude in the SMS/GOES operations. NOAA would like to remove its dependence on TRRR data and determine the orbit and attitude using only imagery data (landmarks only or landmarks with earth-edge data) for several reasons: (1) the avoidance of costly processing of the TRRR data type and (2) orbit and attitude state could be considered a by-product of already existing hardware/software systems. Consequently, NOAA has undertaken an investigation to determine the operational feasibility of determining orbit and attitude for the SMS/GOES spacecraft using imagery alone. Three aspects of this investigation are as follows: (1) determining the orbit/attitude state from imagery only under normal (non-maneuvers) situation, (2) determining the orbit/attitude state from imagery only after a maneuver, and (3) determining the criticality of both quantity and distribution of the landmark data.

II. LANDMARK AND EARTH-EDGE EXTRACTION AND OPERATIONAL DATA PROCESSING PROCEDURES

There are many different resolutions of SMS/GOES data available. The imagery currently used in the orbit and attitude (O/A) determination consists of 4 km x 4 km visible and 8 km x 4 km IR. As part of the ground processing, the earth edges are ascertained using thresholding logic and then stored in the IR documentation. (There are 130 bytes of documentation data attached to each record of IR data.) They are simply the scan (J) and element (I) of the elements of IR data at the boundary between earth and space.

At the end of the ground processing system are ingest computers which store these data (imagery plus documentation). The data are moved onto the VISSR Data Base (VDB). During this process, the IR earth-edge data are extracted. Later, the O/A models will access these data. This data base includes 12 complete visible images of the earth and spans approximately six hours centered at spacecraft noon.

The NOAA Man-Machine Interactive Processing System (MMIPS) access this data base to retrieve one picture at a time. These pictures are displayed on a screen and the light pen is placed on a recognizable landmark feature. The scan and sample of this landmark are printed automatically. This process is repeated throughout this and other visible imagery frames until sufficient landmark data are available for O/A determination. The last step in this process is to add time and beta information to these landmarks (I,J) pairs. Thus, an earth-edge file and a landmark file have been established from which to determine the O/A state.

In NOAA's present operation, these imagery data are complemented with TRRR data. This consists of simultaneous ranging data from three ground sites. Two of these are unmanned and remote; one of them is the prime ground station at Wallops, Virginia.

Presently, TRRR and landmark data are input into the NOAA O/A model (GEODYN). Once the orbit and attitude are recovered, the orbit (not the attitude) is input along with the earth-edge data into the attitude model (PICATT) and an improved attitude solution is obtained. The NOAA SMS/GOES ephemerides are then generated using these solutions. Nearly all user requirements for ephemeris data are satisfied using these ephemerides.

III. EXPERIMENTAL RESULTS

The following results were obtained from three separate spacecraft (GOES-1, GOES-2 and SMS-2). The GOES-2 spacecraft replaced the GOES-1 spacecraft as the operational east spacecraft on August 15, 1977. SMS-2 is the operational west spacecraft. The coverage from these two spacecrafts is shown in Figure III.1.

A. Determination of the Orbit and Attitude State Under Normal (Non-Maneuver) Situations

The GOES-1 and GOES-2 spacecraft were used in this phase of the investigation. The subsatellite position for both of these spacecraft, at the time of the investigation, was approximately 75° West. The data span covered for GOES-1 is from June 23, 1977 thru July 31, 1977. The data span covered for GOES-2 is September 18, 1977 thru September 21, 1977. From Figure III.1, we can see that there exists a number of well-distributed landmarks from the imagery data for these spacecraft.

1. GOES-1 - The procedure used in this phase of the investigation was as follows: starting with an operational a priori estimate and seven-days worth of landmarks from the Man-Machine Interactive Processing System (MMIPS), the GEODYN orbit determination system was used to determine both orbit and attitude from landmarks-only. Next, using the landmark-only orbit and the IR earth edge data in the Horizon Picture Attitude Program (PICATT), we compute a second attitude solution. Thus in reality, we have two daily attitude determinations where the orbits for both solutions are the same. The two solutions described above are then used in the Gridding Error Assessment System to compute the x-direction shift (east-west shift), y-direction shift (north-south shift), and rotation which are used to judge the quality of the solution. The first two of these give an indication of what the grid error would be if these solutions were used in the gridding.

All the landmark-only solutions in this phase of the investigation were determined from seven-days worth of landmarks. The resultant orbit, attitude and grid errors were compared with the operational orbit, attitude, and grid errors and the following results were obtained: (a) Figure III.2 and Figure III.3 show the east-west and north-south grid error produced from each solution in terms of grid errors in the landmark-only orbit solution with the PICATT attitude solution. Table III.1 shows the mean and standard deviations for the grid errors computed by the Gridding Error Assessment System for the three solutions described above. (b) In addition to looking at the grid error produced from each of the solutions, we can also examine the orbit and attitude solutions to see what differences existed. Table III.2 shows the mean orbital differences based upon the sixteen orbit solutions used to produce the grid error in

Figure III.2 and Figure III.3. Table III.3 shows the mean attitude differences based upon the sixteen attitude solutions used to produce the grid errors in Figure III.2 and Figure III.3. From Table III.3, we can see that the attitude solution is considerably improved by the addition of the IR earth-edge data in the attitude solution.

TABLE III.1

<u>GRID ERROR SOURCE</u>	<u>X-DIRECTION SHIFT</u>		<u>Y-DIRECTION SHIFT</u>	
	<u>Mean</u>	<u>Std. Dev.</u>	<u>Mean</u>	<u>Std. Dev.</u>
Landmark Only Orbit & Attitude	-5.724 km	3.537 km	-15.2357 km	5.9745 km
Landmark Only Orbit & PICATT Attitude	-5.2097 km	4.1820 km	-12.1983 km	3.3229 km
Operation Orbit & Attitude	-5.3357 km	7.6966 km	-10.6403 km	6.2384 km

TABLE III.2
Orbital Differences

Landmark Only vs. Operational Solutions

	<u>Mean</u>	<u>Standard Deviation</u>
Semi-Major Axis	233.25 meters	5.00 meters
Eccentricity	0.00001	0.00003
Inclination	0.008 deg	0.005 deg
Mean Longitude	0.008 deg	0.007 deg

TABLE III.3
Attitude Differences

	<u>Landmark Only vs. Operational</u>		<u>Landmark and Earth-Edge vs. Operational</u>	
	<u>Mean</u>	<u>Std. Dev.</u>	<u>Mean</u>	<u>Std. Dev.</u>
Spin Axis Right Ascension	3.86 deg.	6.65 deg.	2.62 deg.	7.78 deg.
Spin Axis Declination	.08 deg.	.01 deg.	.02 deg.	.03 deg.

2. GOES-2 - On September 16, 1977, a landmark-only orbit solution with PICATT attitude was computed and used in the computation of the operational grids used by Wallops CDA to grid the images from GOES-2. The operational grids are computed in three eight-hour periods as follows.

gridding period 1 \equiv 0230Z thru 1030Z
gridding period 2 \equiv 1030Z thru 1830Z
gridding period 3 \equiv 1830Z thru 0230Z

Moreover, only one period of grids is computed per day so that the landmark-only orbit computed on September 16, 1977, was used in the following operational grids:

September 18 for 0230Z thru 1030Z
September 19 for 0230Z thru 1830Z
September 20 for full 24 hours

A number of pictures gridded during those periods were examined and the grid error was measured by hand. Figure III.4 and Figure III.5 shows the hand-measured grid error from those periods. It should be noted that the grid error can be measured by hand to an accuracy of about 7.5 kilometers for GOES-2.

B. Determination of the Orbit and Attitude State After a Maneuver

The Synchronous Meteorological Satellite (SMS-2) was used in this phase of the investigation. The subsatellite position for this spacecraft is approximately 135° West. The data span covered for SMS-2 is June 20, 1977 to June 27, 1977. From Figure III.1, we can see that we do not have as many well-distributed landmarks available from the imagery data for this spacecraft as we had with the GOES spacecraft.

The procedure used in this part of the investigation was as follows: Starting with the post-maneuver predictions for orbit and attitude on June 20 and one day's accumulation of landmarks from the MMIPS, we used the GEODYN orbit determination system to determine both orbit and attitude from landmarks-only. If GEODYN is unable to get a solution, add another day's worth of landmarks and repeat the GEODYN run. Continue this process each time adding another day's worth of landmarks until we are able to get a GEODYN solution.

Using the above procedure, a successful GEODYN solution was achieved with seven day's worth of landmarks. The GEODYN solutions were compared with the corresponding operational solutions and the results are shown in Table III.4.

We can see from Table III.4 that a landmark-only solution was obtained with seven days worth of landmark that agrees very closely with the operational solutions. This was significant, since with the SMS-2 spacecraft, we do not have well-distributed landmarks (most landmarks are along the west coast of the United States).

TABLE III.4

	<u>Landmark Only Orbit & Attitude</u>	<u>Operational Orbit & Attitude Solution</u>
Semi-Major Axis	42166224.8378m	42166009.0m
Eccentricity	0.0001589	0.0001524
Inclination	0.044409 deg.	0.045367 deg.
Mean Longitude	383.4808567 deg.	383.560237 deg.
Right Ascension	19.869378 deg.	19.80943 deg.
Declination	-89.821767 deg.	-89.84232 deg.
Data Span	7 days	2 days

Table III.5 shows the orbit and attitude differences between the post-maneuver landmark-only and post-maneuver operational orbit.

TABLE III.5

	<u>Landmark-Only vs. Operational</u>
Semi-Major Axis	216.83 meters
Eccentricity	0.000006
Inclination	0.009 deg.
Mean Longitude	0.08 deg.
Spin Axis Right Ascension	0.06 deg.
Spin Axis Declination	0.02 deg.

TABLE III.6

	<u>Landmark Only Solution With 3 Sets of Landmark</u>	<u>Landmark Only Solution With 2 Sets of Landmark</u>	<u>Landmark Only Solution With 1 Set of Landmark</u>
Semi-Major Axis	42166224.8378m	42166389.324m	42186470.3063m
Eccentricity	0.001589	0.0001596	0.00064219
Inclination	0.044409 deg.	0.058101 deg.	0.04461 deg.
Mean Longitude	383.4808567 deg.	383.468963 deg.	383.515453 deg.
Right Ascension	19.869378 deg.	19.941449 deg.	19.953716 deg.

TABLE III.6 CONT.

	<u>Landmark Only Solution With 3 Sets of Landmark</u>	<u>Landmark Only Solution With 2 Sets of Landmark</u>	<u>Landmark Only Solution With 1 Set of Landmark</u>
Declination	-89.821767 deg.	-89.849354 deg.	-89.824916 deg.
Data Span	7 days	7 days	7 days
# Elements	126	44	21
# Lines	126	44	21

C. Criticality of Both Quantity and Distribution of the Landmark Data

With both the GOES and SMS-2 spacecrafts, we try to extract landmarks so that we have three separate sets of landmark locations in order to enhance the geometry of the solutions. However, only the SMS-2 spacecraft was used in this phase of the investigation. The procedure used in this investigation was as follows: Start with the post-maneuver predictions for orbit and attitude on June 20 and seven days worth of landmarks with one set of landmarks' locations removed from the landmark data. Then use the GEODYN orbit determination system to determine both orbit and attitude from landmarks-only. Next, remove a second set of landmark locations from the landmark data and compare a second GEODYN orbit and attitude solution. Table III.6 shows the results of these GEODYN solutions as compared with the landmark-only solution from Section B.

IV. CONCLUSIONS

Experimental results from the three data evaluation periods (June 20, June 23, September 18) on the three geostationary spacecrafts (SMS-2, GOES-1, GOES-2) have demonstrated that:

1. Using existing landmark extraction and identification techniques for the east geostationary spacecraft, we can maintain a high quality orbit and attitude state with imagery data only.
2. Using existing landmark extraction and identification techniques for the west geostationary spacecraft, we can recover a high quality orbit and attitude state with imagery data only in approximately seven days. Even though this recovery period appears prohibitively large, we should note that SMS-2 does not have well-distributed landmarks and the addition of IR earth-edge data in the orbit solution should improve the recovery time.
3. Analysis of the landmark data for SMS-2 indicates that the removal of two of the three sets of landmarks from the data would seriously endanger the ability to achieve stable orbital elements. However, it

should be noted that for SMS-2 most of the landmarks extracted are along the west coast of the United States and once the set of west coast landmarks are removed, the geometry is seriously hampered,

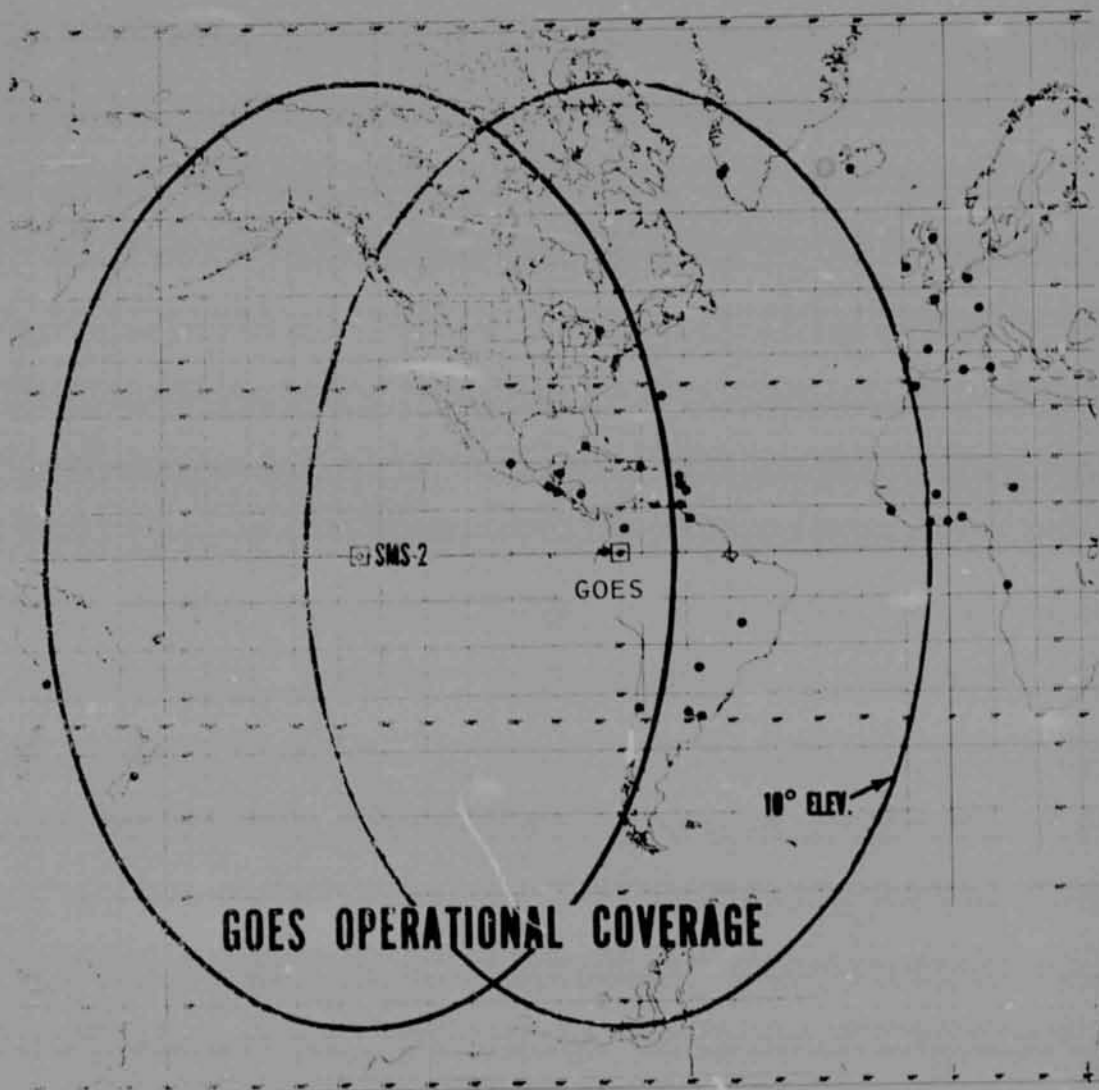


Figure III.1. GOES Operational Coverage.

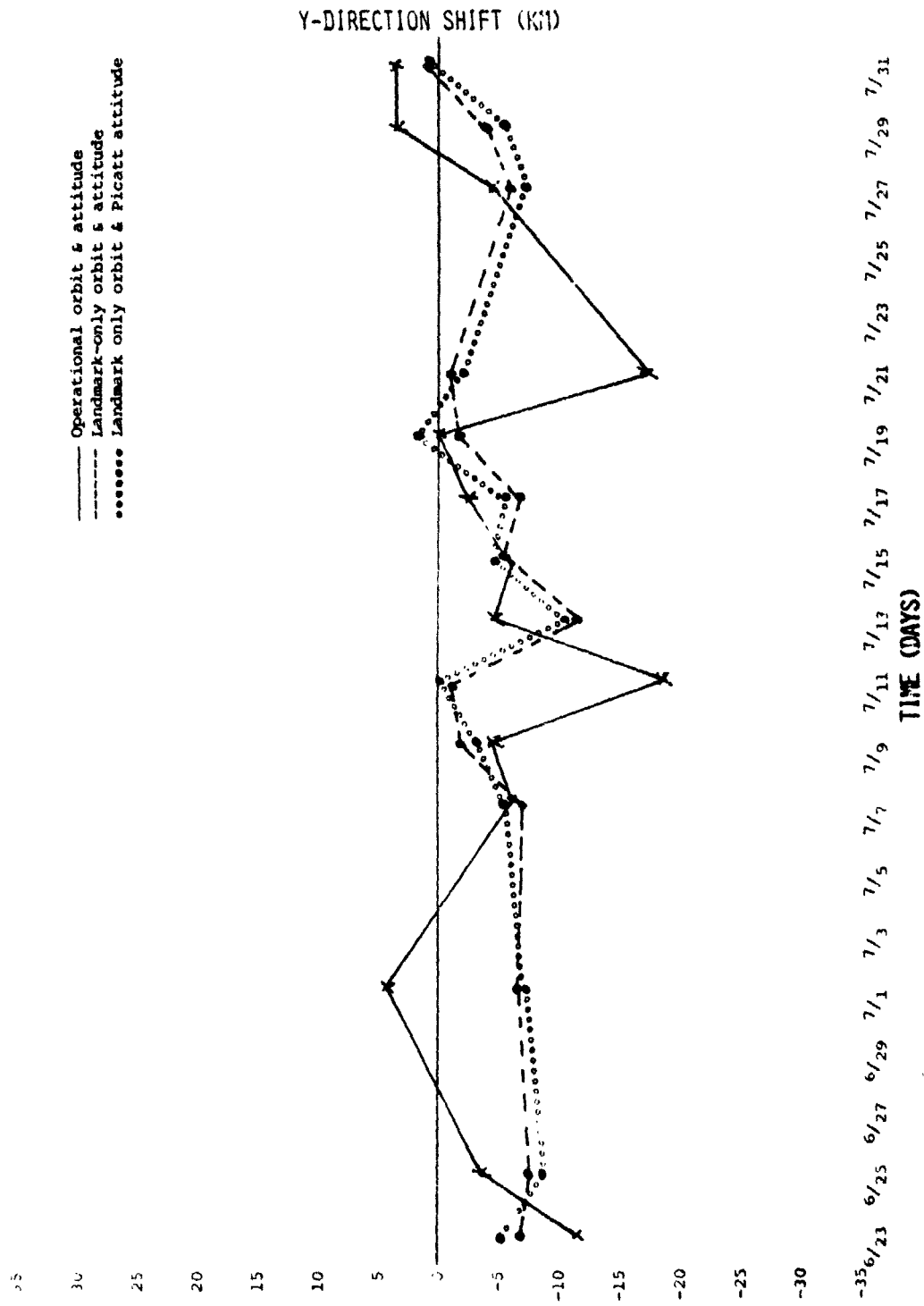


Figure III.2. East-West Grid Error Comparison of Orbit and Attitude Determination Methods.

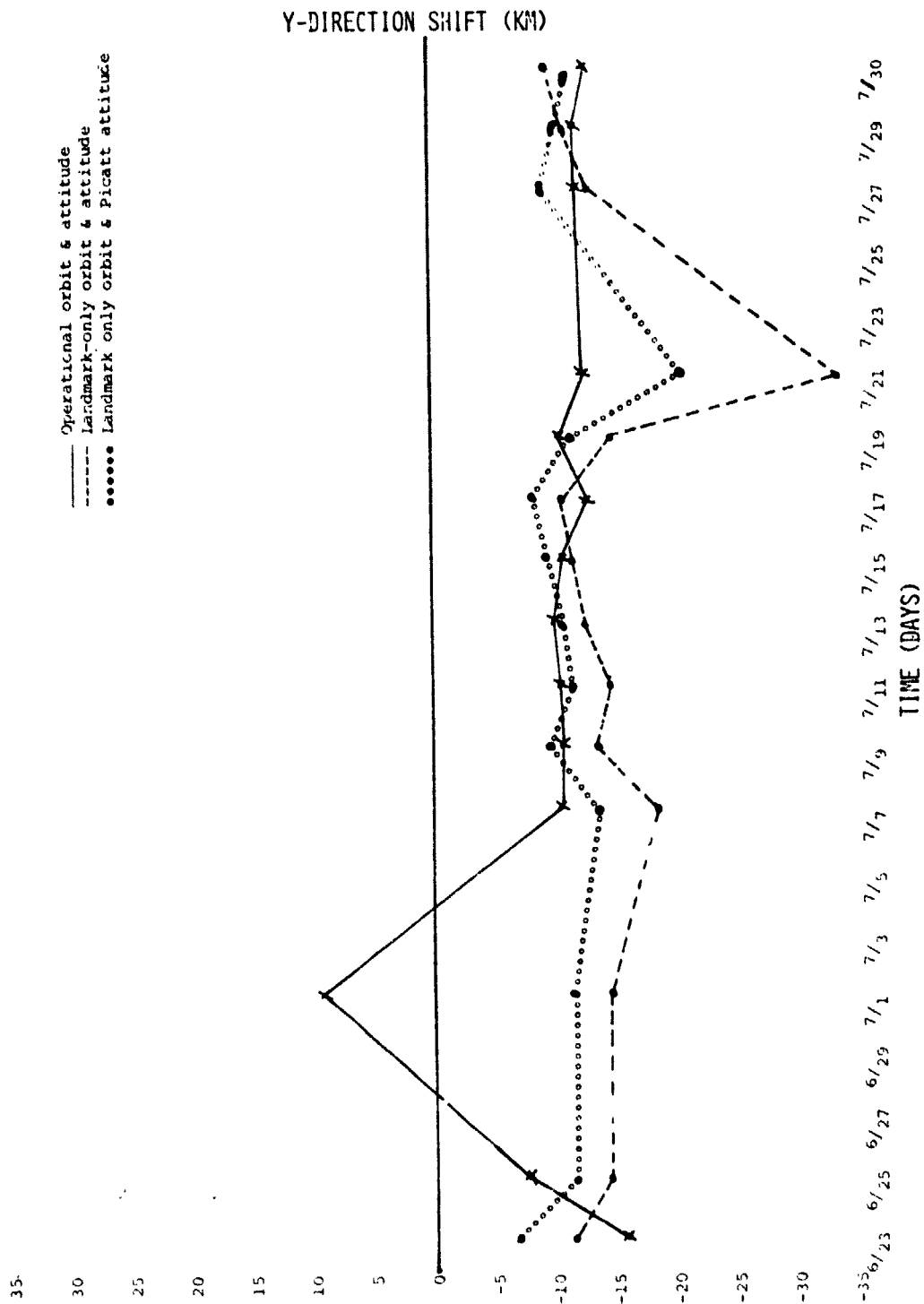


Figure III. 3. North-South Grid Error Comparison of Orbit and Attitude Determination Methods.

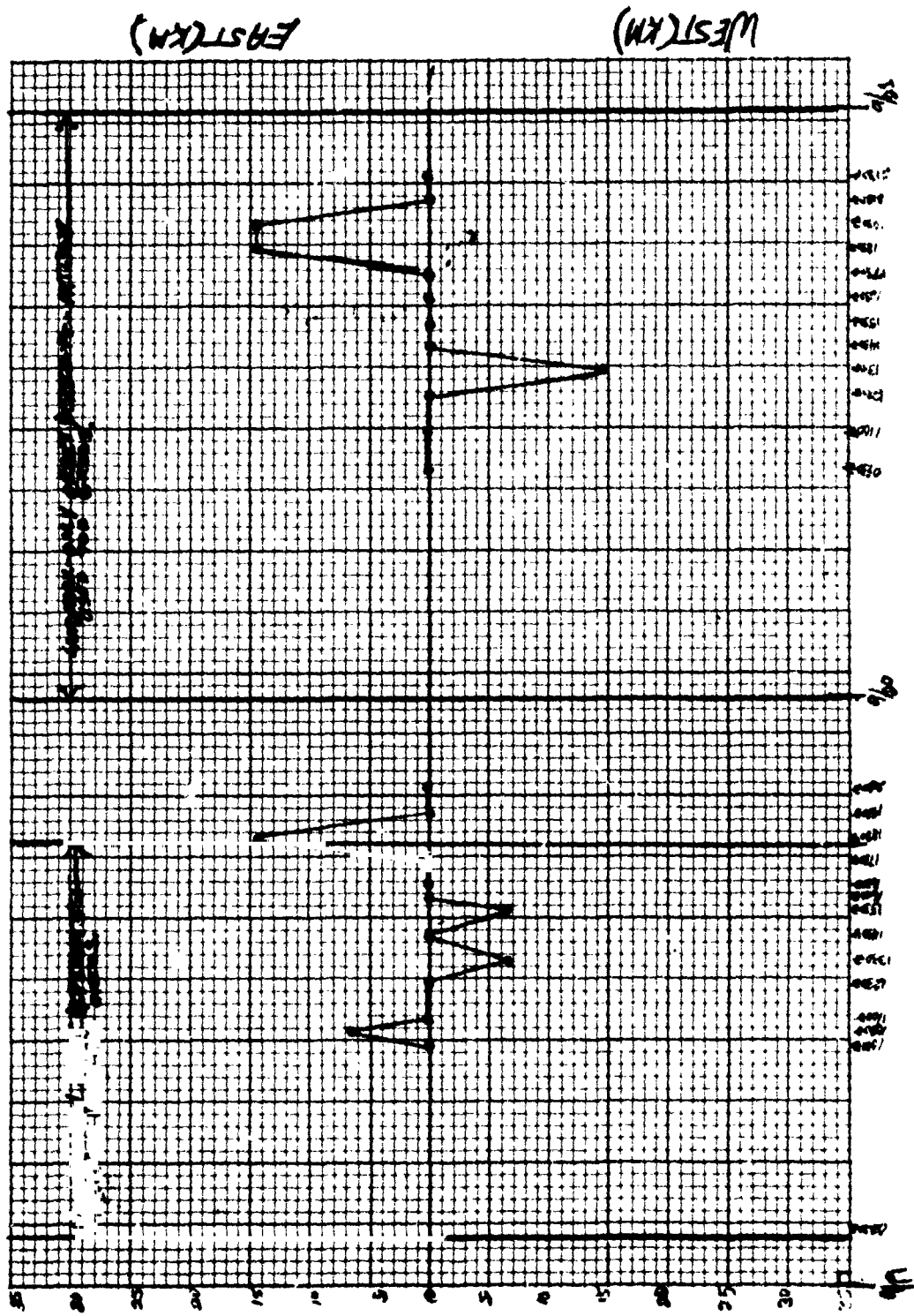


Figure III.4. East-West Hand Measured Grid Error.

ORIGINAL PAGE IS
OF POOR QUALITY

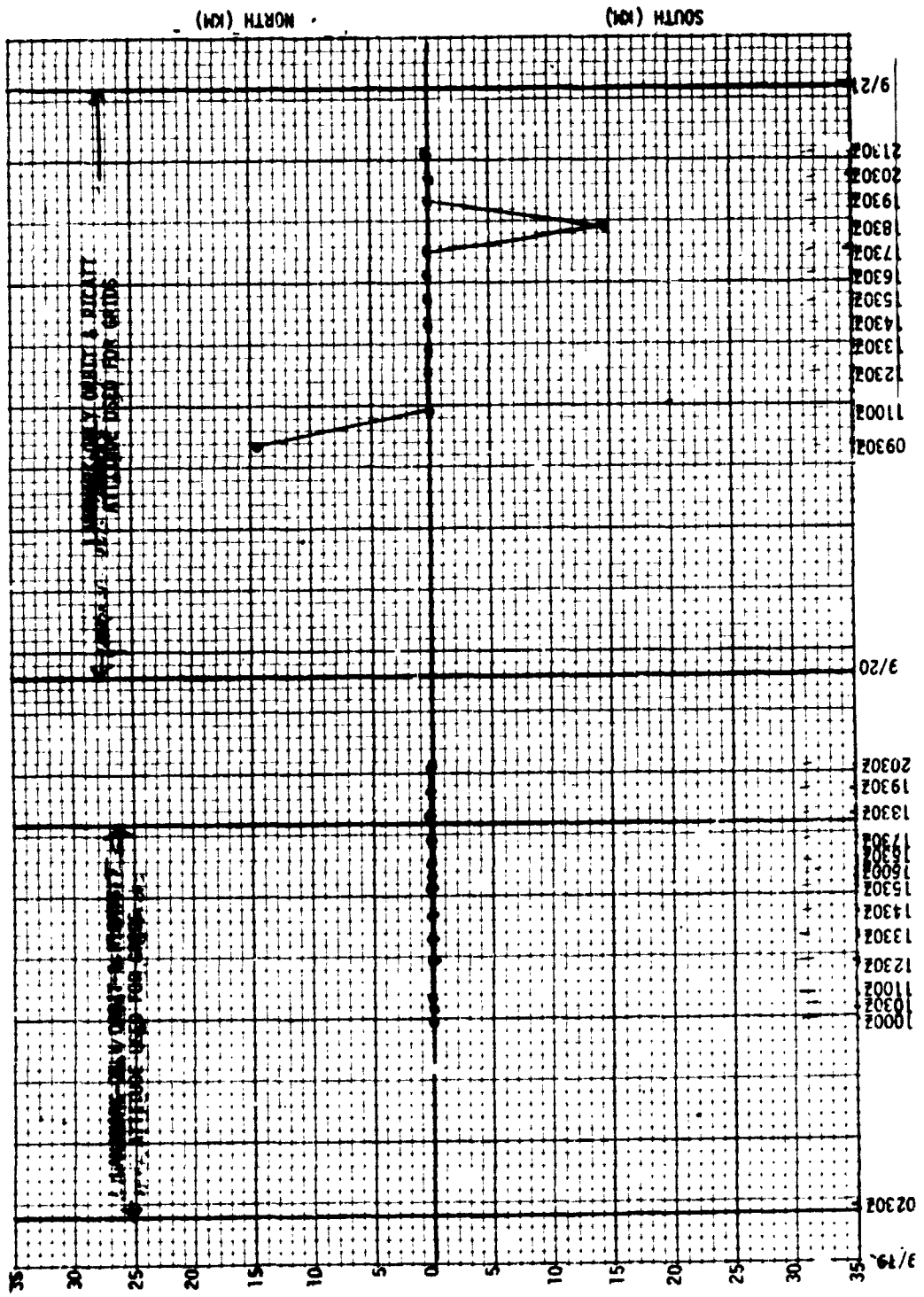


Figure III. 5. North-South Hand Measured Grid Error.

V. ACKNOWLEDGEMENTS

The authors acknowledge the dedicated work of Tim Roemer in generating the numerical results of the experiment.

211
N79-14132

RECURSIVE ESTIMATOR FOR OSO-8 ATTITUDE

Robert D. Headrick and Duke Y. Park*

Computer Sciences Corporation

INTRODUCTION

The validation and early results of the Recursive Estimation Attitude Program (REAP) were presented in an earlier paper (References 1 and 2) in the May 1976 Estimation Theory Symposium. This paper presents modifications and enhancements that have been made to the program since then.

The REAP program is used for research and special production for definitive attitudes for Orbiting Solar Observatory (OSO)-8. The objective is to determine continuous attitudes to ± 0.05 degree accuracy from Sun and star slit sensors mounted on the spinning portion of the spacecraft. The bulk of the attitude production is performed by a Weighted Least Squares (WLS) batch processor, but REAP is used for problem passes such as those involving gas jet maneuvers, sparse star fields, or star sensor saturation by high energy particles in the South Atlantic Anomaly.

The star sensor has a near-vertical azimuth slit and a canted elevation slit, with a single photomultiplier tube as a detector. The Sun sensor similarly has a vertical and a canted slit. Thus, the sensings are in the form of time-tagged events, where the time is taken from the spacecraft clock pulses. Other sensors of lower accuracy are also available: a single-axis magnetometer which gives the time of the rising and falling nulls and a Shaft Angle Encoder (SAE) which gives the relative azimuth between the sail (held approximately normal to the sunline) and the wheel (rotating at about 6 rpm).

*Work supported by Goddard Space Flight Center, National Aeronautics and Space Administration under Contracts NAS 5-11999 and NAS 5-24300.

A diagram of the spacecraft is given in Figure 1. The attitude angles are referenced to the Geocentric Solar Ecliptic (GSE) coordinate system in which the x_E -axis is pointed toward the center of the Sun, z_E is to the ecliptic north pole, and y_E completes the right-handed system. The wheel (or body) z_W -axis orientation is described in terms of roll and pitch angles from these reference axes. The roll angle, ϕ , shown negative for clarity, is taken about

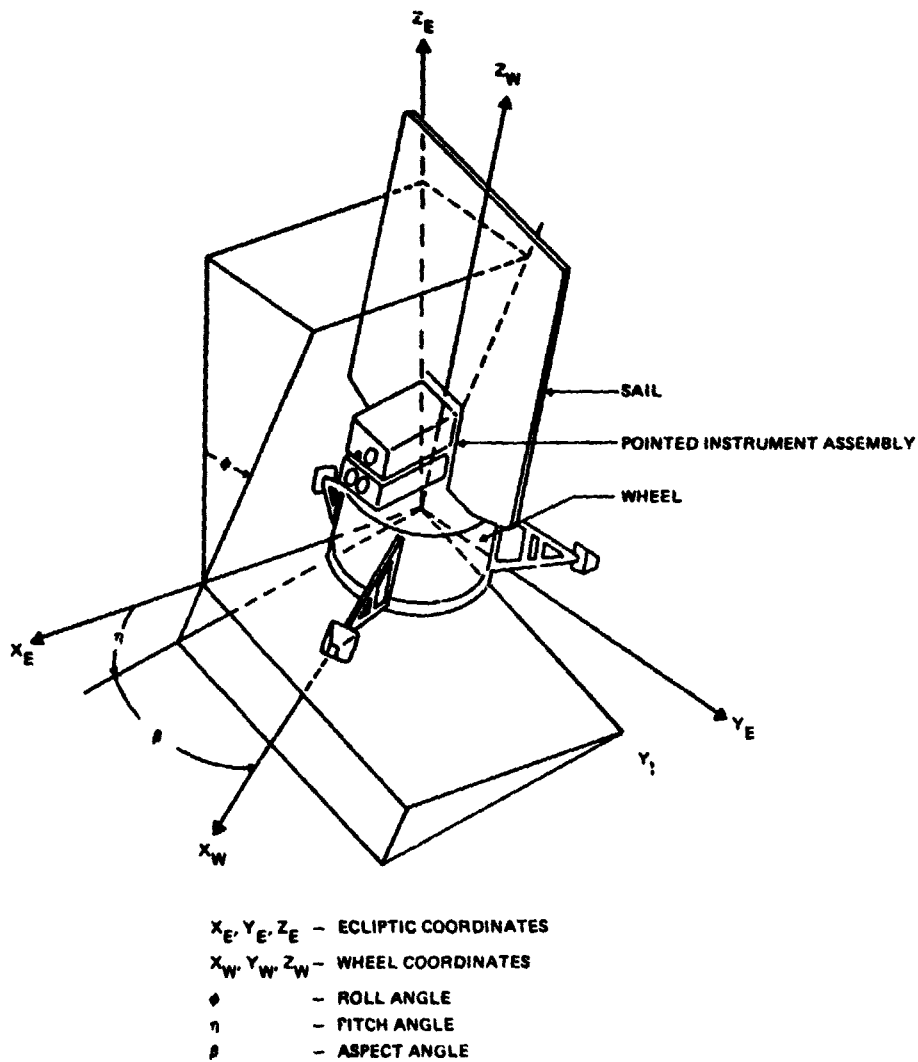


Figure 1. OSO-8 Orientation Angles

the sunline, and the pitch angle, η , is about the intermediate axis, y_1 . The final rotation is about the body z_W - axis through the aspect angle β .

Mathematical Formulation

The computational sequence, which is given in Figure 2, is the same as in the earlier versions. The mathematical formulation, however, has been simplified considerably from the original state representation which included both the attitude quaternion and the angular momentum vector. Since there is no evidence of nutation, this representation was clearly redundant. Now the state vector, \bar{x} , is given by

$$\bar{x} = \begin{bmatrix} \phi \\ \eta \\ \beta \\ \omega \end{bmatrix}$$

where ϕ = roll angle

η = pitch angle

β = aspect angle

ω = spin rate

The measurement error is given by

$$\Delta \bar{y}_j = \bar{U}_j \cdot \bar{V}_j = \bar{U}_j^T D \bar{W}$$

where \bar{U} is the slit normal vector for the j^{th} event, \bar{V} is the reference vector transformed to the body system, \bar{W} is the reference vector in the ecliptic

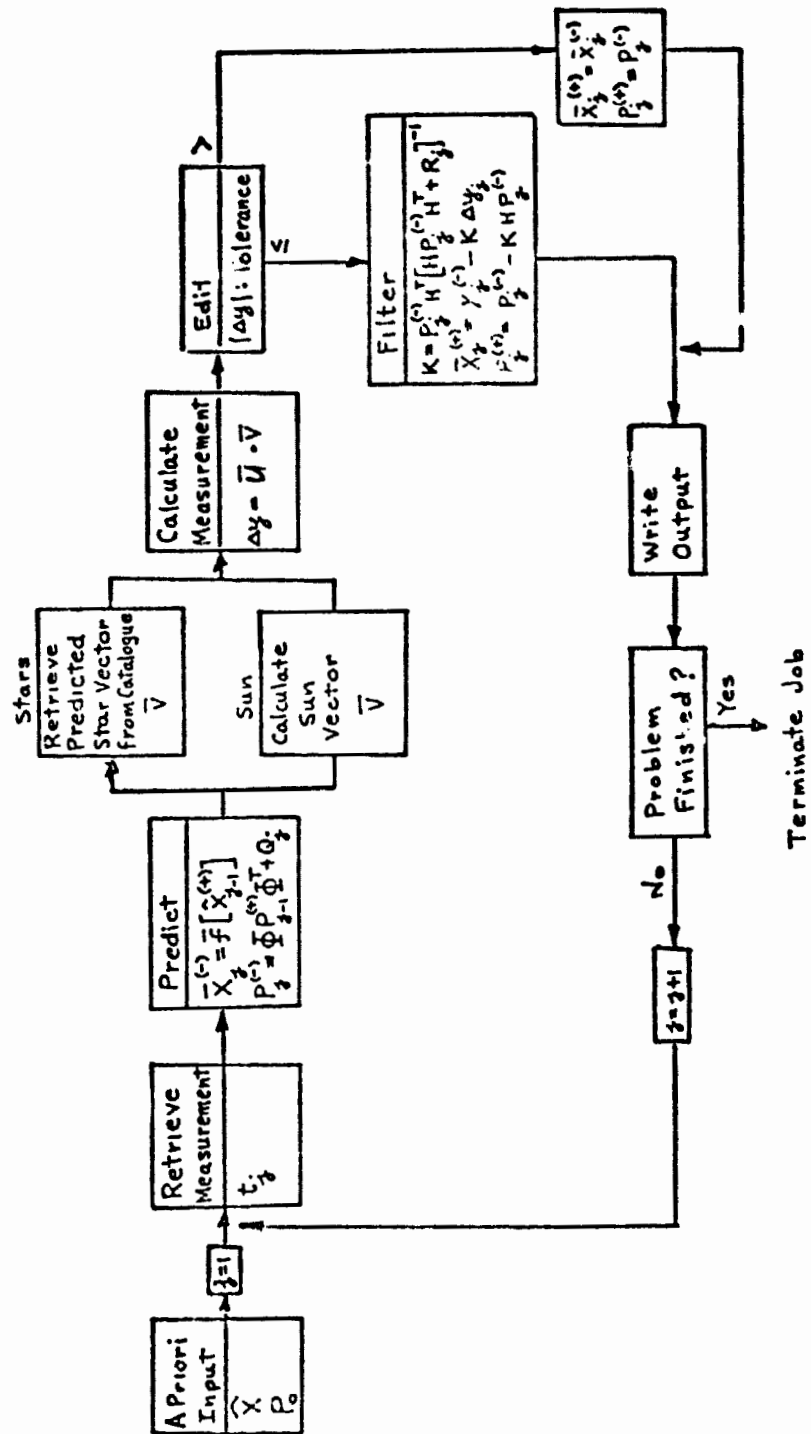


Figure 2. Sequential Estimator Computational Sequence

(GSE) system, and D is the attitude direction cosine matrix referenced to the GSE system, given by

$$D = \begin{pmatrix} c\beta c\eta & c\beta s\eta s\phi + s\beta c\phi & -c\beta s\eta c\phi + s\beta s\phi \\ -s\beta c\eta & -s\beta s\eta s\phi + c\beta c\phi & s\beta s\eta c\phi + c\beta s\phi \\ s\eta & -c\eta s\phi & c\eta c\phi \end{pmatrix}$$

In the predictive step the attitude dynamics have been simplified to the spin-axis approximation, where it is assumed that the body z-axis is aligned with the angular momentum vector (i.e., no nutation occurs). The angular momentum vector \bar{L}_j is computed at each step for use in predictions, but it is not included in the state estimation procedure. It is updated by the equation

$$\bar{L}_{j+1} = \bar{L}_j + \Delta t \sum \text{Torques}_j - \bar{\omega}_{\text{Sun}} \times \bar{L}_j$$

where \bar{L}_j is in GSE coordinates. The various torque models, which are averaged over a spin period, are now computed in the GSE system to avoid conversions. The torque models include

- Gravity-gradient
- Solar radiation
- Magnetic residual and control torques
- Attitude control jets

The $\bar{\omega}_{\text{Sun}}$ term accounts for the rotation of the GSE coordinate system. The state vector is predicted by

$$\bar{x}_{j+1}^{(-)} = \bar{f}(\bar{L}_{j+1}) + \nu_{j+1}$$

where ν_{j+1} is a random noise vector.

The state transition matrix, Φ , is given by

$$\Phi = \frac{\partial \bar{x}_{j+1}}{\partial \bar{x}_j} = \begin{bmatrix} 1 & 0 & 0 & 0 \\ 0 & 1 & 0 & 0 \\ 0 & 0 & 1 & \Delta t \\ 0 & 0 & 0 & 0 \end{bmatrix}$$

The dynamic noise term is given by

$$Q = \begin{bmatrix} Q_1 & 0 & 0 & 0 \\ 0 & Q_1 & 0 & 0 \\ 0 & 0 & Q_1 & 0 \\ 0 & 0 & 0 & Q_2 \end{bmatrix}$$

where Q_1 and Q_2 are constants which account for the unmodeled torques and computational noise.

The measurement sensitivity matrix, H , is given by

$$H = \frac{\partial \Delta y_{j+1}}{\partial \bar{x}_j} = \bar{U}^T \frac{\partial D}{\partial \bar{x}} \bar{W}$$

where the attitude dependence is contained solely in the direction cosine matrix.

To illustrate the simplicity of these partials, we develop them explicitly as

$$\frac{\partial D}{\partial \phi} = \begin{pmatrix} 0 & c\beta s\eta c\phi - s\beta s\phi & c\beta s\eta s\phi + s\beta c\phi \\ 0 & -s\beta s\eta c\phi - c\beta s\phi & -s\beta s\eta s\phi + c\beta c\phi \\ 0 & -c\eta c\phi & -c\eta s\phi \end{pmatrix}$$

$$\frac{\partial D}{\partial \eta} = \begin{pmatrix} -c\beta s\eta & c\beta c\eta s\phi & c\beta c\eta c\phi \\ s\beta s\eta & -s\beta c\eta s\phi & s\beta c\eta c\phi \\ c\eta & s\eta s\phi & -s\eta c\phi \end{pmatrix}$$

$$\frac{\partial D}{\partial \beta} = \begin{pmatrix} -s\beta c\eta & -s\beta s\eta s\phi + c\beta c\phi & s\beta s\eta c\phi + c\beta s\phi \\ -c\beta c\eta & -c\beta s\eta s\phi - s\beta c\phi & c\beta s\eta c\phi - s\beta s\phi \\ 0 & 0 & 0 \end{pmatrix}$$

$$\frac{\partial D}{\partial \omega} = 0$$

The \bar{U} and \bar{W} vectors which pre-and post-multiply the partials $\partial D/\partial \bar{x}$ serve to select and weight the terms in the matrix. For example, if we have a Sun-slit in the body x-z plane, the slit normal is $\bar{U}^T = (0, 1, 0)$. The Sun vector in GSE coordinates is

$$\bar{W} = \begin{pmatrix} 1 \\ 0 \\ 0 \end{pmatrix}$$

Thus, when we carry out the multiplication, we select the (2,1) term of the $\partial D/\partial \bar{x}$ matrices to give

$$H = [0, s\beta s\eta, -c\beta c\eta, 0]$$

These measurement sensitivity matrices are simple enough to allow checking by hand computations.

Note that the roll partial H_{ϕ} is identically zero since the vector product $(\partial D/\partial \phi) \bar{W}$ is zero. Thus, there can be no direct update of the roll angle on Sun data, no matter where the Sun slit is located. Since the a priori covariance matrix is diagonal, the initial roll gain K_{ϕ} is also zero. When the data span begins in Sunlight, the roll update remains zero throughout orbit day. After the star data comes in at orbit night, however, the off-diagonal correlation terms in the covariance matrix build up. During the next orbit day these give rise to a nonzero K_{ϕ} and provide an indirect update to the measured roll angle.

Data Editing

The method of star identification is the direct match technique, which selects out of the catalog that star which has the smallest residual errors as the reference star. In order to avoid misidentifications from the many false triggerings which occur, considerable care is taken in data editing. The total star catalog is reduced to stars brighter than 3.5 magnitude in the swath swept out by the star sensor field of view about the a priori spin axis. Events are edited out for the following conditions:

- Events outside nominal azimuth (counts do not agree with the spacecraft clock)
- Events outside the elevation limits
- Triple-crossing flag in telemetry indicates 3 events (and possible ambiguity) within 125 milliseconds.
- Sensor saturation due to the South Atlantic Anomaly, indicated by more than 128 events during a major frame or 20.48 seconds
- Stars occulted by the Earth
- Stars which are not identified as occurring from both the azimuth and elevation slits. Since the events are considered singly, special

contingent logic is required to hold all candidate slit 1 reference stars and states until the data from slit 2 is processed.

- Events outside fixed tolerance limits
- Events outside adaptive limits. This test has been added since the last paper to provide η -sigma data rejection based on the standard deviation of the residual

$$\sigma_{\Delta y} = \sqrt{H P H^T + R}$$

If $\Delta y > n\sigma_{\Delta y}$, the data is rejected, where n is an input parameter.

Results

Results of the new 4-component model are shown in Figure 3 compared to the earlier solutions, labeled V.2 and V.4. The spin rate agreed so closely with the earlier results that it was not plotted. The oscillations in spin rate at the orbit period are due to thermal expansion. As the spacecraft enters sunlight, it expands, increasing the moment of inertia. Since angular momentum is conserved, the spin rate must decrease. The opposite effect occurs when the spacecraft enters orbit night.

The roll and pitch angle results are shown, where the horizontal bars indicate the allowed error. It can be seen that all versions agree to within ± 0.05 degree. The 4-component pitch solutions show a small systematic oscillation at the orbit period, which was not predicted by the torque models. When the data is turned off, the predicted state follows the dashed (V.2) curve very closely. The cycles at twice the orbit frequency are characteristic of gravity-gradient torques. The new observed pattern is indicative of aerodynamic torques from the fixed sail. These torques were not modeled originally because they were known to average out over an orbit period (Reference 3) and thus not lead to any secular error growth. Also, the aerodynamic terms are very complicated to model accurately.

**OSO-8 DEFINITIVE ATTITUDE
DAY 224 (8/12/75)
NO CONTROL TORQUES**

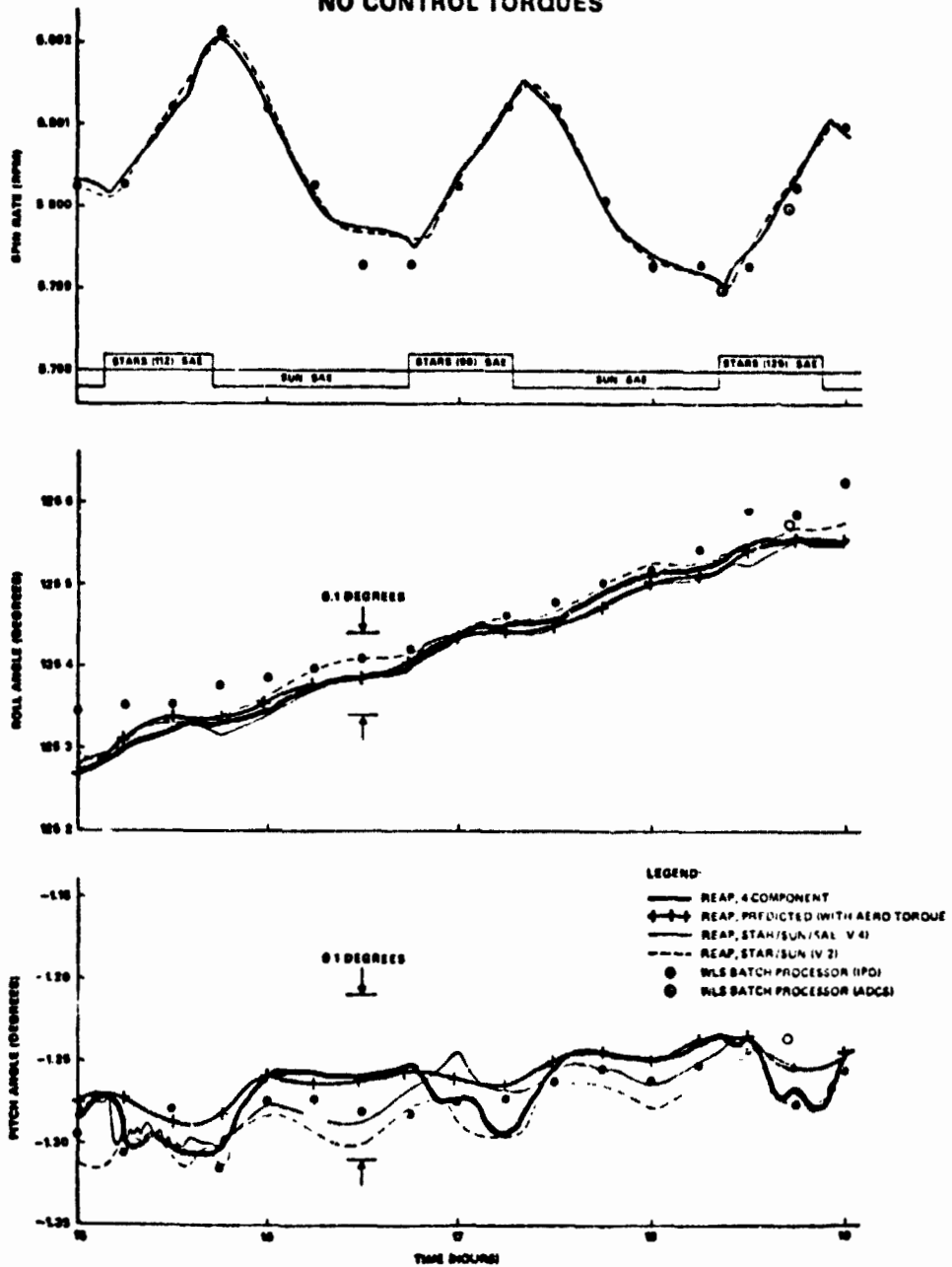


Figure 3. Attitude Results on August 12, 1975, Compared with Earlier Versions and Weighted Least Squares Results

To test whether these oscillations were due to aerodynamics, we incorporated a crude aero torque model into the prediction. This model includes only the sail and assumes a constant density over the circular orbit. The predicted state (with aero torques but without data) agreed very well with the estimated state solutions (with data but without aero torques). It shows the same pattern of alternating deep and narrow valleys, though the deep valleys were not as deep as in the estimated solution.

Conclusions

The oscillations at the orbit period have been shown to be real, due to unmodeled aerodynamic torques. These torques may slightly degrade the accuracy of the solutions during passes with minimal data, but are not required to be modeled for data spans with dense data as in Figure 3. Most of the data processed so far has been with Version 7, which agreed with the 4-component solutions to within 0.02 degrees though it was relatively closer to the V.2 curve. This solution was not plotted to avoid over-complicating the graph.

Equally important, the sensitivity of the 4-component version to unmodeled torques shows that the filter is 'open' to new data. The main parameters to be tuned were the state noise terms Q_1 and Q_2 , which were adjusted to make the attitude standard deviation from the covariance matrix approximately equal to the average deviation of the residuals. It further shows that the earlier version (V.2) was closed and did not follow the data. Version 4 was more open, but the solution also showed artifacts, such as those at 1700, which were due to the multiple path logic.

In addition to being easier to tune than the earlier versions, the 4-component model is also twice as fast. It runs at a ratio of 50:1 of real-time to CPU time on the Univac 1108.

REFERENCES

1. Wagner, W.E., R.D. Headrick, R.J. Wetmore, and H.M. Adelman, "OSO-8 Sequential Attitude Estimation" in Flight Mechanics/Estimation Theory Symposium May 1976, NASA Conference Publication 2022, September 1977.
2. Wagner, W.E., R.D. Headrick, and R.J. Wetmore, "Orbiting Solar Observatory (OSO-8) Recursive Estimation Attitude Program (REAP)--Mathematical Description and Validation", CSC System Description CSC/SD - 76/6069, September 1976.
3. Dunker, E., R. Wetmore, H. Witting, and C. Manders, "Orbiting Solar Observatory-I Attitude Prelaunch and Analysis Report", NASA X-581-75-137, June 1975.

Acknowledgements

The authors would like to acknowledge the assistance of Hank Adelman and Bud Norrod of CSC in designing the modifications and checking out the program. The work was performed under NASA contracts NAS5-11999 and NAS5-24300 at the direction of Gene Smith (Assistant Technical Representative) and Henry Linder (Data Processing Engineer).

PERFORMANCE OF GROUND ATTITUDE
DETERMINATION PROCEDURES
FOR HEAO-1*

Lawrence Fallon III and Conrad R. Sturch

Computer Sciences Corporation
Silver Spring, Maryland

INTRODUCTION

HEAO-1 was placed in a low circular orbit on August 12, 1977. It weighs approximately 3150 kilograms (7000 pounds) and is the heaviest unmanned Earth-orbiting satellite launched by NASA to date. The observatory will survey and map X-ray sources throughout the celestial sphere and will measure low energy gamma-ray flux. HEAO-1 is controlled to scan about the sunline and thus will provide a complete survey of the sky in 6 months. Ground attitude support is provided at GSFC by the HEAO-1 Attitude Ground Support System (AGSS). Information telemetered from Sun sensors, gyroscopes, star trackers, and an onboard computer are used by the AGSS to compute updates to the onboard attitude reference and gyro calibration parameters. The onboard computer utilizes these updates in providing continuous attitudes (accurate to 0.25-degree) for use in the observatory's attitude control procedures. This paper will discuss the relationship between HEAO-1 onboard and ground processing, the procedures used by the AGSS in computing attitude and gyro calibration updates, and the performance of these procedures in the HEAO-1 postlaunch environment.

*Work supported by the Spacecraft Control Programs Branch, Goddard Space Flight Center, National Aeronautics and Space Administration, under Contract NAS 5-11999.

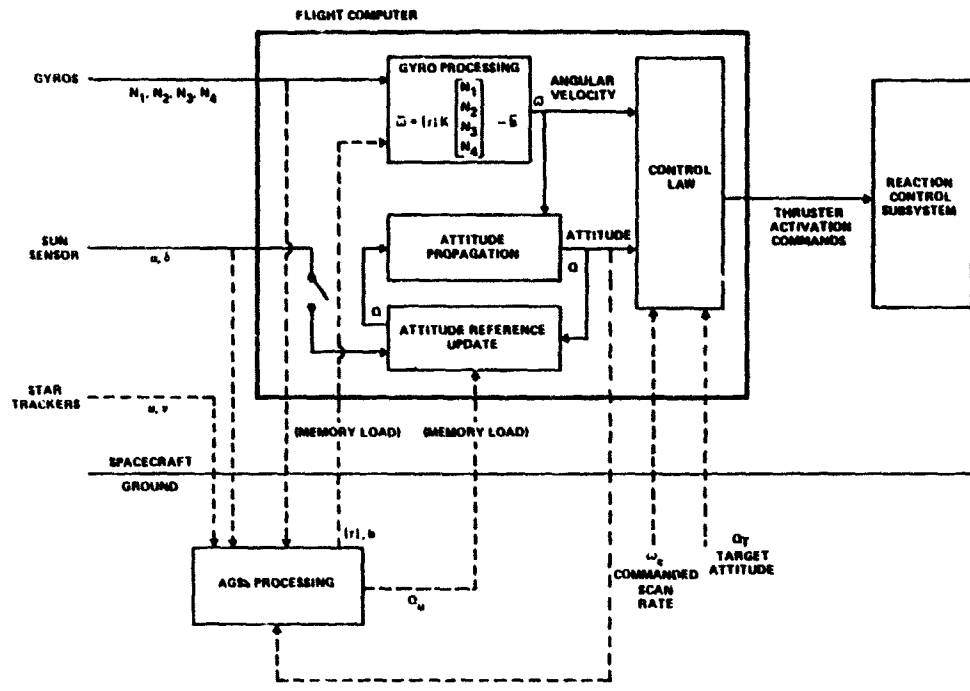


Figure 1. HEAO-1 Onboard and Ground Processing

HEAO-1 ONBOARD AND GROUND PROCESSING

The prime contractor of the HEAO mission, TRW Systems Group of Redondo Beach, California, devised the onboard system of attitude determination and control shown schematically in Figure 1 (Reference 1). This system consists of four Bendix rate-integrating gyroscopes, coarse and fine Sun sensors manufactured by TRW, two star trackers manufactured by the Ball Brothers Research Corporation, a Control Data Corporation (CDC) flight computer, and reaction control thrusters. The gyros measure angular displacements of the observatory during each 320-millisecond minor frame cycle. The input axes of the four gyros are skewed with respect to each other so that complete 3-axis rotational information is provided by any three of the four gyros. Output signals from the gyros are received by the gyro processing module in the flight computer. In this module, a nominal scale factor (K) and a 3-by-4 scale factor

correction and alignment matrix $[\tau]$ are applied to the gyro outputs to compute an angular velocity in the spacecraft reference frame. This angular velocity is further corrected for gyro null shift using a drift rate vector \bar{b} . The resultant angular velocity ($\bar{\omega}$) is available each 320-millisecond minor frame to the control law and to the attitude propagation module.

An incremental rotation quaternion (corresponding to the observatory's rotation during the 320-millisecond minor frame) is constructed in the attitude propagation module using the angular velocity. The observatory's estimate of its attitude is then propagated through the minor frame via quaternion multiplication. This propagated attitude (Q) is then available every minor frame to the control law, and every 40.96 seconds in telemetry.

In the celestial scan control law, the angular velocities and propagated attitudes are compared to a commanded scan rate (ω_c) and a target attitude (Q_T) to generate thruster activation commands for scan rate and Z-axis attitude control. (A celestial point mode to be entered occasionally later in the mission compares Q and Q_T to generate activation commands for 3-axis attitude stabilization.) In the celestial scan mode, target attitudes are sent to the observatory twice a day to cause its Z-axis to follow the sunline within 1 degree.

Errors in the gyro calibration parameters, $[\tau]$ and \bar{b} , cause errors in the angular velocities and hence errors in the propagated attitudes. To prevent the divergence of the observatory's Z-axis from the Sun and to initialize the attitude reference following launch, an attitude reference update procedure was devised by TRW. In this procedure, corrections are applied to the attitude reference based upon ground attitude solutions computed by the AGSS using the telemetered star tracker data. Corrections may also be applied using the two-axis angular displacements of the Sun from the observatory's Z-axis, as measured by the fine Sun sensor. This type of correction provides no attitude improvement about the sunline, but is sufficient to cause the observatory's Z-axis to follow the Sun. To further improve the accuracy of the onboard attitude reference, the

AGSS periodically transmits new values for the gyro drift rate vector, \bar{b} . The AGSS estimates new drift rates by monitoring the divergence of the propagated attitudes from the attitude solutions computed using the star tracker data. The capability for correcting the calibration matrix, $[\tau]$, also exists; but as long as $\bar{\omega}$ is nearly constant, corrections to both \bar{b} and $[\tau]$ are not simultaneously observable. For this reason, it is unlikely that new values for $[\tau]$ will be sent to the observatory until later in the mission. In the attitude control environment, the AGSS is required to compute reference and gyro calibration updates of sufficient accuracy and frequency that the observatory's attitude reference is maintained within a 0.25-degree accuracy level.

FUNCTIONAL OVERVIEW OF THE AGSS

The AGSS was devised by GSFC and Computer Sciences Corporation (CSC) to meet the HEAO-1 attitude support requirements. A functional description of the AGSS is presented in Figure 2. Telemetry from gyros, Sun sensors, star trackers, and the onboard computer is processed, and necessary star catalogs are generated. Stars are selected from a SKYMAP run catalog to form a sub-catalog which is typically a 12-degree-wide band orthogonal to the Sun vector (Reference 2). The major attitude processing sequence of the AGSS is then invoked. The first step in this procedure is to define intervals based upon data continuity and quality. Minor frame data is then processed. In this step, attitudes are propagated to desired times using the gyro data. Star tracker data is edited and calibrated to form observed star unit vectors in the spacecraft reference frame. These vectors are then transformed into a common reference frame using the propagated attitudes at the time of each star tracker observation. Average unit vectors are then computed using approximately 20 sequential sightings of each different star. When this procedure has been completed for all star tracker observations in a particular interval, attitude solution processing is initiated. If an adequate attitude estimate is not available, an attitude acquisition procedure, described below, is used to provide a 3-axis attitude.

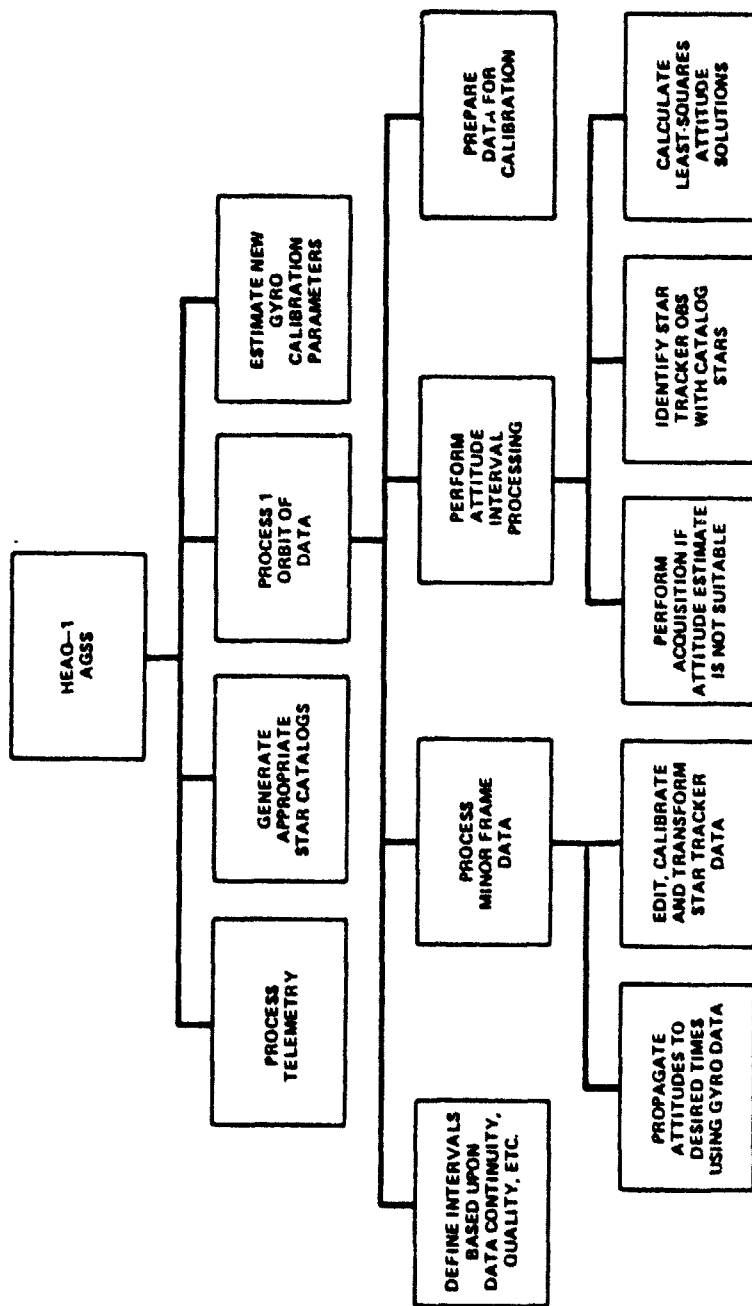


Figure 2. HEAO-1 AGSS Functional Description

When a suitable estimate has been obtained, small segments or "snapshots" of star observations are identified and least-squares attitude solutions are calculated using a procedure also described below. Following computation of several attitude solutions spaced in time throughout the interval of data, an appropriate solution is selected to form an attitude reference update. Solutions and associated propagated attitudes are then assembled and stored for later use in gyro calibration. After this attitude processing sequence has been completed for approximately one orbit of data, a short term drift rate solution is calculated. After several orbits have been processed, the gyro calibration module (see below) is again invoked to estimate a longer term drift rate solution for possible transmission to the observatory. The calibration matrix, $[\tau]$, could also be estimated at this time if sufficient observability is anticipated.

A. Initial Attitude Acquisition

The major inputs for initial attitude acquisition are observed Sun and star unit vectors transformed to a common reference frame and a star catalog in the shape of a band orthogonal to a Sun vector, supplied by ephemeris. This catalog has a limiting magnitude 0.7-magnitude fainter than the star tracker threshold; the stars are arranged in order of azimuth about the catalog pole. Star identification begins with the selection of a key observation, nominally the first observation with intensity brighter than an input limit. The key observation is matched to each observation in turn, yielding tentative X-axis phases. In each case candidates for the other observations are formed by matching the azimuthal difference between observation and catalog stars with the azimuthal difference between the key observation and the star tentatively associated with it. Angular separations between the key observation and the other observations are compared to the separations between the star matched with the key observation and the above candidates. The candidate (if any) which best satisfies this angular separation within a small tolerance is identified with the observation. These identifications are verified by demanding that the angular separation

between the observation and the observed Sun vector match the separation between the catalog star and ephemeris Sun vector. The largest such set of identifications is considered to be correct. A least-squares attitude solution is then computed with this set of identifications using a batch least squares algorithm developed by P. Davenport (Reference 3). To assess the quality of this 3-axis attitude solution, the procedure is repeated with different key observations.

B. Snapshot Attitude Determination

The initial attitude estimate is used to transform the observed star unit vectors to an approximate Geocentric Inertial (GCI) reference frame. A short segment or "snapshot" of the transformed observations is then selected for determination of an improved attitude estimate in the form of a correction quaternion.

The catalog is searched over small intervals of azimuth centered on each observation for stars whose angular separation from the observation is less than an input tolerance. A noncolinear triplet of observations, with separations exceeding specified limits and a minimal number of candidate stars, is selected. Identification of this triplet is made by matching the angular separations of the three observations with corresponding separations of the candidate stars. The other snapshot observations are identified with the candidates whose angular separations from the identified triplet stars best match the corresponding separations between these observations and the triplet of observations. Finally, a least-squares attitude solution for the mid-snapshot time is obtained from the weighted values of the observation unit vectors and the unit vectors of the corresponding catalog stars.

C. Gyro Calibration

Input to the gyro calibration module consists of pairs of snapshot attitude solutions $(Q_{S1}, Q_{S2})_j$ and associated propagated attitudes $(Q_{P1}, Q_{P2})_j$ the two

attitudes in each pair are typically separated in time by approximately 30 to 90 minutes. Also provided are continuous histories of propagated attitudes selected every 41 seconds between each $(Q_{P1})_j$ and $(Q_{P2})_j$ and the values of the gyro calibration parameters, $[\tau]$ and \bar{b} , which were used in calculating each set of propagated attitudes.

Several snapshot pairs are selected, provided that the same $[\tau]$ and \bar{b} values were used in creating the associated propagated attitudes. At least one pair of attitudes is necessary to estimate \bar{b} and at least four pairs are needed to estimate both \bar{b} and $[\tau]$. Corrections to \bar{b} and, optionally, $[\tau]$ are computed using a batch least-squares algorithm developed by P. Davenport (Reference 4). In this procedure, the following loss function is minimized:

$$J = \sum_{j=1}^N [\bar{Z}_j - [H_j] \bar{X}]^T [\bar{Z}_j - [H_j] \bar{X}]$$

where N is the number of snapshot pairs selected; the \bar{Z}_j are the vector parts of the error quaternions given by $(Q_{P1} Q_{S1}^{-1} Q_{S2} Q_{P2}^{-1})$; \bar{X} is a 12-vector containing corrections to \bar{b} and $[\tau]$; and the $[H_j]$ are 3 by 12 matrices containing the partial derivatives of the \bar{Z}_j with respect to \bar{X} . The $[H_j]$ are calculated sequentially using the propagated attitude histories. The \bar{Z}_j would be zero if no errors existed in $[\tau]$ or \bar{b} .

AGSS PERFORMANCE FOLLOWING LAUNCH

A. Initial Attitude Acquisition

The high voltage was applied to the star trackers two days following launch. Initial attitude acquisition was obtained from the data described in the second column of Table 1. The prelaunch gyro calibration parameters were used during processing of the data. The accuracy of the 3-axis attitude solution, estimated to be ± 0.2 -degree per axis, was sufficient for subsequent snapshot processing.

Later in the day, erroneous gyro calibration parameters were transmitted to the spacecraft. The use of these parameters by the onboard computer resulted in a large error in the propagated attitude and necessitated a second initial attitude acquisition attempt described in the third column of Table 1. The star tracker threshold had been commanded to the sixth-magnitude level and the calibration lights turned on. In this mode, observations of calibration lights account for about one-half of the total; these observations are rejected before star identification is attempted. Because the X-axis phase was known to within ± 20 degrees, only one-ninth of the band star catalog (6.7-magnitude-limit) was used for key-observation matches. Computation time was also shortened by requiring identification of only the first 30 star observations. The higher accuracy of the second attitude solution was due to the use of gyro calibration parameters estimated in flight from data following the first attitude acquisition.

B. Snapshot Attitude Determination

Snapshot processing statistics from a typical orbit of data are displayed in Table 2. About two-thirds of the original observations were rejected because they were caused by calibration lights, were excessively noisy, or lay outside the usable star tracker field-of-view. Nearly all of the observations for which identifications were attempted were actually identified. Most of the identifications which were subsequently rejected in the least-squares procedure were rejected due to the presence of a neighboring star within a specified angular separation range. The RMS of the angular residuals between the transformed observations and associated catalog stars is given in the last row of Table 2.

C. Reference and Gyro Calibration Update Procedures

The performance of the reference and gyro calibration update procedure is best assessed by examining the divergence between the onboard attitude reference and AGSS snapshot solutions as a function of time. Figure 3 illustrates the total

Table 1. Initial Attitude Acquisition - 8/14/77

ORBIT	31	42
STATION	HAW	OUI
GMT (HOURS, MINUTES)	5 ^h 28 ^m - 6 ^h 24 ^m	21 ^h 44 ^m - 23 ^h 09 ^m
STAR TRACKER	1	1
THRESHOLD (MAGNITUDE)	4	6
CALIBRATION LIGHTS	OFF	ON
NUMBER OF ACCEPTABLE OBSERVATIONS	50	32
NUMBER OF OBSERVATIONS USED	50	30
UNCERTAINTY IN LONGITUDE ESTIMATE (DEG)	±180	±20
NUMBER OF OBSERVATIONS IDENTIFIED	50	27
RMS RESIDUAL, CALCULATED vs CATALOG POSITIONS, (DEG)	0.051	0.0066
ESTIMATED ERROR, EACH AXIS (DEG)	±0.2	±0.03

Table 2. Typical Snapshot Processing Statistics - From 8/24/77

STAR TRACKER	1	2				
SNAPSHOT	1	2	3	1	2	3
TIME SPAN (MIN)	7.5	7.5	6.1	7.5	7.5	6.8
NUMBER OF ATTEMPTED IDENTIFICATIONS	15	11	10	23	12	14
NUMBER OF OBSERVATIONS IDENTIFIED	14	10	9	21	12	14
NUMBER OF IDENTIFICATIONS USED IN LEAST-SQUARES ATTITUDE SOLUTION	13	7	7	18	12	14
RMS RESIDUAL (DEG)	0.0026	0.0056	0.0051	0.0041	0.0072	0.0082

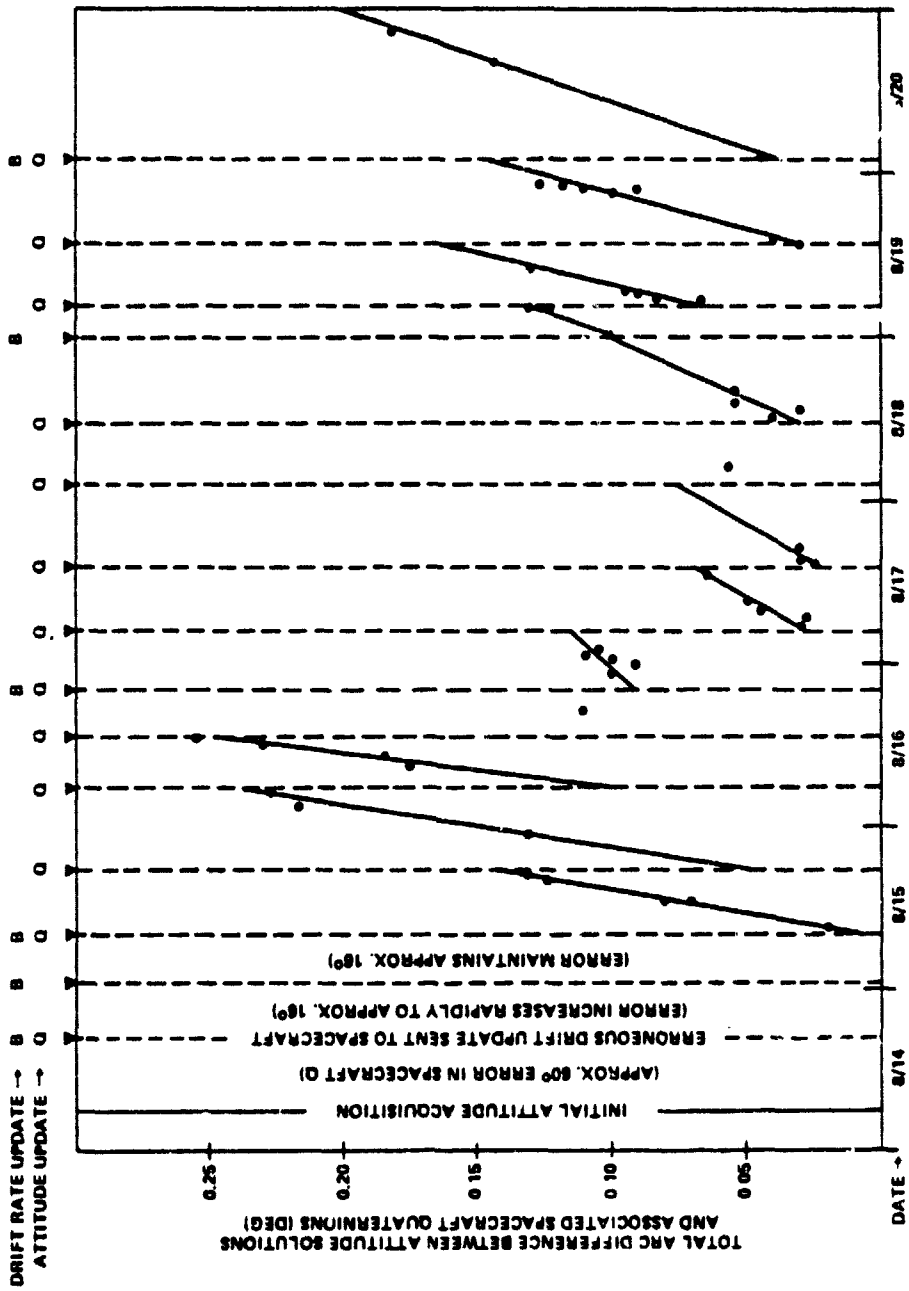


Figure 3. Attitude Propagation Accuracy - Week Following 8/14/77

arc difference between AGSS snapshot solutions and onboard attitudes at the same time, for the week following star tracker turn-on. After initial acquisition and until the first reference update was received, the onboard attitude was in error by approximately 60 degrees (nearly all in phase). When this first reference update was sent, an erroneous drift update was also transmitted. The attitude reference was initially corrected, but it then began to diverge rapidly to an error of nearly 16 degrees (when a correct drift update was received by the observatory). The next reference update caused the onboard attitude error to decrease within the 0.25-degree level. Additional reference and gyro updates further improved onboard accuracy throughout the remainder of the week following August 14.

Onboard propagation accuracy for the second week following star tracker turn-on is illustrated in Figure 4. Excluding the large errors observed on August 22 (caused by an unusually long interval when no data was received by the AGSS), additional improvement in onboard propagation accuracy is observed. Onboard performance after several weeks closely parallels the first half of the week following September 16, as shown in Figure 5. In this period, onboard accuracy is held to near or better than the 0.05-degree level (the level required for post-facto definitive attitude determination). On September 21, however, a commanded scan rate change caused a rapid increase in onboard error due to the strong dependence of drift rate solutions on the scan rate. A new drift rate was estimated using data following the scan rate change, and sent to the observatory on September 22. Propagation accuracy then returned to within the 0.05-degree level.

The gyro drift rate solutions for the week following September 16 are shown in Figure 6. Short-term drift solutions (obtained using data from approximately one orbit) are connected by a bold line. The apparent variation of the X and Y components is due more likely to difficulties in observability than to true drift

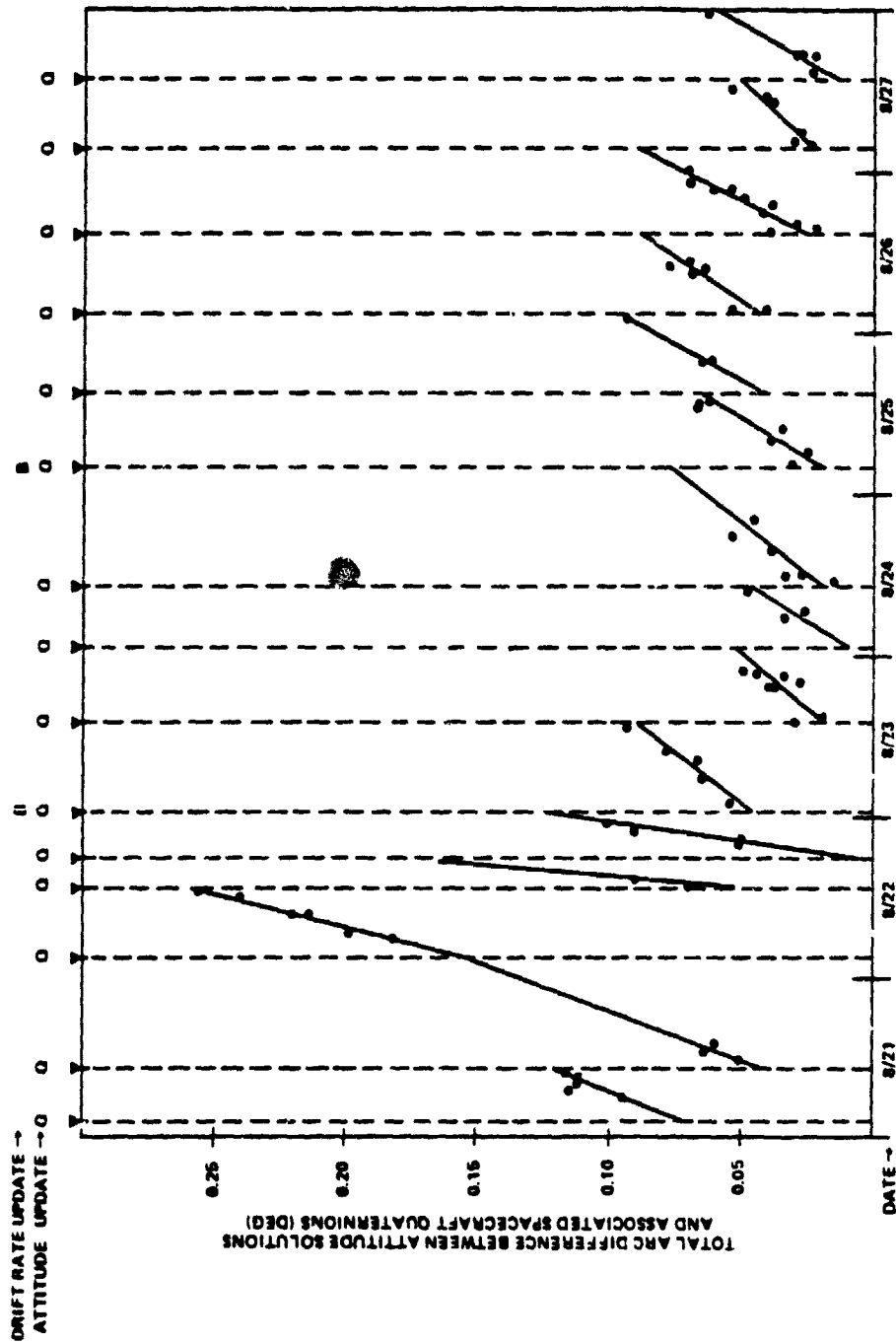


Figure 4. Attitude Propagation Accuracy - Week Following 8/21/77

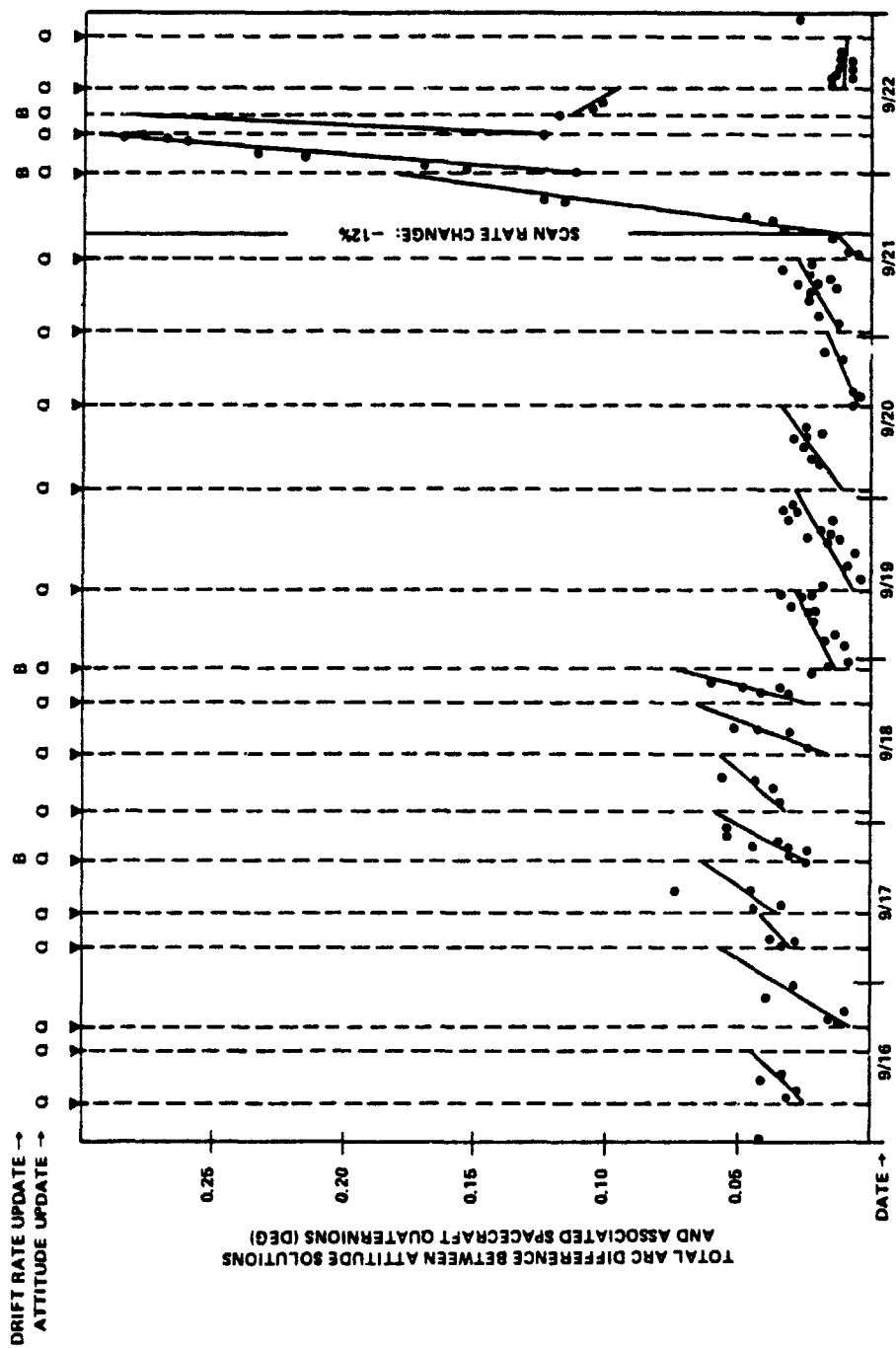


Figure 5. Attitude Propagation Accuracy - Week Following 9/16/77

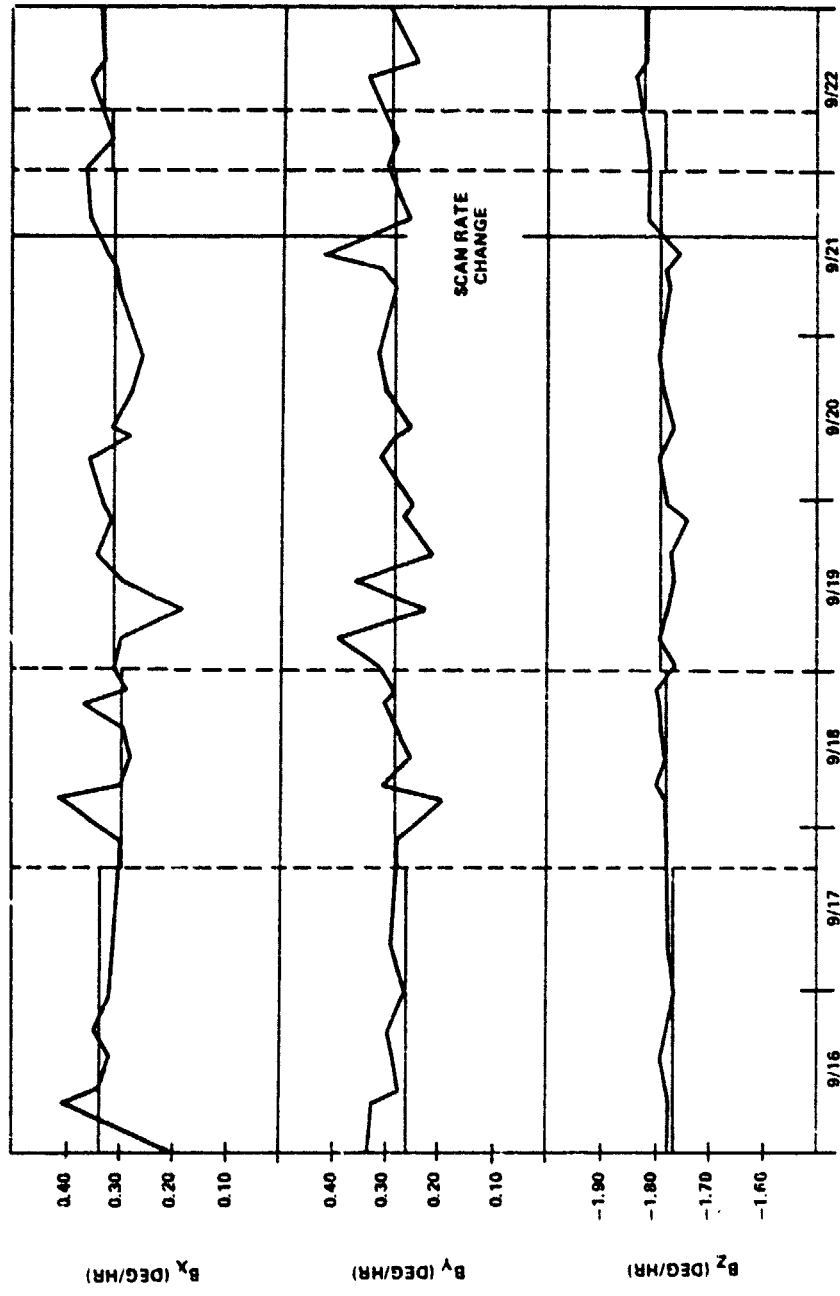


Figure 6. AGSS Drift Rate Solutions - Week Following 9/16/77

variation. The values sent to the observatory are illustrated by a thin horizontal line. These values were estimated using data acquired from several orbits in the 24 hours prior to transmission. The time variation of these longer-term solutions is far less dramatic.

CONCLUSIONS

The postlaunch performance of the AGSS may be summarized as follows:

- Initial attitude acquisition was achieved with sufficient accuracy for subsequent snapshot processing.
- Snapshot processing provides reliable attitudes for reference updates, gyro calibrations, and quality assurance of onboard attitude propagation.
- Attitude updates and gyro calibrations provided by the AGSS enable the onboard computer to maintain its attitude reference to well within the 0.25-degree accuracy requirement (and often within the 0.05-degree definitive accuracy requirement).

The success of the AGSS in its postlaunch support is due in part to the performance of the observatory's attitude sensors, particularly the gyros. The combined performance of the various components of HEAO-1 onboard and ground processing demonstrates the technical feasibility of using an onboard computer to supply attitudes of definitive quality.

ACKNOWLEDGEMENTS

The assistance of C. M. Gray and the HEAO-1 Attitude Operations group is gratefully acknowledged.

REFERENCES

1. D. P. Hoffman, "HEAO Attitude Control Subsystem - a Multimode/Multimission Design", AIAA Guidance and Control Conference, San Diego California, August 16-18, 1976
2. D. M. Gottlieb and C. M. Gray, "SKYMAP System Description: Star Catalog Data Base Generation and Utilization", Computer Sciences Corporation, CSC/SD-76/6041, November 1976
3. J. E. Keat, "Analysis of Least-Squares Attitude Determination Routine DOAOP", Computer Sciences Corporation, CSC/TM-77/6034, February 1977
4. J. E. Keat, "Gyro Calibration Analysis for the High Energy Astronomy Observatory-A (HEAO-A)", Computer Sciences Corporation, CSC/TM-77/6082, June 1977

D13

N79-14134

ISEE-C ATTITUDE DETERMINATION USING
FINE SUN SENSOR DATA ONLY*

Lawrence P. Gunshol
Computer Sciences Corporation

ABSTRACT

The International Sun-Earth Explorer-C (ISEE-C) will be spin stabilized with the spin axis attitude nominally maintained within 1.0 degree of the north ecliptic pole. ISEE-C will be stationed in the vicinity of the Sun-Earth interior libration point where the only significant attitude perturbation is due to solar radiation pressure. The primary attitude sensors are two fully redundant Fine Sun Sensors (FSSs). The specified sensor accuracy after calibration is ± 0.05 degrees for a ± 3 degree range about the spin plane. An operational requirement is to determine the attitude to within 1.0 degree using up to 30 days of FSS data. To do this, we have developed techniques to determine the spin axis attitude using FSS data only. At any given time, the Sun angle specifies the orientation of the spin axis relative to the sunline. The instantaneous time rate of change of the Sun angle is directly proportional to the orientation of the spin axis relative to a reference plane that is normal to the ecliptic. Thus, the spin axis attitude can be determined when sufficient data has been collected to accurately measure the rate of change of the Sun angle. The uncertainties can be computed directly from the uncertainties in the coefficients of the smoothed Sun angle curve.

The FSS-only technique is unique in that ephemeris vectors are required only to transform the attitude results to more conventional coordinate frames. The combination of the mission geometry and the FSS accuracy make ISEE-C an ideal mission for applying this method. However, the technique can be used on other missions, such as spin stabilized geosynchronous missions.

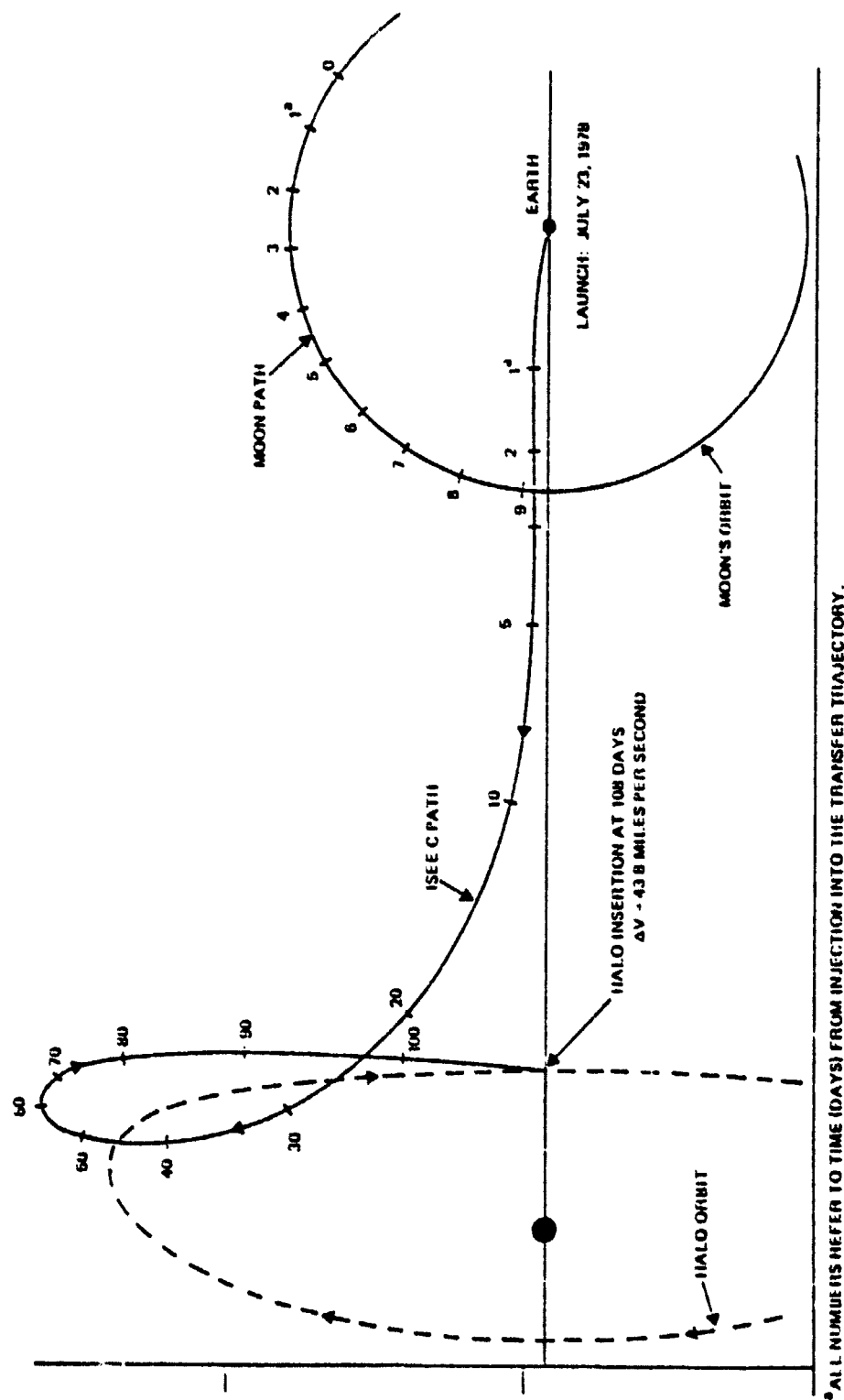
* This work was performed under Contract NAS 5-11999 with NASA's Goddard Space Flight Center.

ISEE Program Overview: The International Sun-Earth Explorer (ISEE) Program is an international cooperative program which will use three coordinated spacecraft to advance knowledge of the magnetosphere, interplanetary space, and their interactions. On October 23, 1977, the ISEE-A (mother) and ISEE-B (daughter) were launched aboard the same Thor Delta launch vehicle into a highly eccentric Earth orbit (apogee equal to 22 Earth radii, perigee equal to approximately 300 km). The third spacecraft, ISEE-C, will be launched aboard a Delta 2914 rocket and will be placed in a heliocentric orbit near the unstable libration point L_1 between the Earth and the Sun, a distance of approximately 4 lunar orbit radii or 0.01 astronomical unit from the Earth. The National Aeronautics and Space Administration has responsibility for development of the ISEE-A and ISEE-C spacecraft; the European Space Agency is responsible for ISEE-B.

Each of the ISEE spacecraft, considered alone, can contribute to scientific knowledge. However the scientific basis for the mission relies on the spatial and temporal resolution obtained by comparing measurements made with identical instruments on ISEE-A and ISEE-B. After launch, ISEE-C will supply information on the upstream solar wind, thereby enhancing the value of the total experiment. For maximum usefulness, this information should be obtained concurrently with measurements on ISEE-A and ISEE-B. A minimum of 2 years of simultaneous data is planned for the mission.

ISEE-C Mission Orbit: An ecliptic plane projection of the nominal ISEE-C transfer trajectory is presented in Figure 1. Following a retro maneuver at approximately injection plus 107 days, ISEE-C will be placed in a roughly elliptical path, termed a halo orbit, about the unstable Sun-Earth interior libration point L_1 . The nominal period of the halo orbit is approximately 6 months.

Figure 2 depicts the halo orbit, and defines a Rotating Libration Point (RLP) coordinate system centered at L_1 . The X axis points toward the Earth-Moon



* ALL NUMBERS REFER TO TIME (DAYS) FROM INJECTION INTO THE TRANSFER TRAJECTORY.

Figure 1. Typical ISEE-C Transfer Trajectory (Ecliptic Plane Projection)

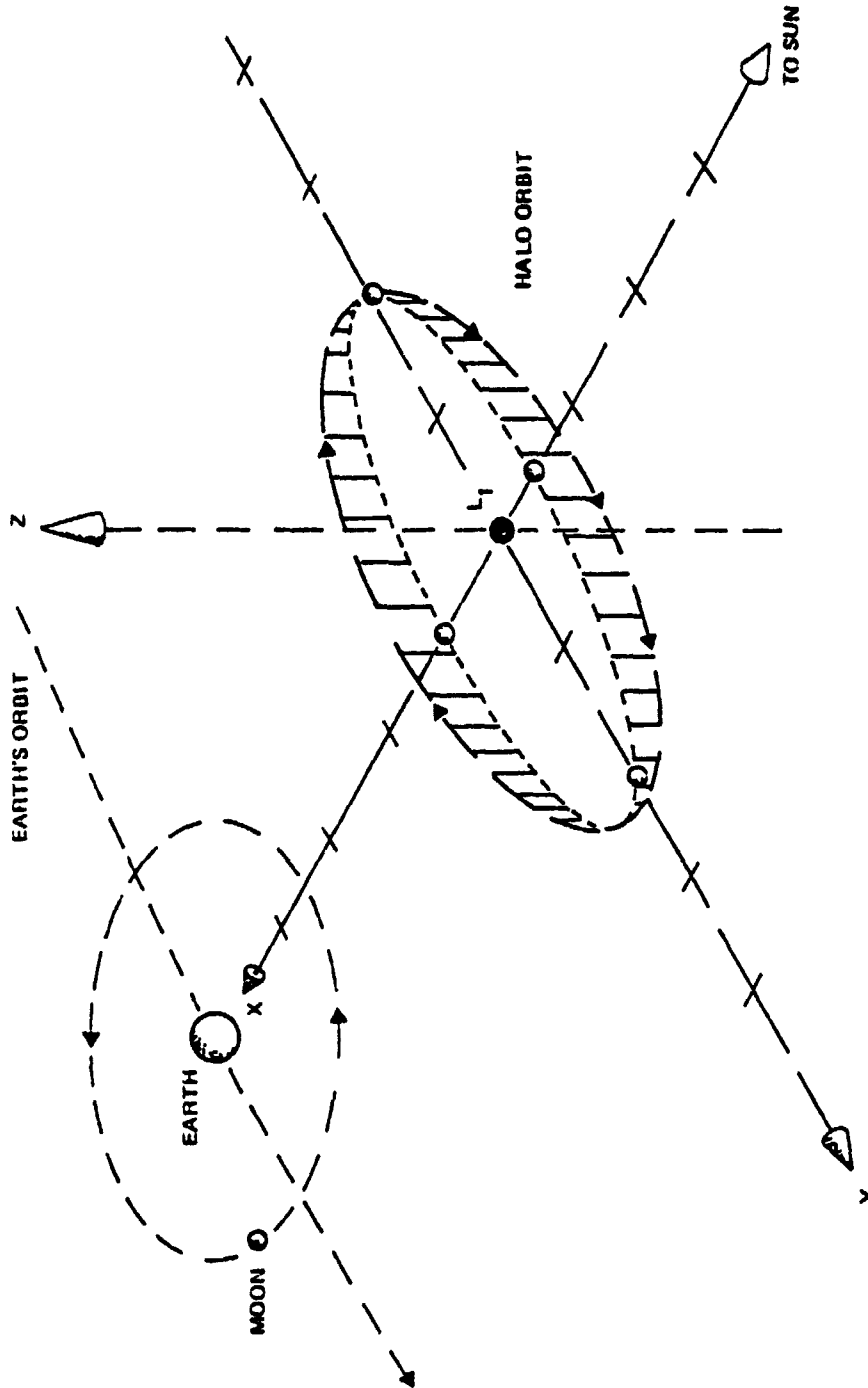


Figure 2. Halo Orbit Around Sun-Earth Libration Point

barycenter, the Z axis points toward the north ecliptic pole (NEP), and the Y axis completes the right-handed coordinate frame. In the RLP, the maximum excursions in the position are $X = +240,000$ km, $-170,000$ km; $Y = \pm 670,000$ km; and $Z = \pm 120,000$ km. The stationkeeping strategy will be to maintain the spacecraft within a torus of radius 5,000 km about the nominal path. Stationkeeping maneuvers will probably be required every 45 to 60 days.

ISEE-C Spacecraft: ISEE-C is spin stabilized, with a nominal spin rate of 19.75 ± 0.2 rpm. As shown in Figure 3, the spacecraft is a 16-sided, drum-shaped structure. It is 161 centimeters high, 174 centimeters in diameter, and has a nominal mass of 457 kilograms. Solar arrays cover the sides of the spacecraft except for a band near the center from which two experiment booms, two inertia booms, and four deployable wire antennas extend. These four wires combined with deployable $\pm Z$ axis wire antennas provide a three-dimensional radio mapping capability.

The tolerance on the spacecraft dynamic balance is small. Prior to deployment of the four radial wires, the maximum spacecraft dynamic imbalance is expected to be less than 0.2 degree. After deployment of the wires, the dynamic imbalance is expected to decrease to approximately 0.1 degree.

ISEE-C Attitude Sensors: A panoramic attitude scanner (PAS) and two fully redundant fine Sun sensors (FSSs) are located on the sides of the spacecraft. The PAS, manufactured by Ball Brothers Research Corporation, is identical to the one flown on the International Ultraviolet Explorer and the ISEE-A spacecraft. The function of the PAS is to map the horizons and terminators of the Earth and Moon by measuring the crossing times relative to a Sun crossing.

The FSS system is manufactured by the Adcole Corporation. It is similar to other Adcole digital Sun sensors, employing a quartz block with optical masking of an array of silicon photocells and having a command slit to generate

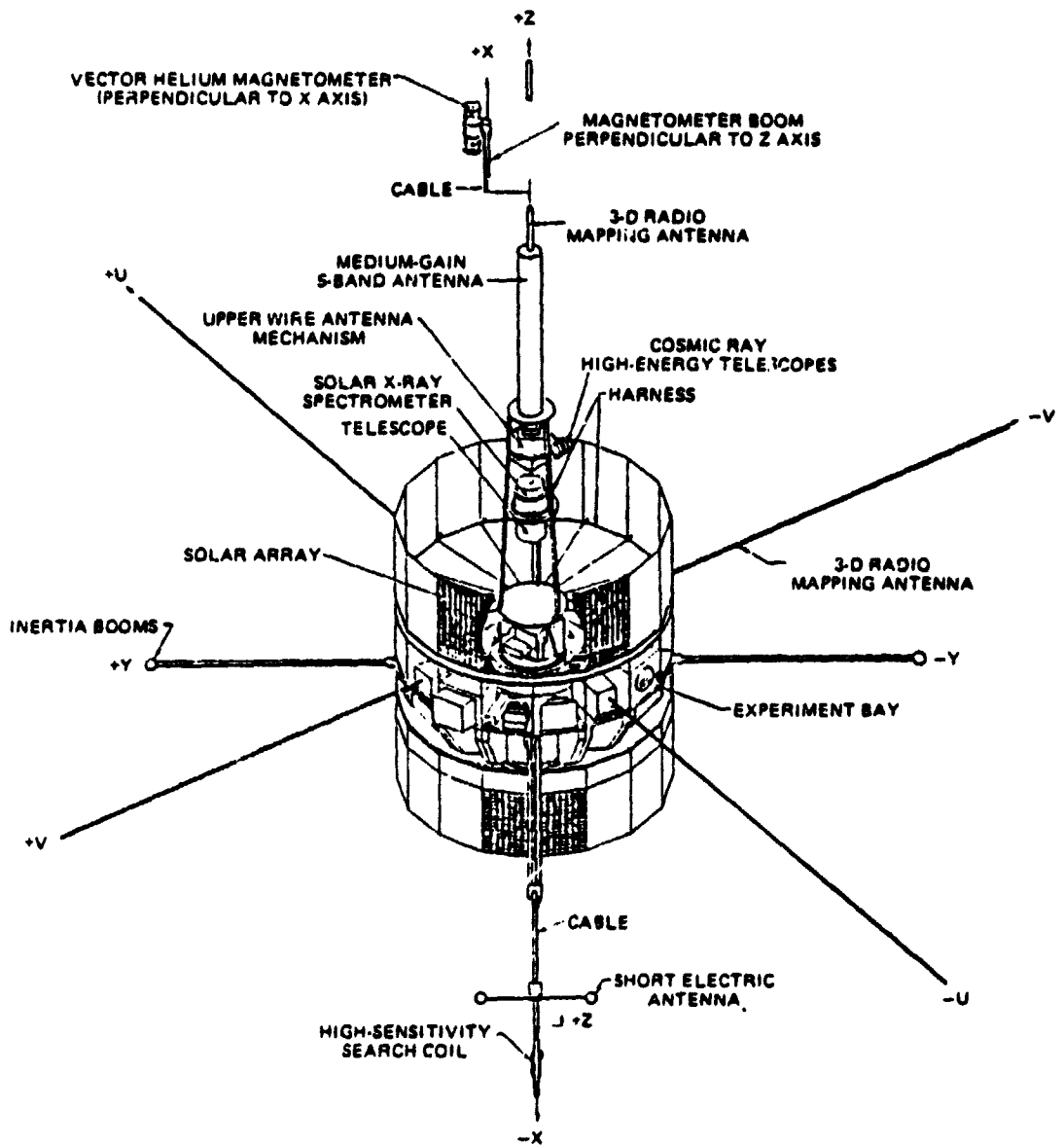


Figure 3. ISEE-C Configuration

the command pulse. The fan-shaped field of view of each FSS is specified to be 128 ± 2 degrees in width. The FSSs measure the angle between the sunline and a reference axis fixed in the sensor. This measurement is readily converted to the Sun angle, β , between the spacecraft spin axis and the sunline.

The FSSs operate on a 5 Volt system. The output is biased, quantized in 20 millivolt counts, and telemetered to the ground. In the range $-1^\circ \leq \beta \leq 1^\circ$, the system provides for a resolution of 0.003 degree. The measurement noise is specified to be less than 0.005 degree. When the spacecraft is spinning between 5 and 25 revolutions per minute, the accuracy of the Sun angle measurement is as follows.

<u>Range of β</u> <u>(Degrees)</u>	<u>Accuracy</u> <u>(Degrees)</u>
25-50; 130-154	± 0.25
50-87; 93-130	± 0.1
87-93	± 0.05

The increased accuracy in the $87 \leq \beta \leq 93$ degree range is due to calibration of the sensor which was performed by the manufacturer. A calibration table was generated for both FSSs at 0.1-degree intervals over the specified Sun angle range. Each point in the table gives a correction term ($\delta\beta$) to be added to the measured Sun angle. The root mean square (RMS) residual errors following application of the calibration data have been computed to be 0.008 and 0.004 degree for FSS 1 and 2, respectively. The maximum residual errors following application of the calibration data for FSS 1 and 2 have been computed to be 0.03 and 0.01 degree, respectively. A plot of the residual errors for FSS 2 is presented in Figure 4.

The FSS mounting tolerance is very small. The sensors are to be aligned with respect to the spacecraft body axes to within 0.005 degree. As a result, it is anticipated that the only significant Sun angle bias source will be the aforementioned spacecraft dynamic imbalance of 0.2 degree or less.

ISEE-C FINE SUN SENSOR
CALIBRATION
SENSOR HEAD # 2
APRIL 12, 1977

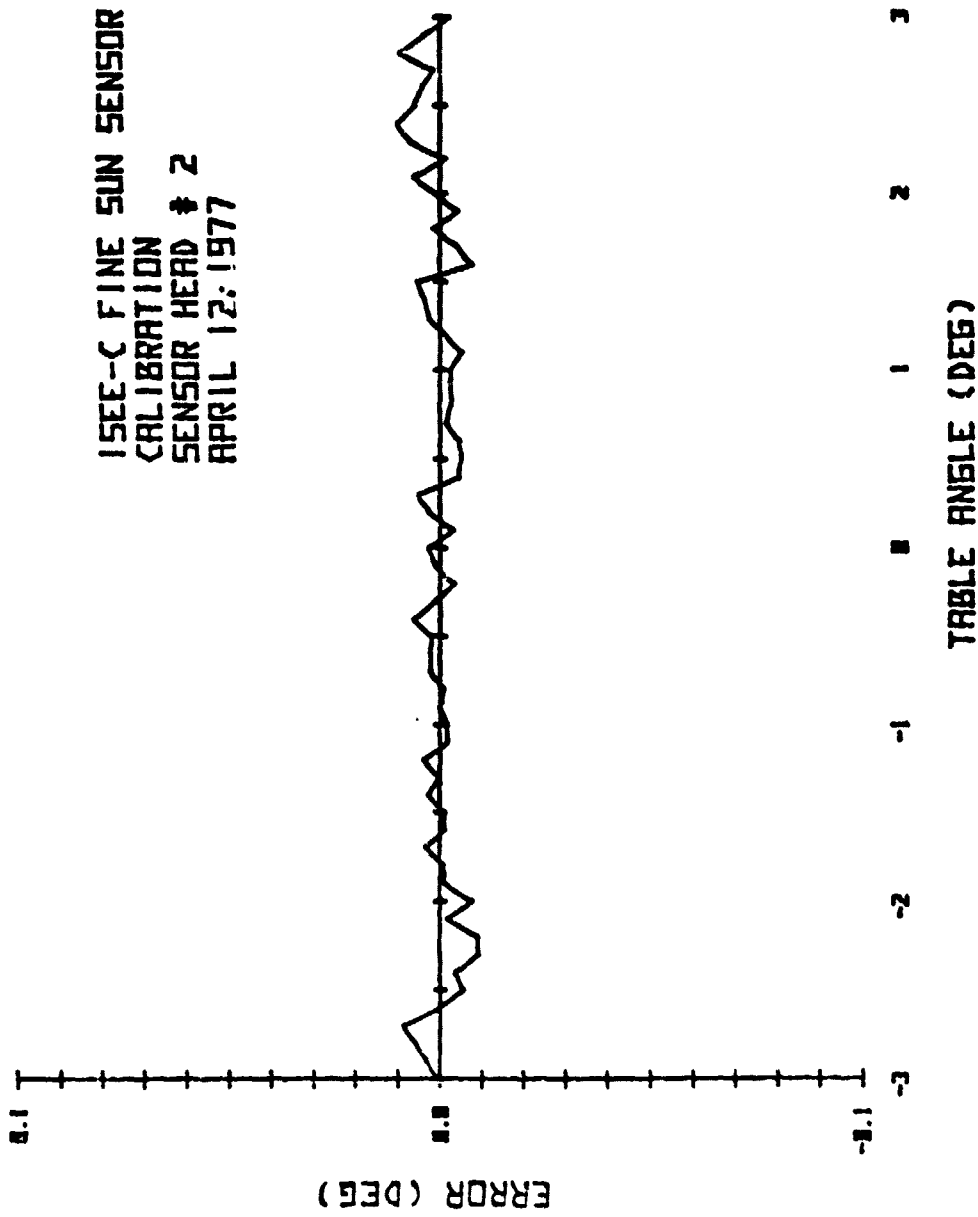


Figure 4. FSS Measurement Errors Following Calibration

ISEE-C Attitude Determination and Control Requirements The ISEE-C attitude control requirement in its mission orbit is to maintain the spin axis to within 1 degree of the North Ecliptic Pole (NEP). The attitude is to be determined to an accuracy of 1 degree.

The spin axis attitude will be perturbed as a result of both orbit maneuvers and solar radiation pressure torque. Studies have shown that solar radiation torque will cause the spin axis to precess along a small circle on the celestial sphere with a period of 1 year. The angular radius of the small circle at the start of the halo orbit is predicted to be approximately 0.5 degree. This results in a precession rate of approximately 0.008 degree per day. The angular radius of the precession circle is expected to decrease throughout the mission lifetime because of the shift in the center of mass relative to the center of pressure resulting from fuel usage. A precession radius of approximately 0.2 degree is anticipated when the tanks are empty.

Because of the halo orbit geometry, the quality of the attitude information provided by the PAS will vary significantly with position in orbit. In order to meet the 1 degree attitude determination accuracy requirement, up to 30 days of FSS data at an attitude perturbed only by the solar radiation pressure torque will be processed. The techniques described below that have been developed to perform this task are termed FSS-only techniques.

Coordinate Systems: To perform the FSS-only computations, three coordinate frames are required: (1) the Geocentric Equatorial Inertial (GCI) coordinate system, (2) the Geocentric Solar Ecliptic (GSE) coordinate system, and (3) the Geocentric Sun Line-of-Sight Rotating (GSR) coordinate system.

The GCI coordinate system is Earth centered. The X_{GCI} axis points toward the vernal equinox of date; the Z_{GCI} axis is normal to the true equator date; and the Y_{GCI} axis completes the right-handed system. The sunline and

spacecraft vectors in GCI at time t are represented by \vec{U} and \vec{R} , respectively. (The unit sunline vector in GCI is \hat{U} .) The corresponding velocity vectors are $\dot{\vec{U}}$ and $\dot{\vec{R}}$, respectively. Relative to the spacecraft, the sunline position and velocity vectors are

$$\vec{U}_A = \vec{U} - \vec{R} \quad (1)$$

$$\dot{\vec{U}}_A = \dot{\vec{U}} - \dot{\vec{R}} \quad (2)$$

The corresponding unit vectors are

$$\hat{U}_A = \frac{\vec{U} - \vec{R}}{|\vec{U} - \vec{R}|} \quad (3)$$

$$\hat{\dot{U}}_A = \frac{\dot{\vec{U}} - \dot{\vec{R}}}{|\dot{\vec{U}} - \dot{\vec{R}}|} \quad (4)$$

The GSE coordinate system is defined as follows. The X_{GSE} axis points toward the Sun. The Z_{GSE} axis points toward the north ecliptic pole (NEP). The Y_{GSE} axis completes the right-handed system. The GCI coordinate system is related to the GSE coordinate system by the following transformation matrix.

$$\begin{pmatrix} X \\ Y \\ Z \end{pmatrix}_{\text{GSE}} = \begin{bmatrix} \cos L & \sin L \cos \epsilon & \sin L \sin \epsilon \\ -\sin L & \cos L \cos \epsilon & \cos L \sin \epsilon \\ 0 & -\sin \epsilon & \cos \epsilon \end{bmatrix} \begin{pmatrix} X \\ Y \\ Z \end{pmatrix}_{\text{GCI}} \quad (5)$$

where L is the celestial longitude of the Sun, and ϵ is the obliquity of the ecliptic.

The GSR coordinate system is defined as follows. The X_{GSR} axis is aligned with \hat{U}_A (the geocentric unit vector parallel to the line-of-sight from the spacecraft to the Sun). The Y_{GSR} axis is defined by the following expression

$$\hat{Y}_{\text{GSR}} = \frac{\hat{N}\hat{E}\hat{P} \times \hat{U}_A}{|\hat{N}\hat{E}\hat{P} \times \hat{U}_A|} \quad (6)$$

where $\hat{N}\hat{E}\hat{P}$ is a unit vector pointing toward the north ecliptic pole. The Z_{GSR} axis completes the right-handed system.

Referring to Figure 5, the unit spin axis vector, \hat{A} , is defined by the coordinates β and EL. β is the aspect angle of the sunline relative to \hat{A} . EL is the dihedral angle between the $X_{\text{GSR}} - Z_{\text{GSR}}$ plane and the plane defined by X_{GSR} and \hat{A} . EL is positive in the sense $\hat{Y}_{\text{GSR}} \times \hat{Z}_{\text{GSR}}$.

It follows that

$$\hat{A} = \cos \beta \hat{X}_{\text{GSR}} - \sin \beta \sin \text{EL} \hat{Y}_{\text{GSR}} + \sin \beta \cos \text{EL} \hat{Z}_{\text{GSR}} \quad (7)$$

The GSR coordinate system is aligned with the GSE coordinate system by using the following transformation matrix

$$\begin{pmatrix} X \\ Y \\ Z \end{pmatrix}_{\text{GSE}} = \begin{bmatrix} \cos \gamma_N \cos \gamma_E & -\sin \gamma_E & \cos \gamma_E \sin \gamma_N \\ \sin \gamma_E \cos \gamma_E & \cos \gamma_E & \sin \gamma_N \sin \gamma_E \\ -\sin \gamma_N & 0 & \cos \gamma_N \end{bmatrix} \begin{pmatrix} X \\ Y \\ Z \end{pmatrix}_{\text{GSR}} \quad (8)$$

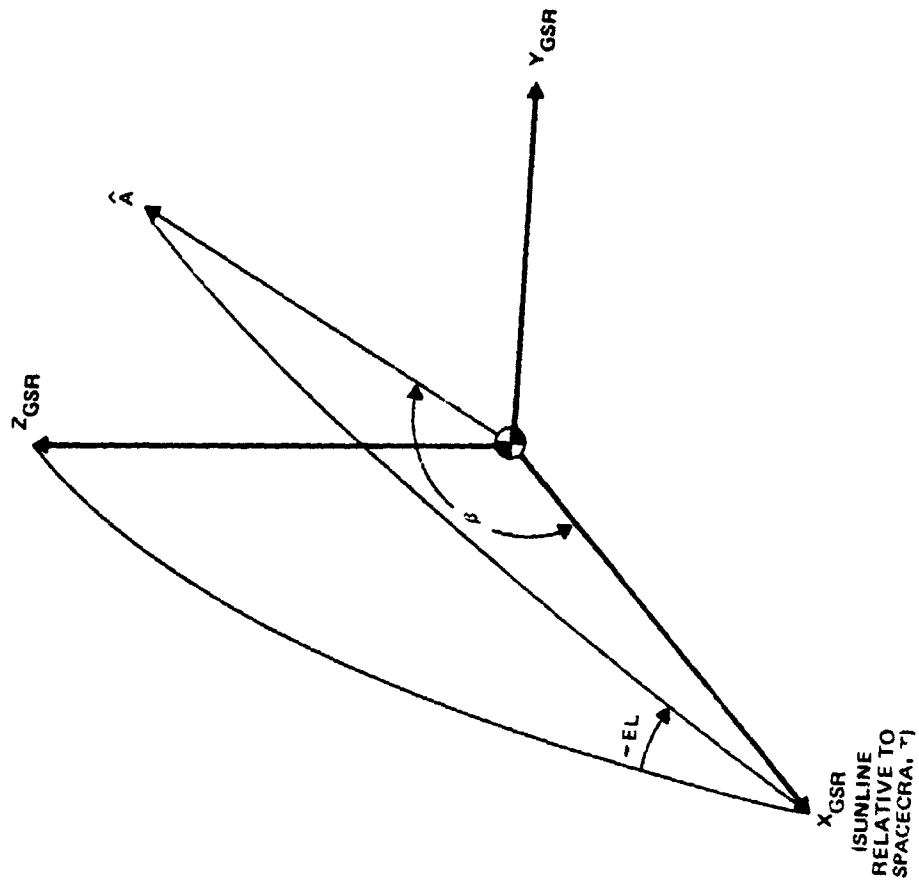


Figure 5. GSR Coordinate System

where

$$\gamma_N = -\sin^{-1} (\hat{U}_A \cdot \hat{NEP}) \quad (9)$$

$$\gamma_E = -\sin^{-1} \left[\frac{\hat{NEP} \times \hat{U}_A}{|\hat{NEP} \times \hat{U}_A|} \cdot (\hat{NEP} \times \hat{U}) \right] \quad (10)$$

FSS-Only Attitude Determination Equations: We denote time-dependence for an arbitrary vector, \vec{V} , as $\vec{V}(t)$. Figure 6 depicts the GSR coordinate frame on the unit celestial sphere at arbitrary time t . Here, the size of the locus of the sunline relative to the spacecraft is exaggerated for clarity. In reality, the maximum angular deviation of $\hat{U}_A(t)$ above or below the ecliptic for the ISEE-C mission orbit is approximately 0.05 degree. The maximum angular deviation of $\hat{U}_A(t)$ from the true sunline $\hat{U}(t)$ as measured in the ecliptic is approximately 0.25 degree.

The normal to the instantaneous plane of motion of $\hat{U}_A(t)$ is computed as follows.

$$\hat{n}(t) = \frac{\vec{U}_A(t) \times \vec{U}_A(t)}{|\vec{U}_A(t) \times \vec{U}_A(t)|} \quad (11)$$

The angle ζ between the instantaneous plane of motion of $\hat{U}_A(t)$ and the $X_{GSR} - Y_{GSR}$ plane is

$$\zeta = -\sin^{-1} \left(\hat{n}(t) \cdot \frac{\hat{NEP} \times \hat{U}_A(t)}{|\hat{NEP} \times \hat{U}_A(t)|} \right) \quad (12)$$

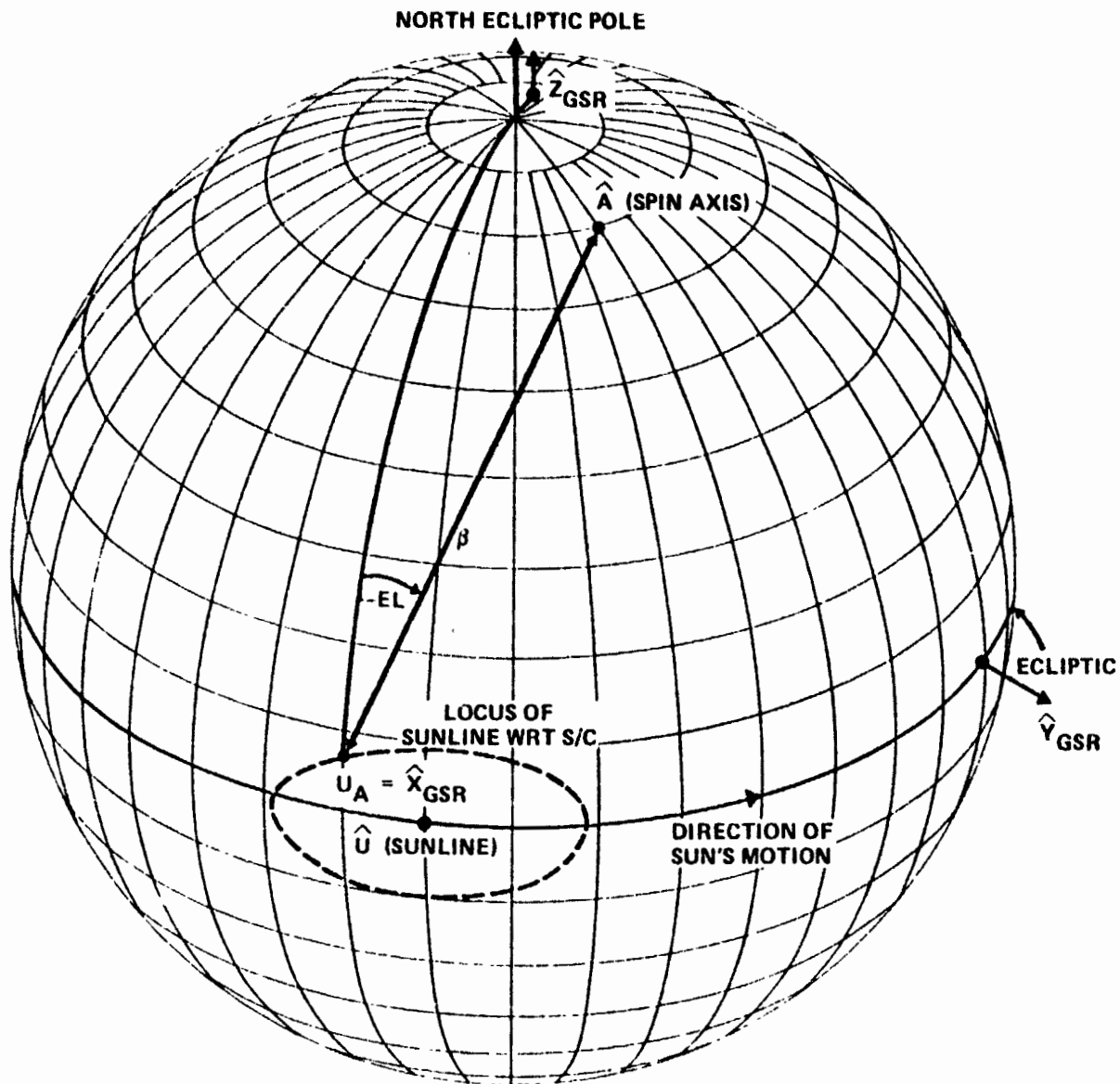


Figure 6. FSS Measurement Geometry

The instantaneous angular velocity of $\hat{U}_A(t)$ is

$$\omega_A = \cos^{-1} \left((\vec{U}_A(t) + \vec{U}_A(t)) \cdot \vec{U}_A(t) \right) \quad (13)$$

Holding the GSR frame fixed at t , the unit sunline relative to the spacecraft at time t^1 (where $t^1 = t + \delta t$) is computed as follows.

$$\begin{aligned} \hat{U}_A(t) = & \cos(\omega_A(t^1-t)) \hat{X}_{GSR} + \cos \zeta \sin(\omega_A(t^1-t)) \hat{Y}_{GSR} \\ & + \sin \zeta \sin(\omega_A(t^1-t)) \hat{Z}_{GSR} \end{aligned} \quad (14)$$

In the same frame of reference, the spin axis at time t^1 is

$$\begin{aligned} \hat{A}(t^1) = & \cos(\beta(t) + \delta_1) \hat{X}_{GSR} - \sin(\beta(t) + \delta_1) \sin(EL(t) + \delta_2) \hat{Y}_{GSR} \\ & + \sin(\beta(t) + \delta_1) \cos(EL(t) + \delta_2) \hat{Z}_{GSR} \end{aligned} \quad (15)$$

where δ_1 and δ_2 are perturbations in $\beta(t)$ and $EL(t)$, respectively, resulting from solar radiation pressure torque.

Using Equations (14) and (15), the Sun angle at time t^1 is computed to be

$$\begin{aligned} \beta(t^1) = & \cos^{-1} \left[\cos(\beta(t) + \delta_1) \cos(\omega_A(t^1-t)) \right. \\ & - \sin(\beta(t) + \delta_1) \sin(EL(t) + \delta_2) \cos \zeta \sin(\omega_A(t^1-t)) \\ & \left. + \sin(\beta(t) + \delta_1) \cos(EL(t) - \delta_2) \sin \zeta \sin(\omega_A(t^1-t)) \right] \end{aligned}$$

Differentiating with respect to t^1

$$\begin{aligned} \frac{\partial \beta(t^1)}{\partial t^1} = & [\omega_A \cos(\beta(t) + \delta_1) \sin(\omega_A(t^1 - t)) \\ & + \omega_A \sin(\beta(t) + \delta_1) \sin(EL(t) + \delta_2) \cos \zeta \cos(\omega_A(t^1 - t)) \quad (16) \\ & - \omega_A \sin(\beta(t) + \delta_1) \cos(EL(t) + \delta_2) \sin \zeta \cos(\omega_A(t^1 - t))] / \sin \beta(t^1) \end{aligned}$$

Note that the perturbations δ_1 and δ_2 are small relative to the motion of the sunline. By taking the limit of Equation (16) as δt approaches zero, we obtain

$$\lim_{\delta t \rightarrow 0} \frac{\partial \beta(t^1)}{\partial t^1} = \dot{\beta}(t) = \omega_A \cos \zeta \sin EL(t) - \omega_A \sin \zeta \cos EL(t) \quad (17)$$

which becomes, after rearranging terms,

$$\sin EL(t) = \frac{\dot{\beta}(t)}{\omega_A \cos \zeta} + \tan \zeta \cos EL(t) \quad (18)$$

Equation (18) in general is solved as a quadratic in terms of $\sin EL(t)$. However, as noted previously, the ISEE-C spin axis will be aligned within 1 degree

of the NEP . Thus $EL(t)$ is a small angle, and it follows that

$$EL(t) \approx \frac{\dot{\beta}(t)}{\omega_A \cos \zeta} + \tan \zeta \quad (19)$$

From the equation, it is evident that: (1) the instantaneous value of EL is directly proportional to the instantaneous time rate of change of β , and (2) Sun angle bias errors do not affect the computation of EL .

Simulations have shown that the ISEE-C halo orbit Sun angle measurements over a full year can be accurately fit to a sine wave model including the fundamental and second harmonic frequencies. The linearized form of the analytical curve is as follows.

$$\beta(t) = C_0 + C_1 \cos \omega t + C_2 \sin \omega t + C_3 \cos 2 \omega t + C_4 \sin 2 \omega t \quad (20)$$

where $\omega = 1$ revolution per year and t is measured relative to an attitude reference time. Differentiating with respect to time yields

$$\dot{\beta}(t) = -\omega C_1 \sin \omega t + \omega C_2 \cos \omega t - 2 \omega C_3 \sin 2 \omega t + 2 \omega C_4 \cos 2 \omega t \quad (21)$$

Shorter arcs of data can be fit using either a sine wave model with fundamental frequency only, or using a low-order polynomial. Regardless of the analytical model employed, a smoothed value of $\beta(t)$ and $\dot{\beta}(t)$ at arbitrary time t within the interval of data can be evaluated. Attitude determination then proceeds as follows.

1. Compute $EL(t)$ using Equations (12), (13), and (19)
2. Compute $\hat{A}(t)$ in GSR using Equation (7)

3. Transform $\hat{A}(t)_{\text{GSR}}$ to GSE using Equation (8)
4. Transform $\hat{A}(t)_{\text{GSE}}$ to GCI using the inverse transformation defined by Equation (5)
5. $\hat{A}(t)_{\text{GCI}}$ can then be converted to right ascension and declination using the standard equations

FSS-Only Attitude Uncertainty: Referring to Equation (19), the instantaneous elevation angle is a function of ζ , ω_A , and $\dot{\beta}$. Both ζ and ω_A can be computed from the spacecraft ephemeris using Equations (12) and (13). Analysis has shown that the ISEE-C elevation angle computed in mission orbit will not be sensitive to errors in either ζ or ω_A . The maximum error in EL corresponding to the anticipated uncertainties in spacecraft ephemeris will be less than 0.01 degree. The uncertainty in EL will thus be a function of $\dot{\beta}$ uncertainty alone. The variance in EL is computed as follows.

$$\sigma_{\text{EL}}^2 = \frac{\sigma_{\dot{\beta}}^2}{\omega_A^2 \cos^2 \zeta} \quad (22)$$

where $\sigma_{\dot{\beta}}^2 = [h_i]^T [P] [h_i]$

$[P]$ is the covariance matrix of error in the analytic curve coefficients

$[h_i] = \partial \dot{\beta} / \partial C_i$, where C_i are the analytic curve coefficients

Note that $[P]$ should be computed using the maximum relative uncertainty in β measurements, $\sigma_{\beta \text{ MEASUREMENT}}^2$. This will avoid an unrealistically large weighting of the Sun angle measurements.

The variance in β can be computed as follows

$$\sigma_{\beta}^2 = -g_i^T [P] g_i + \sigma_{\beta \text{ BIAS}}^2 \quad (23)$$

where $[g_i] = \partial\beta/\partial C_i$
 $\sigma_{\beta \text{BIAS}}^2$ = Sun angle bias variance

The attitude uncertainty (standard deviation of the arc length between the true and estimated spin axis attitude vectors) is

$$\sigma_{\text{ARC}} = \sqrt{\sigma_{\text{EL}}^2 + \sigma_{\beta}^2} \quad (24)$$

FSS-Only Prelaunch Attitude Uncertainty Predictions: ISEE-C FSS-only pre-launch attitude uncertainty predictions are presented in Figure 7 as a function of data span and data rate. Each Sun angle sample consists of a group of averaged measurements such that the effects of measurement noise and residual spacecraft nutation (following maneuvers) are minimized. A value of 0.03 degree was used for the relative uncertainty in β measurements, $\sigma_{\beta \text{MEASUREMENT}}$, in the computation of the covariance matrix of error [P]. This corresponds to the maximum error observed following sensor calibration. A value of 0.20 degree was used for $\sigma_{\beta \text{BIAS}}$. This corresponds to the aforementioned maximum anticipated offset between the spacecraft principal axes and geometric axes.

Referring to the figure, it is seen that the ISEE-C attitude can be determined to within an accuracy of 1 degree or better using data arcs of at least 10 days. Attitude accuracy is a function of data rate for shorter data arcs. Improved accuracies are obtained using the higher data rates. However, for data arcs exceeding 20 days, attitude accuracy cannot be improved using higher data rates.

Applicability of FSS-Only Technique to Other Missions: Equation (19) can be solved for $\dot{\beta}$ as follows.

$$\dot{\beta} = \omega_A \cos \zeta \sin \text{EL} - \tan \zeta \cos \text{EL} \quad (25)$$

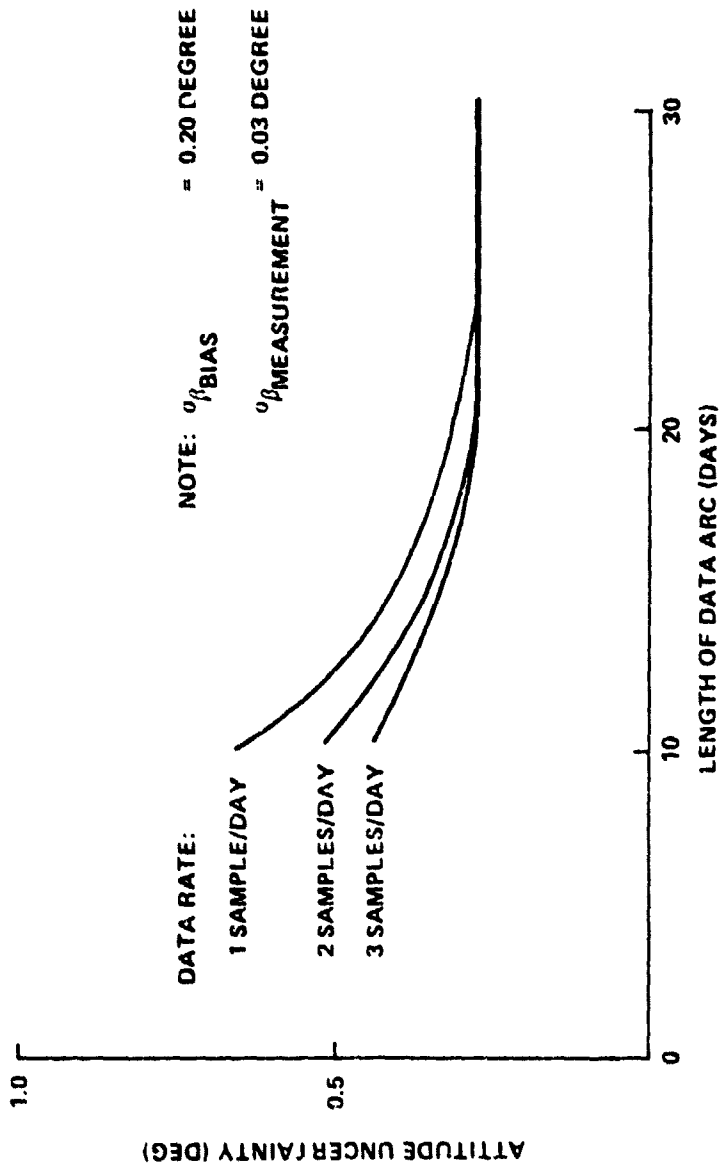


Figure 7. FSS-Only Definitive Attitude Determination Uncertainty (Prelaunch Predictions)

Differentiating with respect to EL , one obtains the following.

$$\frac{\partial \dot{\beta}}{\partial EL} = \omega_A \cos \zeta \cos EL + \tan \zeta \sin EL \quad (26)$$

Taking the inverse of the above expression,

$$\frac{\partial EL}{\partial \dot{\beta}} = \frac{1}{\omega_A \cos \zeta \cos EL + \tan \zeta \sin EL} \quad (27)$$

For ISEE-C, the motion of the spacecraft relative to the sunline is small. As a result, the maximum value of ζ is on the order of 0.1 degree. By inspection of Equation (27), it is seen that small errors in $\dot{\beta}$ will be transformed into large errors in the computation of EL when EL approaches 90 degrees. For example, when EL equals 60-degrees, the error magnification factor is approximately 2. Thus, the FSS-only attitude determination technique is not applicable to ISEE-C when EL is very large.

There are other missions to which the FSS-only technique can be applied. For example, spin stabilized geosynchronous satellites are often oriented toward the north celestial pole. Also, the solar radiation pressure torque effect is normally small. For such missions, EL will vary between ± 23.5 degrees. The maximum value of ζ will be less than 0.4 degree. The maximum $\dot{\beta}$ error magnification factor computed using Equation (27) is approximately 1.1. It is concluded that the FSS-only attitude determination technique can be applied to these missions. The attitude determination accuracy obtained will, of course, be a function of the relative accuracy of the Sun sensor.

Summary and Conclusions: Techniques have been developed to determine the ISEE-C spin axis attitude using a finite arc of smoothed Sun angle data. The

techniques differ from more conventional attitude determination methods in that ephemeris vectors are required only to transform the attitude results to standard coordinate frames. The slowly-varying ISEE-C spin axis attitude dynamics resulting from solar radiation pressure torque are automatically accounted for in the attitude determination process.

It is assumed that the ISEE-C FSS system will perform in orbit according to specifications. It is also assumed that the FSS mounting tolerances and ISEE-C spacecraft dynamic imbalance tolerances will not be exceeded. Given these assumptions, the ISEE-C spin axis attitude can be determined to within 1.0 degree with the FSS-only techniques using up to 30 days of FSS data. The FSS-only techniques can also be applied to other missions, such as spin stabilized geosynchronous missions.

INFRARED HORIZON SCANNER ATTITUDE
DATA ERROR ANALYSIS FOR SEASAT-A*

M. C. Phenneger, C. Manders,
C. B. Spence, Jr., M. Levitas,
and
G. M. Lerner

ABSTRACT

This talk presents the results of a study of the effect of variations in the Earth's seasonal and geographical horizon radiance on the location of the infrared horizon as measured by ITHACO scanwheels. ** Two types of variations are considered. These are (1) systematic variations of the mean (averaged over all longitudes) atmospheric radiance due to macroscopic changes in temperature as a function of latitude and season and (2) random variations in atmospheric radiance due to microscopic fluctuations (weather). The effect of variations in the scanner wheel speed on the attitude determination accuracy is also presented. The computed horizon radiance and wheel speed variation - induced attitude errors are then combined with errors caused by sensor alignment and electronics tolerances to obtain an overall estimate of the Seasat-A pitch and roll angle accuracy.

* Work supported by the Attitude Determination and Control Section, Goddard Space Flight Center, National Aeronautics and Space Administration, under Contract No. NAS 5-11999.

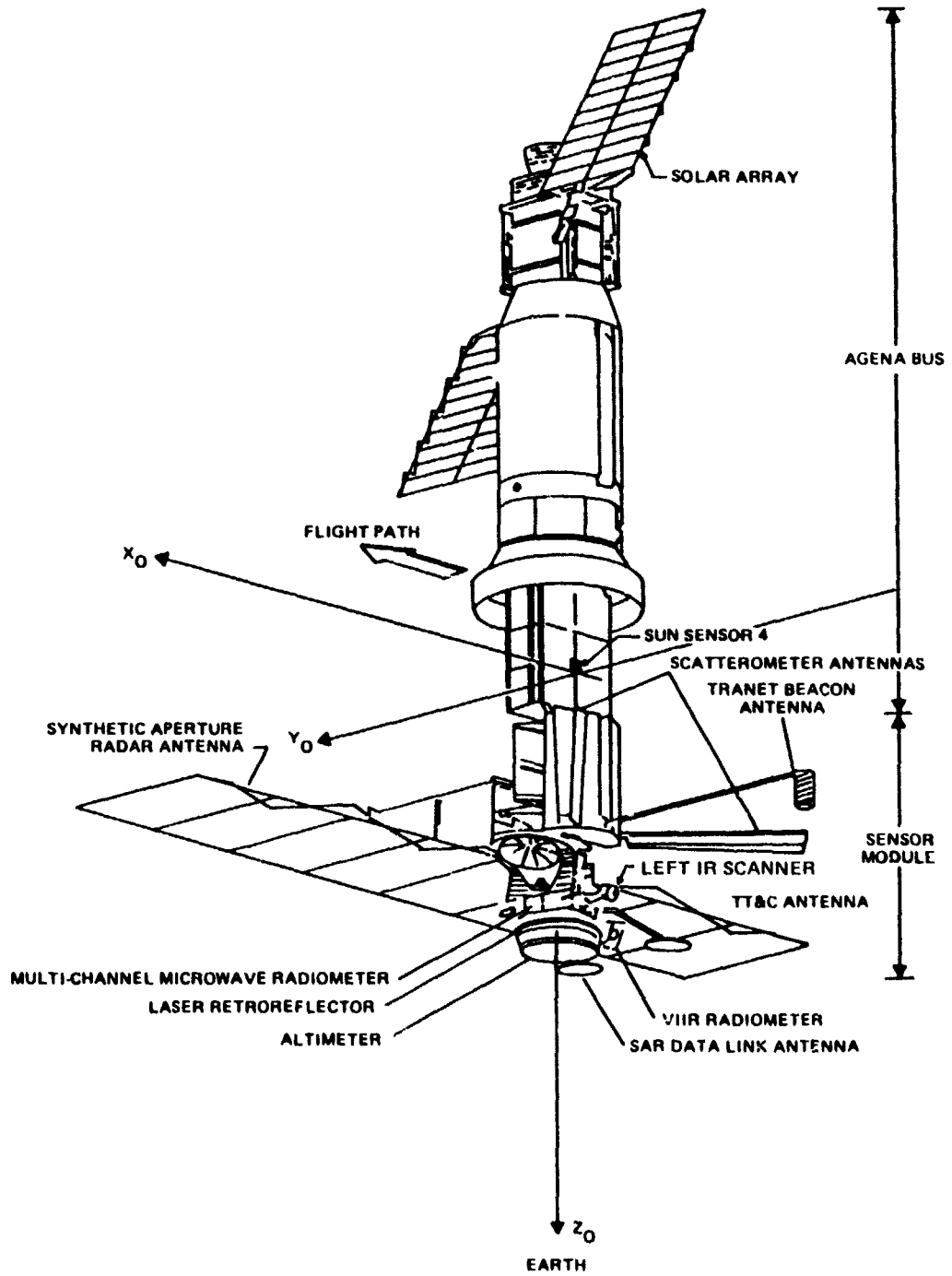
** Scanwheel is registered trademark of ITHACO, Inc.

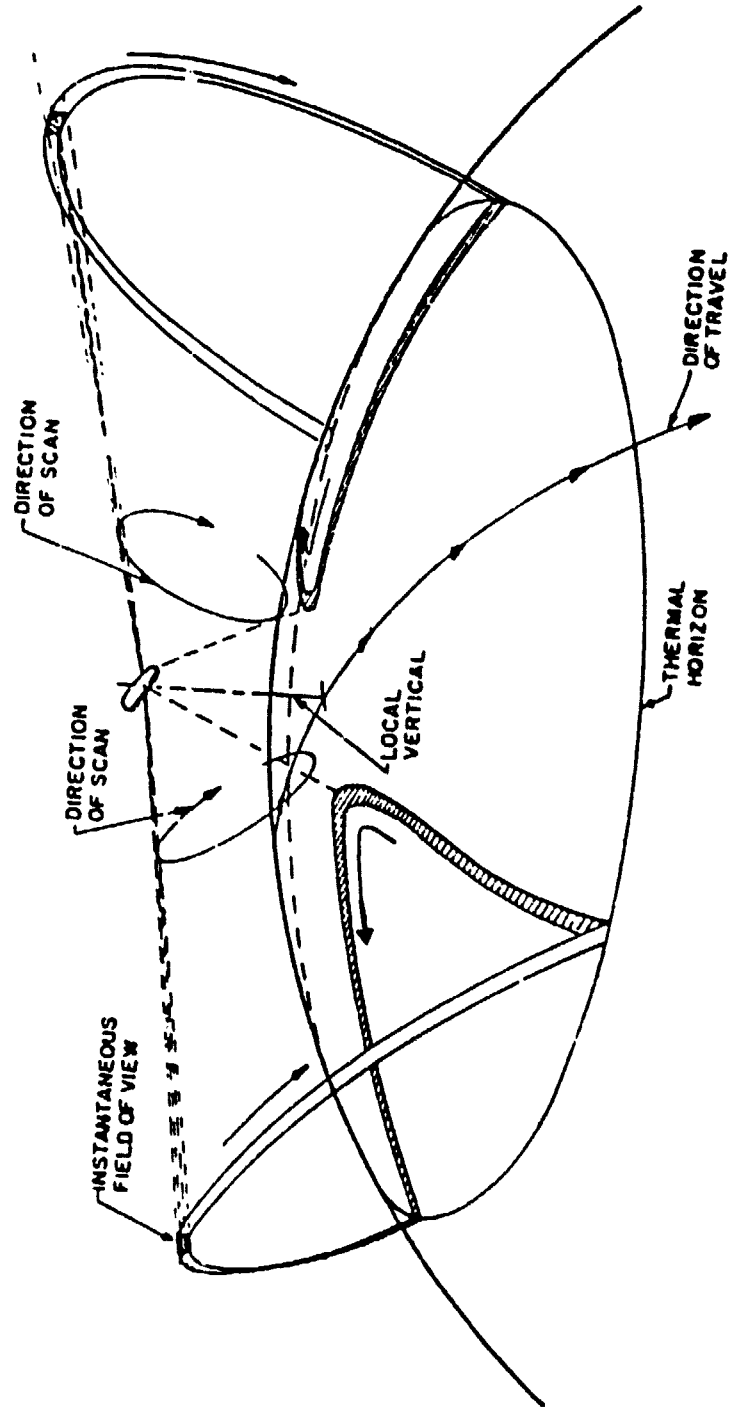
THE SEASAT-A INFRARED SCANNER ATTITUDE ERROR ANALYSIS¹³

M. PHENNEGER, G. LERNER, C. MANDERS, C. SPENCE, M. LEVITAS

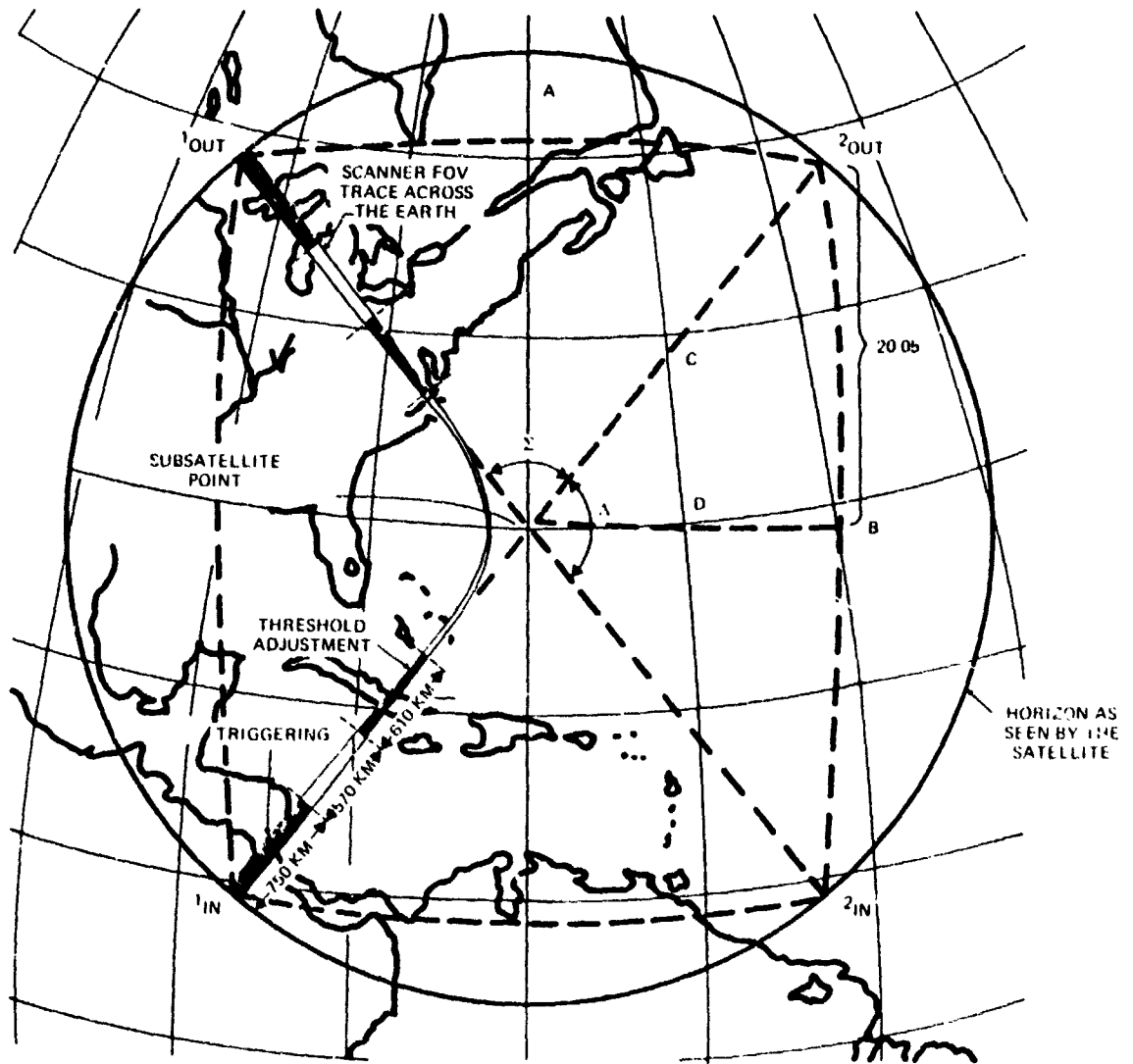
- SEASAT-A ATTITUDE SYSTEM OVERVIEW
- SOURCES OF ERROR IN THE IR SCANNER ATTITUDE SYSTEMS
- THE RESPONSE OF THE SEASAT IR SCANNERS TO GEOGRAPHICAL VARIATIONS IN THE EARTH'S INFRARED RADIANCE
- THE RESPONSE OF THE IR SCANNERS TO COLD CLOUDS
- SUMMARY OF RESULTS

ON-ORBIT SEASAT CONFIGURATION

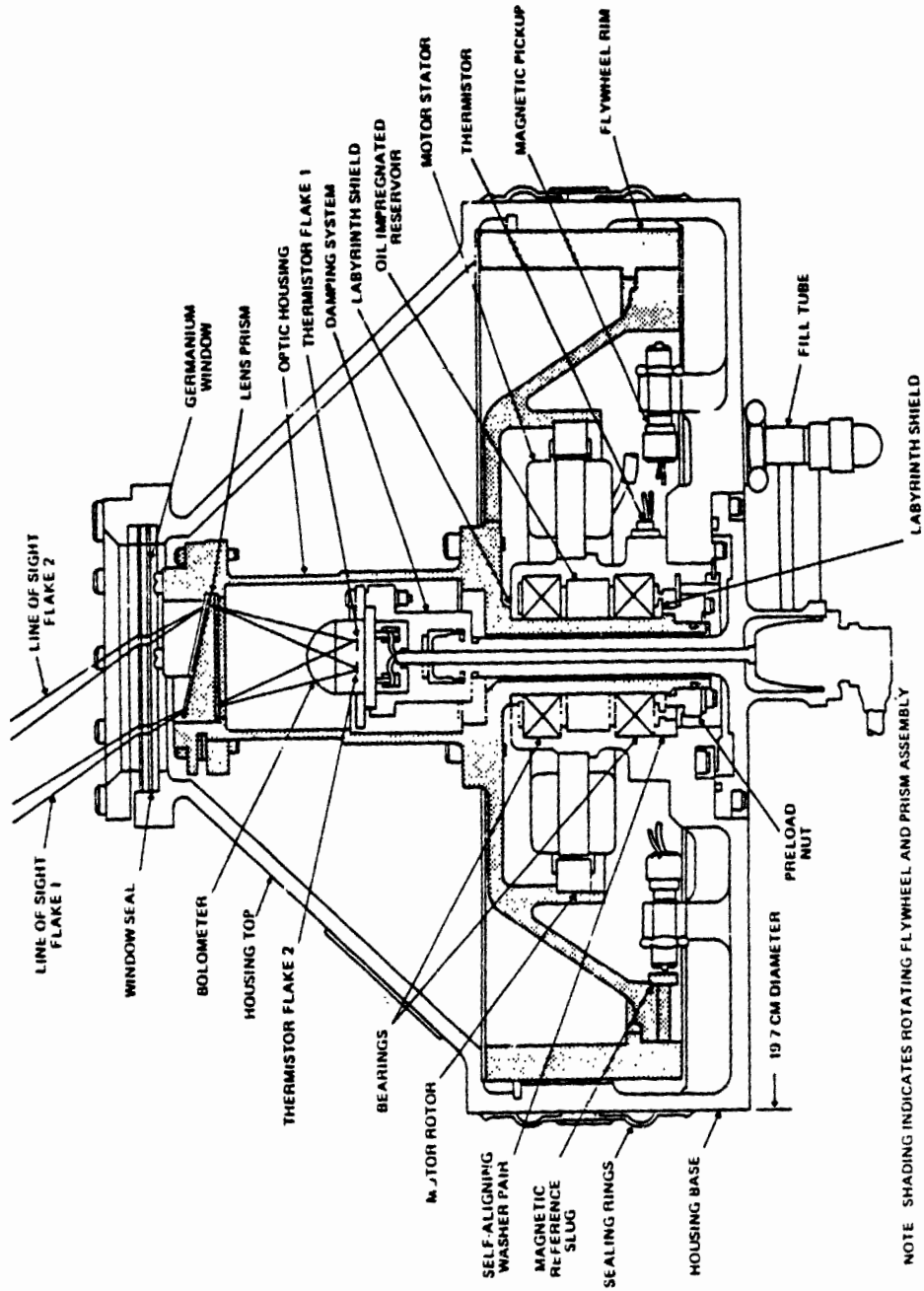




PATH OF HORIZON SCANNER ACROSS THE EARTH



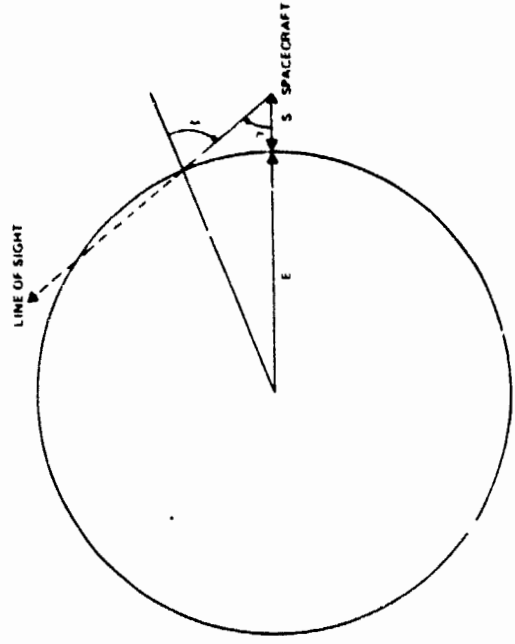
SAS-3 TYPE B SCANWHEEL (COURTESY ITHACO CORPORATIC I)



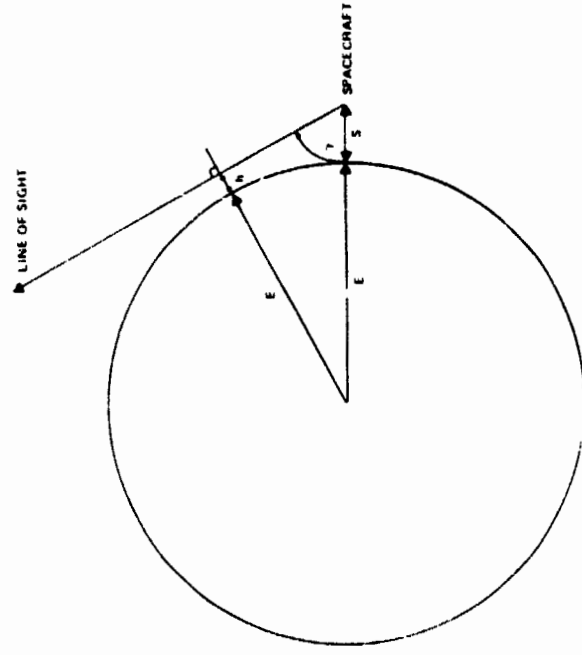
ERROR SOURCES

- IR SCANNER MISALIGNMENT
- VARIATIONS IN THE GEOMETRY OF THE FIELD OF VIEW
- ELECTRONIC NOISE
- LONG AND SHORT-TERM INSTABILITIES IN THE ONBOARD ELECTRONICS
- SCANNER WHEEL SPEED EFFECTS
- GEOGRAPHIC VARIATIONS IN THE EARTH'S INFRARED RADIANCE

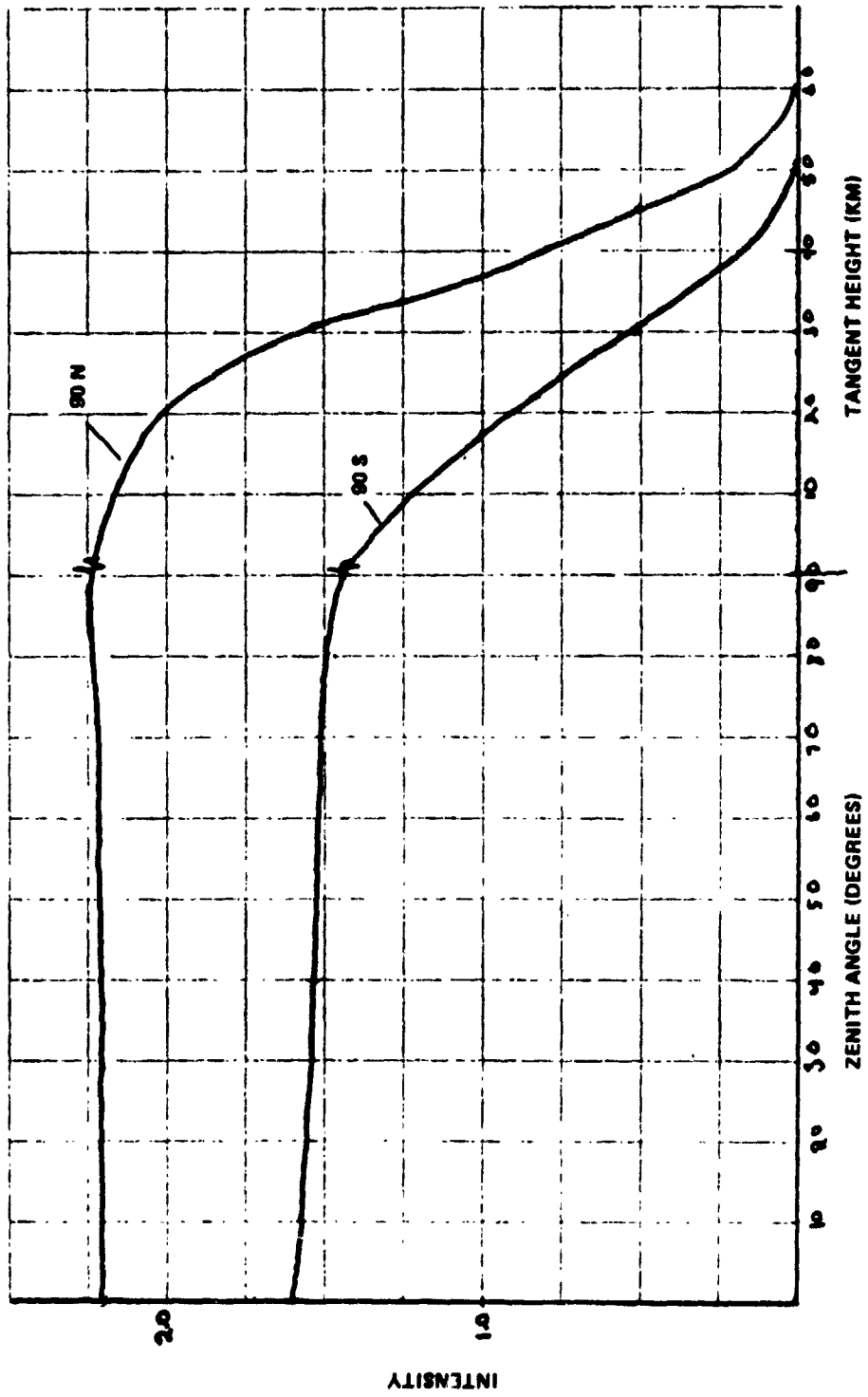
DEFINITION OF ZENITH ANG. E. ζ



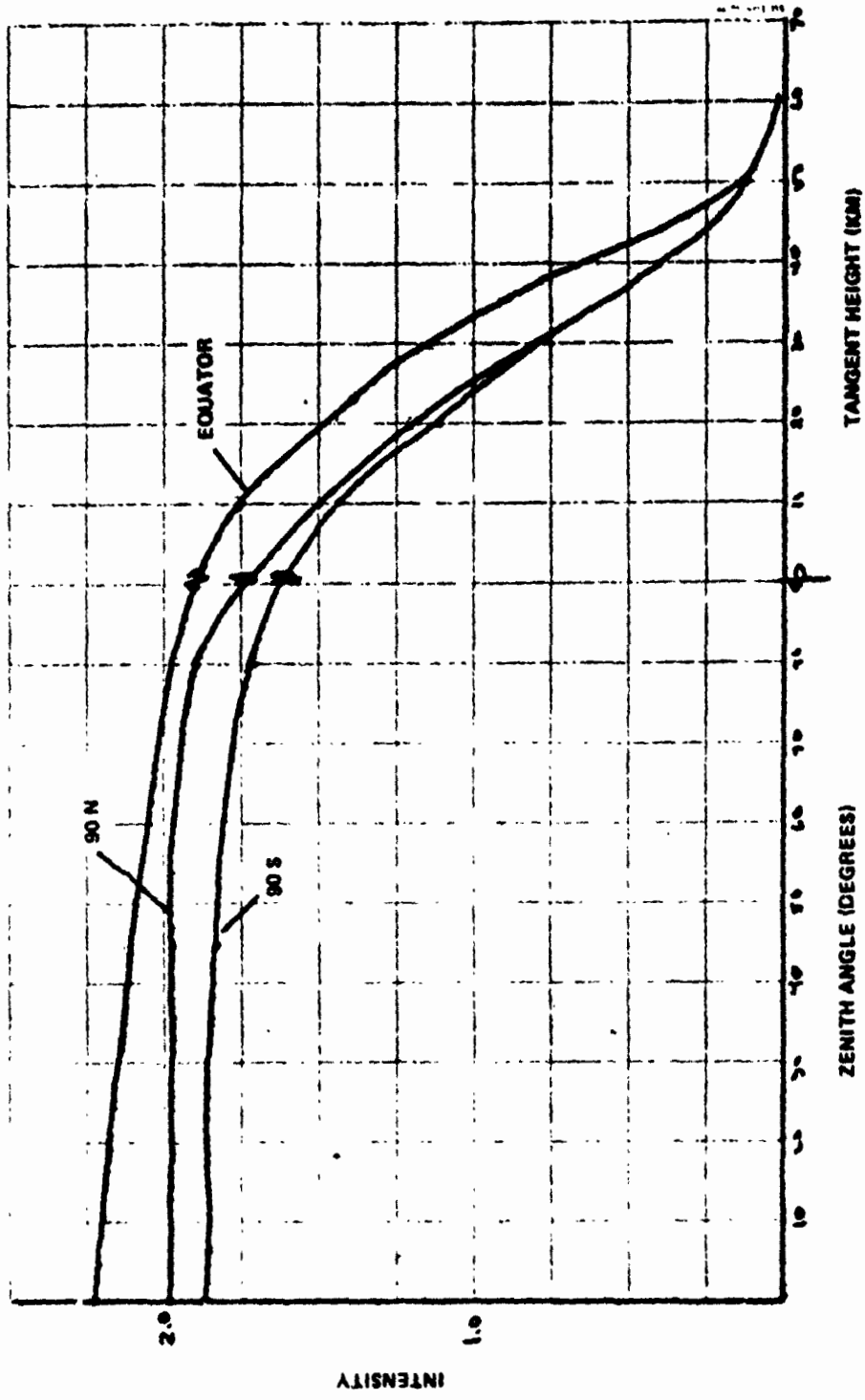
DEFINITION OF TANGENT HEIGHT, h

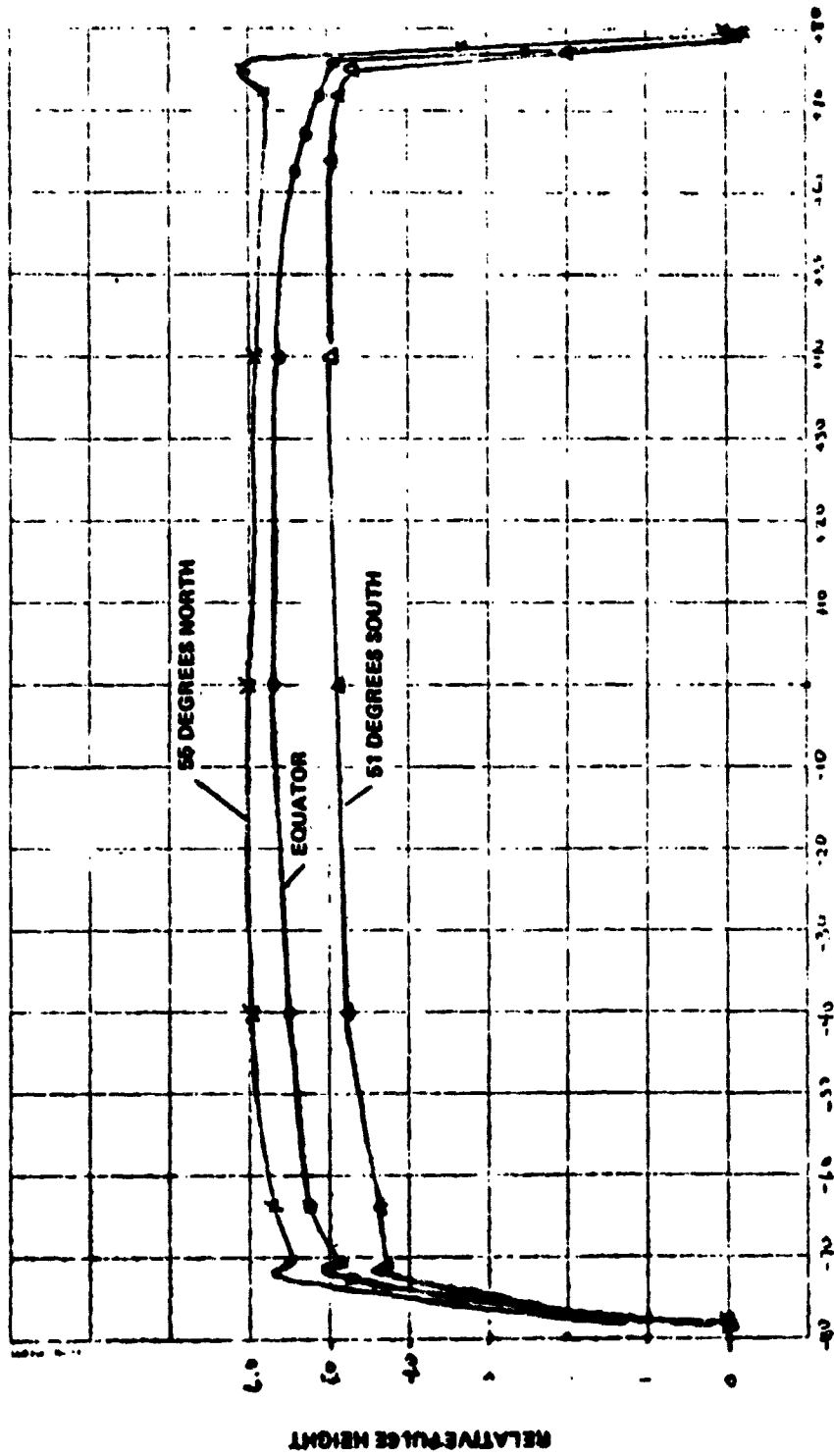


EARTH RADIANCE PROFILES FOR THE
NORTH AND SOUTH POLE IN JULY



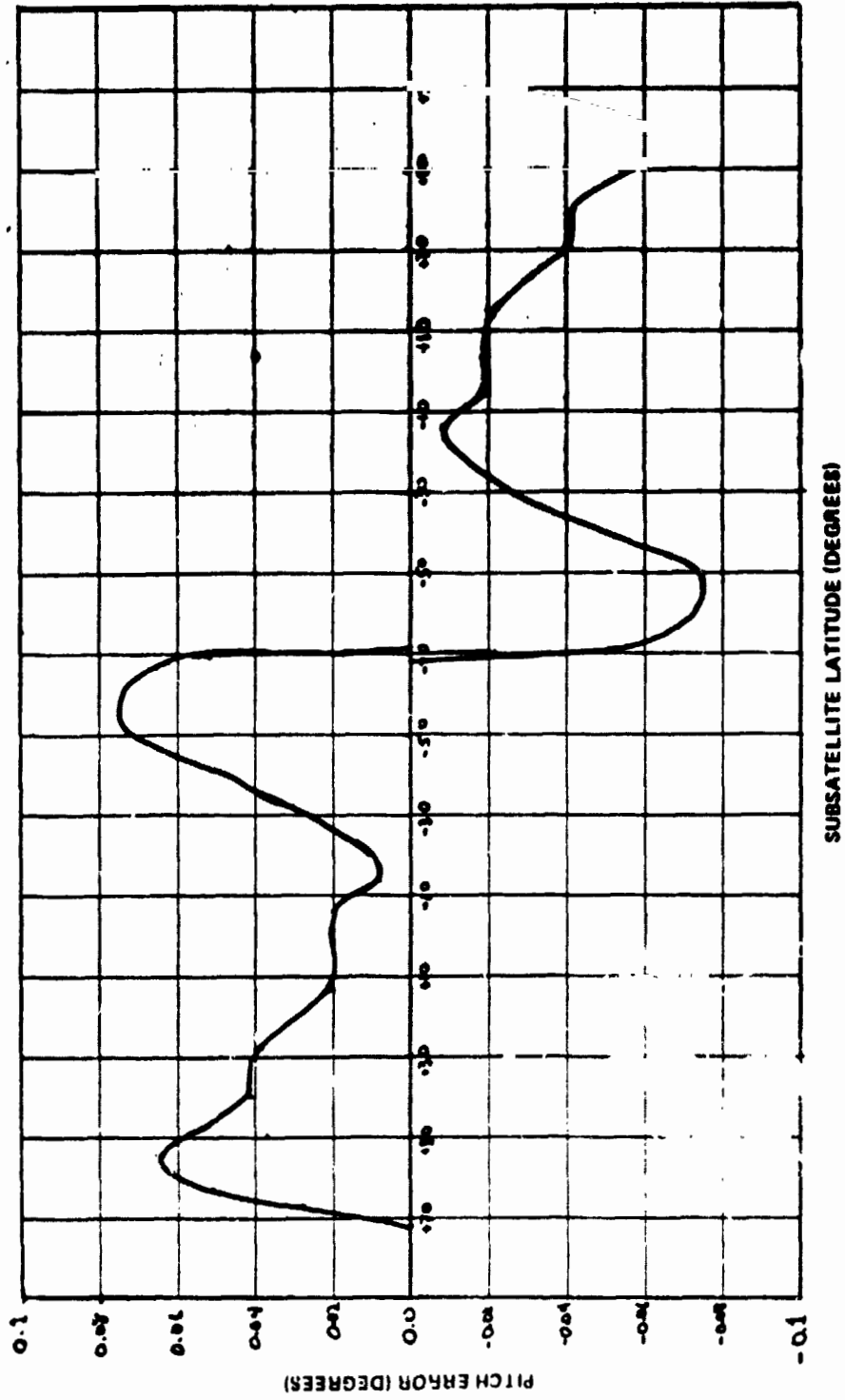
EARTH RADIANCE PROFILES FOR THE
NORTH AND SOUTH POLE AND EQUATOR IN APRIL



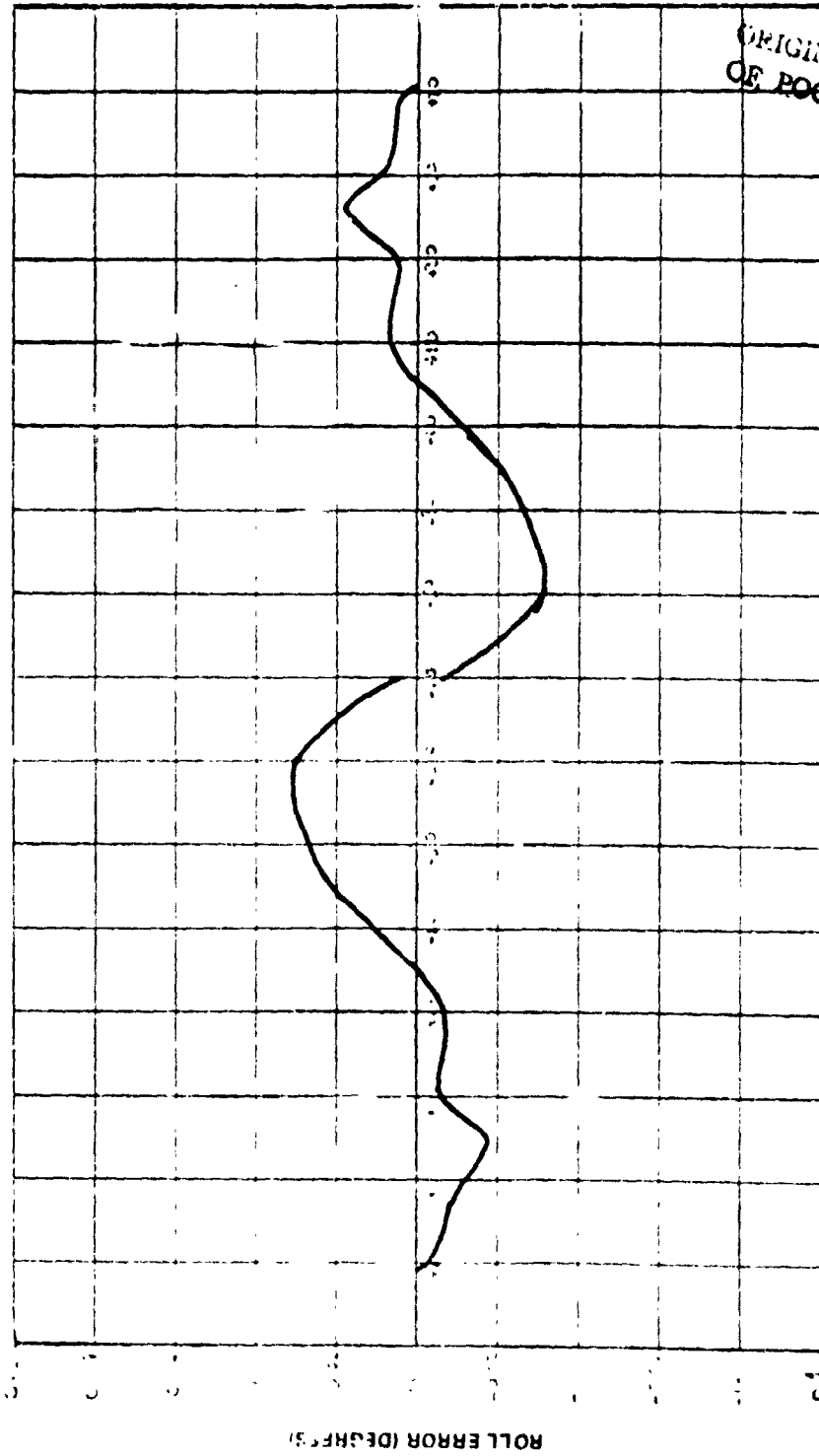


RIGHT IR SCANNER OUTPUT PULSES IN JULY

PITCH ERRORS FROM THE GEOGRAPHIC VARIATIONS
 IN THE EARTH'S INFRARED HORIZON RADIANCE IN JULY
 (SEASAT-A)



PITCH ERRORS FROM THE GEOGRAPHIC VARIATIONS
IN THE EARTH'S INFRARED HORIZON RADIANCE IN APRIL
(SEASAT-A)



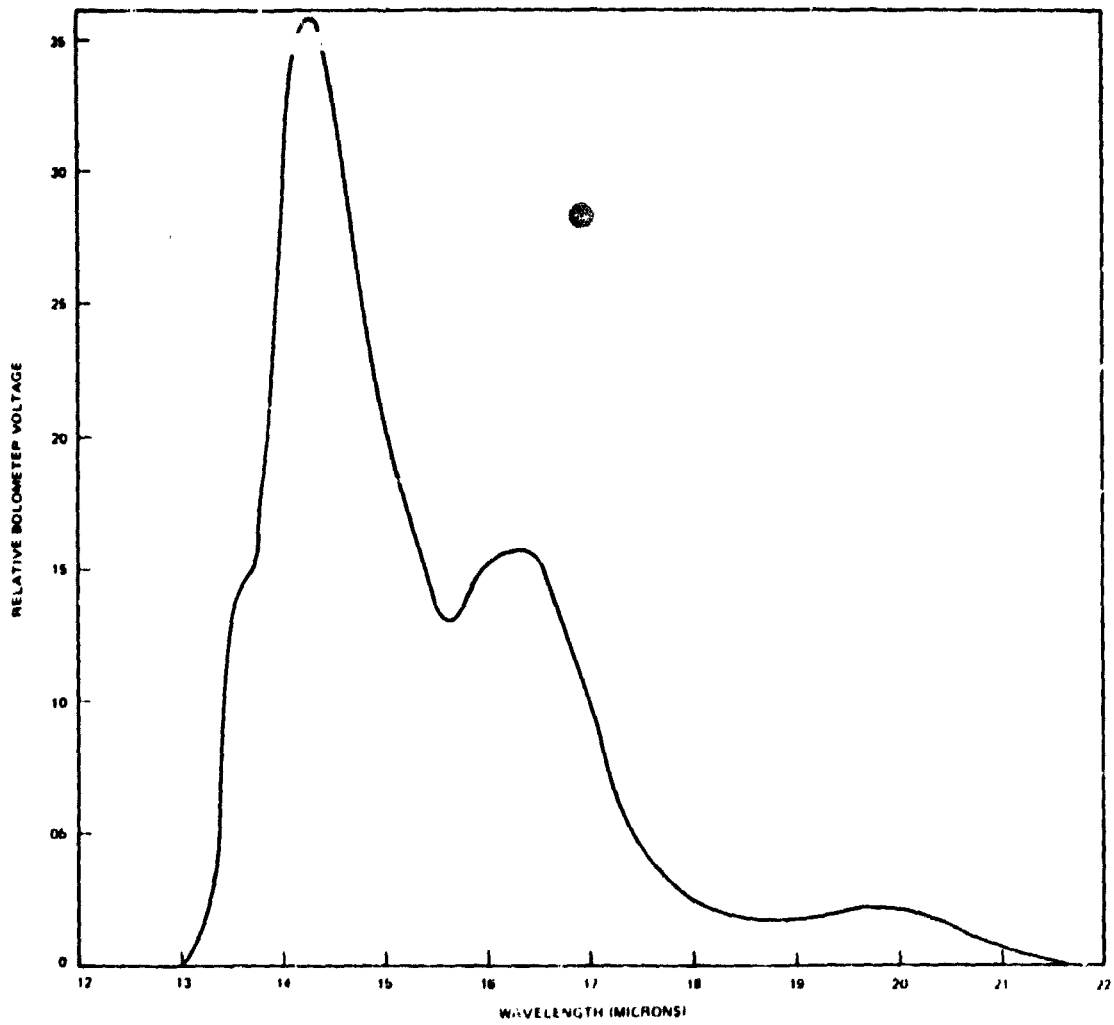
ORIGINAL PAGE IS
OF POOR QUALITY

SUBSATELLITE LATITUDE (DEGREES)

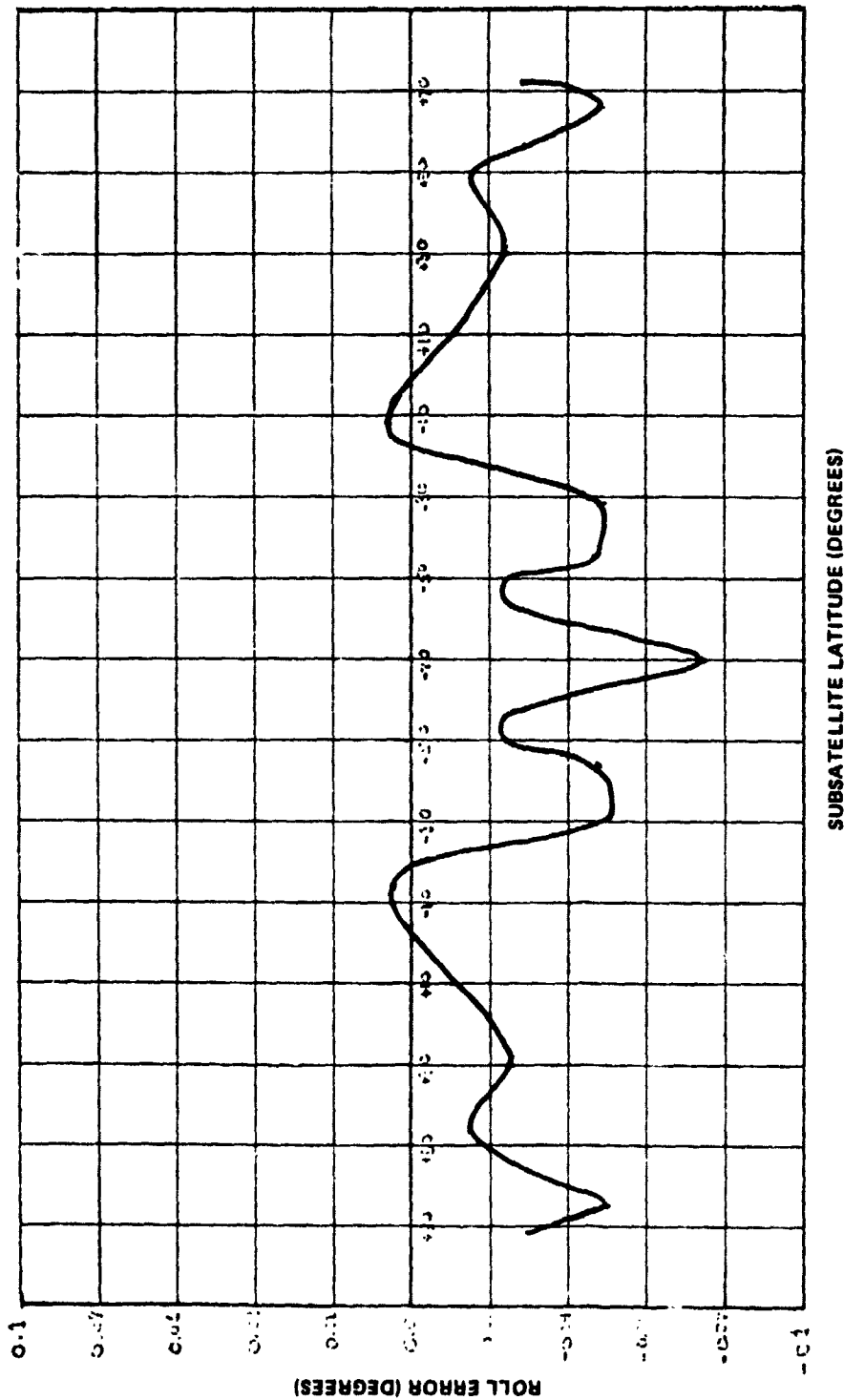
ROLL ERROR (DEGREES)

01

SEASAT OPTICS SPECTRAL RESPONSE

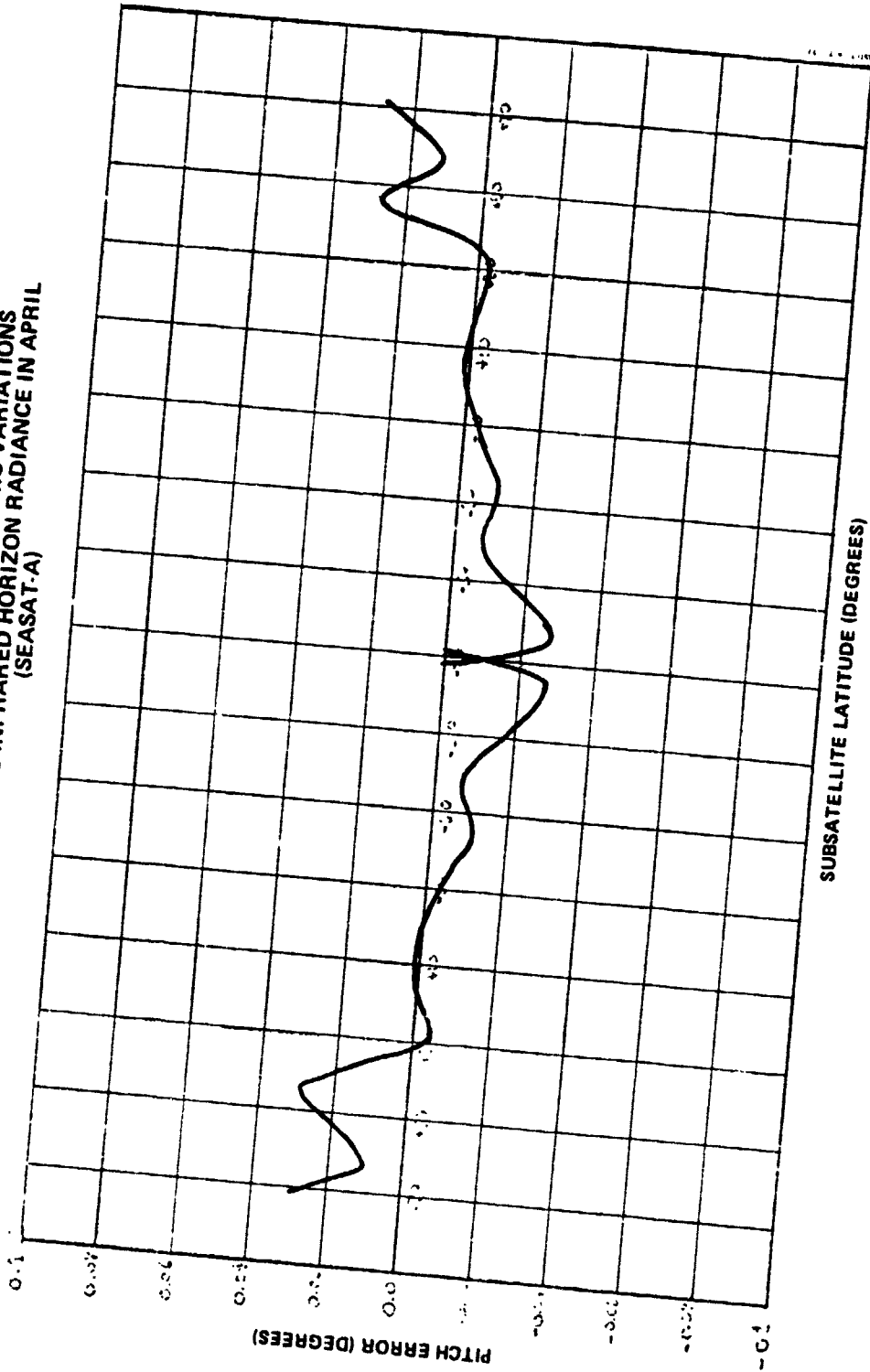


ROLL ERRORS FROM THE GEOGRAPHIC VARIATIONS
IN THE EARTH'S INFRARED HORIZON RADIANCE IN JULY
(SEASAT-A)

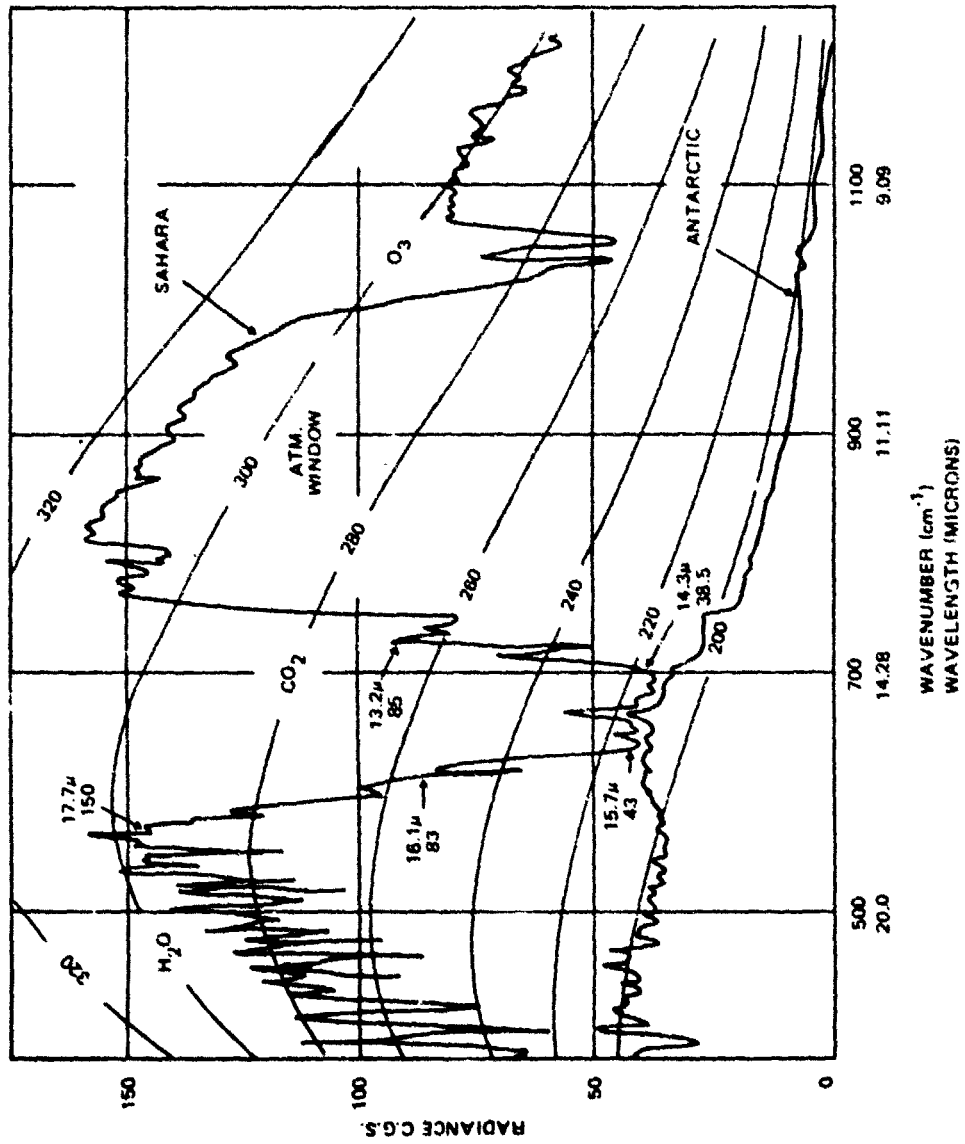


Handwritten signature or initials

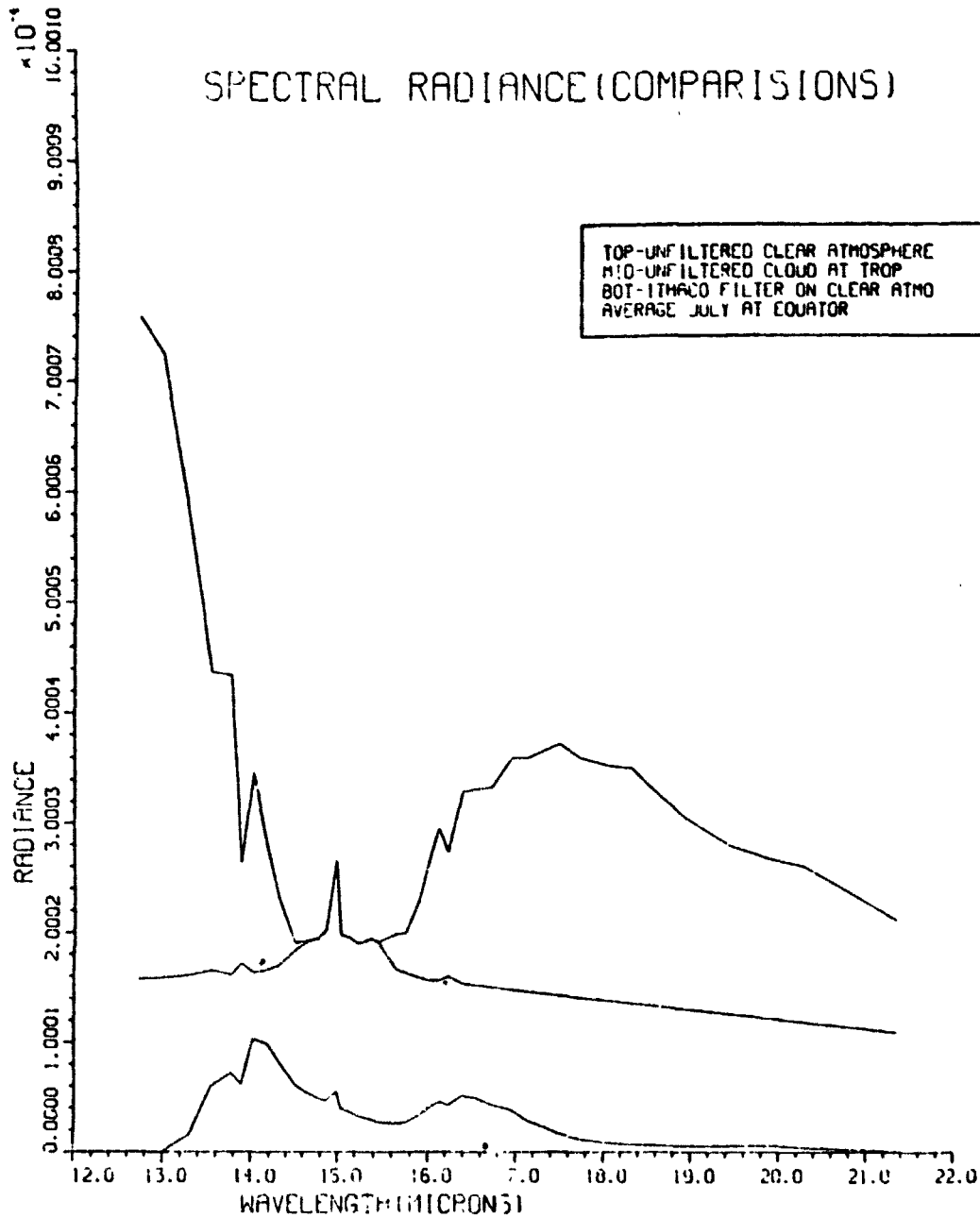
**ROLL ERRORS FROM THE GEOGRAPHIC VARIATIONS
IN THE EARTH'S INFRARED HORIZON RADIANCE
(SEASAT-A)**



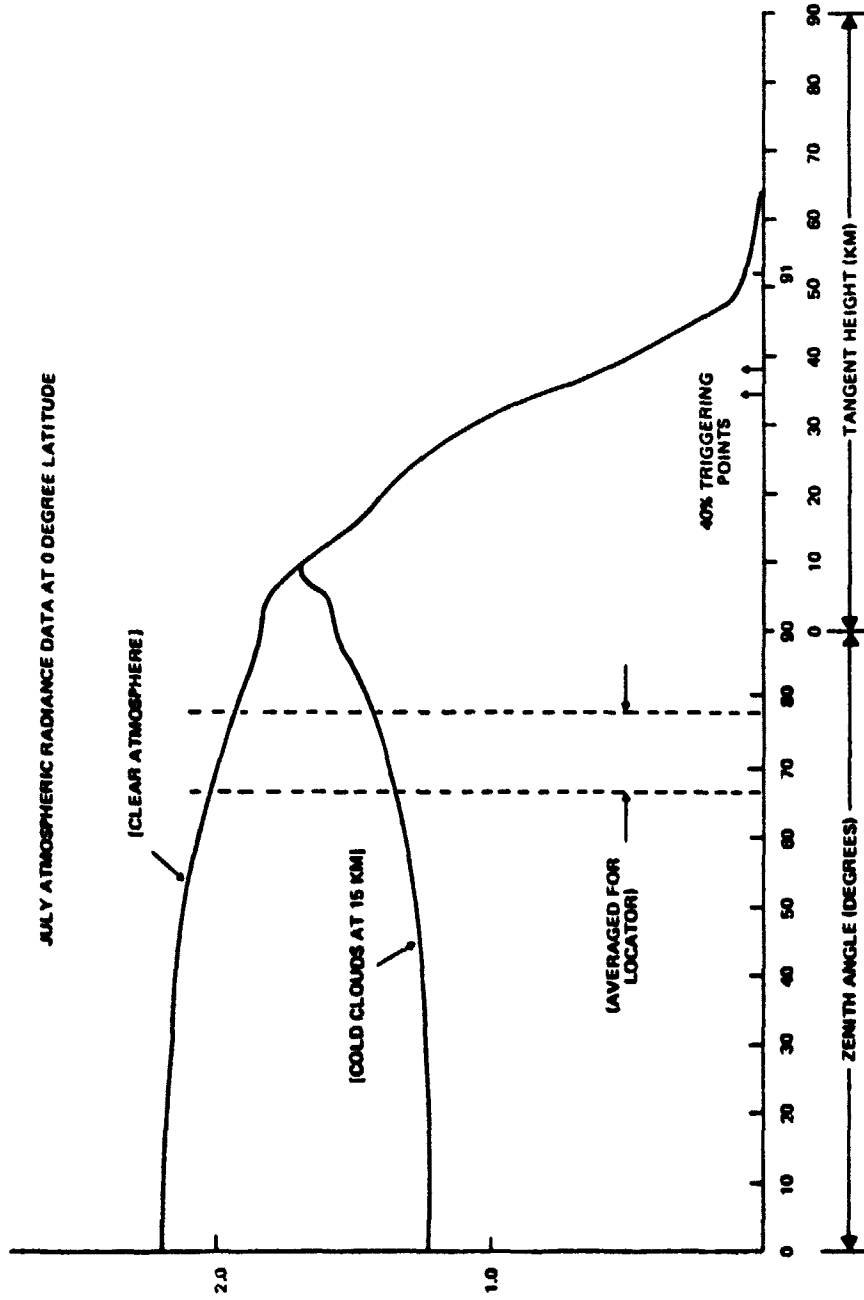
THE EARTH IR EMISSION FROM THE SAHARA AND THE ANTARCTIC



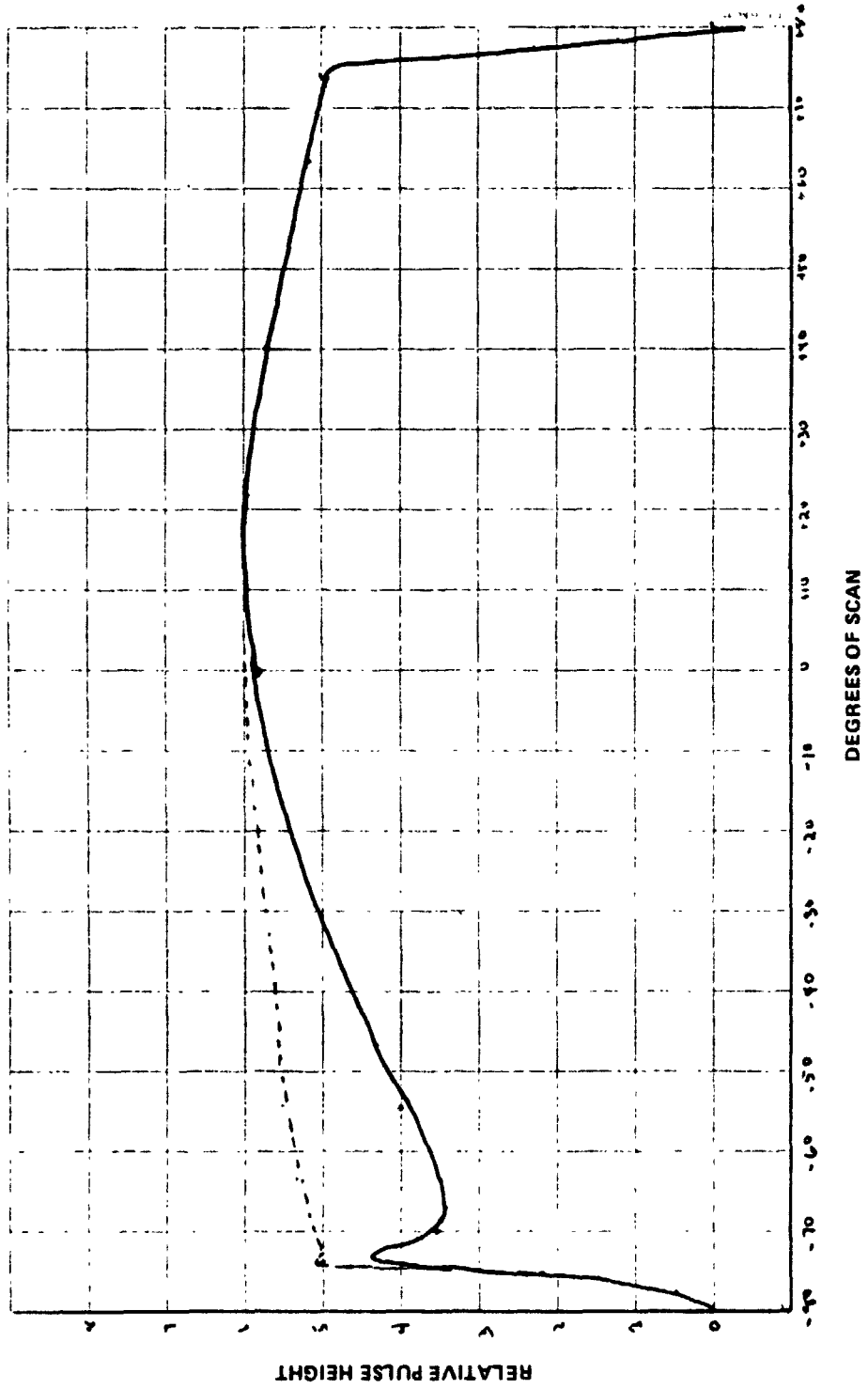
SIMULATION OF THE COLD CLOUD EFFECT ON THE EARTH'S RADIATION SPECTRUM



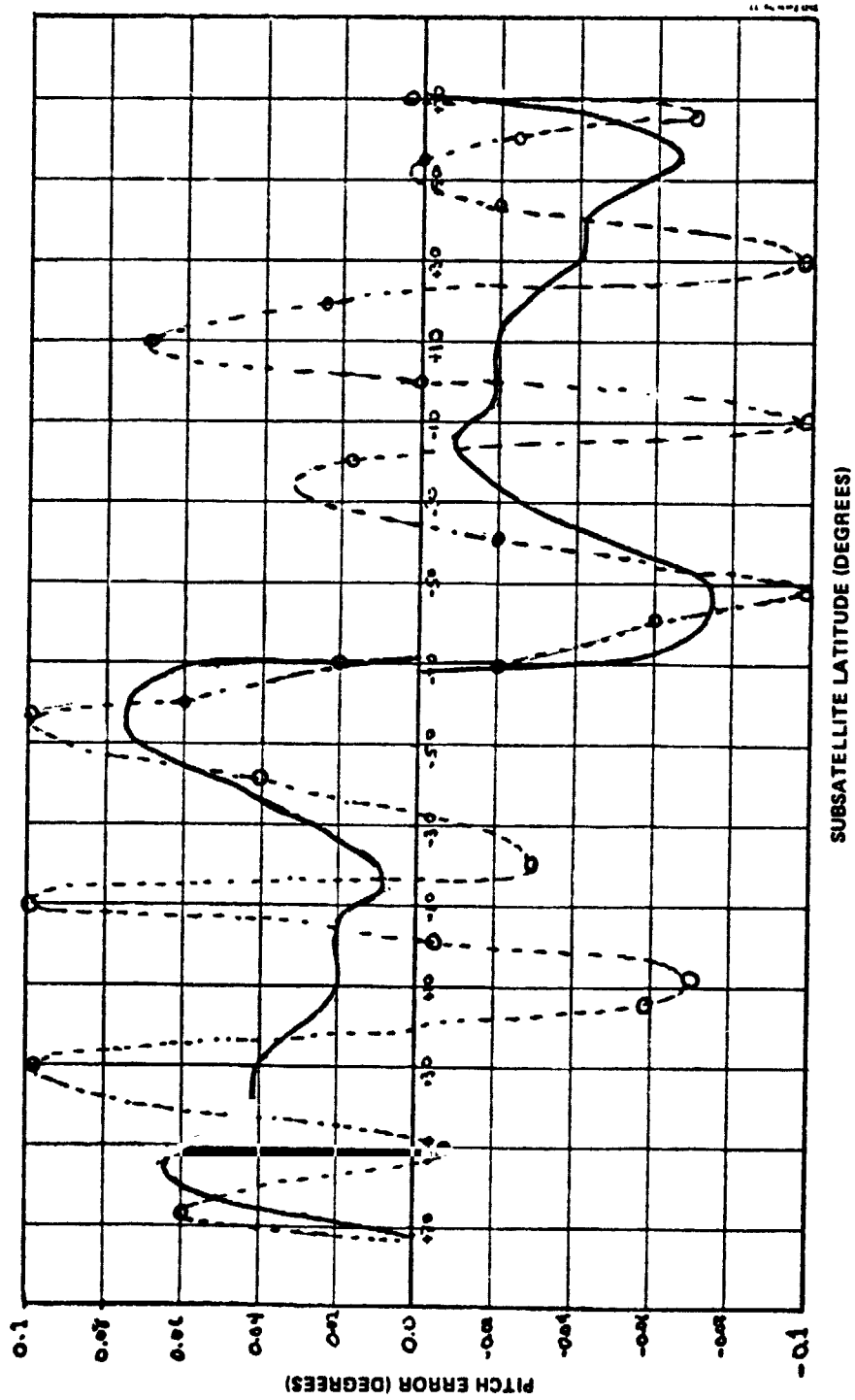
AVERAGE AND COLD CLOUD RADIANCE PROFILES AT THE EQUATOR IN JULY



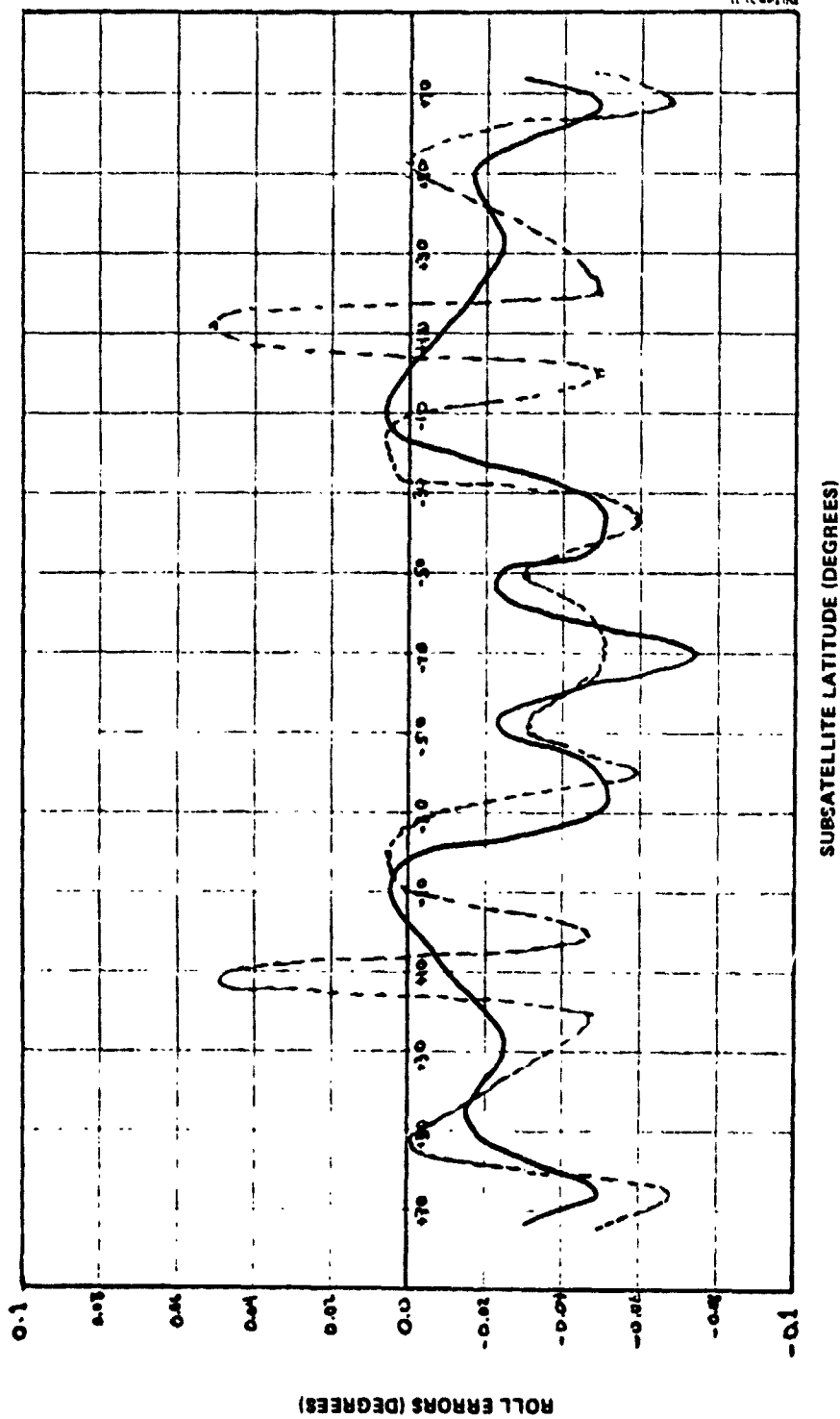
THE RIGHT SCANNER EARTH PULSE AT A
SUBSATELLITE LATITUDE OF 8.9 DEGREES NORTH
WITH AND WITHOUT A COLD CLOUD



JULY PITCH ERRORS WITH COLD CLOUDS IN THE
EARTH RADIANCE MODEL AT $\pm 80, \pm 80, \pm 40$
AND 0 DEGREE LATITUDE



JULY ROLL ERRORS WITH COLD CLOUDS IN THE EARTH RADIANCE MODEL
AT ± 90 , ± 80 , ± 40 AND 0 DEGREES LATITUDE



CONCLUSIONS

- GEOGRAPHIC HORIZON RADIANCE VARIATIONS CONTRIBUTE A LARGE PART OF THE ERROR
- A VARIABLE THRESHOLD SYSTEM IS CAPABLE OF REDUCING THE PEAK ERRORS BY ROUGHLY A FACTOR OF TWO
- THE ERRORS INDUCED BY GEOGRAPHIC EFFECTS ARE LARGER IN JANUARY AND JULY THAN IN APRIL AND OCTOBER BECAUSE THE EARTH RADIANCE PROFILE TENDS TO BE MORE UNIFORM IN APRIL AND OCTOBER
- COMPENSATING FOR THE GEOGRAPHICAL EFFECTS CAN BE DONE WITH AN ACCURACY THAT IS LIMITED BY THE SENSITIVITY OF IR SCANNER TO THE WEATHER
- THE SENSITIVITY OF AN IR SCANNER TO GLOBAL WEATHER IS PROPORTIONAL TO THE PERCENTAGE OF SPECTRAL BANDPASS BELOW 14.3 MICRONS AND ABOVE 15.7 MICRONS
- FOR THE SEASAT IR SCANNER THE EFFECTS FROM CLOUDS AT THE TOP OF THE TROPOPAUSE ARE ABOUT 0.1 DEGREE
- THE COLD CLOUD EFFECT IS MORE PRONOUNCED AT THE EQUATOR THAN AT THE POLES
- THE ACCURACY OF APPLYING A CORRECTION TO THE SEASAT IR SCANNER DATA FOR SEASONAL AND GEOGRAPHIC RADIANCE VARIATIONS IS LIMITED BY COLD CLOUD PHENOMENON WHICH ARE A DIRECT RESULT OF THE RELATIVELY BROAD BANDPASS OF THE IR SCANNER

6M

ATTITUDE ACQUISITION CONTINGENCY STUDIES
FOR
THE APPLICATIONS EXPLORER MISSIONS-A/HEAT CAPACITY
MAPPING MISSION (AEM-A/HCMM) SPACECRAFT

Whittak Huang, Mihaly G. Grell
and
Gerald M. Lerner

Computer Sciences Corporation

ABSTRACT

The Heat Capacity Mapping Mission (HCMM) is the first of a series of satellites utilizing a basic, modularly designed launch vehicle and satellite support system called the Applications Explorer Missions (AEM) HCMM, to be launched in April 1978 into a 600 km altitude, Sun-synchronous polar orbit, will conduct a thermal mapping of the North American continent to investigate Earth resources' availability. The spacecraft has an attitude control system consisting of wheel-mounted infrared horizon sensor oriented along the negative body Y-axis (the orbit normal for the nominal attitude), a 3-axis magnetometer and 3-orthogonal electromagnetic coils. The magnetometer data is used for mission-mode 3-axis attitude control (pitch = roll = yaw = 0). Control laws, first proposed by Saymor Kant, Peter Hui and Joseph Lidston, which relate the attitude data from the sensors to the control torque commands are used by the onboard attitude computer to achieve attitude acquisition and to maintain the mission-mode attitude.

Attitude acquisition requires maneuvering the spacecraft from the attitude after separation (spinning about the body Z-axis along the velocity vector) to the mission mode attitude. Attitude maintenance consists of pitch control by modulating the scanner wheel speed, momentum control by commanding the X- and Z-axis electromagnets, and roll and nutation control by commanding the Y-axis electromagnet. Yaw is controlled indirectly via gyrocompassing.